NUI Galway
OÉ Gaillimh

Design, Analysis and Testing of a Spiral Blade Vertical-Axis Tidal Turbine

A thesis submitted to the National University of Ireland, Galway
as fulfilment of the requirements for the Degree of Doctor of Philosophy

Shane C. Heavey

April 2021

Research Supervisors: Prof Seán Leen & Dr Patrick McGarry

Mechanical Engineering, National University of Ireland, Galway

Abstract

The aim of this thesis is to develop a combined analytical, computational and experimental methodology for characterisation and optimisation of the hydrodynamic performance of a novel vertical-axis tidal turbine concept. A primary objective is to develop experimentally validated, efficient, numerical predictive tools with the capability to allow the design and assessment of different turbine configurations for optimal power performance. The two numerical modelling approaches adopted and developed are (1) blade element momentum (BEM) theory, developed within MATLAB®, and (2) computational fluid dynamics (CFD) methods, using the Reynolds-averaged Navier Stokes (RANS) equations within ANSYS Fluent®. The model predictions are supported and validated by physical test data from two facilities: (1) a new small-scale tow tank facility setup at NUI Galway and (2) a state-of-the-art medium-scale recirculation flume at IFREMER, Boulogne Sur Mer. The methodologies and tools developed are more generally applicable for assessment of other existing and novel turbine designs.

The primary focus of the work is the patented Brí Toinne Teoranta (BTT) vertical-axis tidal turbine. This concept's novelty arises from the blades' spiral geometry, which is intended to overcome highlighted limitations of existing vertical-axis turbines, potentially giving increased power efficiency and improved self-starting capabilities over current vertical-axis designs. The design concepts encompass various blade shapes, including an ellipsoidal design, varying height-to-diameter ratios, and a cylindrical design. A set of geometric equations is established here for applicability to different blade design concepts.

A superior BEM method, including significant improvements in relation to finite aspect ratio effects, dynamic stall, and flow expansion, is presented for hydrodynamic power prediction of vertical-axis turbines. The results are validated against existing experimental data for SANDIA Darrieus and straight-bladed wind turbines. A coupled design optimisation study for the BTT concept is presented to identify peak power performance, with crucial turbine parameters investigated. The optimised turbine gives a 24% higher maximum power coefficient than the base case design; 18% higher than an equivalent straight-bladed design.

A RANS approach, based on transitional flow turbulence modelling, to determine lift and drag coefficients for the NACA0015 profile is developed. Results are validated against published experimental data for a broad range of angles of attack and Reynolds number. Flow visualisations highlight the distinct strengths of this modelling approach in the critical stall region for hydrofoils. Significantly improved BEM predictions are obtained using the RANS lift and drag coefficients, compared to the traditional panel-method dataset, for straight-bladed turbines. A 2D RANS model is also developed and validated for straight-bladed turbines. The new BEM approach achieves a similar accuracy level to the latter with significantly faster run-times, thus providing a viable design tool for vertical-axis tidal turbines.

A procedure for assessment of power performance of a scaled vertical-axis turbine is presented based on testing at the recirculation flume at IFREMER. The power curves for two BTT design concepts are compared using dimensionless parameters, mean power coefficient and tip-speed ratio (*TSR*) at equivalent operational Reynolds numbers. A new cylindrical BTT design (with horizontal support arms) gives more than 25% higher maximum power coefficient than the spherical BTT profile.

An accurate 3D RANS model of the optimised BTT turbine is presented based on a rigorous model development approach. The converged model uses sliding-mesh RANS modelling approach with SST Transition turbulence. The model predicts the peak power coefficient within 6%. Excellent correlation of downstream CFD-predicted and measured flow velocities is demonstrated, providing further confidence in the 3D CFD model.

A comparative assessment of the different modelling approaches developed with the experimental data for the novel BTT turbine design showed that the BEM model, with CFD dataset for NACA 0015 profile, (i) reduced the root means square error by 30%, over the traditional panel method dataset and (ii) gave comparable levels of accuracy to the full 3D CFD simulations for peak power and optimal *TSR*, at a considerably lower computational cost.

A towing tank was designed, developed and fabricated for in-house testing of small-scale prototypes. The effect of turbine orientation on measured torque under constant flow conditions was studied. BEM and CFD models of rotationally constrained turbines gave general agreement with experimental measurements in terms of the effect of towing velocity on torque.

Published Work

The following papers were published during this PhD:

S. Heavey, S. Leen, P. McGarry, "Analytical modelling of a novel tidal turbine," Proceedings of the Twenty-sixth International Ocean and Polar Engineering Conference, Rhodes, Greece, June 26th-July 1st, 2016

S. Heavey, S. Leen, P. McGarry, "Hydrodynamic Modelling of a Vertical Axis Tidal Turbine Using CFD and BEM Methods," European Wave and Tidal Energy Conference, Cork, Ireland, August 28th-September 1st, 2017

S. Heavey, S. Leen, P. McGarry, "Hydrodynamic design and analysis of a novel vertical axis turbine," International Journal of Offshore and Polar Engineering, Volume 28, Issue 4, December 2018

S. Heavey, S. Leen, P. McGarry, "An efficient computational framework for hydrofoil characterisation and tidal turbine design," Ocean Engineering, Volume 171, January 2019

Acknowledgements

First and foremost, I would like to thank my supervisors, Prof Seán Leen, and Dr Patrick McGarry, for their invaluable assistance and direction throughout this research. Your expertise was invaluable in formulating the research questions and methodology, and the insightful feedback you provided pushed me to sharpen my thinking and brought my work to a higher level.

I want to thank MaREI, Science Foundation Ireland (SFI) and Brí Toinne Teoranta for funding this research. I would also like the EU Research and Innovation Programme for their funding through the MaRINET 2 Horizon 2020 project to support the testing at IFREMER in Boulogne-sur-Mer.

I am eternally grateful to Dr Bernard McGuire (RIP), the inspiration behind this turbine design concept. From my limited time spent with Bernard, I could see his immense character and passion for invention. His innovative mind was an inspiration to me. I offer a special thank you to Bobby Willis, whose support and guidance was invaluable throughout my PhD. Bobby always provided encouragement and a helping hand whenever required. Also, special mention to Geraldine Daly, who always made me feel welcome each time I visited Boyle.

I would like to thank the NUI Galway technical staff, notably Bonaventure Kennedy, William Kelly, Pat Kelly, Dermot McDermott and Edward Killculen. The help and guidance they provided, aided the experimental testing performed in this research. Furthermore, I would like to thank my Graduate Research Committee members, Dr Nathan Quinlan, Dr Rory Monaghan, and Dr Padraig Molloy, for their advice throughout this research. I also thank the Masters' students Paul Burke, Heitor Gonzaga and Brian Connelly, who assisted in building the tow tank at NUI Galway

I wish to thank my friends and colleagues in NUIG, particularly Brian, Paddy, Enda, Conor, Donnacha, Tarek, Raydo, and the wider PhD research group. Special thanks to my friends outside of college also.

To my parents, Rory and Mairead, and sisters, Mary and Sinead, for your love, support, and everything you have done to get me this far, helping me through whatever obstacles I have faced, I am extremely grateful.

Finally, I could not have completed this thesis without the support of Órlaith, who provided encouragement, love and support as well as happy distractions to rest my mind outside of my research.

Table of Contents

List of Figures

List of Tables

Nomenclature

Symbol	Definition	Unit
$\ddot{\omega}$	Angular Acceleration	rad s^{-2}
α	Angle of Attack	^{o}
A	Area	m^2
AR	Aspect Ratio	-
$\bar{P}$	Average Power	W
$\bar{C}_P$	Average Power Coefficient	-
$\bar{Q}$	Average Torque	N m
$\bar{C}_{\mathrm{Q}}$	Average Torque Coefficient	-
a	Axial Induction Factor	-
β	Blockage Ratio	-
Re_c	Blade Reynolds Number	-
Q_B	Blade Torque	N m
h_c	Camber to Chord Length Ratio	-
x, y, z	Cartesian Coordinates	-
L	Characteristic Length	m
c	Chord Length	m
Q_{cog}	Cogging Torque	N m
Δ	Delta/Change	-
ρ	Density	kg m^3
D	Diameter	M
F_x^*	Dimensionless Force Coefficient	-
a'	Downstream Interference Factor	-
U'	Downstream Velocity	m s^{-1}
C_D	Drag Coefficient	-
F_D	Drag Force	N
μ	Dynamic Viscosity	kg m^{-1} s^{-1}
Q_e	Electromagnetic Torque	N m
V_{ex}	Excitation Voltage	V
U_∞	Freestream velocity	m s^{-1}
Q_f	Friction Torque	N m
V_*	Friction Velocity	m s^{-1}
Fn	Froude number	-

GF	Gauge Factor	-
R_G	Gauge Resistance	Ω
h, H	Height	m
U_e	Induced Velocity	m s^{-1}
y	Initial First Layer Height	m
Q_{i}	Instantaneous Torque	N m
$C_{\mathrm{Q,i}}$	Instantaneous Torque Coefficient	-
γ	Intermittency	-
L	Length	m
C_L	Lift Coefficient	-
F_L	Lift Force	N
φ	Local Blade Azimuthal Angle	o
δ	Local Blade Inclination Angle	o
Ma	Mach Number	-
τ_{max}	Maximum Shear Stress	MPa
$\mu\varepsilon$	Microstrain	-
I	Moment of Inertia	kg m^2
y^+	Non-dimensional	-
F_N	Normal Force	N
C_N	Normal Force Coefficient	-
N_θ	Number of Angular divisions	-
N	Number of Blades	-
N_z	Number of Height Divisions	-
N_{fine}	Number of Elements in a Fine Mesh	-
N_{coarse}	Number of Elements in a Coarse Mesh	-
P	Power	W
σ_1	Principal Stress	MPa
u_R	Radial Velocity	m s^{-1}
r, R	Radius	m
r	Refinement ratio	-
W	Relative Velocity	m s^{-1}
Q_{res}	Resistive Torque	N m
Re	Reynolds Number	-
ω	Rotational Velocity	rad s^{-1}
σ	Rotor Solidity	-
ϕ	Scalar	-
τ_w	Shear Wall Stress	Pa

C_f	Skin Friction Coefficient	-
c_w	Speed of Sound in Water	m s^{-1}
t	Spiral Parameter	-
C_p	Static Pressure Coefficient	-
α_{ss}	Static Stall Angle of Attack	o
ε	Strain	-
St	Strouhal Number	-
F_T	Tangential Force	N
C_T	Tangential Force Coefficient	-
t_c	Thickness to Chord Length Ratio	-
t	Time	s
$\bar{F}_x$	Time-averaged Streamwise Force	N
λ, TSR	Tip-Speed Ratio	-
Q	Torque	N m
$\widetilde{Re}_{\theta t}.$	Transitional Momentum Thickness Reynolds Number	-
Re_D	Turbine Reynolds Number	-
Tu	Turbulence intensity	-
TVR	Turbulent Viscosity Ratio	-
w	Under Relaxation Factor	-
a	Upstream interference factor	-
U	Upstream Velocity	m s^{-1}
σ_v	Von-Mises Stress	MPa

Abbreviation	**Definition**
BE	Blade Element
BEM	Blade Element Momentum
BTT	Brí Toinne Teoranta
CPU	Central Processing Unit
CFD	Computation Fluid Dynamics
DES	Detached Eddy Simulation
DNS	Direct Numerical Simulation
DMST	Double Multiple Streamtube
ds	Downstream
EMEC	European Marine Energy Centre
FOS	Factor of Safety
FAR	Finite Aspect Ratio
FSI	Fluid-Structure Interaction

HATT	Horizontal-Axis Tidal Turbine
HAT	Horizontal-Axis Turbine
HAWT	Horizontal-Axis Wind Turbine
IFREMER	Institut Français de Recherche pour l'Exploitation de la Mer
IRENA	International Renewable Energy Agency
IWEA	Irish Wind Energy Agency
LES	Large Eddy Simulation
LDV	Laser Doppler Velocimetry
LCOE	Levelised Cost of Electricity
MaREI	Marine and Renewable Energy Ireland
MaRINET	Marine Renewables Infrastructure Network for Emerging Energy Technologies
MST	Multiple Streamtube
NACA	National Advisory Committee for Aeronautics
NUI	National University of Ireland
PISO	Pressure-Implicit with Splitting of Operators
PMEL	Pacific Marine Environmental Laboratory
PM	Panel Method
RPM	Revolutions per Minute
RANS	Reynolds Averaged Navier Stokes
RSM	Reynolds Stress Equation Model
RMSE	Root Mean Square Error
SFI	Science Foundation Ireland
SIMPLE	Semi-Implicit Method for Pressure Linked Equations
SST	Shear Stress Transport
ST	Streamtube
SEAI	Sustainable Energy Authority of Ireland
TRL	Technology Readiness Level
3D	Three Dimensional
THACFT	Transverse Horizontal-Axis Cross-Flow turbine
TOCA	Turbine Orientation Configuration Angle
2D	Two Dimensional
URANS	Unsteady Reynolds Averaged Navier Stokes
us	Upstream
VATT	Vertical-Axis Tidal Turbine
VAT	Vertical-Axis Turbine
VAWT	Vertical-Axis Wind Turbine
WEC	World Energy Council

Chapter 1: Introduction

1.1 General

Climate change, with associated extreme weather events, poses a significant global threat to modern society. The potentially devastating effects of climate change have been well documented worldwide, including catastrophic hurricanes in the US, widespread forest fires in the Arctic, and record droughts in Cape Town. According to the Pacific Marine Environmental Laboratory (PMEL), the acidity of surface ocean waters has increased by about 30% since the beginning of the Industrial Revolution. In seeking to address the causes of climate change and limit the potentially devastating outcomes, new opportunities arise to develop novel technologies required to replace traditional electricity generation methods. The world needs to move towards a sustainable energy future with a much-reduced carbon-intensive economy. The transition to this new sustainable energy world offers potential for entrepreneurs to develop new technologies, business models and skills, which in turn present opportunities for new forms of employment.

1.2 Global Renewable Energy

Attempts have been made on a global scale to address the imminent threat that climate change presents. The Paris Climate Agreements, made by 195 countries at the 21st Conference of Parties (COP-21) of the United Nations Framework Convention on Climate Change, was the first-ever universally recognised, legally binding global climate change regulations. These agreements aim to limit the increase in global world temperature to below 2^{o}C in the future. To achieve this aim, it is essential that each signatory country transition away from burning fossil fuels and invest in new clean, reliable renewable energy technologies. Various potential renewable resources have been identified, including hydrokinetic, wind, wave, biomass, solar and geothermal, and significant progress has been made in recent years utilising these resources to replace fossil fuels. For example, British Petroleum reports that coal consumption has fallen significantly in recent years. In 2016, the total global energy consumption,

attributed to coal, fell to 28%, its lowest level since 2004 (British Petroleum, 2017). In contrast, renewable power has steadily grown in recent years, increasing by 14% in 2016, with wind and solar leading the renewable energy market. However, renewable resources still only account for 4% of the final total global energy consumption.

Energy sustainability is analysed by the World Energy Council (WEC) on three core dimensions: energy security, energy equity and environmental sustainability. It is highly improbable that one renewable resource can meet the total global energy requirement. Therefore, the adoption of a diversified mix of renewable energy sources, combined with improvements in energy storage technology, smart grid integration and efficiency, provide the path to a sustainable and secure energy future. Multiple renewable sources competing with existing fossil fuel technologies will reduce the levelized cost of electricity (LCOE) of each energy source, thereby satisfying the three core dimensions of energy sustainability defined by the WEC. The International Renewable Energy Agency (IRENA) released a report in 2020 comparing the change in LCOE of different renewable energy sources from 2010 to 2019. As highlighted in **Figure 1-1**, there has been a significant reduction in the LCOE for solar photovoltaic, concentrated solar power, and onshore and offshore wind power. All these resources currently offer a competitive alternative to fossil fuels.

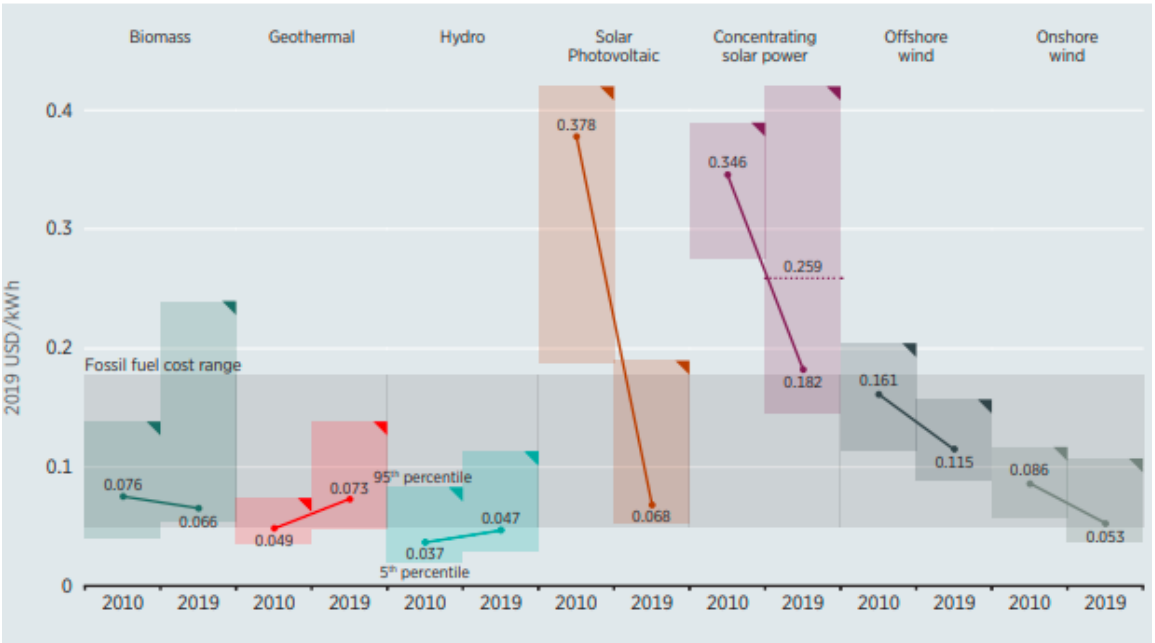

Figure 1-1: Comparison of the global weighted LCOE from utility-scale renewable power generation technologies from 2010 to 2019. The equivalent fossil fuel cost range is also highlighted. (International Renewable Energy Agency, 2020).

1.3 Global Hydrokinetic Energy Conversion

Hydrokinetic energy can be defined in terms of three different resources: tidal (channels and estuaries), ocean (currents), and inland (streams and rivers). Tides are driven by the gravitational forces of the moon and the sun. Ocean currents can be driven by this gravitational force, wind and variations in water masses due to differences in salinity and temperature. Much of the hydrokinetic energy conversion (HEC) technology has focused on tidal energy to date. Ocean currents typically occur in deep waters, which present a challenge in designing appropriate mooring systems, while the application of HEC technologies in rivers face significant environmental and resource prediction issues.

Until recent years, the tidal turbine industry was mainly dominated by small start-up businesses. However, in recent times, as full-scale prototypes are reaching commercialisation, larger engineering and manufacturing companies have entered the market. The tidal turbine industry has progressed to a stage where the most advanced designs have reached full-scale deployment. The leading countries in the development of tidal turbine technologies include the United Kingdom, Ireland, France, Canada and South Korea (World Energy Council, 2016).

1.4 Renewable Energy in Ireland

Ireland is currently failing to address and improve its energy sustainability effectively. As part of Horizon 2020 planning, the EU has set Ireland a target of 16% of final energy use that must be derived from renewable sources by 2020. Ireland's National Renewable Energy Action (NREA) Plan divided this figure into targets of 40%, 12% and 10% of renewable energy sources, allocated to electricity generation, heating and transport, respectively. At the 2017 Engineers Ireland conference, the Irish Wind Energy Association (IWEA) reported that Ireland had fallen significantly behind on these targets due to the notable lack of progression in the heating and transport sector's electrification. Despite being on track for 40% of the electricity generation from renewable sources, mainly due to onshore wind, Ireland is still highly dependent on fossil fuel imports for the heating and transport sector. For Ireland to improve its energy sustainability and move in line with its EU targets of 2020, steps must be taken towards increased electrification of the heating and transport sector. The electrification

of these sectors will consequently increase the requirement for the generation of electricity. Due to the unpredictability of wind energy and the lack of suitable electricity storage options, alternative renewable resources need to be investigated.

1.5 Hydrokinetic Energy Conversion in Ireland

The abundant tidal resources at Ireland's disposal increases the viability of using tidal energy to address the increased electricity generation needs arising from the heating and transport sectors' electrification. Hydrokinetic energy offers an indigenous, non-polluting energy source that could decrease Ireland's over-dependence on fossil fuel imports and reduce greenhouse gas emissions. While other renewable energy sources are also viable options, the predictability and repeatability of the tides offer significant advantages over competing resources. The island of Ireland has an abundant tidal resource available, with Sustainable Energy Ireland (SEI) (currently known as SEAI) reporting a yearly accessible resource of 2,620 GWh, based on prominent tidal resource locations as shown in **Figure 1-2**.

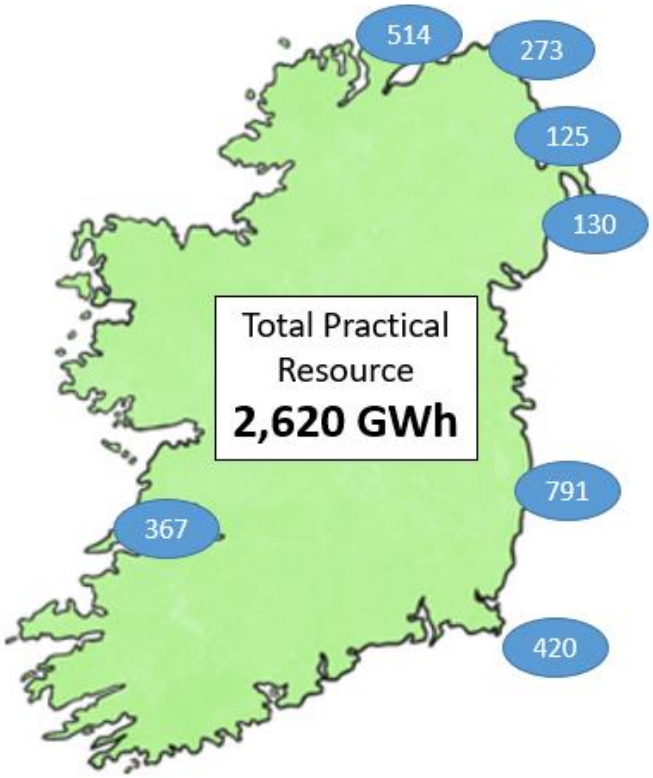

Figure 1-2: Accessible resource assessment for the island of Ireland with the locations with an extensive tidal resource highlighted (O'Rourke et al., 2010).

In recent years, Ireland has taken steps to investigate the potential widespread use of tidal energy. This PhD is funded by Marine, and Renewable Energy Ireland (MaREI), a world-leading Science Foundation Ireland (SFI) funded Research Centre, which has been tasked with combining the expertise of a wide range of research groups and industrial partners. MaREI aims to combine this expertise to solve the main scientific, technical, social, and economic challenges faced by the marine and renewable industry.

1.6 Hydrokinetic Energy Technology

As detailed by the European Marine Energy Centre (2020), there are six primary hydrokinetic stream devices with varying operating principles. These technologies are at different levels of development and commercialisation and have distinct advantages over each other. As this industry is still in its infancy, extensive research is required not only in terms of device power output but also in blade manufacturing techniques, overall system installation and maintenance costs, and environmental impacts. One of the industry's biggest challenges is the assessment of a particular site prior to device installation. Extensive studies are often required to assess any ecological effects that the devices may present to wildlife in the region.

The following section details the different types of hydrokinetic stream devices currently in development.

Horizontal-axis tidal turbine

The horizontal-axis tidal turbine (HATT), also known as an axial flow turbine due to the rotor axis aligning parallel to the incoming flow, is the most common design. The most common HATTs operate on a lift-based design. Certain drag-based HATTs do exist, but they tend to have lower power efficiencies compared to lift-based systems. Lift-based turbines operate on the same principle as aeroplane wings; the turbine blade experiences lift forces due to the blade's relative velocity to the incoming freestream and is pitched at a desirable angle of attack to achieve maximum lift while minimising drag. The lift and drag forces contribute to the torque on the turbine shaft. The rotational speed of the shaft is controlled to optimise the torque and power output of the turbine. The mechanical power can be converted to electricity using a generator.

HATTs are currently at the full-scale prototype deployment and commercialisation stage, with several market leaders emerging over the past ten years. In terms of scale and current technology readiness level (TRL), the three key players at the forefront of large-scale commercialisation in the coming years are Orbital Marine Power, Sabella and SIMEC Atlantis Energy.

Orbital Marine Power, formerly known as ScotRenewables, designed and manufactured a 2 MW twin-rotor turbine design named SR2000, shown in **Figure 1-3** (a). The novel floating technology offers a simple, cost-effective solution for manufacture, installation, and maintenance. The device was installed at the European Marine Energy Centre (EMEC) Orkney in October 2017 and exported more than 3.2 GWh to the Orkney grid during its first year of operation (Orbital Marine Energy, 2020a). Plans are in place to install a new, improved 2.0 MW turbine, known as O2, at EMEC's test site at Fall of Warness in the next year (Orbital Marine Energy, 2020b).

The Sabella D10 tidal turbine, shown in **Figure 1-3** (b), has a rotor diameter of 17 m and has a rated capacity of up to 1 MW. It was successfully demonstrated in 2016 in the Fromveur Passage, France. This turbine was removed in 2018, and following optimisation work, the D10 turbine was reinstalled to complete the second phase of exploration work scheduled to take three years (Sabella, 2020).

SIMEC Atlantic Energy has developed and acquired emerging tidal technologies in the past few years. The AR1500 turbine is a 1.5 MW horizontal axis turbine featuring active pitch and yaw capability. The rotor, shown in **Figure 1-3** (c), is 18 metres in diameter, and the power rating is based on an operational flow speed of 3.0 m/s (SIMEC Atlantic Energy, 2020a). Andritz Hydro Hammerfest AH1000 MK1 turbine is also a three-bladed horizontal axis turbine that incorporates similar pitching and yawing mechanisms to the AR1500 turbine. The turbine, which is rated at 1.5 MW with a rotor diameter of 16 metres, is shown in **Figure 1-3** (d). In October 2017, Phase 1A of the MeyGen tidal stream project in Pentland Firth, Scotland, was completed with the installation of a single AR1500 turbine and three AH1000 MK1 turbines bringing the overall installed capacity of the site to 6 MW (SIMEC Atlantic Energy, 2020b). To date, this site has provided over 27 GWh of electricity to the grid. The construction and installation of two additional AR2000 (2.0 MW) turbines are currently being undertaken as part of MeyGen Phase 1B. MeyGen Phase 1C is presently in the development stage, with plans to install 49 turbines at an estimated

cost of £420m. The SeaGen S turbine, shown in **Figure 1-3** (e), was initially developed by Marine Current Turbines (MCT) and has recently been acquired by SIMEC Atlantic Resources. It is a twin-rotor turbine designed for fixed or floating foundations. The device operated successfully in Strangford Lough, Northern Ireland, from 2008 until 2019, when it was decommissioned.

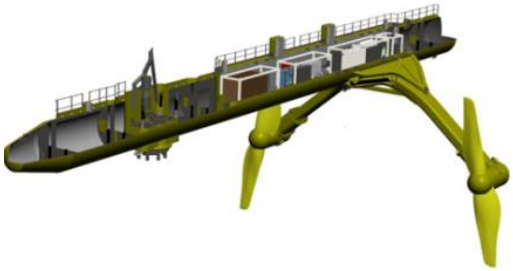

(a) *Orbital Marine Energy*- SR2000 (2 MW)

(b) *Sabella*- D10 (1 MW)

(c) AR1500 (1.5 MW)

(d) AH1000 MK1 (1.5 MW)

(e) SeaGen S (1.2 MW)

Figure 1-3: Current commercial leaders in the development of large-scale HATTs.

Cross-flow tidal turbine

Cross-flow turbines operate on the same fundamental hydrodynamic principle as axial-flow turbines, with lift and drag forces combining to generate a net torque at a specific rotational velocity for peak power performance. The one key difference between the two types of designs is the orientation of the rotor axis. For cross-flow turbines, the axis of the rotor is perpendicular to the incoming free stream flow direction. There are two distinct types of cross-flow turbines, namely, vertical-axis tidal turbines (VATTs), where the turbine shaft is positioned in the vertical plane relative to the flow and, transverse horizontal-axis cross-flow tidal turbines (THACFTs), where the turbine shaft is placed in the horizontal plane relative to the flow. Cross-flow turbines hold distinct geometrical advantages over their axial-flow

counterparts. Due to their geometry, cross-flow turbines can be designed to span a wider area than axial-flow turbines in a relatively shallow flow field. This feature is particularly advantageous for this type of design as it increases the accessible resource.

Several VATT concepts are in the prototype-development phase, with these devices generally targeted towards the small- to medium-scale market. One company leading the way towards commercialising this type of device is HydroQuest, with their straight-bladed turbine design known as OceanQuest (**Figure 1-4**). In 2019, they successfully launched a 1 MW prototype at EDF's Paimpol-Bréhat site in France. Testing is still ongoing and is planned to be completed this year.

Figure 1-4: Hydroquest 1 MW OceanQuest prototype turbine device installed at Paimpol-Bréhat, France (HydroQuest, 2020).

While THACFTs do not have all the same advantages as VATTs, they benefit from operating in even shallower waters than VATTs, thus increasing the accessible tidal resource even further. The Kepler THACFT, developed at the University of Oxford, is an example of this type of turbine design. A 1:20 scaled model was tested in the current and wave tank at Newcastle University, as shown in **Figure 1-5**.

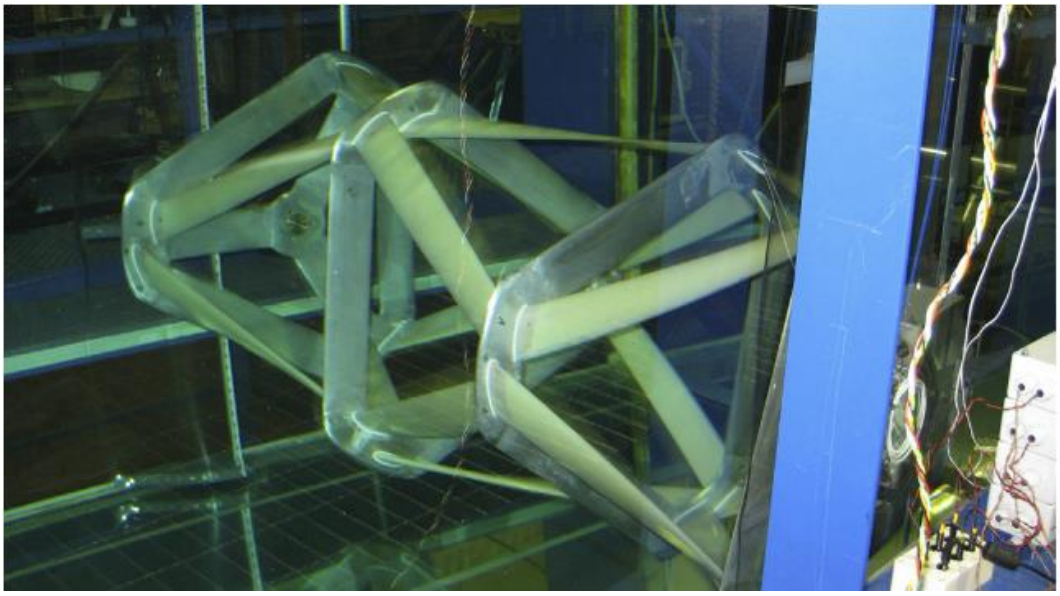

Figure 1-5: 1:20 scale model prototype of the Kepler tidal turbine (Mcadam et al., 2013).

Oscillating hydrofoil

Oscillating hydrofoils consists of a single blade which may be generated from one or more blade profiles. For a given positive or negative angle of attack, the hydrofoil will rise or fall in an oscillating motion. The motion of the oscillating arm can be used to drive a hydraulic system to generate power. This type of device is typically suited to shallower sites. One example of this type of design is the Stingray concept design developed by the University of Strathclyde, shown in **Figure 1-6**. In recent years researchers have focused predominantly on modelling this design, with limited experimental testing and large-scale deployment.

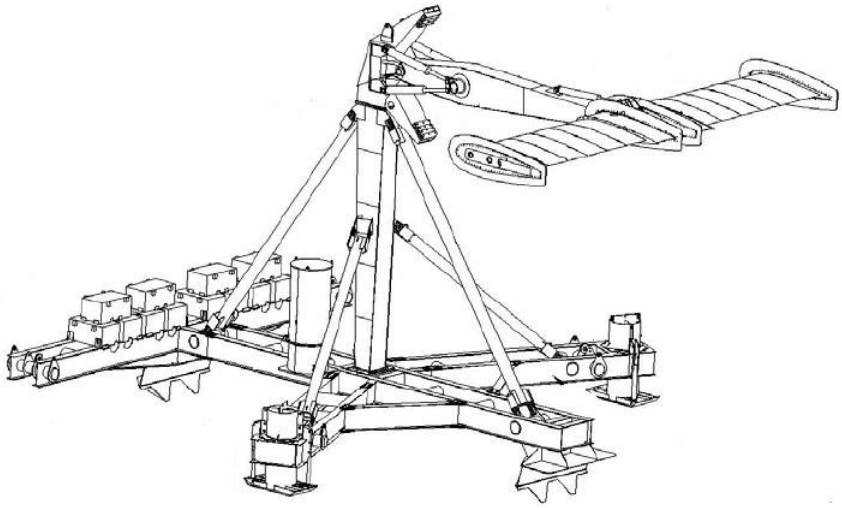

Figure 1-6: Stingray Oscillating hydrofoil prototype design (University of Strathclyde, 2005)

Tidal kite

A tidal kite consists of a hydrodynamic wing that is attached to a turbine. The kite is tethered by a cable to a fixed point, typically on the ocean floor bed. The wing flies in a predefined pattern, and as the hydrodynamic lift force varies, the kite is accelerated. This acceleration leads to the turbine experiencing a water flow speed several times that of the actual current flow speed at that location. This design widens the accessible resource as it can be installed in an area that does not typically have high tidal stream velocities. One commercial group, Minesto, have been the world leader in this type of device. In 2019, Minesto installed a 20 kW DG500 tidal kite prototype, shown in **Figure 1-7**, at the Holyhead deep-water site off the coast of North Wales. The project is ongoing.

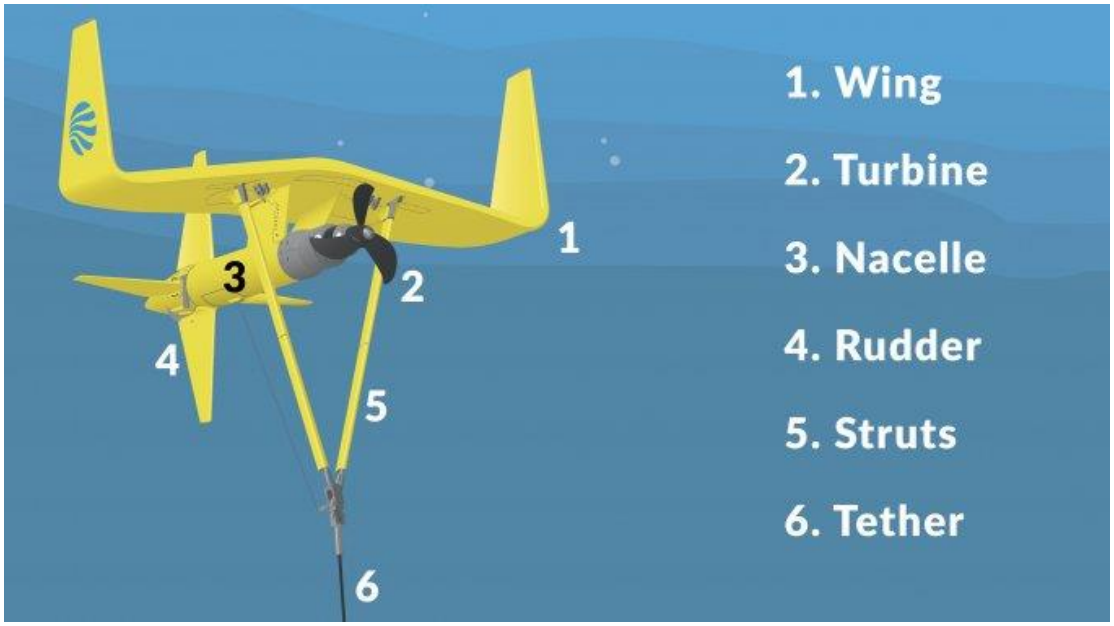

Figure 1-7: Minesto DG500 design prototype (Minesto, 2020)

Archimedes screw

The Archimedes screw turbine is a helical corkscrew-shaped device, as shown in **Figure 1-8**. It is widely used in river-based applications. Energy is generated as the water flows through the turbine and rotates the device. The slow motion of the screw leads to the requirement of a gearbox for electrical power generation. Due to the slow motion of the screw, this design is seen as the most fish-friendly turbine design. An example of this design is the Flumill Archimedes screw turbine, shown in **Figure 1-8**.

Figure 1-8: Flumill Archimedes screw turbine (European Marine Energy Centre 2020)

Ducted turbine

A venturi duct turbine, also known as a shrouded turbine, can implement the axial- or cross-flow technologies discussed above. The duct accelerates the flow through the turbine rotor, allowing a greater power output from a smaller diameter turbine. Another benefit of the duct is that it can design to reduce the turbulence of the flow entering the turbine. The flow of water can also be controlled and concentrated on optimising the turbine performance. One example of this technology was developed by Tidal Energy Pty Ltd, who installed a VATT in their shroud, as shown in **Figure 1-9**.

Figure 1-9: Davidson-Hill Venturi turbine (Tidal Energy Pty Ltd, 2013)

1.7 The Brí Toinne Teoranta Concept

Early-stage VATTs were perceived as having low efficiency compared to their axial-flow counterparts; however, recent designs have seen a renewed interest in vertical-

axis turbines, primarily vertical-axis wind turbines (VAWTs), but also VATTs (Roberts et al., 2016). Innovative blade designs have seen these designs begin to compete with axial-flow turbines in terms of power performance (Battisti et al., 2016; Chen et al., 2016; Preen and Bull, 2015).

VATTs possess several distinct advantages over their HATT designs. As VATTs are omnidirectional, a pitching or yawing mechanism is typically not required to adjust the turbine blades to face the incoming flow. While some straight-bladed turbines incorporate blade pitching systems, they are not an essential requirement. Another advantage of VATTs is the ability to have vital electrical components, e.g., generator, rectifier, etc., above water. Fewer mechanical components and electric hardware above water lead to simpler operating systems, fewer reliability issues and lower maintenance costs for VATTs. Dabiri (2011) noted that although stand-alone VAWTs often demonstrate reduced power efficiencies than their HAWT counterparts, this reduction is eliminated by the fact that VAWT can be located closer together. The flow deflected around one VAWT can be collected by a VAWT in close proximity.

One drawback of VATTs, related explicitly to straight-bladed fixed-pitch turbines, is the widely varying angle of attack, especially at low rotational speeds (Kirke and Lazauskas 2011). Fixed-pitch straight-bladed devices are liable to stall, reducing the overall device performance, hampering their ability to self-start, and imposing additional stresses on the blades and other components due to rapidly fluctuating torque pulsations. There is also a hydrodynamic interaction between each turbine blade, as blades in the downstream region of the turbine will encounter the wake produced by the blades upstream. While introducing a pitching mechanism can alleviate some of these issues and reduce these fluctuating loads, this adds cost and complexity to the device.

The focus of this research is a novel Brí Toinne Teoranta VATT concept shown in **Figure 1-10**. The novelty of this type of turbine arises from the spiral geometry of the blades (Patent number US 8690541, McGuire, 2014). Each blade is defined in terms of an upper spiral and a lower spiral and has a constant hydrofoil cross-section along its entire length. The upper and lower spirals are of the opposite hand and extend from each end to meet at the mid-height. The blade's spirals extend around the main central rotational axis through an angular distance of approximately 60^{o}.

Figure 1-10: Bri Toinne Teoranta turbine concept design.

The Brí Toinne Teoranta design aims to lessen the highlighted disadvantages of existing vertical-axis turbines. This design concept's proposed advantages include increased power efficiency and improved self-starting capabilities over current vertical-axis designs. Due to the spiral blade design, the magnitude of the cyclic loads will be reduced, leading to an extended fatigue life for the blades and other device components, e.g. bearings, struts, supports. It is envisaged that the final design will be targeted towards small to medium-scale deployment (< 100 kW) in both tidal- and river-based applications. The ability to vary and optimise the design for different height-to-diameter turbine ratios will facilitate installing this device at an extensive range of locations. There is also the possibility of incorporating this design into a venturi duct style device to increase power output further.

As with all other tidal turbine designs and projects at the commercialisation stage, this design will encounter the same challenges others face regarding securing finance, selecting suitable materials, determining the LCOE of the technology, remote locations installations, and manufacturing capability. It is envisaged that this turbine design will exceed other designs in terms of reliability and power output and will be a favourable option for renewable energy investors.

1.8 Research Aim and Objectives

The overall aim of this research is to develop a combined analytical, computational and experimental methodology for characterisation of the hydrodynamic performance of a novel vertical axis tidal turbine. Specifically, the main issue to be addressed is the

novel device's viability and its specific advantages and disadvantages relative to competing devices. It is envisaged that the methodologies and tools developed in this research will be more broadly applicable in the assessment of other existing and novel turbine designs.

The following objectives are set to achieve the research aim of this PhD:

- Develop a blade element momentum (BEM) model, which facilitates the efficient characterisation and design optimisation of the hydrodynamic performance of different variations of the Brí Toinne Teoranta design.
- Establish detailed two-dimensional computational fluid dynamics (CFD) models to establish a computational based dataset of lift and drag coefficients as a function of angle of attack and Reynolds number for use as input into the BEM model developed above.
- Develop a three-dimensional transient CFD model of the Brí Toinne Teoranta rotor for detailed hydrodynamic analysis of the device, including accurate modelling of turbulence effects.
- Perform experimental investigations into different scales of prototype designs to evaluate the novel device's mechanical power performance and validate the BEM and CFD models developed.

1.9 Thesis Layout

Chapter 2 presents a literature review of modelling techniques and physical testing methods relating to tidal turbines. Computational fluid dynamics and blade element momentum theory directly related to vertical-axis turbines are discussed. Previous blade element momentum and computational fluid dynamics models are identified. Scaled experimental test facilities and results for existing tidal turbines are also highlighted. The specific gaps in the research that this thesis aims to address are outlined.

Chapter 3 describes the blade element momentum (BEM) model code developed for the Brí Toinne Teoranta turbine. Novel geometrical equations are presented which encapsulate the various turbine blade designs. Additional features to improve the BEM model's accuracy, such as dynamic stall, flow expansion, finite aspect ratio effects and a shear velocity profile, are also included. The modelling approach is validated against previously published experimental data for two different vertical-axis turbine designs.

A complete design parametric optimisation study of the Brí Toinne Teoranta turbine design is presented, and its power performance is compared with an equivalent straight-bladed turbine.

Chapter 4 outlines the two-dimensional unsteady Reynolds-averaging Navier-Stokes (URANS) models developed during this research, including details on turbulence model selection and other modelling techniques. Two-dimensional single hydrofoil models are presented to identify lift and drag coefficients as a function of the angle of attack and Reynolds number. These lift and drag coefficients are used as input into the BEM model presented in Chapter 3 and into assessing the self-starting capabilities of a straight-bladed and Brí Toinne Teoratnta turbine design. A two-dimensional URANS model is also developed of a straight-bladed vertical-axis turbine to directly compare computational requirements and accuracy with the combined BEM-CFD methodology.

Chapter 5 details a test setup at NUI Galway for a small-scale prototype. Elements of the towing tank design and instrumentation are presented. The results from these experimental runs are used to validate preliminary model results based on blade element theory and steady-state RANS models.

Chapter 6 details the experimental testing of the two prototype designs. Detailed information is included in this Chapter on the development and calibration of the various instrumentation used during the testing. The devices' mechanical power performance is determined over a range of flow velocities and tip speed ratios. The wake characteristics of the Brí Toinne Teoranta design is examined. A full three-dimensional URANS model of the novel blade geometry is presented in Chapter 6. Experimental results are used to validate the URANS modelling approach adopted and also the combined BEM-CFD methodology presented in Chapter 4.

Finally, the author's conclusions and recommendations for future research are detailed in Chapter 7.

Chapter 2: Literature Review of Modelling Techniques and Physical Testing of Vertical-Axis Turbines

2.1 Introduction

This chapter presents a review of the theory and literature relating to the modelling and testing techniques applied to turbines. While this research focuses on tidal turbine design modelling and testing, much of the theory and its application have been developed from established wind turbine research; this will be referred to in some cases. As the Brí Toinne Teoranta turbine is a vertical-axis design, the focus of this review will be placed on the inherent challenges faced by this design and modelling of such turbines.

This chapter layout is as follows: In **Section 2.2 Blade Element Momentum (BEM) Modelling**, the theory behind blade element momentum modelling and its current implementation is presented. **Section 2.3 Computational Fluids Dynamics (CFD) Modelling** presents the theory behind the CFD simulations and a review of literature for two-dimensional (2D) and three-dimensional (3D) simulations. Some aspects of the CFD modelling literature discussed in this chapter relate directly to the development of tidal turbines, while other aspects concentrate on CFD modelling in general, including numerical methods, turbulence model selection, meshing techniques, and discretisation studies. **Section 2.4 Experimental Testing of Tidal Turbines** details the physical testing of scaled models, including standards and best practices and some test case analysis. Finally, in **Section 2.5 Conclusions,** the openings in the literature that this research aims to address are presented.

2.2 Blade Element Momentum (BEM) Modelling

2.2.1 Introduction

Blade element momentum (BEM) models have been the cornerstone of the modelling of both wind and tidal turbines. This modelling technique combines two theoretical models to allow computation of the aerodynamic or hydrodynamic forces on the blade by equating the momentum loss from the fluid to the forces on the blade elements. BEM modelling has been used for both horizontal- and vertical-axis, wind and tidal turbines (Beri, 2011; Goundar and Ahmed, 2013; Masters et al., 2011; Myers and Bahaj, 2006).

The first theoretical model implemented is momentum theory within a streamtube, treating the turbine blade as an actuator disc. The second model is blade element theory which examines the forces on the hydrofoil as the blade rotates. In the following sections, the theory and its application will be discussed in more detail.

2.2.2 Momentum Theory

Froude's momentum theory (1889), also referred to as actuator disk theory is an ideal actuator disk model. This model is used to estimate the power available from a volume of fluid passing through a rotor. It can be applied to any turbine. Certain assumptions are made, including:

- Homogeneous, steady-state, one-directional flow.
- Inviscid flow.
- The far upstream and far downstream pressures are equal to the ambient pressure.
- There is a uniform thrust and velocity over the rotor area.
- A control volume is assumed in which fluid only flows through the inlet and leaves through the outlet.
- The rotor is infinitely thin.

The actuator disc causes a reduction in velocity, which is the source of a pressure change within the streamtube. By applying the conservation of momentum to the control volume, the net force on the contents within the stream tube can be calculated. The force is equal and opposite to the streamwise axial force, F_x, referred to as the

thrust force. Using the conservation of linear momentum for a steady-state, incompressible, one-dimensional flow, F_x is defined as:

$$F_x = U_1(\rho_1 A_1 U_1) - U_4(\rho_4 A_4 U_4) \tag{2.1}$$

where U is the fluid velocity, ρ is the fluid density, A is the cross-sectional area, and the subscript number indicates the location of the cross-section, as shown in **Figure 2-1**. In steady-state flow, the mass flow rate is defined as:

$$\dot{m} = \rho_1 A_1 U_1 = \rho_4 A_4 U_4 \tag{2.2}$$

Therefore, the thrust force can be defined as:

$$F_x = \dot{m}(U_1 - U_4) \tag{2.3}$$

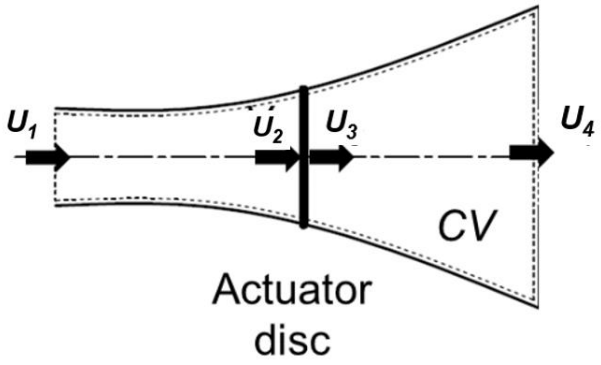

Figure 2-1: Image of a single actuator disc showing the velocities and different stages.

As no work is assumed to be done on either side of the actuator disc, Bernoulli's equation is used for the two control volumes on either side of the actuator disc.

$$p_1 + \frac{1}{2}\rho U_1^2 = p_2 + \frac{1}{2}\rho U_2^2 \tag{2.4}$$

and,

$$p_3 + \frac{1}{2}\rho U_3^2 = p_4 + \frac{1}{2}\rho U_4^2 \tag{2.5}$$

where p is the pressure at the specified location. The far upstream and far downstream pressures are assumed equal ($p_1 = p_4$) and the velocity across the disc does not vary ($U_2 = U_3$). An alternative way of expressing F_x is to calculate the net sum of forces upstream and downstream of the disc:

$$F_x = A_2(p_2 - p_3) \tag{2.6}$$

Solving $p_2 - p_3$, and substituting into equation (2.6), the thrust force can be expressed as:

$$F_x = \frac{1}{2}\rho A_2 (U_1^2 - U_4^2) \tag{2.7}$$

Equating equation (2.4) and (2.5), the following equation is derived for U_2:

$$U_2 = \frac{U_1 + U_4}{2} \tag{2.8}$$

The interference factor, a, is defined as the fractional decrease in fluid velocity from the freestream velocity to the actuator disc:

$$a = \frac{U_1 - U_2}{U_1} \tag{2.9}$$

From this definition, the fluid velocity at the actuator disc and in the wake of the disc can be defined in terms of the axial induction factor and freestream velocity, as:

$$U_2 = U_1(1 - a) \tag{2.10}$$

And,

$$U_4 = U_1(1 - 2a) \tag{2.11}$$

Finally, from equations (2.7), (2.9) and (2.10), the axial streamwise force on the disc is calculated by:

$$F_x = \frac{1}{2}\rho A U_1^2 [4a(1 - a)] \tag{2.12}$$

Double actuator disc theory provides a more accurate representation compared to single actuator disk theory for vertical-axis turbines, as the fluid flows through the rotor swept area twice. These two sections are referred to as the upstream and downstream halves of the turbine. The turbine in question can be represented as a pair of actuator disks in tandem, as shown in **Figure 2-2**. For the upstream portion, the incoming velocity is the freestream velocity, U_∞. The induced velocity, U, is at the turbine blade and the fully developed wake velocity for the upstream is also referred to as the induced equilibrium velocity, U_e. For the downstream portion, the incoming velocity is the wake velocity from the upstream half, U_e and the induced velocity at the turbine blade downstream is U'. U_W is the wake velocity.

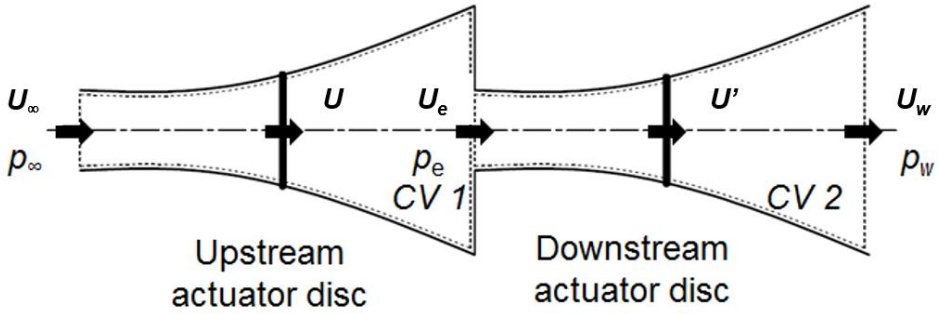

Figure 2-2: Image of double actuator disk theory showing the velocities associated with each stage

2.2.3 Blade Element Theory

2.2.3.1 Background

As fluid flows over a solid object, the fluid molecules are free to move about the solid object as they are not closely bound to each other. The molecules can have varying values of pressure and velocity at different locations close to the object. Bernoulli's equation describes the relationship between the pressure and the velocity in a fluid. The principle states that if the velocity changes around an object, the pressure will change also.

$$P_1 + \rho g z_1 + \frac{1}{2}\rho U_1^2 = P_2 + \rho g z_2 + \frac{1}{2}\rho U_2^2 = const \tag{2.13}$$

where P is the static pressure, ρ is density, g is gravity, z is height, and U is the velocity. The subscripts 1 and 2 indicate two different locations in the fluid flow.

By integrating this pressure difference around the object, the hydrodynamic force on the object can be calculated. This force can be resolved into the lift force (F_L) component, acting perpendicular to the flow of fluid, and the drag force (F_D) component, acting parallel to the incoming flow. An alternative method to calculate the hydrodynamic force on an object is to integrate the velocity distribution around the object to produce a net moment (M) on the fluid. Applying Newton's third law, this moment on the fluid will result in an equal and opposite reaction on the body.

As fluid flows over an object, a frictional force is formed between the two mediums. This frictional force has an equal and opposite force on both the solid and the fluid. The surface experiences a dragging force in the direction of the fluid flow, tangential to the surface. The fluid experiences a deceleration force which decreases with its local flow velocity. The shear stress (τ) experienced by the fluid is directly proportional to

the fluid's viscosity. The viscosity of the fluid (μ) is defined as its resistance to deformation by shearing stresses. This force related to the shear stress, also known as the skin friction drag, is resolved into components parallel and perpendicular to the incoming flow. The total lift and drag forces experienced by an object is a summation of the forces due to pressure and shearing stresses.

In summary, forces and moments acting on an object caused by the fluid flow are due to two sources:

- The variation of pressure over the object's surface.
- The shear stress distribution over the object's surface.

The pressure acts perpendicular to the surface while the shear stress acts perpendicular to this pressure, i.e. tangential to the surface. The net effect of the pressure and shear stress integrated over the entirety of the object's surface is the resultant force and moment acting on that body.

2.2.3.2 Blade Element Theory

Drzewiecki (1892) developed a model which examines the velocities and associated forces acting on a blade element. The assumptions of blade element theory are:

- Forces on the blade elements can be determined by the two-dimensional lift and drag coefficients (C_L and C_D)
- There is no hydrodynamic interaction between the various blade elements

The blade profile shown in **Figure 2-3** is an example of blade element theory applied to a vertical-axis turbine blade in a freestream velocity flow, U_∞, with a rotational velocity, ω.

The angle of attack, α, as shown in **Figure 2-3**, is the angle between the vector, representing the relative motion between the body and the fluid and the chord line of the profile. The chord line is the straight line joining the leading and trailing edge of the profile. The angle of attack is calculated from the following equation:

$$\alpha = \tan^{-1}\left(\frac{U_\infty \sin(\theta)}{U_\infty \cos(\theta) + \omega r}\right) \tag{2.14}$$

where θ is the blade azimuthal angle, i.e. blade position, and r is the turbine radius.

The relative velocity of the fluid to the blade, W, is calculated as follows:

$$W = \frac{U_\infty \sin(\theta)}{\sin \alpha} \tag{2.15}$$

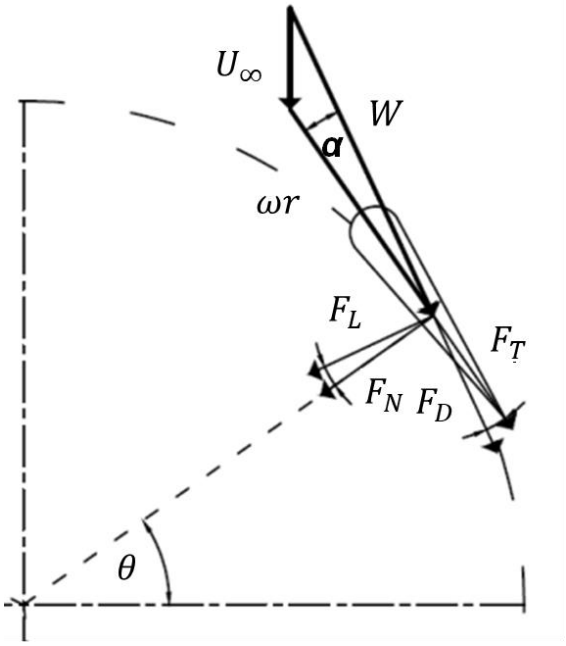

Figure 2-3: Image of a blade element theory showing the forces and velocities associated with the blade element of a vertical-axis turbine. θ is the azimuthal angle, α is the angle of attack), W is the relative velocity of the fluid relative to the blade, ωR is the tangential velocity of the blade element, and U_∞ is the freestream velocity.

The lift and drag force, F_L and F_D are calculated as follows:

$$F_L = \frac{1}{2}\rho \Delta H c C_L W^2 \tag{2.16}$$

$$F_D = \frac{1}{2}\rho \Delta H c C_D W^2 \tag{2.17}$$

where ρ is the fluid density, ΔH is the blade height, and c is the blade chord length. The lift and drag coefficients, C_L and C_D, are vital inputs for blade element theory calculations. These coefficients are discussed in detail in **Section 2.2.3.3 Blade Section Data**.

F_L and F_D are resolved into the normal and tangential forces acting on the blade element, F_N and F_T, as follows:

$$F_N = F_L \cos \alpha + F_D \sin \varphi \tag{2.18}$$

$$F_z = F_L \cos \varphi - F_D \sin \varphi \tag{2.19}$$

The streamwise force, F_x, on the blade element in the flow direction is calculated by:

$$F_x = -F_N \sin\theta + F_T \cos\theta \tag{2.20}$$

2.2.3.3 Blade Section Data

Lift and drag coefficients are typically derived from experimental or numerical methods. Different blade profiles have varying flow characteristics under the same flow conditions. Blade profiles are designed to generate a significant lift force while minimising the drag force encountered under specified operating conditions. The main applications of blade profiles include aircraft, wind turbines, fans, compressors, and tidal turbines. The characteristics of a blade profile are dependent on several factors, including the shape of the profile, Reynolds number (Re), Mach number (Ma) and angle of attack (α).

The Reynolds number is a dimensionless parameter in fluid mechanics which describes the relationship between the inertial and viscous forces in a fluid. The characteristics of a blade profile are highly dependent on the operational Reynolds number, Re_c, defined as:

$$Re_c = \frac{\rho W c}{\mu} \tag{2.21}$$

where μ is the dynamic viscosity of the fluid (Pa S). Specific blade profiles have been designed specifically for low Reynolds number operation (Selig and Guglielmo, 1997). The Mach number, Ma, is a dimensionless parameter which describes the compressibility of the fluid:

$$Ma = \frac{V}{c} \tag{2.22}$$

where c is the speed of sound in the specified fluid. Aerofoils at low Mach numbers (Ma < 0.3), as opposed to hydrofoils, are the focus of much of the literature. Compressibility effects at these low Mach numbers are small, so this aerofoil data is assumed to be applicable for hydrofoils.

The most studied series of blade profiles are the NACA four-digit series. The National Advisory Committee for Aeronautics (NACA) developed these well-studied profiles (Jacobs and Sherman, 1937; Sheldahl and Klimas, 1981). The shape of the profile is described by the numbers after the word “NACA”, referring to a combination of thickness distribution and a mean or camber line, e.g. NACA 0015, NACA 2412. For the NACA 0015, the first two digits, “00”, indicate that the aerofoil has no camber,

while "15" indicates the aerofoil has a maximum thickness of 15% chord length. For the NACA 2412 profile, the first two digits, "24", indicate that the aerofoil has a maximum camber of 2% located 40% along the chord from the leading edge. Again, the second two digits, "12", indicate a maximum thickness of 12% of the chord length. More complex NACA series includes the five-, six-, seven and eight-digit series. Certain blades adopt a cambered profile, i.e. the blade profile is non-symmetric. These types of profiles have the benefit of generating lift at an angle of attack of 0°. This profile is often adopted for horizontal-axis turbines. Cambered blades typically experience stall conditions at lower angles of attack, so they are often not considered for vertical-axis turbines designs that experience a wide range of attack angles.

Different numerical methods have been developed to determine C_L and C_D including panel methods and CFD modelling. CFD datasets are typically limited in their investigation into the effects of Reynolds Number and angle of attack. Details of these CFD analyses are presented in **Section 2.3.2.1 Single Blade Modelling**.

Panel methods are implemented for solving for linear, inviscid, irrotational flow about at body (Erickson, 1990). Several panel method tools are available to developers, including JavaFoil (Hepperle, 2018) and XFOIL (Drela and Youngren, 2013) as examples. Sheldahl and Klimas (1981) used the code developed by Eppler and Somers (1980)- simply referred to as Eppler's code. This code was used to produce results for several NACA profiles, including the NACA 0015 profile, which is the focus of this study. C_L and C_D were presented in tabular form for angles of attack for 1° increments from 0°-27° for Reynolds number varying from $1x10^4$ to $5x10^6$. The dataset presented also included experimental data for angles of attack range from 30° to 180°, in 5° increments. At these higher angles of attack, Reynolds number independence is assumed. Similarly, at these higher angles of attacks, Reynolds number independence is also assumed between thicker blade profiles, e.g. NACA0015, NACA0018, NACA0024. As this data is the most complete dataset published, it is extensively used as input for vertical-axis turbines BEM models.

A sample of this dataset detailing the C_L and C_D variation with angle of attack and Reynolds number for the NACA015 profile is presented in **Figure 2-4**. The strong impact of Reynolds number on the onset of stall can be identified. At lower Reynolds number, $Re < 10^4$, the data shows negative C_L in the post-stall region. However, this

panel method data is not without criticism, particularly in the stall and post-stall region. Dominy *et al.* (2007) compared the dataset to limited experimental data available for a NACA0012 blade profile. They noted that the panel method calculations predicted earlier onset of stall at a lower angle of attack and that a more significant reduction in lift was experienced in the post-stall region. As is observed from this data, $\alpha > 35^{o}$, in the deep stall region, are undesirable due to the reduced lift and increased drag experienced at these conditions. Turbine blades should be designed and operated in a manner to avoid these detrimental angles of attacks.

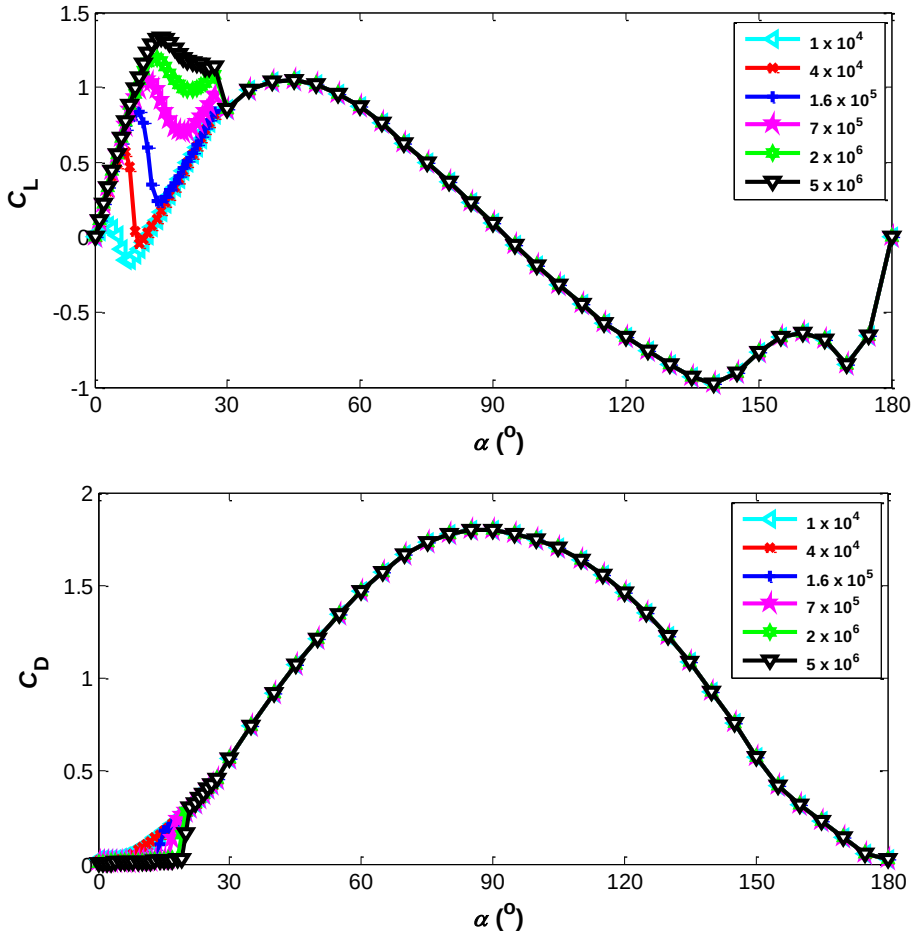

Figure 2-4: Sample of the C_L and C_D dataset for the NACA0015 showing the variation of coefficients with angle of attack and Reynolds number. This data is a combination of panel method derived values and experimental measurements (Sheldahl and Klimas, 1981)

Experimentally measured coefficients are available from some sources; however, this data is typically limited and not extensive enough to cover the wide range of operating conditions experienced by vertical-axis turbines. For example, in the case of the

commonly used NACA 0015 profile, experimental characterisation is limited to a small range of attack angles (Jacobs and Sherman, 1937) or a small range of Reynolds number (Sheldahl and Klimas, 1981).

2.2.3.4 Stall Characteristics

One key feature of blade flow behaviour is stall, which contributes to a sudden drop in lift and an increase in drag as the blade's angle of attack increases, highlighted in the lift and drag coefficients presented in **Figure 2-4**. The angle at which the lift coefficient begins to reduce is referred to as the static stall angle of attack. **Figure 2-5** details an example of a static blade in un-stalled (A) and stalled (B) operation. Blade A is at a lower angle of attack. As the flow accelerates over the leading edge and upper surface of the blade, it remains attached. Under these flow conditions, this blade has favourable operation for maximising lift while minimising drag. As the angle of attack increases, Blade B, the flow becomes separated from the upper surface. As the adverse pressure gradient towards the blade's trailing edge increases, the flow in the boundary layer will reduce, eventually resulting in recirculating flow and causing the blade to stall.

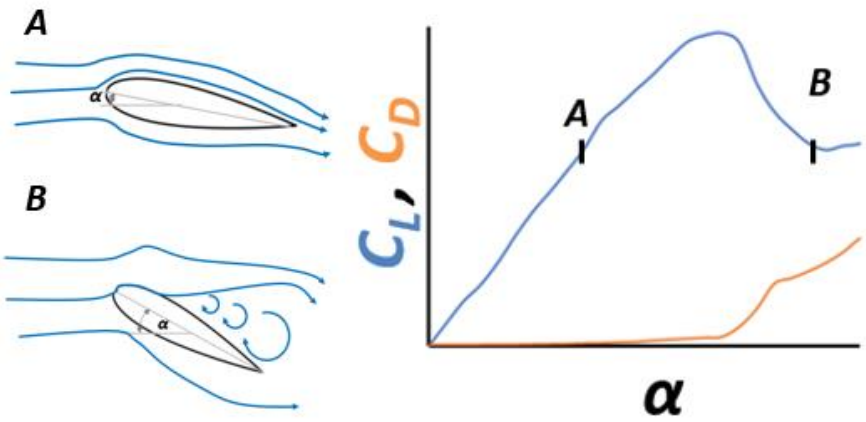

Figure 2-5: Schematic of an un-stalled (A) and stalled (B) blade with associate lift and drag coefficient indicated.

Dynamic stall is a transient flow effect experienced by blades due to rapidly changing angles of attack. **Figure 2-8** from Leishman (2002) details the various stages of dynamic stall and the effects on the lift, drag and moment coefficients. Dynamic stall is notably different to static stall discussed above. It is observed that the lift and drag coefficients at a given angle of attack can vary significantly whether the flow is

separated or attached. As the angle of attack increases, there is a delay in the onset of stall as the flow remains attached to the blade's upper surface, resulting in an increased maximum lift coefficient compared to a blade under quasi-steady-state conditions. As the angle of attack continues to increase, the flow eventually becomes fully separated, causing a severe adverse pressure gradient in the boundary layer resulting in a rapid drop in the lift coefficient. As the angle of attack subsequently decreases to a lower value, the flow becomes reattached to the surface of the blade.

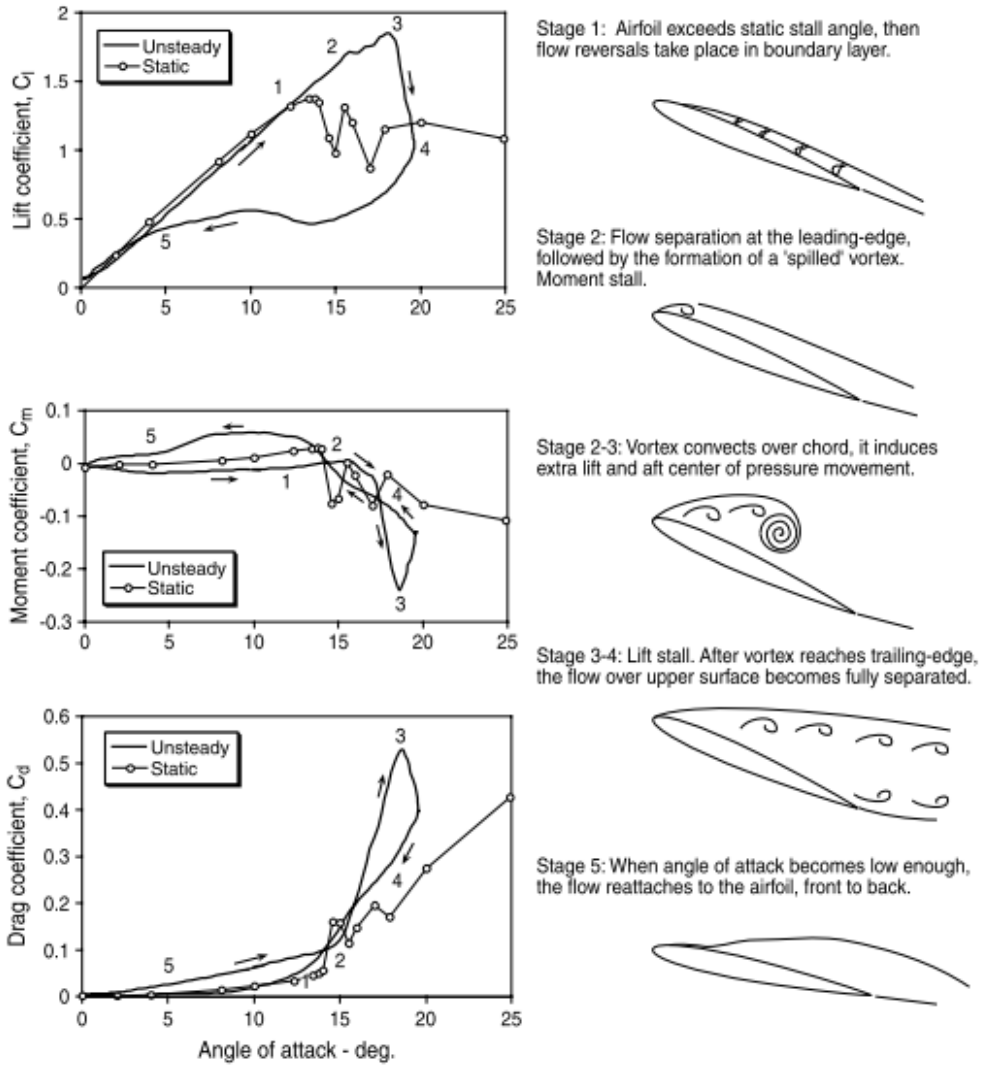

Figure 2-6: Stages of dynamic stall with corresponding steady and unsteady lift, drag and moment coefficient variation with angle of attack included (Leishman, 2002).

2.2.4 Implementation and Validation of BEM Models

As BEM models are typically implemented at an early stage of the device design, comparisons to experimental data are not widely available. Much of the validation of BEM models has been completed for vertical-axis wind turbines.

In general, the power performance of a turbine is studied by establishing the power coefficient, $\bar{C}_P$, over a range of tip speed ratios (*TSR*). $\bar{C}_P$ and *TSR* are dimensionless parameters that readily facilitate hydrodynamic performance comparison for turbines of different specifications and under different assumed flow conditions.

The *TSR* is the ratio of the blade radial speed to the incoming flow velocity and is defined as:

$$TSR = \frac{\omega R}{U_\infty} \tag{2.23}$$

where ω is the rotational velocity of the turbine, R is turbine radius and U_∞ is the freestream velocity.

$\bar{C}_P$ is the ratio of mechanical power output to the overall power available from the fluid, and is calculated as follows:

$$\bar{C}_P = \frac{P}{0.5\rho A U_\infty^3} \tag{2.24}$$

where P is the power output from the turbine and A is the frontal area of the turbine ($A = Diameter(D) \times Height\ (H)$).

Betz limit is the theoretical maximum power coefficient achievable by a turbine (Betz, 1920), i.e. the maximum mechanical power extractable by the turbine from the kinetic energy in the flow. The Betz limit value is 16/27 (0.592); however, current turbine designs never achieve close to this limit, with the maximum power coefficient ranging from 0.35 – 0.50 from existing technologies.

The rotor solidity, σ, is another dimensionless parameter investigated. It is defined as the ratio of the turbine blade area to the total frontal area of the turbine:

$$\sigma = \frac{NcL}{A} \tag{2.25}$$

where N is the number of blades and L is the length of the blade.

The turbine Reynolds number, Re_D, which is a crucial design factor when analysing turbine scaling factors, is defined as:

$$Re_D = \frac{\rho U_\infty D}{\mu} \tag{2.26}$$

Several BEM models have been developed over the years for turbine power performance prediction. Templin (1974) was the first to develop a momentum-based model for vertical axis wind turbines. This model is based on actuator disk theory and assumes that the turbine's induced velocity is constant. It is therefore referred to as a single streamtube model.

Strickland (1975) expanded the single streamtube into a multiple streamtube model (MST). For this calculation, the rotor's swept area is divided into multiple streamtubes, and for each of these streamtubes, the momentum equation and forces on the blade elements are solved. The MST model allows the tangential and normal forces acting on the blade elements to be calculated as a function of blade position. The MST model also allows for the incorporation of a fluid velocity profile.

Results from this Strickland's DART- DARrieus Turbine MST model were compared to wind tunnel test data for two 2-metre diameter turbines, one two-bladed and three-bladed. A limited dataset of C_L and C_D for were obtained from a study by Jacobs and Sherman (1937) were used as input for the model. As shown in **Figure 2-7**, the MST model predictions show a marked improvement on the single streamtube model's predictions when comparing results to experimental data.

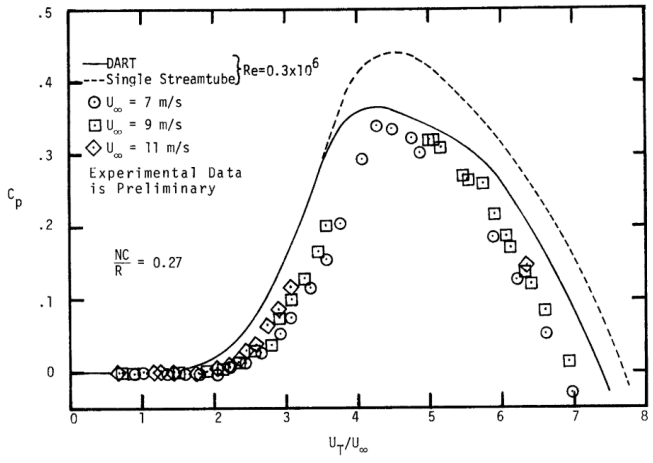

Figure 2-7: Comparison of single streamtube and multiple streamtube model results against experimental test data by Strickland (1975). U_T/U_∞ is the ratio of the radial velocity of the turbine blade to the freestream velocity, i.e. *TSR*.

One major pitfall of the MST model is its failure to account for the variation of incoming velocity, which the downstream half of the rotor experiences. To overcome this issue, two actuator disks are placed in tandem to analyse the upstream and downstream halves of the rotor separately (see **Figure 2-2**). Paraschivoiu (1982), as well as Reed and Sharpe (1980), developed similar models, referred to as double multiple streamtube (DMST) models. For DMST models, separate upwind and downwind interference factors are calculated, with the upwind wind interference factor used to calculate the flow velocity for the downstream portion of the turbine. Paraschivoiu (1982) developed a DMST model and compared the predicted power coefficient variation with tip-speed ratio to experimental data, as shown in **Figure 2-8**. A superior agreement is shown with the DMST model. The C_L and C_D dataset implemented in this study is from NASA and Sandia Laboratories' test data. The author also highlighted the ability to determine the aerodynamic loads variation with blade position which could be used for the structural analysis of Darrieus vertical-axis wind turbines.

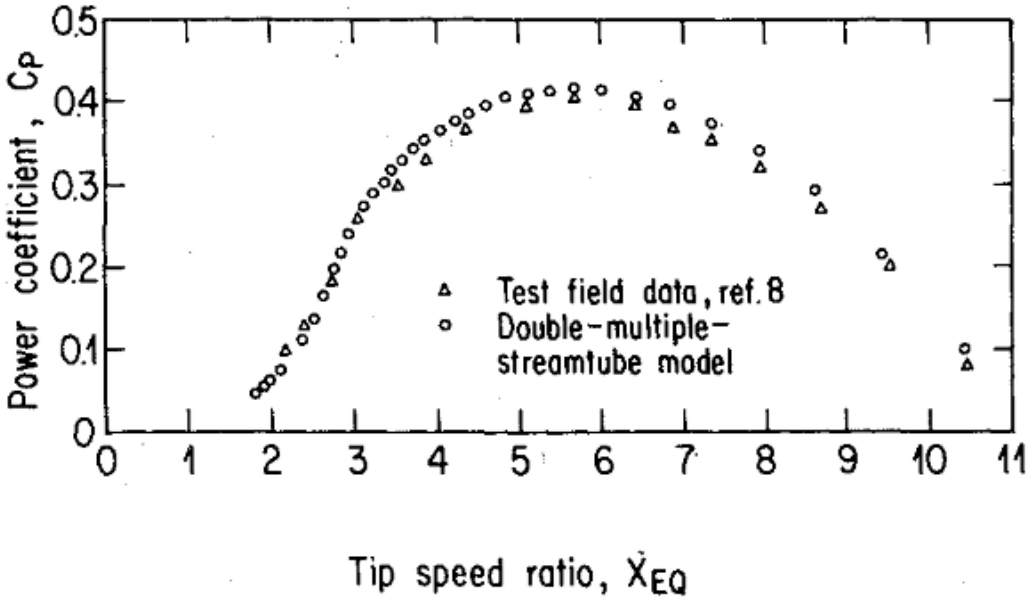

Figure 2-8: Comparison of the variation of C_P with *TSR* between DMST results from the model developed by Paraschivoiu (1982) and experimental test data for a Darrieus wind turbine

Through the years, additional considerations have been introduced to improve the accuracy of DMST models, including dynamic stall, flow expansion and finite aspect

ratio effects. The Gormont model (Gormont, 1973), with additional modifications (Berg, 1983; Massé, 1981), has proven to be an accurate model to predict dynamic stall effects of vertical axis wind turbines. Finite aspect ratio corrections (Abbott and Von, 1959; Viterna and Corrigan, 1982) have also been implemented to correct the C_L and C_D to improve the accuracy of DMST models.

Castelli, Fedrigo and Benini, (2012) assessed the accuracy of their BEM model, which is based on the DMST model developed by Paraschivoiu (1982), with further considerations including the Gormont dynamic stall model with the additional modifications of Masse and Berg, finite aspect ratio correction and a flow expansion correction for the downstream portion of the operating cycle. The model results shown in **Figure 2-9** were compared to the experimental data from SANDIA's 3-bladed 17 m Darrieus turbine. With these improvements, the model accurately predicted the peak power coefficient at the correct optimal *TSR*. There are notable discrepancies between the model predictions and the test data at higher *TSR*, which are attributed to the inability of the BEM model to include secondary flow effects. Examples of these flow effects include the flow around supports and the shaft, which are challenging to include in a BEM model and require in-depth CFD or experimental analysis.

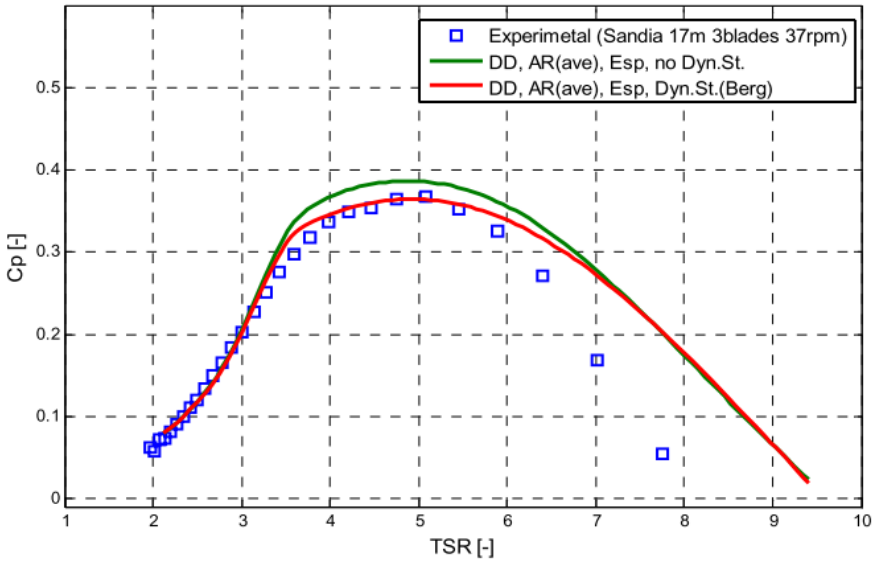

Figure 2-9: Comparison of C_P with *TSR* between DMST results from the model developed by Castelli, Fedrigo and Benini (2012) and experimental test data for SANDIA three-bladed 17m diameter rotor.

While many BEM approaches adopt an iterative approach when solving for the interference factor, convergence challenges have been noted when using this approach

to solve for highly loaded turbines, i.e. high solidity and, or high *TSR* (Gupta and Leishman, 2005; Klimas and Sheldahl, 1978). These challenges are easied with the introduction of a relaxation scheme when iteratively solving for the interference factor (James, 1996). However, this solution does not assist in all cases. McIntosh et al. (2009) suggest an alternative to the iterative approach based on a method similar to a physical stall hysteresis. Mannion et al. (2020) have shown that this method can provide accurate predictions of the power coefficient variation with *TSR* for a high solidity VAWT. The results presented in **Figure 2-10** show that this BEM model accurately predicts the maximum power coefficient within a maximum and minimum error of 18.6% and 5.6%, respectively, at the correct optimal *TSR*.

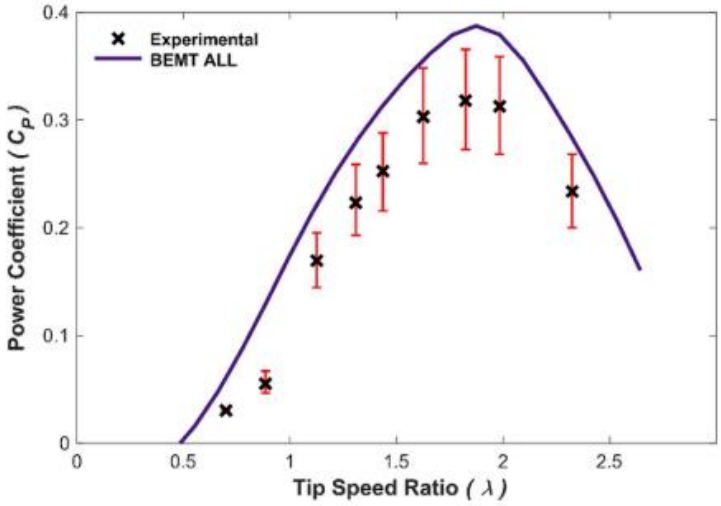

Figure 2-10: Comparison of C_P with *TSR* between DMST results from the BEM model developed by Mannion et al. (2020) and experimental test data with associated error bars for a high solidity VAWT.

2.3 Computational Fluids Dynamics (CFD) Modelling

2.3.1 CFD Theory

2.3.1.1 General

Computational fluid dynamics (CFD) modelling is a technique implemented in industrial and research settings to simulate the behaviour of fluids in different conditions. Applications range from HVAC systems to combustion chambers to aeroplane design. Different approaches are available within CFD packages, dependent on the desired results and computational resources. For this research, the emphasis is

placed on the widely used Reynolds averaged Navier-Stokes (*RANS*) models. Turbulence modelling, the implementation of numerical methods, mesh definition, the verification and validation of results, and two- vs three-dimensionality, are all key factors to be considered when developing RANS models.

This section discusses the mathematics, which is the foundation of the CFD models included in this thesis. Due to CFD being an extensive topic, the theory discussed in this chapter focuses solely on the theory applicable to this research- the design and analysis of tidal turbines. Several texts were consulted for the various theoretical aspects of CFD. The theory relating to the Navier-Stokes equations is taken from Ferziger and Peric (2002) and Wilcox (1998). More details on the derivations of the equations in this section can be found in these texts. The turbulence model equations are taken from Menter (1994), Wilcox (1998) and Menter et al. (2006). Solver theory and other aspects relating to how the RANS equations are solved are taken from the ANSYS Fluent Theory Guide (ANSYS, 2009) and the ANSYS Fluent User guide (ANSYS, 2013). Ferziger and Peric (2002), American Institute of Aeronautics and Astronautics (1998) and Roache (1997) were the texts consulted for information on the verification and validation of CFD results. The nomenclature used in this section may vary from nomenclature in these references. This is to ensure consistency in nomenclature within this thesis.

Fluid flow is governed by three conservation laws which lead to the Navier-Stokes equations. These three conservation laws are as follows:

- Conservation of Mass (the continuity equation)
- Conservation of Momentum (Newton's 2nd Law)
- Conservation of Energy (1st Law of Thermodynamics)

For the tidal and wind energy industry, due to the negligible fluctuations in thermodynamic changes, the conservation of energy can be generally ignored. ANSYS Fluent, the commercial CFD software used in this research, solves the conservation equations for mass and momentum. The energy conservation is solved for flows involving heat transfer or compressibility. These types of flows are not the focus of this research, so the energy equation is not considered.

The conservation of mass states that the mass of a system (M_{sys}) is neither created nor destroyed in fluid flows. The conservation of mass in differential equation form for a three-dimensional flow of infinitesimal volume ($\partial x\ \partial y\ \partial z$) is stated as:

$$\frac{\partial \rho}{\partial t} + \left(\frac{\partial}{\partial x}(\rho u) + \frac{\partial}{\partial y}(\rho v) + \frac{\partial}{\partial z}(\rho w) \right) = 0 \tag{2.27}$$

where ρ is the fluid density, t is time, u, v and w are the three components of the velocity vector ($\vec{V}$).

For the conservation of momentum for a system, Newton's second law is applied, which states that the rate of change of momentum in a system is equal to the sum of the forces acting on the system. For many engineering problems faced, including this research, the assumption that the fluid is inviscid is not reasonable. For Newtonian fluids, such as water and air, where there is a linear relationship between stresses and the rates of deformation, the differential equations for the conservation of momentum using Cartesian coordinates for an incompressible fluid are given by:

$$\rho \left(\frac{\partial u}{\partial t} + u\frac{\partial u}{\partial x} + v\frac{\partial u}{\partial y} + w\frac{\partial u}{dz} \right) = \rho g_x - \frac{\partial p}{\partial x} + \mu \left(\frac{\partial^2 u}{\partial x^2} + \frac{\partial^2 u}{\partial y^2} + \frac{\partial^2 u}{\partial z^2} \right) \tag{2.28}$$

$$\rho \left(\frac{\partial v}{\partial t} + u\frac{\partial v}{\partial x} + v\frac{\partial v}{\partial y} + w\frac{\partial v}{\partial z} \right) = \rho g_y - \frac{\partial p}{\partial y} + \mu \left(\frac{\partial^2 v}{\partial x^2} + \frac{\partial^2 v}{\partial y^2} + \frac{\partial^2 v}{\partial z^2} \right) \tag{2.29}$$

$$\rho \left(\frac{\partial w}{\partial t} + u\frac{\partial w}{\partial x} + v\frac{\partial w}{\partial y} + w\frac{\partial w}{\partial z} \right) = \rho g_z - \frac{\partial p}{\partial z} + \mu \left(\frac{\partial^2 w}{\partial x^2} + \frac{\partial^2 w}{\partial y^2} + \frac{\partial^2 w}{\partial z^2} \right) \tag{2.30}$$

2.3.1.2 Turbulence modelling

Turbulence modelling is a crucial facet of computational fluid dynamics. Turbulent flow is characterised by chaotic changes in the pressure and flow velocity of the fluid field. These fluctuations mix transported quantities such as momentum, energy, and species concentration. These fluctuations may be minimal in terms of magnitude and time-scale and hence are computationally expensive to solve directly in practical engineering calculations. The following are features of turbulent flow:

- Unsteadiness: Turbulent flow is highly unsteady, even if the mean flow is steady.
- Three-dimensionality: While the time-averaged velocity field might be only in two dimensions, the instantaneous field changes in all three spatial dimensions.

- Diffusion: The increased rate of the mixing of mass, momentum and energy in turbulent flow is caused by enhanced diffusivity.
- Vorticity: Turbulent flows are rotational and can be characterised by significant variations in vorticity.
- Dissipation: As turbulence decays, its kinetic energy transfers from larger eddies to smaller eddies and eventually, the lost energy is irreversibly converted into internal energy in the fluid. This process is known as the turbulent energy cascade.
- Wide range of scales: Turbulent flow has a broad spectrum of time and length scales. The Reynolds number influences this range of scales.
- Coherent structures: Turbulent flow contains coherent structures which are repeatable patterns and can be determined. However, the random component of turbulent flows causes these patterns to vary in size, strength, and time scale.

Methods have been developed to develop a model with a minimal level of complexity but still capable of capturing the relevant physical nature of the problem. A brief overview is presented here.

Direct numerical simulation (DNS) is the most accurate approach to solving the Navier-Stokes equations for simulations that have any level of turbulent flow. The entire ranges of spatial and temporal scales of the turbulence are resolved. The computational grid must be fine enough for all the spatial scales of the turbulence, from the smallest dissipative scales (Kolmogorov scales), up to the integral scale associated with the motions containing most of the kinetic energy. As DNS requires a very high-resolution grid and very refined temporal scales, the computational cost of DNS is exceptionally high.

Large-eddy simulation (LES) is an alternative approach for numerically analysing CFD problems. For LES, the large eddies in the flow are resolved directly, while small eddies are modelled. LES, therefore, falls between DNS and Reynolds-averaged Navier-Stokes approach (discussed in the next section) in terms of the fraction of the resolved scales. The justification for the LES approach lies in the fact that whilst the behaviour of the larger eddies tends to be more problem-dependent, the smaller eddies are generally isotropic and show a universal behaviour. LES must be three-dimensional and time-dependent; therefore, while it is not as computationally

expensive as DNS, the computational cost of these simulations is beyond the computational resources of this research.

2.3.1.3 Reynolds Averaging

For Reynolds-averaging approaches to turbulence, all the unsteadiness in the flow is averaged out. The concept of expressing a quantity as the sum of its mean and fluctuating parts was introduced by Reynolds (1895). This concept is used to form the average of the Navier-Stokes equations, i.e. the Reynolds averaged Navier-stokes (RANS) equations. The non-linearity of the Navier-Stokes equations lead to momentum fluxes that act as stresses throughout the flow. Equations are derived from resolving these stresses, which result in additional unknown quantities, leading to the closure issue of the RANS equations, i.e. the need to establish an adequate number of equations to solve all unknowns.

Three different averaging concepts have been introduced for turbulence modelling research, namely time average, spatial average and ensemble average. For time averaging, an instantaneous flow variable is expressed as $f(x_i, t)$. For spatial averaging, the average is taken over all spatial coordinates by doing a volume integral. Ensemble averaging is the most general type of averaging. As an example, using Reynolds decomposition, the velocity can be divided up into a time-averaged value, $\bar{u}_i$, and a fluctuation about this value, u_i':

$$u_i(x_i, t) = \bar{u}_i(x_i) + u_i'(x_i, t) \tag{2.31}$$

Likewise, for scalar quantities such as pressure, energy, or species concentration, in a steady-state flow, a scalar, ϕ in this example, is written as a superposition of the time-averaged value and a fluctuation component about that value:

$$\phi_i(x_i, t) = \bar{\phi}_i(x_i) + \phi_i'(x_i, t) \tag{2.32}$$

Substituting expressions, such as equations (2.31) and (2.32), for the flow variables into the continuity and momentum equations yields the ensemble-averaged RANS equations. Using Cartesian coordinates, they can be expressed as:

$$\frac{\partial}{\partial x}(\rho\bar{u}) + \frac{\partial}{\partial y}(\rho\bar{v}) + \frac{\partial}{\partial z}(\rho\bar{w}) = 0 \tag{2.33}$$

$$\rho\left(\frac{\partial \bar{u}}{\partial t}+\bar{u}\frac{\partial \bar{u}}{\partial x}+\bar{v}\frac{\partial \bar{u}}{\partial y}+\bar{w}\frac{\partial \bar{u}}{dz}\right) = \rho g_x-\frac{\partial \bar{p}}{\partial x}+\mu\Delta\bar{u}-\rho\left(\frac{\partial \overline{u'u'}}{\partial x}+\frac{\partial \overline{u'v'}}{\partial y}+\frac{\partial \overline{u'w'}}{\partial z}\right) \tag{2.34}$$

$$\rho\left(\frac{\partial \bar{v}}{\partial t}+\bar{u}\frac{\partial \bar{v}}{\partial x}+\bar{v}\frac{\partial \bar{v}}{\partial y}+\bar{w}\frac{\partial \bar{v}}{\partial z}\right) = \rho g_y-\frac{\partial \bar{p}}{\partial y}+\mu\Delta\bar{v}-\rho\left(\frac{\partial \overline{v'u'}}{\partial x}+\frac{\partial \overline{v'v'}}{\partial y}+\frac{\partial \overline{v'w'}}{\partial z}\right) \tag{2.35}$$

$$\rho\left(\frac{\partial \bar{w}}{\partial t}+\bar{u}\frac{\partial \bar{w}}{\partial x}+\bar{v}\frac{\partial \bar{w}}{\partial y}+\bar{w}\frac{\partial \bar{w}}{\partial z}\right) = \rho g_z-\frac{\partial \bar{p}}{\partial z}+\mu\Delta\bar{w}-\rho\left(\frac{\partial \overline{w'u'}}{\partial x}+\frac{\partial \overline{w'v'}}{\partial y}+\frac{\partial \overline{w'w'}}{\partial z}\right) \tag{2.36}$$

The RANS continuity and momentum equations for incompressible flow without body forces are written in Cartesian tensor form as follows:

$$\frac{\partial(\rho\bar{u}_i)}{\partial x_i}=0 \tag{2.37}$$

$$\frac{\partial(\rho\bar{u}_i)}{\partial t}+\frac{\partial}{\partial x_j}\left(\rho\bar{u}_i\bar{u}_j+\rho\overline{u_i'u_j'}\right)=-\frac{\partial \bar{p}}{\partial x_i}+\frac{\partial \bar{\tau}_{ij}}{\partial x_j} \tag{2.38}$$

where $\bar{\tau}_{ij}$ are the mean viscous stress tensor components, given by:

$$\bar{\tau}_{ij}=\mu\left(\frac{\partial \bar{u}_i}{\partial x_j}+\frac{\partial \bar{u}_j}{\partial x_i}\right) \tag{2.39}$$

The equation for the mean of any scalar quantity can be written as:

$$\frac{\partial(\rho\bar{\phi})}{\partial t}+\frac{\partial}{\partial x_j}\left(\rho\bar{u}_j\bar{\phi}+\rho\overline{u_j'\phi'}\right)=\frac{\partial}{\partial x_j}\Gamma\left(\frac{\partial \bar{\phi}}{\partial x_j}\right) \tag{2.40}$$

The Reynolds stresses in equation (2.38), $\rho\overline{u_i'u_j'}$, means that the RANS equations are not closed, i.e. there are more variables than equations. A turbulence model, which expresses the Reynolds stress tensor using time-averaging quantities, is required to close the RANS equations. Due to the complexity of turbulence, no single turbulence model has the capability of representing all aspects of turbulent flow. The selection of the turbulence model is dependent on the physics of the problem, the computational power available and the desired accuracy of the solution. Turbulence models can be

classified into two types: Reynolds stress equation models (RSM) and eddy-viscosity models. RSM requires six additional transport equations, one for each stress term. The advantage of the RSM is that they do not require isotropy in the stresses, as all stresses are computed directly. While it is physically the most complete model, it requires significantly more CPU effort than eddy-viscosity models.

Eddy-viscosity models require the solution of a fewer number of transport equations, typically one or two but more recently four. Eddy-viscosity models use the Boussinesq assumption (Boussinesq, 1897) that the Reynolds stresses are proportional to the mean flow gradients:

$$-\rho\overline{u_i'u_j'} = \mu_t\left(\frac{\partial\bar{u}_i}{\partial x_j}+\frac{\partial\bar{u}_j}{\partial x_i}\right)-\frac{2}{3}\rho k\delta_{ij} \tag{2.41}$$

Where μ_t is the eddy viscosity, δ_{ij} is the Kronecker delta and k, the turbulent kinetic energy per unit mass, is given by:

$$k = \frac{1}{2}\overline{u_i'u_i'} = \frac{1}{2}\left(\overline{u_x'u_x'}+\overline{u_y'u_y'}+\overline{u_z'u_z'}\right) \tag{2.42}$$

2.3.1.4 Turbulence Models

Algebraic solutions offer the most straightforward method for the turbulence closure problem. Two of the most commonly implemented zero-equations are the Baldwin and Lomax (1978) and Smith and Cebeci (1967) models. For zero-equation models, no additional equations are required to describe the transport of turbulent quantities, stresses, or fluxes. By not modelling the transport of turbulence, the zero-equation models cannot accurately predict any flows which have non-local mechanisms such as the history effect, i.e. the influence of flow processes downstream of the event. Therefore, zero-equations models are typically employed solely to attached boundary-layer flow simulations, where the flow can be modelled using only local relations.

One equation models include an equation that is derived for one turbulent quantity, typically the turbulent kinetic energy, k, or the eddy viscosity, υ. The Spalart and Allmaras (1992) model is a standard one-equation model. This turbulence model solves a modelled transport equation for the kinematic eddy viscosity, $\bar{\upsilon}$.

Two or more equation models are the most widely developed and implemented turbulence models. In addition to modelling the turbulent kinetic energy, k, the

turbulent length scale or equivalent is modelled. Common two-equation turbulence models include the k-ε (Launder and Spalding, 1972) and k-ω (Wilcox, 1988) models. Two turbulence models are the focus of this research namely the k-ω shear-stress transport (SST) model, a variation of the standard k-ω turbulence model; and the SST Transition model which is based on the k-ω SST model with two additional transport equations for the intermittency and transitional Reynolds number.

The k-ω SST model (Menter, 1994) is a two-equation model based on the earlier standard k-ω model. This turbulence model switches between the standard k-ε model in the far field, free-stream region and the k-ω model at the wall surfaces, with a well-defined boundary layer. The benefit of the k-ω SST model is in its ability to switch between the two turbulence models, thereby using the strengths of both turbulence models in different regions of the domain. The k-ε model predicts the flow in the free stream very well, but it does not accurately predict high flow separation or reverse flow situations from the wall, both of which are possible situations for hydrofoils, especially at high values of angles of attack. Contrastingly, the k-ω model performs well for near-wall conditions but encounters difficulties with defining inlet free-stream turbulence properties. A blending function, F_1, is implemented to combine both turbulence models. When F_1 = 1, in the near-wall region, the k-ω model is activated. Away from the wall surface, this blending function allows the k-ε turbulence model to be activated. This feature makes the k-ω SST model more accurate and capable of modelling a more comprehensive range of flows than the standard k-ω model. Details on the formulation of this turbulence model are available in **Appendix A.1**.

The Langtry-Menter four equation SST Transition turbulence model (Langtry et al., 2006; Menter et al., 2006), also known as the γ-$\widetilde{Re}_{\theta t}$ SST turbulence model is based on the SST k-ω turbulence model, with two additional equations. The SST k-ω model is a fully turbulent model which assumes that all the fluid in the model domain is turbulent; however, this may not be the case, so the SST Transition model incorporates two additional equations for the intermittency (γ) and the transitional momentum thickness Reynolds number ($\widetilde{Re}_{\theta t}$).

The intermittency equation is used to determine whether the SST Transition model should be active. When γ is zero, the production of turbulent kinetic energy is suppressed, and the flow is effectively laminar. When γ is equal to one, the SST

Transition model is fully active, and the flow is assumed to be fully turbulent. $\widetilde{Re}_{\theta t}$ controls the transition criterion between the laminar and turbulent flow. The critical Reynolds number, $\widetilde{Re}_{\theta c}$, occurs where intermittency begins to increase in the boundary layer. It occurs upstream of the transition Reynolds number, $\widetilde{Re}_{\theta t\iota}$, as turbulence must first build up to appreciable levels in the boundary layer before any change in the laminar profile can occur. As a result, $\widetilde{Re}_{\theta c}$ is the location where turbulence starts to grow and $\widetilde{Re}_{\theta t}$ is the location where the velocity profile starts to deviate from a purely laminar profile. Details on the formulation of this turbulence model are available in **Appendix A.2**.

2.3.1.5 Wall Modelling

The presence of a surface affects the flow in its vicinity. At the surface, the velocity of a viscous fluid must be 0 to satisfy the no-slip condition, resulting in a boundary layer forming in the region close to the wall. The fluid velocity in this boundary layer can be divided up into three layers, indicated in **Figure 2-11** (ANSYS, 2013). The region closest to the wall is the viscous layer, also known as the laminar sublayer, due to the general laminar flow conditions observed. In this region, the viscous forces of the fluid are dominating over the fluid's inertial forces. Outside the viscous layer is the buffer layer, also referred to as the blending region. In this region, the fluid is subject to both viscous and turbulent shear stresses. The region at the outside is the outer or turbulent layer, where turbulent flow dominates.

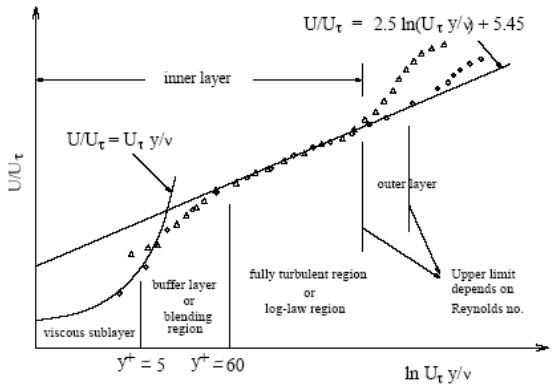

Figure 2-11: The relationship between the dimensionless velocity and non-dimensional wall distance (ANSYS, 2013).

There are generally two approaches to modelling the flow in a near-wall region: wall functions or a near-wall model approach. Wall functions are based on semi-empirical formulas used to link the viscous region close to the wall to the fully turbulent region.

This approach is suitable for high Reynolds number flows and is often favoured due to its reduced computational time.

Both the k-ω SST and Transition SST turbulence models adopt the near-wall model approach and require an adequately refined boundary layer at wall surfaces. The recommended best practice mesh refinement guidelines along a wall are a maximum y^+ value of 1, with a mesh expansion ratio of less than 1.1 and roughly 75-100 nodes in the streamwise direction.

The y^+ value is a non-dimensional wall distance which indicates how fine or coarse a mesh is along a wall surface, defined as:

$$y^+ = \frac{yV_*}{\upsilon} \tag{2.43}$$

where y is the first cell height, υ is the fluid viscosity, and V_*, the friction velocity is defined as:

$$V_* = \frac{\tau_w}{\rho} \tag{2.44}$$

where τ_w is the shear stress of the fluid at the wall defined as:

$$\tau_w = \mu \left(\frac{\partial u}{\partial y}\right)_{y=0} \tag{2.45}$$

where μ is the dynamic viscosity.

2.3.1.6 Fluent Solver Theory

Analytical solutions of the Navier-Stokes equations can only be carried out for the most straightforward calculations. For any practical cases, a numerical solution is required for solving the Navier-Stokes equations. Several CFD techniques exist for numerically solving the Navier-Stokes equations. For this study, ANSYS Fluent® is employed as a two- and three-dimensional, pressure-based, incompressible flow solver. A pressure-based solver is typically implemented for low-speed incompressible flows. The velocity field is obtained from the momentum equations. The continuity and momentum equations are manipulated to develop a pressure equation used to determine the pressure field. The governing integral equations are solved for the conservation of mass, momentum, and, when necessary, energy and other scalars, i.e. turbulence. When solving the RANS equations, the flow field needs to be discretised spatially into a computational grid. Fluent® adopts a control-volume

based technique (Versteeg and Malalasekera, 1995) to convert a general scalar transport equation to an algebraic equation that is solved numerically. This approach consists of integrating the transport equation about each control volume, giving a discrete equation that expresses the conservation law on a control-volume basis.

In Fluent®, the discrete values of a scalar are stored at the cell centres. The face values are required for the convection terms, and these must be interpolated from the cell centre values. For this interpolation, an upwind scheme is used, meaning the face value is derived from quantities in the cell upstream relative to the direction of the normal velocity. The second-order upwind scheme is generally the preferred option due to reduced interpolation errors. If stability issues arise, the first-order upwind scheme may be employed initially to obtain a stable solution before switching to second-order. It should be noted that while simulations implementing the first-order discretisation typically leads to a quicker converged solution, they are generally deemed less accurate. For simple simulations where the flow is aligned with the grid, the first-order scheme may provide accurate results. However, when the flow is not aligned with the grid, as is the case with triangular and tetrahedral elements, first-order discretization schemes increase the numerical diffusion in the simulations.

For transient simulations, the governing equations must be discretised in time. Temporal discretisation requires the integration of over a specified time interval, Δt. Implicit and explicit time integration methods are available. The explicit time-stepping formulation is only available when the density-based solver approach is selected. A second-order implicit temporal discretisation scheme is recommended as it offers improved accuracy over first-order schemes, provided stability issues do not occur.

The evaluation of the gradients is required to construct values of a scalar at the cell faces and for computing secondary diffusion terms and velocity derivative. The gradient of a given scalar is used to discretise the convection and diffusion terms in the flow conservation equations. The least squares cell-based & Green Gauss node-based approaches are the most accurate, especially for unstructured meshes. The Green Gauss cell-based is less accurate but is much less computationally expensive.

Fluent® stores the pressure and velocity at the centre of each cell. When discretizing the momentum equation, the pressure value at the face between the two cells is

required. The standard and second-order schemes use interpolation methods, with the second-order scheme generally the preferred option unless stability issues arise. PRESTO! solves for the pressure on the cell faces and is, therefore, more computationally expensive. This scheme gives more accurate results for problems with high Rayleigh number flows or and strong body forces.

A pressure-based solver allows the flow problem to be solved in a segregated or coupled manner. The following options are available in Fluent® for coupling the pressure and velocity:

- Semi-Implicit Method for Pressure Linked Equations- SIMPLE (segregated):
- Semi-Implicit Method for Pressure Linked Equations, Consistent- SIMPLEC (segregated)
- Pressure-Implicit with Splitting of Operators- PISO (segregated)
- Coupled (coupled)

For the segregated algorithms, the momentum and pressure-based continuity equations are solved sequentially, which may result in slow convergence. With the Coupled algorithm, the momentum and pressure-based continuity equations are solved simultaneously. This method is more robust and is a good choice for transient simulations with poor quality meshes or a large time step.

Further details and the formulation employed for the pressure-based solver, spatial discretisation, temporal discretisation, under-relaxation of variables and equations, and more are available in the ANSYS Fluent Theory Guide (2009).

2.3.1.7 Boundary Conditions

When solving the Navier-Stokes equations, appropriate initial conditions and boundary conditions need to be applied. For the simulations of Chapters 5 and 6, the following boundary conditions are applied.

Inlet: An inlet velocity boundary condition, which specifies the velocity components and turbulence quantities, is applied. The turbulent inlet conditions are calculated by specifying the turbulent flow conditions, e.g. turbulent intensity (Tu) and turbulent viscosity ratio (TVR).

Outlet: A static pressure value is defined as the boundary condition at the outlet. Outlet turbulent conditions are defined similarly to that of the inlet boundary conditions.

Wall: The wall boundary condition is used to bound fluid and solid regions. For viscous flow, a no-slip condition is enforced at the wall, i.e. the tangential fluid velocity is equal to the wall velocity, and the normal velocity component is set to zero. Alternatively, shear stress can be specified at the wall. Roughness on the wall surface can also be included for turbulent flow.

Symmetry: A symmetry boundary condition can be used to reduce the computational requirements of a simulation. The flow field and geometrical features must be symmetric. The constraints of a symmetry boundary condition are that the velocity normal to the boundary and the gradient of scalar quantities normal to the boundary are all set to zero.

Interface: An interface is defined between two different bodies which share a common boundary. It is implemented for simulations that include a moving reference frame or sliding mesh models.

2.3.1.8 Errors, uncertainty, verification and validation

Integrity in CFD results is achieved by obtaining acceptable levels of uncertainty and error in the results. These levels of uncertainty and error are obtained through a process of verifying and validating the results.

Uncertainty is defined as a potential deficiency of the modelling process that is due to the lack of knowledge. Error is defined as a recognisable deficiency in modelling that is not due to a lack of knowledge. Errors can be classified into two types, acknowledged error and unacknowledged error.

1. Types of acknowledged error
    - Physical approximation error: This error is defined as the difference between the actual flow and the solution to the conservation equations, which is often attributable to turbulence model assumptions, e.g. the use of the k-ε turbulence model for simulations with high flow separation would lead to significant errors due to the model's inability to predict flow separation accurately.
    - Computer round-off error: This error is associated with the representation of floating-point numbers on the computer and the accuracy at which these numbers are stored.
    - Iterative convergence error: This error can be attributed to the difference between the exact and iterative solution. A convergence criterion is set by the

user, which determines when the simulation will stop running. This error can be investigated by picking a key variable at a critical point in the flow field and monitoring its value variation from iteration to iteration.

- Discretisation error: This error is relating to both spatial and temporal discretisation errors. This error is reduced to zero as the mesh size increases and the time step decreases. This error can be assessed by carrying out spatial and temporal discretisation studies.

2. Types of unacknowledged error
   - Computer programming error: This error is concerning possible errors or bugs within the code being implemented.
   - User error: This error is associated with the human setting up, running, and analysing the simulation.

To assess the quality of a CFD model, verification and validation of the results are necessary. In the Verification and Validation Guide published by the American Institute of Aeronautics and Astronautics (1998), verification is defined as "*The process of determining that a model implementation accurately represents the developer's conceptual description of the model and the solution of the model*", and validation is defined as "*The process of determining the degree to which a model is an accurate representation of the real world from the perspective of the intended uses of the model".*

Verification of the results involves examining the error due to mistakes in the code and the incorrect implementation of conceptual models. For this research, which involves the use of a commercial CFD package, mistakes in the CFD code are not the primary focus for the verification of the results. The errors attributed to the implementation of conceptual models can be attributed to discretisation errors, both spatial and temporal, iterative convergence errors and consistency in the CFD solution. For the verification assessment, CFD results are compared to exact analytical results. By comparing CFD results to highly accurate numerical solutions, the accuracy of the CFD code can be examined.

Validation of the results examines if the computational models implemented in the CFD code agree with real-world physics. Like the verification assessment process, discretisation errors, iterative convergence errors and consistency in the CFD solution

are examined. For the validation assessment, model uncertainties are also examined, and CFD results are compared to experimentally measured values.

The spatial discretisation error can be analysed by performing a grid convergence study which involves performing the CFD simulation for two or more successively refined grids. Richardson extrapolation was discussed by Roache (1997), and it is used to calculate the exact solution based on the convergence and refinement ratio determined using a series of three or more increasingly refined meshes. Before applying Richardson extrapolation, it is necessary to determine the apparent convergence condition. Richardson extrapolation may only be implemented when R^*, defined in equation (2.46), is less than 1, i.e. monotonic convergence.

$$R^* = \frac{\phi_2 - \phi_1}{\phi_3 - \phi_2} \tag{2.46}$$

R^* > 1 Monotonic divergence
1 > R^* > 0 Monotonic convergence
0 > R^* > -1 Oscillatory convergence
R^* < -1 Oscillatory divergence

where ϕ is a measured value and the subscripts 1, 2 and 3 indicated three successively refined meshes with a constant refinement ratio, r, defined as:

$$r = \left(\frac{N_{\text{fine}}}{N_{\text{coarse}}}\right)^{\frac{1}{2}} \tag{2.47}$$

where N_{fine} is the number of elements in the fine mesh and N_{coarse} is the number of elements in the coarse mesh. The order of convergence, *p*, is defined as:

$$p = \frac{\ln\left(\frac{\phi_2 - \phi_1}{\phi_3 - \phi_2}\right)}{\ln(r)} \tag{2.48}$$

Richardson's extrapolation value for ϕ is calculated as follows:

$$\phi = \phi_1 + \frac{\phi_1 - \phi_2}{r^p - 1} + HOT \tag{2.49}$$

Evaluating the iterative convergence error involves examining the changes from iteration to iteration for each equation being solved. These changes are referred to as the residuals and are generally scaled or normalised. An acceptable level of aim is for the residuals to reduce a certain number of magnitudes, typically 3-4 orders, before deeming that a converged solution has been achieved. Specific quantities, such as the

lift force on a body, may also be tracked from iteration to iteration. A user-defined convergence criterion can be set for these quantities.

Consistency must be achieved in the CFD solution. For example, for a CFD problem with a specified inlet velocity and zero-gauge pressure at the outlet, with no additional source terms, the mass flow should remain the same throughout the CFD simulation.

2.3.2 Literature review of CFD methods application to turbine modelling

2.3.2.1 Single Blade Modelling

As highlighted in **Section 2.3.1 CFD Theory**, common numerical modelling methods within CFD are direct numerical simulation (DNS), large-eddy simulations (LES), and Reynolds-averaged Navier-Stokes (RANS) modelling. DNS involves solving all scales of the flow and is the most accurate modelling technique. LES involves solving the most significant scale motions of flow and modelling the small-scale motions. For RANS modelling, all the unsteadiness in the turbulent flow is averaged. Due to the complexity of turbulence, it is unlikely that any single RANS turbulence model is fully capable of representing all turbulent flows. However, it has proven to be an accurate means of determining the average forces on a large scale body (Stergiannis et al., 2016).

DNS has previously been utilised to predict the flow around NACA profiles. However, due to the enormous computational expense, this study has been limited to the analysis of a single angle of attack (α) value at a single Reynolds number (Re). Flow visualisations from a study by Shan, Jiang and Liu (2005) study a NACA0012 aerofoil with an angle of attack of 4^o and Reynolds number of 10^5 are presented in **Figure 2-12**. Their analysis detailed the key flow patterns around the aerofoil, flow separation, the detached shear layer, vortex shedding, breakdown to turbulence and the reattachment of the boundary layer.

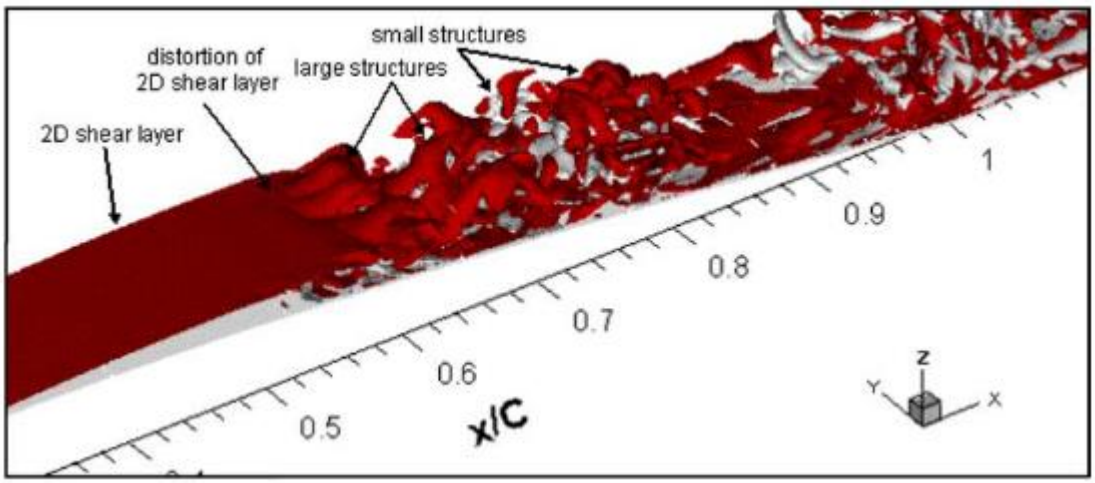

Figure 2-12: Three-dimensional iso-surface of instantaneous spanwise vorticity detailing the flow patterns for a NACA0012 blade profile (α = 4º, Re = 10^5) (Shan, Jiang and Liu 2005).

The LESFOIL project is a comprehensive study of the application of LES for aerofoils (Mellen et al., 2003). The research focuses on the Aerospatiale A-aerofoil at α = 13.3º, Re = 2 x 10^6. Results from several partners were included in the report and it was concluded that for this aerofoil, under these conditions, a relatively high angle of attack and high Reynolds number, LES simulations only provides significant advantages over RANS simulations when near-wall turbulent structures are adequately resolved, and the transition from laminar to turbulent flow is simulated correctly. The grid resolution required to achieve a successful LES based solution is significantly more refined than the grid resolution requirement for similar RANS simulations.

The use of the RANS modelling approach for the simulation of aerofoils is a well-established research field. Details of some of the literature relating to these studies are listed in **Table 2-1**. CFD results typically focus on metrics such as C_L and C_D variation with α or the variation of the static pressure coefficient (C_p) or skin friction coefficient (C_f) with distance along the chord (x/c). These results are compared to equivalent experimental data where available.

As noted above in S**ection 2.3.1.3 Reynolds Averaging**, turbulence model selection and mesh definition are of primary concern when performing RANS simulations. Concerning turbulence modelling selection for studying blade profiles, the treatment of the transition from laminar to turbulent flow conditions in the boundary layers is of interest. Three different approaches have been considered in the literature reviewed.

For the first method, boundary layers are treated as fully turbulent. This is the most common approach implemented and is usually applied when the presence of laminar flow in the boundary layer has a negligible effect on the overall flow, i.e. low angles of attack. Previous CFD RANS approaches which adopted this method to determine C_L and C_D data for aerofoils have been limited to low pre-stall angles of attack due to use of Spalart-Allmaras, $k-\varepsilon$, or $k-\omega$ turbulence models (Azeez and Paul, 2014; Şahin and Acir, 2015; Dash, 2016; Sagmo, Bartl and Saetran, 2016). Discrepancies have been identified in the literature in this approach for predicting coefficients at higher angles of attack with the implementation of these turbulence models due to the failure of these models to capture flow separation and other transition effects accurately.

A second method involves identifying a transition point where the flow changes from laminar to turbulent, otherwise known as forced transition. This method requires detailed experimental studies, as presented by Douvi et al. (2012), and has proven to improve the accuracy of the predictions; however, it is difficult to accurately predict the transition point without the availability of previous experimental data.

The third methods involve the implementation of recently developed transition turbulence models. The strengths of the SST Transition model (Menter et al., 2006) in predicting the laminar to turbulent transition and flow separation has been discussed in detail in **Section 2.3.1.4 Turbulence Models**. The SST Transition model has previously been implemented for symmetric and non-symmetric aerofoil analyses (Counsil and Goni Boulama, 2013; Genç, 2010;).

Table 2-1: Summary of RANS simulations from the literature including blade profile; the range of angles of attack and Reynolds numbers studied; selection of turbulence model; and results recorded.

Reference	Blade Profile	Re	α	Turbulence model	Results
(Douvi et al., 2012)	NACA 0012	3×10^6	-12° to 14°	S-A, Realizable $k-\varepsilon$, $k-\omega$ SST	C_L/C_D vs α C_D ($\alpha = 0$) vs Re
(Azeez and Paul, 2014)	NACA 63-018	3×10^6, 6×10^6, 9×10^6	0° to 16°	S-A	C_L/C_D vs α
(Şahin and Acir, 2015)	NACA 0015	6.8×10^5	0° to 20°	S-A, $k-\varepsilon$	C_L/C_D vs α
(Dash, 2016)	NACA 0012	1×10^6	4° to 10°	Realizable $k-\varepsilon$	C_L/C_D vs α, C_p vs x/c
(Sagmo et al., 2016)	NREL S826	1×10^5	-16° to 24°	S-A, $k-\omega$, Realizable $k-\varepsilon$	C_L/C_D vs α, C_p vs x/c
(Genç, 2010)	NACA 64A006	5.8×10^6	2° to 11°	$k-k_L-\omega$, SST Transition, $k-\omega$ SST, $k-\varepsilon$	C_L/C_D vs α, C_p vs x/c C_f vs x/c
(Counsil and Goni Boulama, 2013)	NACA 0012, SD-7003	4.8×10^4 to 2.5×10^5	0° to 8°	SST Transition	C_L/C_D vs α, C_p vs x/c C_f vs x/c

2.3.2.2 RANS Turbine Modelling

Two dimensional CFD models have been widely implemented in the analysis process of vertical-axis turbines. As detailed in **Table 2-2**, a wide variety of turbulence models, total number of mesh elements, time step increments, solver settings and other aspects of these simulations have been investigated in the literature. One part of the approach which is common in all simulations is the adoption of the sliding mesh setup. For this transient approach, two separate grid domains are defined, one rotating circular zone including the turbine geometry and one stationary, fixed rectangular zone, which defines the extent of the computational domain. A sliding mesh interface is defined between the two zones, across which values are interpolated.

The simulations performed in the references listed in **Table 2-2** are mainly run with the commercial software ANSYS Fluent®. A pressure-based solver approach is favoured over a density-based based solver, although there is no consensus in the literature on the specific solver approach adopted within ANSYS Fluent®. Balduzzi et al. (2016) tested the Coupled, SIMPLE (Semi-Implicit Method for Pressure-Linked Equations) and PISO (Pressure-Implicit with Splitting of Operators) algorithms for solving between the pressure and velocity within the pressure-based solver and concluded that the Coupled algorithm offered the best solution in terms of robustness and accuracy. Maître et al. (2013) and Almohammadi et al. (2012) both adopted the SIMPLE algorithm, while Lanzafame et al. (2014) used the PISO algorithm.

Second-order spatial discretion schemes are favoured for solving the transport equations. Maître et al. (2013), Almohammadi et al. (2013), and Mannion et al. (2018) applied first-order discretisation schemes for the initial part of the simulations to improve the stability of the solution before switching to second-order discretisation schemes to improve the accuracy for the remaining rotations. Benefits of second-order discretization schemes include reducing interpolation errors and the correct computation of numerical diffusion (Blazek, 2001).

Mesh definition, especially the dimensionless wall distance, y^+ value, equation (2.43), is of concern in the development of 2D URANS simulations

of turbines. The selection of turbulence modelling approaches influences the required y^+ value. Balduzzi et al. (2016), Almohammadi et al. (2012), Mannion et al. (2018) and Maître et al. (2013) all adopted either the $k-\omega$ SST or SST Transition model, which both require a refined mesh definition, $y^+<1$ at wall surfaces, i.e. the blade surfaces. Daroczy et al. (2015) implemented numerous RANS turbulence models, including the $k-\varepsilon$ Realizable with Wall Functions ($y^+>30$), noting that the results from this appraoach failed due to the challenge in maintaining an appropriate cell aspect ratio was not possible with the $y^+>30$ requirement.

Ensuring a mesh is of adequate resolution is crucial in ensuring an accurate solution is achieved while minimising computational expenses. A similar statement is true when considering time step size selection. Too large a time step and the complex flow phenom are not captured accurately; too small a time step, the computational time to achieve a converged solution becomes unrealistic. In general, for turbine modelling, time-steps are normalised with the azimuthal angle rotation per time step. Time steps from the literature range from 0.1^o to 2^o azimuthal angle increments. Balduzzi et al. (2016) noted the requirement for smaller time steps at lower *TSR* values due to regions of large flow separations.

The Fluent solver manual recommends residual convergence criterion for the transport equations of 1×10^{-5}. Additional simulations outputs, such as the total turbine torque, are generally also assessed to determine convergence. Some literature assumed a converged solution was achieved when the average torque per rotation varied by less than 1% between subsequent rotations, while other literature set a convergence target of < 0.1% for this variation.

Results presented focus on validating model predictions of power curves ($\bar{C}_P$ vs *TSR*) against experimental data. When comparing model predictions with physical test results, blockage effects must be considered when appropriate. Bachant and Wosnik (2016) noted large discrepancies when comparing model predictions to experimental test data for their three-bladed vertical-axis turbine, partly attributed to the failure of 2D models to accurately capture blockage effects. These discrepancies were investigated by Mannion et al.

(2018), who concluded that for 2D simulations, the domain width needed to be extended to provide a blockage value equivalent to that of the 3D model. Mannion et al. (2018) presented results, both highlighting the improved model predictions with this consideration, **Figure 2-13 (b)**, and also the strengths of the SST Transition turbulence model in accurately predicting the power coefficient variation with *TSR*.

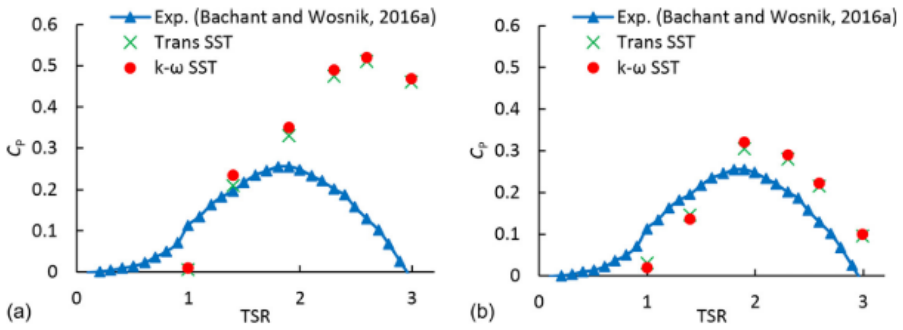

Figure 2-13: Two-dimensional CFD model predictions for power coefficient variation with TSR for **(a)** High Blockage model and **(b)** Low Blockage model

Other literature ensured that the computational domain was broad and, or symmetry boundary conditions were included to simulate a turbine in an open field. Balduzzi et al. (2016) present maximum power coefficient predictions within 5% of experimental values at the correct *TSR*. In addition to power curves, flow visualisation plots of vorticity magnitude and streamline plots are presented by Almohammadi et al. (2012) and Maître et al. (2013), facilitating the analysis of the complex flow features at the aerofoil wall, including flow separation and vortex shedding.

Table 2-2: Summary of 2D RANS simulations from the literature of vertical-axis wind and tidal (water) turbines including turbine dimensions; recommended turbulence model, mesh definition, solver settings & time step size.

Reference	Wind /Tidal	Turbine Parameters (Blade Profile, *N*, *c*, *D*)	Turbulence model	Number of elements	Solver Details	Time Step Size (º/step)
(Balduzzi et al., 2016)	Wind	NACA0018, 3, 0.246 m, 1.9 m	k- ω SST	4.1 x 10^5	Coupled; Spatial Discretisation: 2nd order	0.135º - 0.405 º
(Almohammadi et al., 2012)	Wind	NACA0015, 3, 0.4 m, 2.5m	SST-Transition	5.5 x 10^5	SIMPLE; Spatial Discretisation: 2nd order	0.14º - 0.72 º
(Daroczy et al., 2015)	Wind	NACA0015/ 21/ 25, 3, 0.16 m, 3 m	Spalart–Allmaras k - ε Realizable, k - ω SST SST-Transition	5.4 x 10^5	Coupled; Spatial Discretisation: 2nd order	0.5º
(Maître et al., 2013)	Tidal	NACA0018, 3, 0.032, 0.175 m	k - ω SST	4 × 10^5	SIMPLE; Spatial Discretisation: 1st & 2nd order	1 º
(Lanzafame et al., 2014)	Wind	NACA0015, 3, 0.4 m, 2.5 m	SST-Transition	7 × 10^5	PISO, Spatial Discretisation: 2nd order	0.5º
(Almohammadi et al., 2013)	Wind	NACA0015, 3, 0.4 m, 2.5 m	SST-Transition, RNG k- ε	5 × 10^4 - 2.1 × 10^6	SIMPLE; Spatial Discretisation: 1st & 2nd order	~0.1 º
(Bachant and Wosnik, 2016)*	Tidal	NACA0020, 3, 0.14 m, 1 m	k–ω SST, Spalart–Allmaras	5 × 10^5	PISO-SIMPLE hybrid,	~0.5º
(Mannion et al., 2018)	Tidal	NACA0020, 3, 0.14 m, 1 m	k–ω SST and SST Transiton	9.8 × 10^5	Coupled; Spatial Discretisation: 1st & 2nd order	0.2º

*Simulations ran with OpenFOAM pimpleDyMFoam solver

Due to constraints on computational resources, three-dimensional modelling of vertical-axis turbine had been considered computationally prohibitive (Li et al., 2013) until significant developments in recent years. A list of 3D RANS studies of vertical-axis turbines, both wind- and tidal-based, are listed in **Table 2-3**. Include in this table details of the turbine design, turbulence model and results recorded. Many of the learnings, in terms of turbulence model selection, solver settings and convergence criterion, are taken from the development of 2D models listed above and integrated into the development of 3D models.

Marsh et al. (2015) adopted the k-ω SST turbulence model when studying a straight-bladed vertical-axis tidal turbine design. An extensive spatial and temporal discretization studies established a total mesh size of $17.2 \times 10^{6,}$ and a time step equivalent to 0.9^{o} of rotation was required to achieve a spatial and temporal converged solution. They also concluded that

Alaimo et al. (2015) studied both a straight and helical VAWT through the RANS approach while implementing the k-ε turbulence model with enhanced wall treatment. The results presented highlighted the greater torque experienced by the helical design at lower *TSR*, indicating a lower start-up speed for this type of design.

Bhargav et al. (2016) studied the influence of fluctuating wind conditions on VAWT while implementing the Transition SST turbulence model. Results presented correlate well with experimental predictions for steady-state operation, especially at the peak power coefficient. They highlighted the importance of 3D simulations when analysing the real-world performance of VAWT due to their ability to capture critical tip flow effects under fluctuating winds.

Chowdhury et al. (2016) implemented three turbulence models, namely k-ω SST, RNG k-ε and Spalart-Allmaras, when analysing a VAWT in upright and tilted operation. They noted that results obtained with the k-ω SST turbulence model matched best with experimental data, while results using the one-equation Spalart-Allmaras turbulence model provide the worst predictions.

Mannion et al. (2018) presented 3D CFD model predictions, **Figure 2-14**, from simulations with both the SST Transition and *k-ω* SST turbulence models for a straigh-bladed VATT. Both approaches accurately reproduce the experimental results, with the SST Transition model offering a slight improvement at predicting the peak power coefficient. They also included a comparison with equivalent 2D simulations. The 3D simulations demonstrated improved accuracy across all *TSR*, although at a significantly higher computational cost, over five times the cost of equivalent 2D simulations.

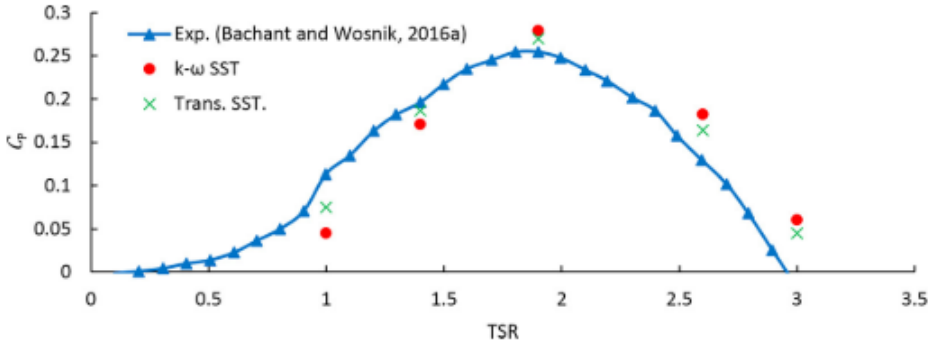

Figure 2-14: Validation of 3D CFD modelling approach with two turbulence models against experimentally measured power curves (Mannion et al., 2018).

Table 2-3: Summary of 3D RANS simulations of vertical axis wind and tidal turbines including turbine dimensions; *TSR* studied; and domain size;

Reference	Wind/ Tidal	Turbine Parameters (Blade Profile, N, c, $D \times H$)	Turbulence model	Y+ value	Number of elements	*TSR*	Time Step (º/step)
(Marsh et al., 2015)	Tidal	NACA $63_4$021, 3, 0.06 m, 0.91 m × 0.68 m	$k-\omega$ SST	< 1	17.2 ×10^6	1.5 to 3.5	0.9º
(Alaimo et al., 2015)	Wind	NACA 0021, 3, 0.3 m, 1.98 m × 1.15 m	$k-\varepsilon$ enhanced wall treatment	< 10	9.5 × 10^6	0.4 to 1.8	3.6º
(Orlandi et al., 2015)	Wind	NACA 0018, 2, 0.08 m, 0.755 m x 0.5 m	$k-\omega$ SST	< 5	2.7 × 10^6	2 to 4.6	1º
(Chowdhury et al., 2016)	Wind	NACA 0018, 2, 0.08 m, 0.75 m × 0.5 m	$k-\omega$ SST, RNG k-ε, Spalart-Allmaras	N/A	2.9 × 10^6	2.9 to 3.5	N/A
(Bhargav et al., 2016)	Wind	NACA 0015, 3, 0.45 m, 2.7 m × 3 m	SST Transition	< 1	2.8 × 10^6	0.8 to 2.3	2º
(Mannion et al., 2018)	Tidal	NACA0020, 3, 0.14 m, 1 m	SST Transition, $k-\omega$ SST	< 1	21.8 × 10^6	1 to 3	0.25º

2.4 Experimental Testing of Tidal Turbines

2.4.1 Introduction

Up until recent years, much of the focus on physical testing of vertical-axis turbines had been placed on wind-based turbines from over 30 years ago (Paraschivoiu, 1982; Sheldahl et al., 1980; Worstell, 1978). The recent interest in vertical-axis tidal turbines has seen new test facilities built, testing protocols established, and research papers published focusing on advancing this technology.

Physical testing of scaled prototypes allows developers to:

- Establish key performance metrics.
- Optimise various turbine design aspects- both mechanical and electrical systems.
- Validate computational models.
- Securing funding for future development by advancing the technology readiness level (TRL).

2.4.2 Standards and Best Practices

In recent years as the tidal energy industry has emerged, testing protocols, best practice guides and in-depth research into the testing of scaled prototypes through to full-scale deployments have been established.

Technology readiness level (TRL), initially introduced by NASA, is used to measure the progression of a new technology through various stages of testing and development. These different stages of physical testing and development applicable to tidal turbines are shown in **Figure 2-15** (McCombes et al., 2012). Initially, for TRL 1 - 4, small scale prototypes are tested to establish proof of concept. These tests are performed in a controlled environment. Once the proof-of-concept is attained, the guide recommends that a medium scale prototype is tested in a controlled lab environment to establish TRL 5. This study focuses on an investigation devoted to understanding the physical flow phenomena of the design to develop a better knowledge of the turbines' hydrodynamic features. At this stage, flow visualisation tools such as a laser doppler velocimeter or a particle image velocimeter can be used to observe the behaviour of the flow through and past the turbine. The repeatability

and accuracy of the tests should provide confidence in a near final-optimised blade design. In addition to physical testing, CFD modelling, finite element analysis (FEA) and costing should also be considered at this stage of the development.

The next stage of development is to test an operational scaled device in an uncontrolled environment, i.e. sea trials. At this stage, large scale sub-system testing, including establishing a power take-off (PTO) system, should also be considered. TRL 7-10 is the commercialisation deployment stage. At this stage, the system operation and control should be finalised, and all other aspects of the device should be verified. The device should not be subject to any significant design changes. Full-scale testing is for finalising systems operation and control.

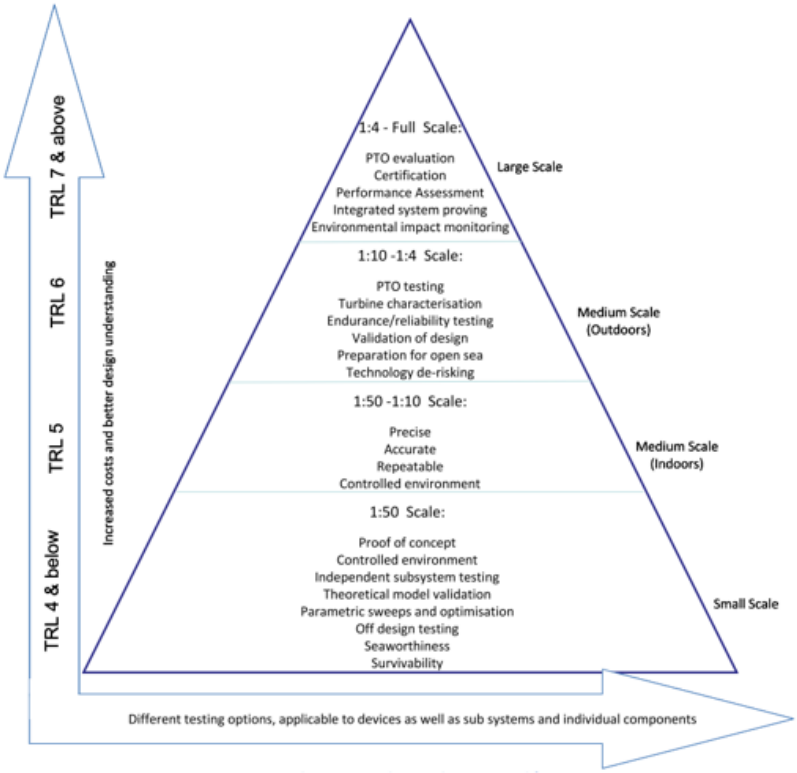

Figure 2-15: Requirements of the various TRL stages in the development of a tidal energy converter, cumulating to full-scale deployment and commercialisation (McCombes et al., 2012)

At any stage of development, when performing scaled testing, the three laws of similitude need to be considered (McCombes et al., 2010). This scaling of physical properties laws has been taken from the well-established practice used for ship propeller testing and applied to tidal energy converters. The laws include:

- Geometric similarity- the device geometrical dimensions need to be scaled between the model and prototype.
- Kinematic similarity- geometric similarity and all velocity ratios must be the same at the model and prototype scale.
- Dynamic similarity- kinematic similarity plus all kinematic quantities must be the same, e.g. Reynolds Number, Froude Number.

Geometric similarity is generally easily achieved by scaling parameters such as blade height, radius, chord length, etc. When comparing devices of identical shape and different scale, the tip-speed ratio is fundamental to ensure the kinematic similarity is achieved. For scaled prototypes with smaller dimensions, there are two options to maintain kinematic similarity; increase rotational velocity or decrease the free-stream velocity.

For a scaled prototype, it is typically not possible to obtain dynamic similarity as only one kinematic quantity can be matched. The kinematic quantities which should be considered are Reynolds number, Re, Froude number, Fn, and Strouhal number, St. Re is defined as the ratio between the inviscid and viscous forces in a fluid flow. Assuming the device is fully immersed, its performance is mainly dependent on the Reynolds number. Fn is the ratio between inertia and gravity forces acting on a fluid mass in the presence of a free surface. Froude number scaling is necessary when the device interacts with the free surface and is typically implemented for testing scaled wave energy converters. St is defined as the ratio between a characteristic time associated with a periodic phenomenon and time associated with the flow velocity. The Strouhal number is also important for the performance of oscillating foils and may influence the wake shed by structural members.

The equations for these kinematic quantities are defined as follows:

$$Re = \frac{UL}{\upsilon} \tag{2.50}$$

$$Fn = \frac{U}{\sqrt{gL}} \tag{2.51}$$

$$St = \frac{fL}{U} \tag{2.52}$$

Where U is a characteristic velocity, L is a characteristic Length scale, υ is the kinematic viscosity, g is gravity, and f is the periodic phenomenon frequency.

One additional non-dimensionless parameter which needs to be considered is the Cavitation number. Cavitation occurs due to rapid changes of pressure in a liquid, which lead to the development of small vapour-filled cavities in areas of low pressure. As these cavities collapse near the blade surface wall, they can cause material damage contributing significantly to the wear of blades and components. Dedicated test facilities where the pressure can be controlled are required to perform scaled cavitation tests.

An important aspect of scaled model testing is the control system implemented (Elsaesser et al., 2013). In a full-scale deployment, the turbine will generate electric power and supply this power to the grid. The voltage from the permanent magnet generator is passively rectified, and the alternating DC voltage is then inverted, filtered, transformed, and grid-connected. The estimated tidal speed is compared with the measured tidal speed, and this value is used to control the rotational speed of the turbine. A similar setup can be used in early-stage testing; however, this would require a fully designed PTO system. It is difficult to scale these losses relating to the drive-train friction with prototype size; hence early-stage model results can only give a limited understanding of the full-device performance. Instead, it is recommended that smaller-scale testing generally focuses on determining the mechanical power from the turbine design. For this, a control system is required for these tests, typically involving controlling the rotational speed of the turbine or controlling the load on the turbine, i.e. torque control. Rotational speed regulated tests are more familiar with the variable speed drives commonly used to vary the rotational velocity of the turbine over a range of values to encapsulate a specific range of *TSR* for a given freestream velocity. For the load control systems, an electro-mechanical brake is used to vary resistive loads on the shaft.

2.4.3 Test Options

There are several test facilities available for small to medium-scale controlled laboratory tests (McCombes et al., 2012). These facilities can be classified into two categories: towing tanks, where the device is towed by a motorised carriage while

water is at rest, and recirculating flumes where the device is kept fixed while water is forced to flow through. Examples of towing tanks and recirculating flumes available for testing small and medium-scale prototypes are listed in **Table 2-4**. Additional features at specific test facilities include flow characterisation instrumentation, equipment to measure drag force, wavemakers and flow velocity profiling.

Table 2-4: Details of the commonly used towing tank facilities used to test scaled prototypes

	KHL, Strathclyde University (UK)	**CNR INSEAN (IT)**	**LIR Facility (IRE)**	**CNR INSEAN (IT)**	**MARIN (NL)**	**University of New Hampshire (USA)**	**IFRMER, Boulogne sur Mer (FR)**
Type	Towing Tank	Recirc. Flume	Towing Tank	Towing Tank	Towing Tank	Towing Tank	Recirc. Flume
Length [m]	76	10	25	220	252	36	18
Width × Depth [m]	4.6 × 2.5	3.6 × 2.25	3 × 1.2	9 × 3.5	10.5 × 5.5	3.6 × 2.5	4 × 2
Velocities [m s^{-1}]	0.1 to 5	0.3 to 5	0.1 to 1.5	0.1 to 10	0.1 to 9	0.1 to 3	0.1 to 2.2
Turbulence intensity [%]	N/A	2.5 to 12	N/A	N/A	N/A	N/A	1.5 to 15
Additional Features	Wavemaker (regular or irregular waves 0.5m – 1.2m)	Cavitation channel, LDV, PIV, high-speed cameras	Wavemaker,	Wavemaker, LDV, PIV, high-speed cameras	Wavemaker	Wavemaker, PIV	LDV

Gaurier *et al.* (2015) carried out a comparative Round Robin testing programme as part of the EC FP VII MaRINET project to evaluate the differences between recirculation flumes and towing tanks. A three-bladed horizontal axis tidal turbine of diameter 0.7 m was tested in four different test facilities to assess variation between test sites and methods. Results from two towing tanks at CNR-INSEAN and Strathclyde University; and two recirculating flumes at CNR-INSEAN and IFREMER were included in this study. The variation of the measured $\bar{C}_P$ with *TSR* between the different test sites was round to be negligible, as shown in **Figure 2-16**. A higher standard deviation in the results for $\bar{C}_P$ was observed at the two recirculating flumes, which is attributable to the presence of a certain level of turbulent intensity in the flow at these test sites.

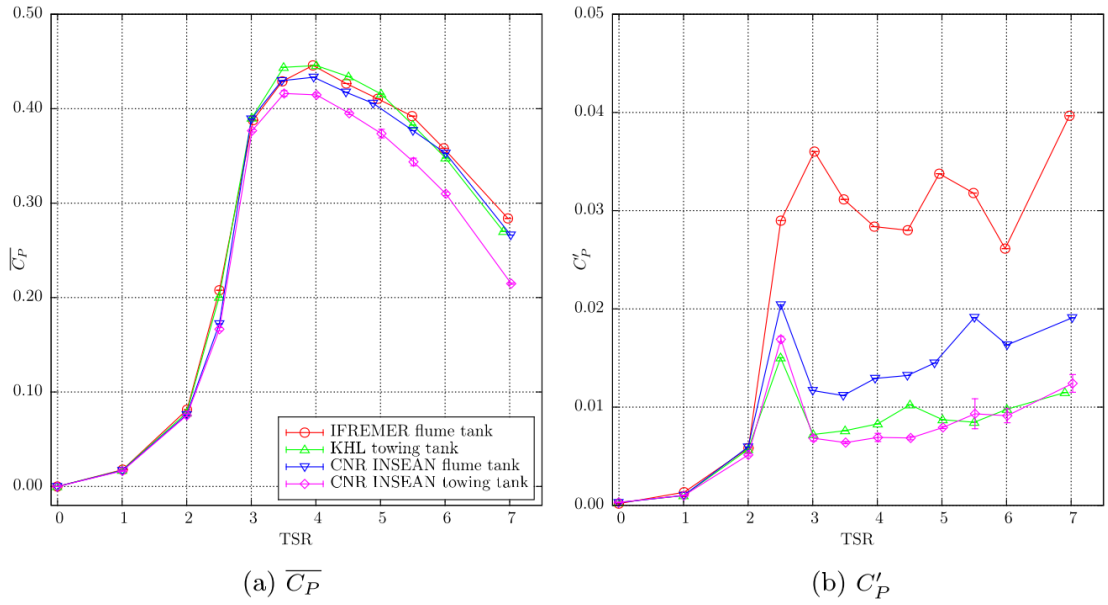

Figure 2-16: Variation of the (a) Mean and (b) standard deviation average power coefficient obtained for each *TSR* at the four different test facilities (U_∞ = 1.2 m s^{-1}) (Gaurier et al., 2015)

Mycek et al. (2014) examined the effect the ambient turbulence intensity upstream of the turbine has on the behaviour of horizontal axis tidal turbines. Turbulence intensities of 3% and 15% were investigated, and it was found that the mean power performance of the turbine was hardly influenced by variation in turbulence intensity. It was found that variation of ambient turbulent intensity does affect the standard deviation of the power coefficient and thrust coefficient.

In general, the power performance results from towing tanks and recirculating flumes are the same, and any differences may be attributed to the difference between the onset flow turbulence; there are certain design aspects of the design which cannot be assessed in towing tanks. For example, it is not possible to assess mooring systems in a towing tank. Tow tanks tests are typically carried out at atmospheric pressure, where the tank pressure cannot be controlled, so the effects of cavitation cannot be examined. It is easier to include flow velocity profiling for tests in recirculating flumes.

Full-scale devices which are close to commercialisation have been tested at the European Energy Centre at the Fall of Warness grid-connected site in Scotland. This test site has 8 test berths, ranging from depths of 12 m to 50 m, with a maximum tidal flow speed velocity of 4 m s^{-1}. Each test berth is equipped with fibre-optic cables, which allow developers to control the turbine and monitor data. The duration of test time which turbines operate at this site varies from a few months to a couple of years. Orbital's SR1-2000 2MW tidal turbine was tested at this site between October 2016 and September 2018. During this time, the turbine provided over 3 GWh of electricity to the Scottish grid. At the European Marine Energy Centre (EMEC) test site, an Integrated Monitoring Pod is available to assist testing. The pod monitors various environmental aspects of the effects of tidal turbines installations, including detection of sea life and measuring density, temperature, turbulence, tidal currents, etc., in a real-world application.

The Portaferry Tidal Test site in Strangford Lough, Northern Ireland, is another test site that has been used to test full-scale devices. This large shallow sea lough offers the opportunity for developers to test floating or fixed full-scale devices in real tidal flow conditions under realistic currents and turbulence levels. Marine Current Turbines installed the SeaGen prototype in 2008. The 1.2 MW turbine operated between 18 and 20 hours per day until decommissioning in 2019 and exported 11.6 GWh of electricity to the grid.

Along with the hydrodynamic analysis of turbine performance, test facilities are also available to analyse other aspects of tidal turbine design. Full-scale structural testing of composite, reinforced concrete, and metallic ocean energy structures, including structural testing of tidal stream blades under fatigue and static loading, is available at the Heavy Structures Laboratory at NUI Galway and ORE Catapult- blade test site. A

rotary test PTO test rig is available at the LIR- National Ocean Test Facility in Cork, Ireland. This rig consists of a standard six-pole, 15 kW machine operated from a universal variable speed AC Emerson UniDrive. It offers developers an opportunity to assess PTO options for their initial scaled prototype devices.

2.4.4 Testing and Results

Results from scaled experimental testing typically focus predominately on establishing the variation of C_P with *TSR* for different turbine designs. The effect of Reynolds number scaling and rotor solidity are often included in these analyses. Some studies include analysis of the self-start ability of the turbine or characterisation of flow downstream of the turbine.

Numerous examples detailing experimental testing of scaled horizontal-axis tidal turbines are available in the literature. Batten et al. (2008) tested a three-bladed horizontal-axis turbine of diameter 0.8 m and noted a peak $\bar{C}_P$ of 0.45 at *TSR* of 6. Also included in this series of scaled tests were investigations into cavitation effects and the effect of tidal velocity profile on blade loadings. O 'Doherty et al. (2009) performed tests on a 0.5 m diameter three-bladed turbine in a water flume that had a uniform flow profile with a magnitude of 1 m s^{-1}. They recorded a maximum power coefficient of ~0.4 and also concluded that this value was not influenced within the range of blade pitch angles investigated (3^o – 9^o). Seo et al., (2016) identified a maximum power coefficient of 0.278 at TSR of 3.5, for a three-bladed 0.4 m diameter turbine at a towing tank facility.

Focusing on the testing of vertical-axis tidal turbines, Bachant et al. (2016) performed a detailed analysis of a 1:6 scale vertical axis turbine in a towing tank facility in the University of New Hampshire (tank details in **Table 2-4**). The power performance and drag coefficient were determined for a 1.075 m diameter, straight three-bladed turbine. A maximum $\bar{C}_P$ of 0.37 was recorded at *TSR* of 3.1, corresponding with an overall device drag coefficient, C_D = 0.84. The effect of Reynolds number, shown in **Figure 2-17**, was also analysed with the average power coefficient appearing to convergence at $Re_D = 1 \times 10^6$.

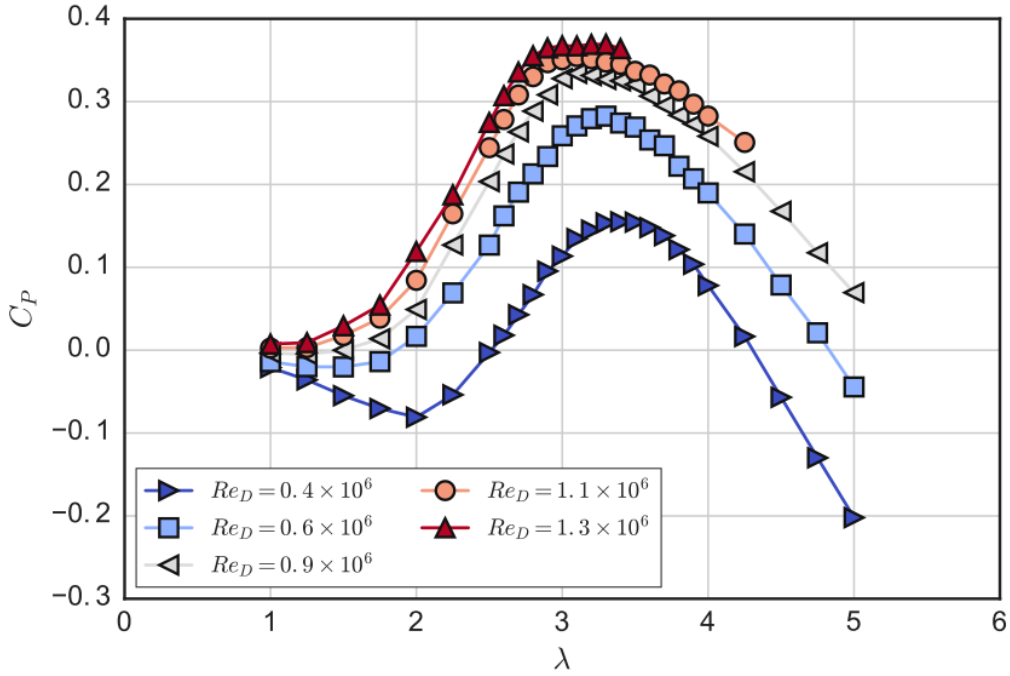

Figure 2-17: Effect of Reynolds number on the variation of C_P with *TSR* (λ) for a 3-bladed vertical-axis tidal turbine (Bachant et al., 2016)

Bachant and Wosnik (2015) also tested non-straight-bladed vertical-axis turbines at the University of New Hampshire's towing tank. Two different turbines were tested: the Gorlov Helical Turbine (GHT), shown in **Figure 2-18** and the Lucid Spherical Turbine (LST). The LST intended purpose (LucidEnergy, 2020) is for application in circular cross-section gravity-flow pipes such as drainage pipes. Both turbines have a 1 m^2 frontal area with 140 mm chord extruded NACA 0020 foil sections, though their tilted orientation changes their projected profiles along the blade path, making some slight differences between the two designs. Tests results showed that in a low-blockage towing tank, the cylindrical GHT outperformed the spherical LST in terms of maximum $\bar{C}_P$. The GHT reached a maximum $\bar{C}_P$ of 0.35 at *TSR* = 2.3, while the LST, designed for higher blockage flow conditions, achieved a maximum $\bar{C}_P$ of 0.14 at *TSR* = 2.2.

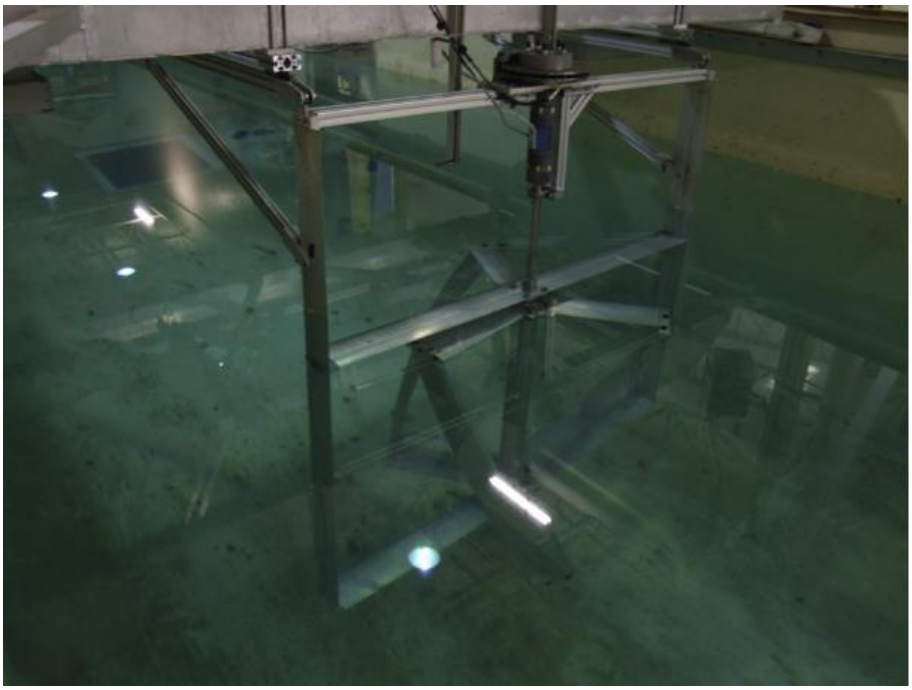

Figure 2-18: Test setup of the GHT at University of New Hampshire's towing tank (Bachant and Wosnik, 2015)

Mannion et al. (2019) tested a novel flow accelerating high solidity vertical-axis tidal device at IFREMER's recirculation flume at Boulogne-sur-Mer (**Figure 2-19 (a)**). They presented results, shown in **Figure 2-19** (b), of a peak power coefficient for this device of close to 0.40. They also characterised the accelerated flow around a bluff body using the laser Doppler velocimeter at this facility and used this data to validate their CFD model.

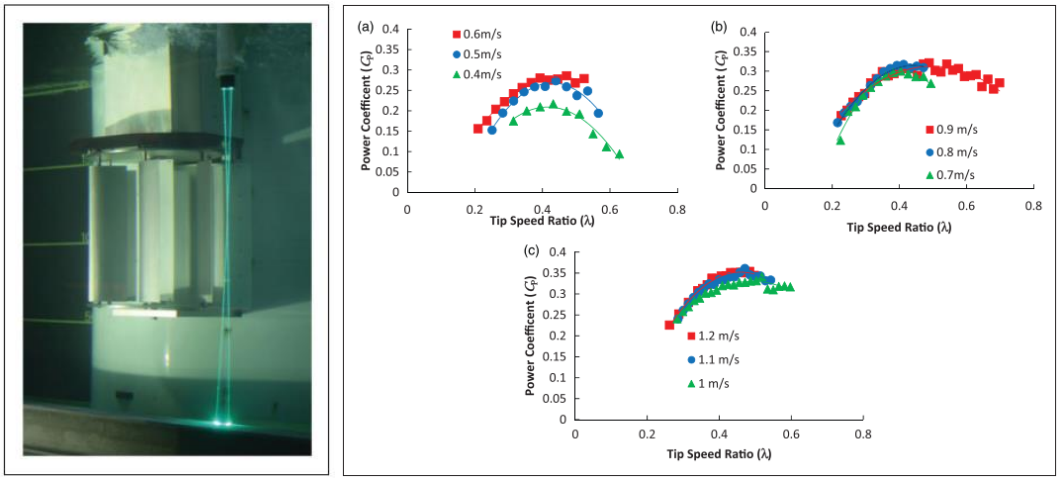

(a) **(b)**

Figure 2-19: (a) Flow accelerating high solidity vertical-axis tidal device; **(b)** Variation of power coefficient with *TSR* at different freestream velocities (Mannion et al., 2019a)

Shiono, Suzuki and Kiho (2000) examined a straight-bladed vertical-axis turbine at the University of Tokyo's circulating water tank at the Maritime Safety Agency Research Centre. An electromagnetic brake was installed to control the load on the turbine, and a torque transducer was used to record the torque. Tests were performed at flow speeds ranging from 0.6 to 1.4 m s^{-1}. The effect of rotor solidity on power performance at a flow speed of 1 m s^{-1} was also examined by varying the number of blades and testing blades of different chord lengths. They concluded that for a constant number of blades, the turbine efficiency reaches a maximum for a rotor solidity of 0.179. They also examined the self-starting ability of the design based on the number of blades. Results of this analysis are shown in **Figure 2-20**. With an increasing number of the blades, the incidences of a negative starting torque are reduced and that a four-bladed turbine would self-start regardless of the blade's orientation.

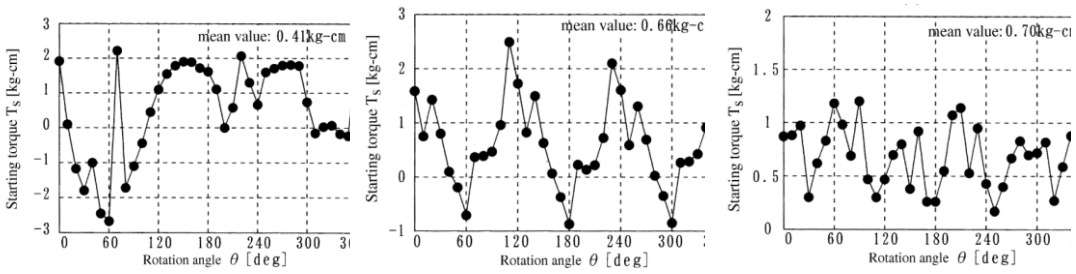

(a) 1-Blade (b) 3-Blade (c) 5-Blade

Figure 2-20: Analysis of the starting torque variation with azimuthal angle of straight-bladed vertical-axis tidal turbines with different number of blades

2.5 Conclusions

The overall aim of this research is to develop a combined analytical, computational, and experimental methodology for the characterisation of the hydrodynamic performance of the novel Brí Toinne Teoranta vertical axis tidal turbine concept. The framework for this research is presented in **Figure 2-21**.

BEM models are a vital design tool for quickly analysing different parametric features of turbine design. The three-dimensionality of the Brí Toinne Teoranta turbine blades require a set of geometric equations which describe aspects of the blade's features. These geometric equations will be used as input for a new DMST BEM model with additional considerations to improve its accuracy. The BEM approach adopted for this research is detailed in **Chapter 3**.

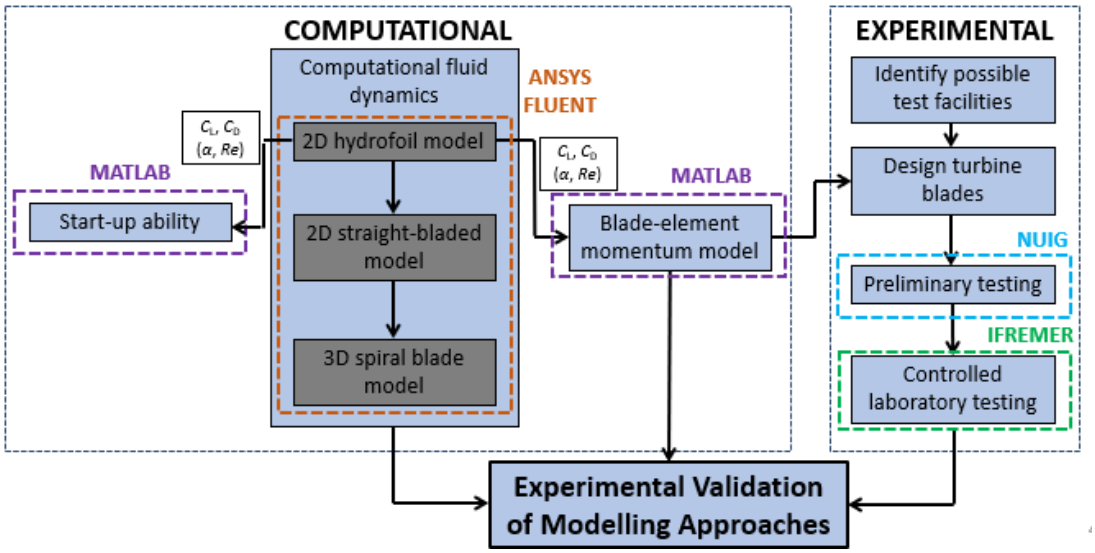

Figure 2-21: Overview of the research methodology

As highlighted in **Section 2.2.3.3.**, a dataset of C_L and C_D is vital input for any DMST model. Due to their design, vertical-axis turbines experience widely varying angles of attack at different stages of operation. Existing DMST implement the combined panel method-experimentally derived dataset provided by Sheldahl and Klimas (1981). However, the panel method is not accurate for conditions that result in flow separation, i.e. it should not be used for high values of α and/or low values of Re. **Figure 2-22** presents a comparison of panel method predictions to experimentally measured C_L for Re = 8.4× 10^4. The method does not accurately predict the stall region, which occurs for α > 8°.

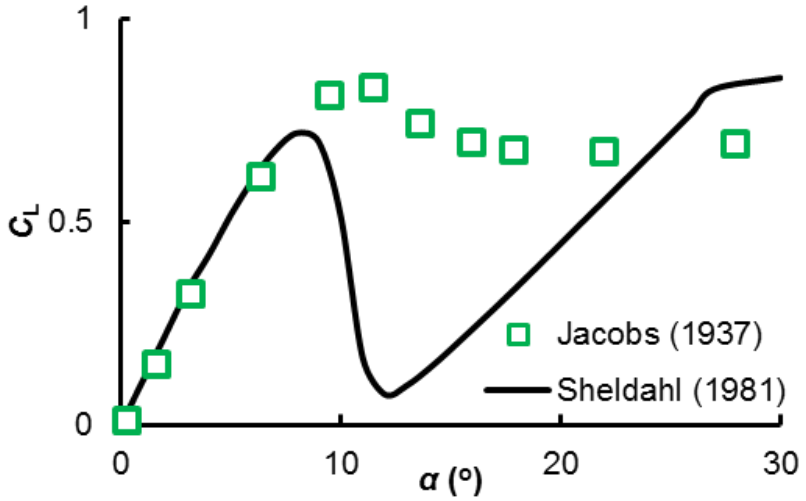

Figure 2-22: Comparison between Panel Method data (Sheldahl and Klimas, 1981) and experimental results (Jacobs and Sherman, 1937) of lift coefficient variation with angle of attack for NACA0015 (Re = 8.4 × 10^4).

While these approaches are very computationally efficient, they fail to capture flow separation, the laminar separation bubble (LSB), and flow reattachment. These phenomena are strongly influenced by the laminar to turbulent flow transition in the hydrofoil boundary layer and contribute significantly to the prediction of lift and drag forces in the critical stall region, shown in **Figure 2-23**. RANS CFD modelling with the implementation of the SST Transition model (Menter et al., 2006) has been shown to predict the laminar to turbulent transition and flow separation (Langtry et al., 2006).

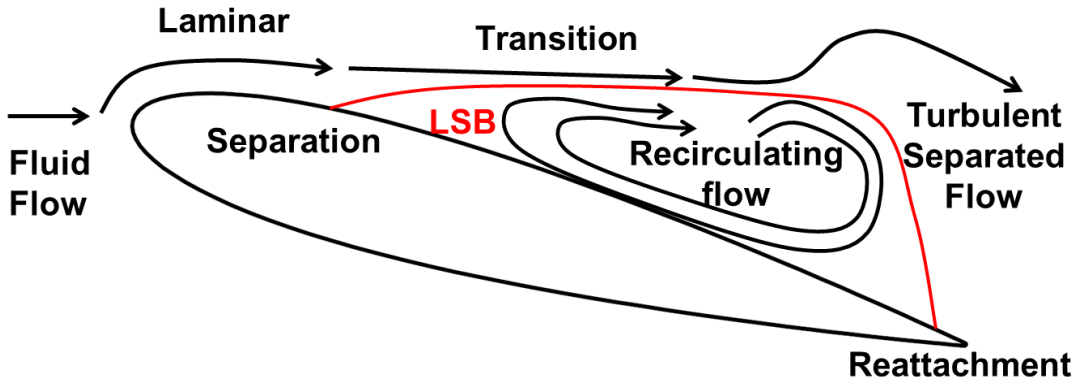

Figure 2-23: Flow structures around a hydrofoil under stall conditions.

The SST Transition model has previously been implemented for symmetric and non-symmetric aerofoil analyses (Counsil and Goni Boulama, 2013, 2012; Genç, 2010). In all cases, the superior ability of the SST Transition model to predict the flow around the aerofoil is presented. However, these studies have only simulated a limited range of values of *Re* and α. BEM analysis of vertical axis turbines requires data for an extensive range of *Re* and α, hence the requirement for a comprehensive study to assess the capability of the SST Transition model to predict C_L and C_D over this desired range. Such information will provide accurate input for BEM analysis of the Brí Toinne Teoranta design so that initial design parametric studies can be performed efficiently. Due to recent advances in computing power CFD analysis of hydrofoils, under a wide range of test conditions with a sufficiently high spatial and temporal discretisation, and an appropriate turbulence model presents an alternative methodology to determine C_L and C_D hydrofoil datasets for a wide range of flow conditions. Details of this analysis are presented in **Chapter 4**.

The analysis of the self-starting capability of vertical-axis turbines is well documented in the literature (Dominy et al., 2007; Hill et al., 2009; Nguyen et al., 2015). This

feature is influenced by the starting blade position, turbine design, resistive loads and flow conditions. Dominy et al. (2007) noted the significant importance of such capabilities for small to medium-scale low-cost turbines. A significant advantage of such devices is lost if external assistance is required to effect start-up. Results comparing the start-up capabilities between a straight-bladed design and the novel design, using a time-marching blade element theory approach, are presented in **Chapter 4**. The CFD derived hydrodynamic coefficients dataset is important input into this model.

Bachant and Wosnik (2015) carried out physical testing on helical designed vertical-axis turbines. They commented that neglecting the benefits of the reduced torque triple effects, it was still uncertain whether helical turbines were more effective at power conversion compared to equivalent straight-bladed counterparts. They recommended further investigations into the three-dimensionality of internal and near-wake flows. This research aims to investigate these flow characteristics for the BTT turbine through three-dimensional CFD models presented in **Chapter 5**.

Referring to **Figure 2-21**, the testing aim and overall direction of this research is to achieve TRL 5 for the Brí Toinne Teoranta device design. Preliminary small-scale testing to form proof of concept is established at NUI Galway. Medium-scale design validation testing is performed at the state-of-the-art test facilities at IFERMER Boulogne sur Mer. This physical testing not only provides specifics on the device performance but results are also implemented in the validation of the numerical and computational tools. Details on the physical testing and model validations are presented in **Chapter 5** and **Chapter 6**.

To summarise, this research aims to fill a gap in the literature in the computational modelling of next-generation spiral-type vertical-axis turbine designs. This research focuses on one such design and aims to optimise the novel concept for peak power performance which also quantifying the accuracy and computational resources of blade element momentum and RANS-CFD modelling techniques through experimental validation.

Chapter 3: Blade Element Momentum Model for a Novel Spiral-Type Vertical-Axis Turbine Design Concept

3.1 Introduction

Blade element momentum models are a standard design analysis and optimisation tool for both horizontal- and vertical-axis, wind and tidal turbines. The models are developed by combining actuator disc theory and blade element theory and allow the computation of the hydrodynamic forces on the turbine blades. The models are based upon equating the rate of change of momentum in the flow to the streamwise force on the blades within a streamtube. BEM models have shown to produce accurate predictions of measured experimental results. In this chapter, a new double-multiple streamtube (DMST) modelling approach for the spiralling blade design is developed, with additional considerations to improve the accuracy of the model. The DMST approach (Beri, 2011; Castelli et al., 2012; Mannion et al., 2020; Paraschivoiu, 1982) has shown to give more accurate predictions than multiple streamtube models (Strickland, 1975) and single streamtube models (Templin, 1974). The novel aspect of the DMST model developed in this Chapter is that it steps through both blade height and blade position when solving the blade element momentum equations, which facilitates the analysis of complex turbine designs.

There are four sections in this chapter. In **Section 3.2 Turbine Geometrical Design and Operation**, various turbine design parameters and operational metrics are presented. The geometrical equations which define the novel blade designs, including local parametric equations, are included. The dimensionless parameters used to describe vertical-axis turbines are also included in this section. In **Section 3.3 Model Development**, the theory, relating specifically to vertical-axis turbines, leading to the development of a blade element momentum model, is presented. Additional considerations to improve the accuracy of this modelling technique and details on the

model implementation are also included. **Section 3.4 Results** is divided into four sub-sections: model validation, design optimisation, a detailed study of the optimised design operational characteristics, and finally, a comparison with currently existing technology. In **Section 3.5 Chapter Conclusions**, the findings of the BEM study are summarised. The limitations and shortcomings of this form of modelling are discussed. Future work addressing these shortcomings and further model validation is mentioned.

This chapter aims to:

- Establish a set of geometrical equations to describe various forms of the Brí Toinne Teoranta blade geometry.
- Demonstrate the capability of BEM modelling to predict the performance of existing vertical-axis turbines by comparing BEM predictions with published experimental data.
- Predict the power performance of the initial design and, following on from that, perform a design optimisation study of different novel turbine designs based on the BTT concept.

3.2 Turbine Geometrical Design and Operation

The Brí Toinne Teoranta vertical-axis tidal turbine concept, hereafter referred to as the BTT turbine, encompasses many variations of spiralling blade designs. The initial base case design is shown in **Figure 3-1**.

Figure 3-1: Brí Toinne Teoranta (BTT) design concept- Spherical/Ellipsoidal design.

In creating a BEM model of the novel turbines, a set of geometrical equations is needed to calculate local parameters, which form the basis of the BEM model. Each blade is of constant hydrofoil cross-section along its entire length and defines an upper spiral and a lower spiral. The two spirals are of opposite hands and extend from each end to meet mid-way between the two ends. The spirals of the blade extend around the main central rotational axis through a maximum angular distance, $\Delta\varphi$, of approximately 60^o at the midplane, as shown in **Figure 3-2 (b)**.

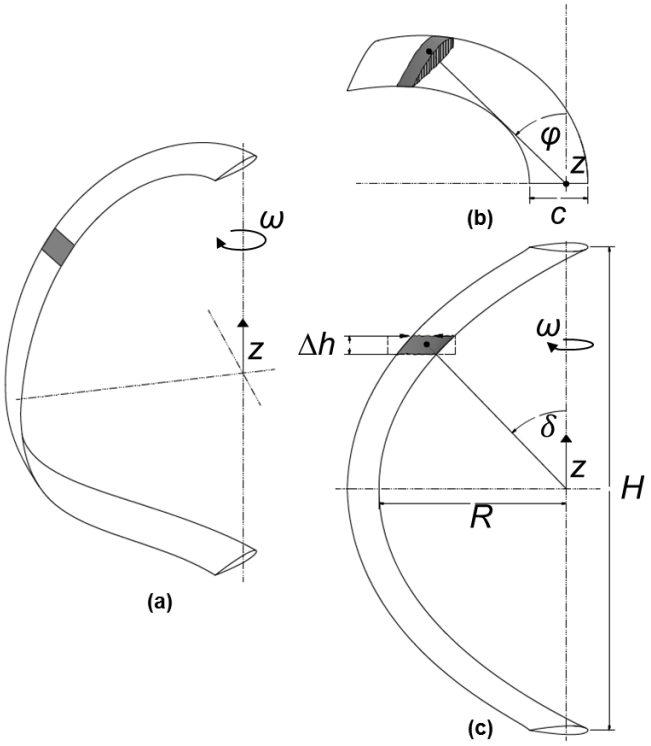

Figure 3-2: Definition of BTT spherical blade geometry: **(a)** isometric view of single blade showing the axis of rotation, *z*, and rotational velocity and direction, ω; **(b)** plan view showing chord length, *c*, and local azimuthal angle, θ, for a specific blade section; and **(c)** elevation view detailing the local blade inclination angle, γ, for a specified blade section of height of Δh, total turbine height, *H*, and maximum blade radius, *R*.

The spirals are defined in terms of their x and y Cartesian coordinates as follows:

$$x = t\ \cos t \tag{3.1}$$

$$y = t\ \sin t \tag{3.2}$$

where t is the spiral parameter ($0 < t \leq 1$).

For each turbine blade, the local azimuthal angles (blade positions) will vary along the length of the blade. The Turbine Orientational Configuration Angle (TOCA) is utilized

to describe the overall blade's angular position. As a reference point, when the midplane of the turbine blade is directed towards the incoming flow, the overall blade orientation is defined as a TOCA of 0°. For this blade orientation (TOCA = 0°), the local azimuthal angle at the midplane would be 0°, and for the top and bottom of the blade, the local azimuthal angle would be +60°. This convention is used to describe a turbine blade's position throughout this thesis.

The local height of each section can be calculated by projecting a 2D spiral, with x and y Cartesian coordinates, onto an ellipsoid. The z coordinate is calculated as:

$$z = R\sqrt{1 - \left(\frac{x}{H}\right)^2 - \left(\frac{y}{H}\right)^2} \tag{3.3}$$

Where R is the turbine radius, and H is the turbine height. The blade centrelines for a three-bladed turbine are shown in **Figure 3-3**. The radius, r, at each blade height from the central rotor axis, is given by:

$$r = \sqrt{x^2 + y^2} \tag{3.4}$$

The local additional azimuthal angle, $\Delta\varphi$, and angle of the blade to the horizontal axis of the turbine, δ, are calculated at each blade section height, as follows:

$$\Delta\varphi = \tan^{-1}\left(\frac{y}{x}\right) \tag{3.5}$$

$$\delta = \tan^{-1}\left(\frac{z}{r}\right) \tag{3.6}$$

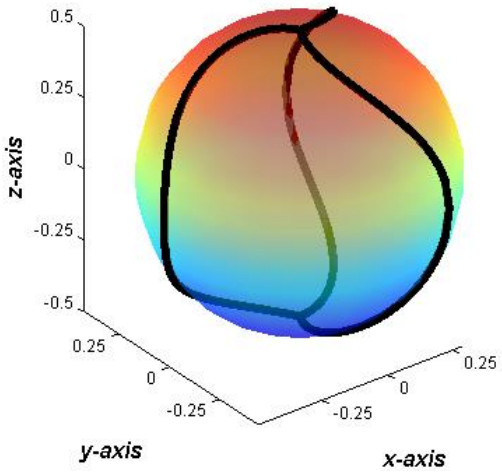

Figure 3-3: Centrelines for a three-bladed spherical BTT turbine design.

3.3 Model Development

3.3.1 Model Implementation

The first theoretical model implemented is momentum theory within a streamtube, treating the turbine blade as an actuator disc, as shown in **Figure 3-4 (a)**. Froude's momentum theory (1889), sometimes referred to as actuator disk theory is a model of an ideal actuator disk. This model is used to provide an estimate of the power available from a volume of fluid passing through a rotor. The actuator disc causes a reduction in velocity, which in turn is the source of a pressure change within the streamtube. By applying the conservation of momentum to the control volume, the net force on the contents within the streamtube can be calculated. The second model is blade element theory (Drzewiecki, 1892) which examines the forces on the hydrofoil as the blade rotates, as shown in **Figure 3-4 (b)**. Blade element momentum theory equates the momentum losses to the forces on the blade elements within each streamtube. Two-dimensional hydrofoil lift and drag coefficients are utilized to calculate the forces on each blade element. These hydrofoil characteristics, C_L and C_D, are established based on the local angle of attack, α, and the local Reynolds number, Re_c of a blade element. The angle of attack is the angle between the resultant velocity and the chord line of the hydrofoil.

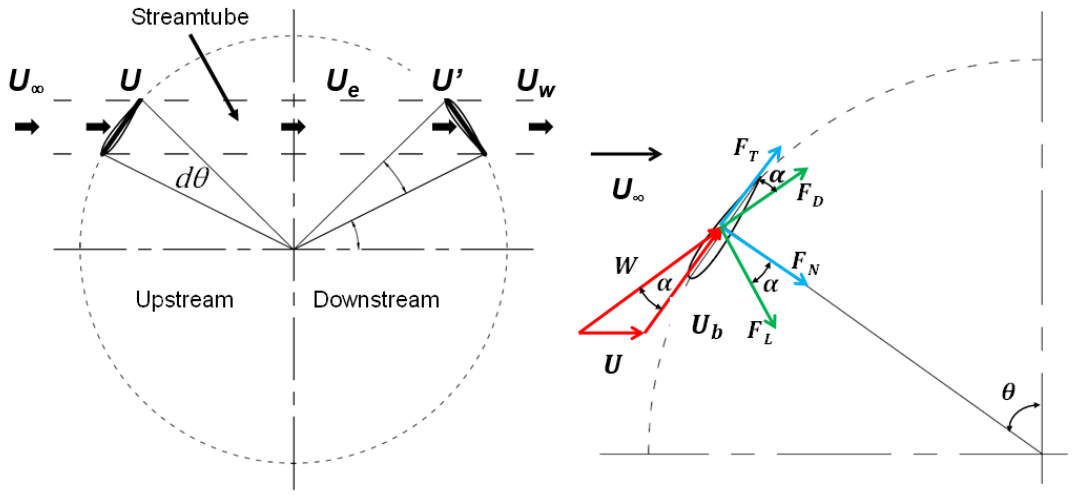

(a) **(b)**

Figure 3-4: (a) Momentum theory and **(b)** Blade element theory applied to a blade element in a streamtube for a vertical-axis turbine.

The methodology of the blade element momentum code, developed in MATLAB®, is presented in **Figure 3-5**. A numerical code has been developed to generate the desired turbine blade geometry. Model parameters and inputs into this algorithm are listed in **Table 3-1**.

Table 3-1: BEM model parameters and inputs.

Mesh parameters:	
Number of heights (N_z)	40
Number of azimuthal angles (N_θ)	180
Fluid conditions: Seawater at 5 ºC	
Density ρ	1025 kg/m^3
Viscosity μ	0.00162 Ns/m^2
Freestream Velocity U_∞	2 m s^{-1}

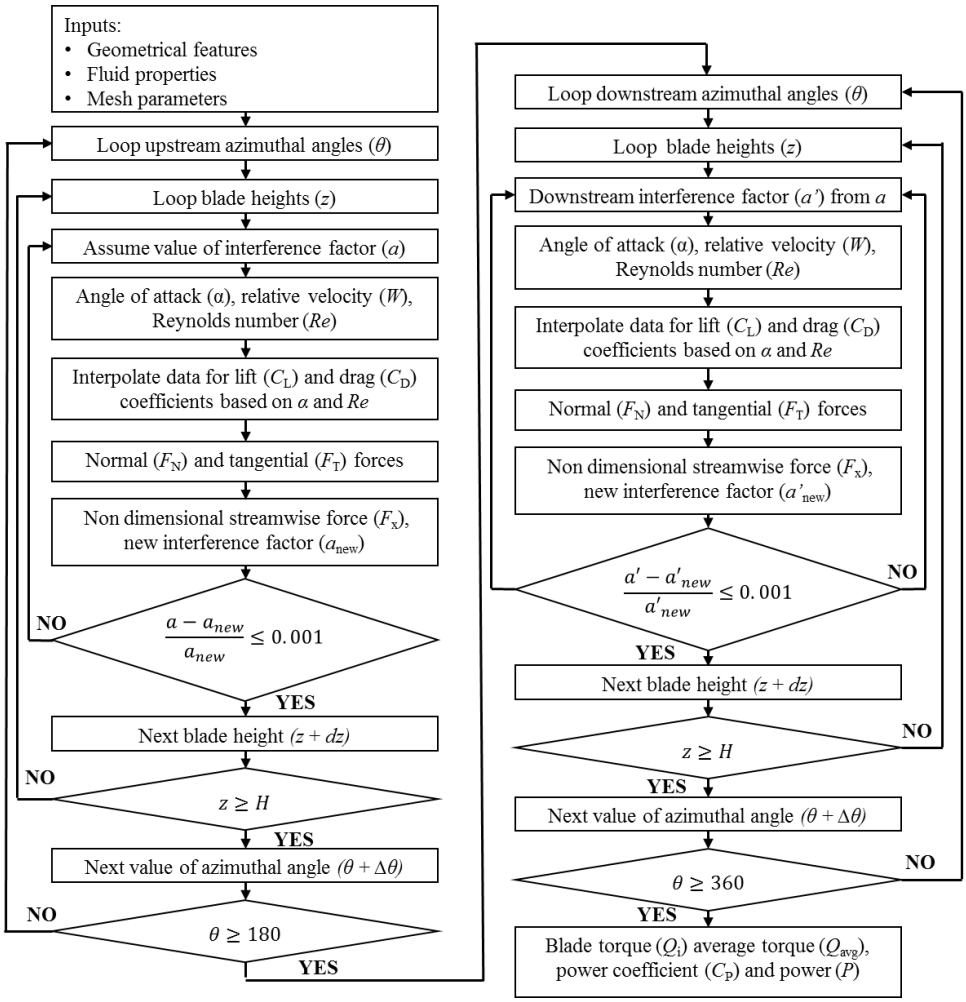

Figure 3-5: Flowchart for DMST model.

The rotor of the turbine is divided into N_θ divisions, i.e. the number of streamtubes. One such streamtube is shown in **Figure 3-4 (a)**. The fixed angle, $\Delta\theta$, of each streamtube, is:

$$\Delta\theta = \frac{2\pi}{N_\theta} \tag{3.7}$$

The cross-sectional area of each streamtube, A_{ST}, is calculated by:

$$A_{ST} = r\Delta\theta \sin(\theta + \Delta\varphi)\,\Delta h \tag{3.8}$$

where r is the local turbine radius, and Δh is the height of the blade element. The time-averaged streamwise force, $\bar{F}_x$, of the momentum equation from Glauert's blade element theory, is given by:

$$\bar{F}_x = 2\rho A_{ST} U(U_\infty - U) \tag{3.9}$$

where ρ is the density of the fluid. For a rotor with N blades, each blade element will pass through every single streamtube once per revolution as the upstream and downstream streamtube are analysed separately. Thus, the average streamwise force on each blade element is:

$$\bar{F}_x = NF_x \frac{\Delta\theta}{2\pi} \tag{3.10}$$

where $\bar{F}_x$ represents the streamwise force on the blade element. By equating the streamwise momentum, equation (3.13), and the streamwise forces exerted by each blade element, equation (3.14), the following equation can be derived:

$$\frac{NF_x}{4\pi\rho\Delta h r \sin(\theta + \varphi){U_\infty}^2} = \left(\frac{U}{U_\infty}\right)\left(1 - \frac{U}{U_\infty}\right) \tag{3.11}$$

To obtain F_x it is necessary to determine the forces acting on the hydrofoils. The incoming velocity, V, is divided into components parallel and perpendicular to the radial velocity. The angle of attack, α, and relative velocity, W, are given by:

$$\alpha = \tan^{-1}\left(\frac{U\sin(\theta - \varphi)\sin\delta}{U\cos(\theta - \varphi) + \omega r}\right) \tag{3.12}$$

$$W = \frac{U\sin(\theta - \varphi)\sin\delta}{\sin\alpha} \tag{3.13}$$

The local Reynolds number, Re_c, is defined as:

$$Re_c = \frac{\rho W c}{\mu} \tag{3.14}$$

where μ is the dynamic viscosity. The tangential and normal forces, F_T and F_N act parallel and perpendicular to the and are defined as

$$F_T = \frac{1}{2} C_T \rho \frac{\Delta h c}{\sin \delta} W^2 \tag{3.15}$$

$$F_N = -\frac{1}{2} C_N \rho \frac{\Delta h c}{\sin \delta} W^2 \tag{3.16}$$

where C_T and C_N are the normal and tangential force coefficients defined as:

$$C_T = C_L \sin \alpha - C_D \cos \alpha \tag{3.17}$$

$$C_N = C_L \cos \alpha + C_D \sin \alpha \tag{3.18}$$

with C_L and C_D obtained from the local angle of attack. C_L and C_D play a critical role in the performance prediction of vertical axis turbines. C_L and C_D are dependent on Reynolds number, Re, and Mach number, Ma (i.e. compressibility effects). The local Reynolds number has a significant impact on C_L and C_D in the stall region. Aerofoils at low Mach numbers (Ma < 0.3), as opposed to hydrofoils, are the focus of much of the literature. Compressibility effects at these low Mach numbers are small, so this data is assumed to be applicable for hydrofoils. A relatively complete dataset available for NACA foils was compiled by Sheldahl and Klimas (1981). The latter carried out experimental testing in wind tunnels on NACA 0009, 0012 and 0015 aerofoil for a limited number of Reynolds numbers and also presented tabulated data, based on both experimental and numerical data for a broader range of Reynolds number, 4×10^5 to 1×10^7, for seven symmetrical aerofoils. A panel method code (Eppler, 1978) was used to calculate values for C_L and C_D for which experimental data was not available. An example of a dataset is shown in **Figure 3-6** and **Figure 3-7** for the NACA 0015 profile for an applicable limited range of α.

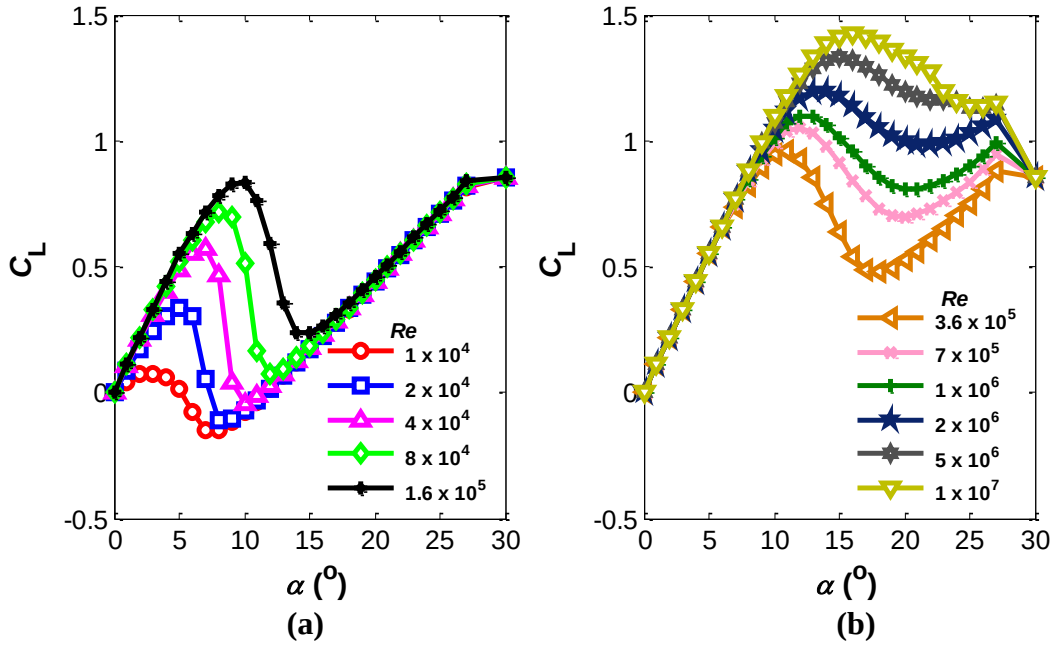

Figure 3-6: Lift coefficient as a function of angle of attack and Reynolds number for a NACA 0015 profile taken from a dataset compiled by Sheldahl and Klimas (1981). (a) Re from 1×10^4 – 1.6×10^5 and (b) Re from 3.6×10^5 – 1×10^7

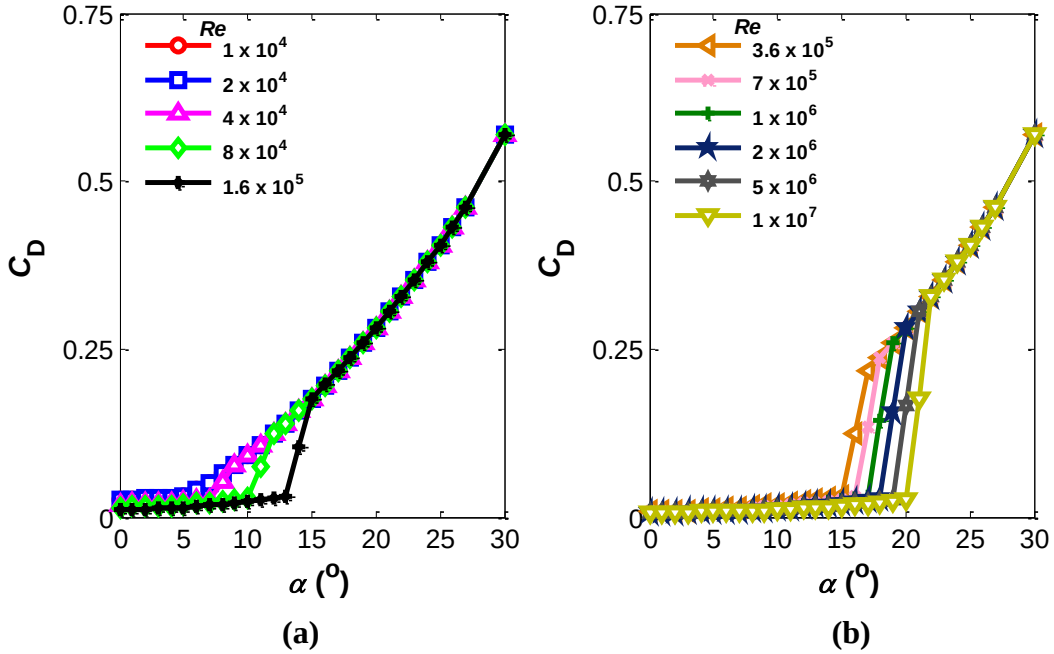

Figure 3-7: Drag coefficient as a function of angle of attack and Reynolds number for a NACA 0015 profile taken from a dataset compiled by Sheldahl and Klimas (1981). **(a)** *Re* from 1×10^4 – 1.6×10^5 and **(b)** *Re* from 3.6×10^5 – 1×10^7.

The resultant force of F_N and F_T in the direction of the freestream flow is known as the streamwise force, F_x, and is defined as:

$$F_x = -(F_N \sin\delta \sin(\theta - \varphi) + F_T \cos(\theta - \varphi)) \tag{3.19}$$

To relate the momentum and blade element theory a dimensionless force, F_x^*, is defined from the left-hand side of equation (3.15):

$$F_x^* = \frac{NF_x}{4\pi\rho\Delta h r \sin(\theta - \varphi)\, U_\infty^2} \tag{3.20}$$

Glauert's correction (Glauert, 1926) is implemented in the algorithm to calculate a new interference factor.

$$a_i = \begin{cases} F_x^* + a_{i-1}^2 & \text{when } a < 0.4 \\ F_x^* + \left(\frac{5 - 3a}{4}\right) a_{i-1}^2 & \text{when } a > 0.4 \end{cases} \tag{3.21}$$

where a is the upstream interference factor defined as:

$$a = 1 - \frac{U}{U_\infty} \tag{3.22}$$

U_e, the induced velocity at the equator plane is defined as:

$$U_e = U_\infty(1 - 2a) \tag{3.23}$$

For the downstream portion of the turbine, U is replaced by U' and U_∞ is replaced by U_e, giving:

$$U' = U_e(1 - a') \tag{3.24}$$

with a', the downstream interference factor defined as:

$$a' = 1 - \frac{U'}{U_e} \tag{3.25}$$

An initial value for the upstream interference factor is assumed, and equation (3.25) is solved iteratively with a convergence criterion of 10^{-4} for a. For the downstream interference factor, the initial interference factor is assumed to be the converged value from the upstream portion. The process is repeated until convergence has been reached for each of the upstream and downstream streamtubes. This iterative approach has led to convergence failure for highly loaded rotors (i.e. high solidities and/or high *TSR*) (Gupta and Leishman, 2005). The introduction of an under-relaxation factor, w (taken as 0.3), helps improve the convergence for these high blade loadings (James, 1996):

$$a_{new} = wa_{old} + (1 - w)a_{old} \tag{3.26}$$

The average torque per cycle is defined as:

$$\bar{Q} = \frac{N}{N_\theta} \sum_{1}^{N_\theta} F_T r \tag{3.27}$$

and, thus, the average rotor power, $\bar{P}$, per rotation is:

$$\bar{P} = \bar{Q}\omega \tag{3.28}$$

with ω defined as the rotational velocity of the turbine.

3.3.2 Dynamic Stall Model

The lift and drag coefficients presented in **Figure 3-6** and **Figure 3-7** are static coefficients, i.e. these coefficients are calculated for a blade profile at a fixed angle of attack. As the angle of attack is continually varying as the blades rotate, a dynamic stall model is required to adjust the static coefficients to more accurate values. Dynamic stall has the most significant effect at low *TSR* where the local angle of attack is greater than the static stall angle (α_{ss}). As the blade rotates, the angle of attack changes and a vortex is shed from the leading edge of the hydrofoil.

Dynamic stall is dependent on a wide range of parameters, including hydrofoil shape, mean angle, Mach number, Reynolds number and the rate of change of angle of attack. The dynamic stall model implemented in this BEM code is based on Gormont (1973), with modifications by Massé (1981) and Berg (1983) included. Gormont's model empirically mimics the hysteresis response of an aerofoil by defining a reference angle of attack at which the static two-dimensional coefficient data is considered.

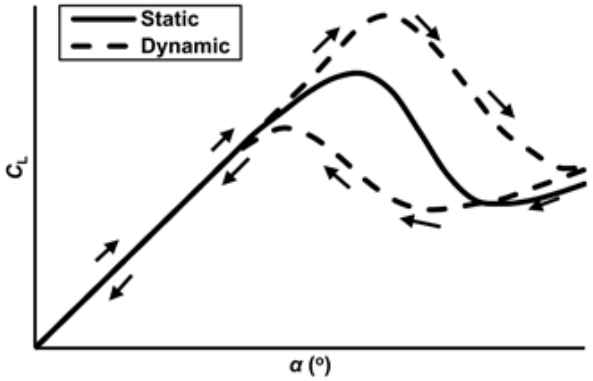

Figure 3-8: Comparison between dynamic and static lift coefficient with the variation of the angle of attack

For the Gormont dynamic stall model, reference angles of attack α_L^G and α_D^G are calculated as follows:

$$\alpha_L^G = \alpha - (K_1 \times \Delta\alpha_L^G) \tag{3.29}$$

$$\alpha_D^G = \alpha - (K_1 \times \Delta\alpha_D^G) \tag{3.30}$$

where α is the original angle of attack, defined by equation (3.16), and K_1 is defined as:

$$K_1 = \begin{cases} 1.0 & \dot{\alpha} \geq 0 \\ -0.5 & \dot{\alpha} < 0 \end{cases} \tag{3.31}$$

where $\dot{\alpha}$ is the time derivative of the angle of attack. $\Delta\alpha_L^G$ and $\Delta\alpha_D^G$ are calculated by:

$$\Delta\alpha_L^G = \begin{cases} y_{L,1} \times S & S <= S_C \\ \left(y_{L,1} \times S_C\right) + \left(y_{L,2} \times (S - S_C)\right) & S > S_C \end{cases} \tag{3.32}$$

$$\Delta\alpha_D^G = \begin{matrix} y_{D,1} \times S & S <= S_C \\ \left(y_{D,1} \times S_C\right) + \left(y_{D,2} \times (S - S_C)\right) & S > S_C \end{matrix} \tag{3.33}$$

where:

$$S = \sqrt{\left|\frac{c_w \dot{\alpha}}{2W}\right|} \tag{3.34}$$

$$S_c = 0.06 + (1.5 \times (0.06 - t_c)) \tag{3.35}$$

$$Y_{L,2} = y_{L,max} \times \max\left(0, \frac{Ma - M_{L,2}}{M_{L,1} - M_{L,2}}\right) \tag{3.36}$$

$$Y_{D,2} = y_{D,max} \times \max\left(0, \frac{Ma - M_{D,2}}{M_{D,1} - M_{D,2}}\right) \tag{3.37}$$

$$Y_{L,1} = \frac{y_{L,2}}{2} \tag{3.38}$$

$$Y_{D,1} = 0 \tag{3.39}$$

$$y_{L,max} = 1.4 - (6 \times (0.06 - t_c)) \tag{3.40}$$

$$y_{D,max} = 1.0 - (2.5 \times (0.06 - t_c)) \tag{3.41}$$

$$Ma = \frac{W}{C_w} \tag{3.42}$$

$$M_{L,1} = 0.4 + (5 \times (0.06 - t_c)) \tag{3.43}$$

$$M_{L,2} = 0.9 + (5 \times (0.06 - t_c)) \tag{3.44}$$

$$M_{D,1} = \frac{y_{L,2}}{2} \tag{3.45}$$

$$M_{D,2} = 0 \tag{3.46}$$

c_w is the speed of sound in water, W is the relative velocity (equation 3.17) and t_c is the ratio of the maximum blade thickness to chord length.

$$C_L^G = C_L(\alpha_0, Re) + m(\alpha - \alpha_0) \tag{3.47}$$

$$C_D^G = C_D\left(\alpha_D^G, Re\right) \tag{3.48}$$

α_0 can be taken as any angle of attack, typically the zero-lift angle of attack. m is defined as:

$$m = min\left(\frac{C_L\left(\alpha_L^G, Re\right) - C_L(\alpha_0, Re)}{\alpha_L^G - \alpha_0}, \frac{C_L(\alpha_{ss}, Re) - C_L(\alpha_0, Re)}{\alpha_{ss} - \alpha_0}\right) \tag{3.49}$$

As the Gormont model was initially used to predict the performance of helicopter rotors, certain modifications were needed to apply this model to vertical-axis turbines. Massé proposed the following equations:

$$C_L^M = \begin{cases} C_L + \left[\frac{A_M\alpha_{ss} - \alpha}{A_M\alpha_{ss} - \alpha_{ss}}\right](C_L^G - C_L) & \text{when } \alpha < A_M\alpha_{ss} \\ C_L & \text{when } \alpha > A_M\alpha_{ss} \end{cases} \tag{3.50}$$

$$C_D^M = \begin{cases} C_D + \left[\frac{A_M\alpha_{ss} - \alpha}{A_M\alpha_{ss} - \alpha_{ss}}\right](C_D^G - C_D) & \text{when } \alpha < A_M\alpha_{ss} \\ C_D & \text{when } \alpha > A_M\alpha_{ss} \end{cases} \tag{3.51}$$

where A_M is an empirical constant and C_L^G and C_D^G are the coefficients calculated from the Gormont model. Massé (1981) proposed A_M = 1.8. Continuing on from Massé's modification, Berg (1983) proposed that A_M = 6 gave better agreement with experimental data for a SANDIA wind turbine. Berg also recommended that α_{ss} be taken as the angle where C_L is no longer increasing linearly as opposed to previous work, which took α_{ss} as the angle of maximum C_L.

3.3.3 Flow Expansion Model

One of the initial assumptions of BEM theory is that the streamtubes run parallel to each other. This, however, is not the case owing to the principle of continuity. The flow in the downstream half of the turbine is lower than the upstream half, and this is taken into consideration with the implementation of a flow expansion model. This model assumes that the flow expands perpendicular to the incoming flow direction. Flow expansion effects are most visible at conditions of high loading, i.e. high *TSR* or high rotor solidity, where the flow appears to travel around the turbine as opposed to through it.

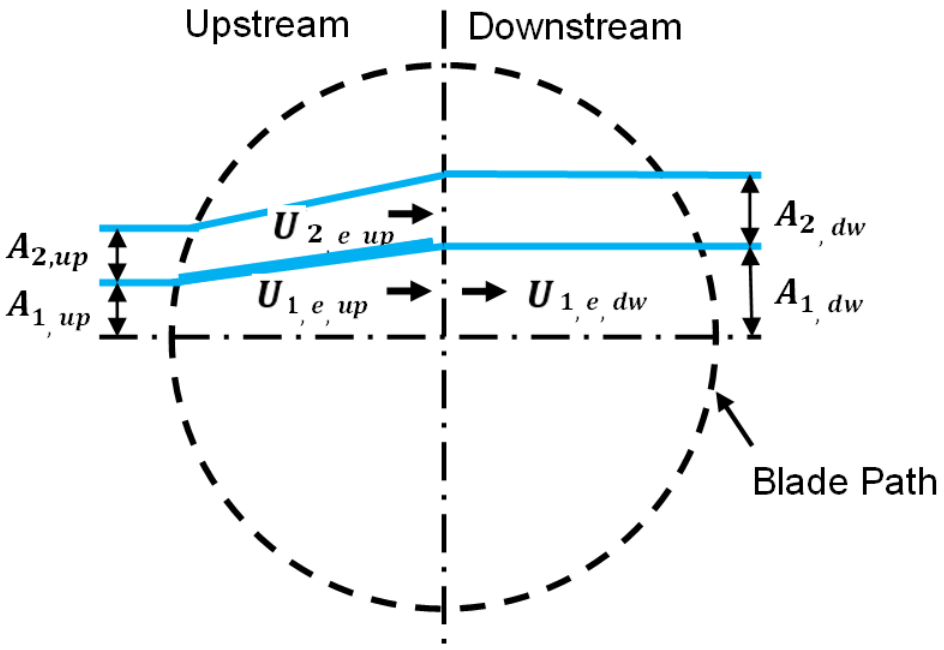

Figure 3-9: Graphical representation of flow expansion model showing the relationship between velocities and cross-sectional area to ensure the conservation of mass within the streamtube

Read and Sharpe (1980) introduced a method of accounting for flow expansion by introducing two different equilibrium induced velocities at the mid-plane between the upstream (us) and downstream (ds) portion of the turbine, $U_{e,us}$ and $U_{e,ds}$. The upstream induced equilibrium velocity is calculated by equation (3.27), and the area of the upstream streamtube is given by equation (3.12). By applying the continuity equation, the area of the downstream, A_{ds}, streamtube can be calculated as follows:

$$A_{ds} = \frac{U_{\infty} A_{us}}{U_{e,us}} \tag{3.52}$$

Based on this calculated downstream area, different equations are implemented to calculate $U_{e,ds}$. If $(A_{1,us} + A_{2,us} - A_{1,ds}) > 0$, then:

$$U_{1,e,us} = U_{1,e,ds} \tag{3.53}$$

$$U_{2,e,ds} = \frac{U_{1,e,ds}(A_{1,ds} - A_{1,us}) + U_{2,e,us}(A_{1,us} + A_{2,us} - A_{1,ds})}{A_2} \tag{3.54}$$

On the other hand, if $(A_{1,us} + A_{2,us} - A_{1,ds}) < 0$, then:

$$U_{2,e,ds} = U_{1,e,us} \tag{3.55}$$

3.3.4 Finite Aspect Ratio Effects

The blade aspect ratio, *AR*, is defined as the ratio of the chord, c, to blade length, L:

$$AR = \frac{L}{c} \tag{3.56}$$

Finite *AR* effects need to be considered, as the C_L and C_D data used in the BEM code assumes infinitely long blades. Based on whether the angle of attack is greater or less than the static stall angle (α_{ss}), different methods are used to calculate corrected C_L and C_D for hydrofoils of finite *AR*. For an infinite *AR*, C_L is over-predicted at all angles of attack, while C_D is under-predicted for $\alpha < \alpha_{ss}$ and over-predicted for $\alpha > \alpha_{ss}$, where α_{ss} is the static stall angle.

For the finite *AR* correction, Lanchester-Prandtl theory, from Abbot and Von Doenhoff (1959) and White (2009), is used to modify C_L and C_D for $\alpha < \alpha_{ss}$. The lift coefficient can be approximated as follows:

$$C_L \approx \frac{2\pi(\sin(\alpha + 2h_c))}{1 + (2/AR)} \tag{3.57}$$

where h_c is the ratio of the blade profiles maximum camber to its chord length. The following equations detail the calculation of the effective coefficient of drag and angle of attack as a function of the aspect ratio, lift coefficient and infinite aspect ratio values ($C_{D,AR=\infty}$, $\alpha_{AR=\infty}$):

$$C_D = C_{D,AR=\infty} + \frac{C_L^2}{\pi \times AR} \tag{3.58}$$

$$\alpha = \alpha_{AR=\infty} + \frac{C_L}{\pi \times AR} \tag{3.59}$$

Viterna and Corrigan (1982) developed a model to correct the C_L and C_D data for angles of attack in the stall and post-stall region up to 90°.

$$C_{L,V-C} = A_1 \sin(2\alpha) + A_2 \frac{\cos^2(\alpha)}{\sin(\alpha)} \tag{3.60}$$

$$C_{D,V-C} = B_1 \sin^2(\alpha) + B_2 \cos(\alpha) \tag{3.61}$$

where:

$$A_1 = \frac{C_{D,max}}{2} \tag{3.62}$$

$$B_1 = C_{D,max} \tag{3.63}$$

$$C_{D,max} = \begin{cases} 1.11 + (0.018 \times AR) & AR > 50 \\ 2.01 & AR \leq 50 \end{cases} \tag{3.64}$$

$$A_2 = \left(C_L(\alpha_{ss}, Re) - C_{D,max}\sin(\alpha_{ss})\cos(\alpha_{ss})\right) \times \frac{\sin(\alpha_{ss})}{\cos^2(\alpha_{ss})} \tag{3.65}$$

$$B_2 = C_D(\alpha_{ss}, Re) - \frac{C_{D,max}\sin^2(\alpha_{ss})}{\cos(\alpha_{ss})} \tag{3.66}$$

Castelli et al. (2012) noted an overprediction of the lift coefficient and decrease in drag coefficient in post-stall operation and suggested a linear interpolation between the 2D dataset and Viterna and Corrigan predictions to improve accuracy:

$$C_L = \frac{C_{L,AR=\infty} + C_{L,V-C}}{2} \tag{3.67}$$

$$C_D = \frac{C_{L,AR=\infty} + C_{L,V-C}}{2} \tag{3.68}$$

3.3.5 Shear Velocity Profile

A freestream tidal velocity profile has been implemented in this code to replicate typical operating conditions. The 1/7th power law was used for this tidal velocity profile. Velocities at each of the individual streamtube heights are calculated as:

$$U_\infty(h) = U_{\infty,max}\left(\frac{h}{H_{EQ}}\right)^{\frac{1}{7}} \tag{3.69}$$

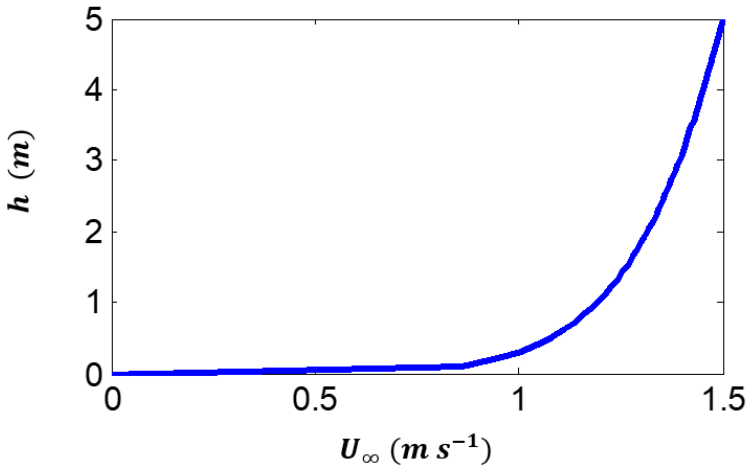

Figure 3-10: Shear velocity profile for a freestream velocity of 1.5 m s^{-1} using the 1/7th power law.

3.4 Results

All the results presented in this section were produced using the Sheldahl and Klimas (1981) blade section data.

3.4.1 Model Validation

Due to the lack of vertical-axis tidal turbine test data available, the BEM model is validated against previously published experimental vertical axis wind turbine data. The similar range of Reynolds number (Re) and insignificant compressibility effects at the low Mach numbers ($Ma < 0.3$) experienced during these wind tests means the results are suitable for validating the tidal turbine-based code developed in this research. Two distinct turbine design were included in this study.

Table 3-2: Vertical-axis turbine geometrical parameters for BEM validation study

Parameter	**Turbine A (Worstell, 1978)**	**Turbine B (McLaren, 2011)**
Height (H)	17 m	3 m
Diameter (D)	17 m	2.5 m
Chord (c)	0.61 m	0.4 m
Number of blades	3	3
Blade profile	NACA0015	NACA0015
Blade shape	Darrieus	Straight

The BEM model is initially implemented for a vertical axis wind turbine, for which there is a previously published experimental dataset (Worstell, 1978). The turbine analysed is a SANDIA 17 m diameter 3-bladed Darrieus turbine, full details listed in **Table 3-2**, Turbine A.

Figure 3-11: Three-bladed Darrieus wind turbine (Worstell, 1978).

The power curves as a function of *TSR* from the model and test data are compared in **Figure 3-12**. The present model shows close agreement with the experimental results for *TSR* values below the peak power value, ~5.5. A root-mean-square error (RMSE) of 0.029 is observed between the model and the test data with the model over-predicting power performance for all *TSR*. The model over-predicts peak $\bar{C}_P$ the test data by approximately 5%. For *TSR* values above this, the model more significantly over-predicts relative to the experimental data, with an RMSE of 0.097. It is worth noting, however, that this regime is generally considered sub-optimal for turbine performance, and typical operating conditions should avoid high *TSR*.

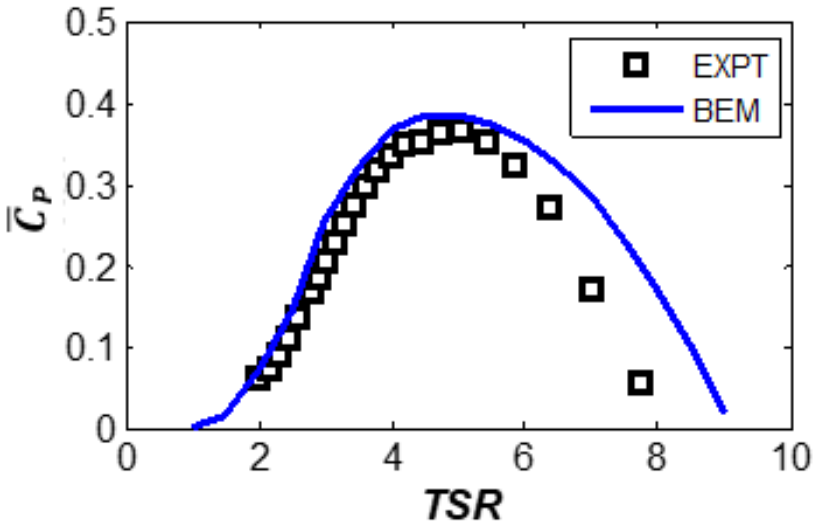

Figure 3-12: Comparison of BEM model predictions against test data for the variation of power coefficient with *TSR* for a three-bladed Darrieus wind turbine (Worstell, 1978).

The second turbine analysed is a 3-bladed vertical-axis turbine (McLaren, 2011) **(Turbine B**, details in **Table 3-2). Figure 3-13** presents a comparison between the experimental and BEM model predictions of the variation of $\bar{C}_P$ with *TSR*. The model successfully captures the general power curve trend of increasing $\bar{C}_P$ with increasing *TSR*. While the model predicts a peak $\bar{C}_P$ value within 5% of the experimental value, the optimal model *TSR* is 2.25 compared to an experimental value of 1.8. The model underpredicts power by up to 40% at lower *TSR*. These model under predictions may be attributable to the lift and drag coefficient datasets used as input in the BEM code, as will be discussed further in **Chapter 4.** These discrepancies are more pronounced at lower Reynolds Numbers and are likely why there are more significant discrepancies between the model and experimental data for the straight-bladed smaller turbine, **Turbine B**. Further experimental validation of the BEM model specifically for the BTT turbine design is included in **Chapter 6.**

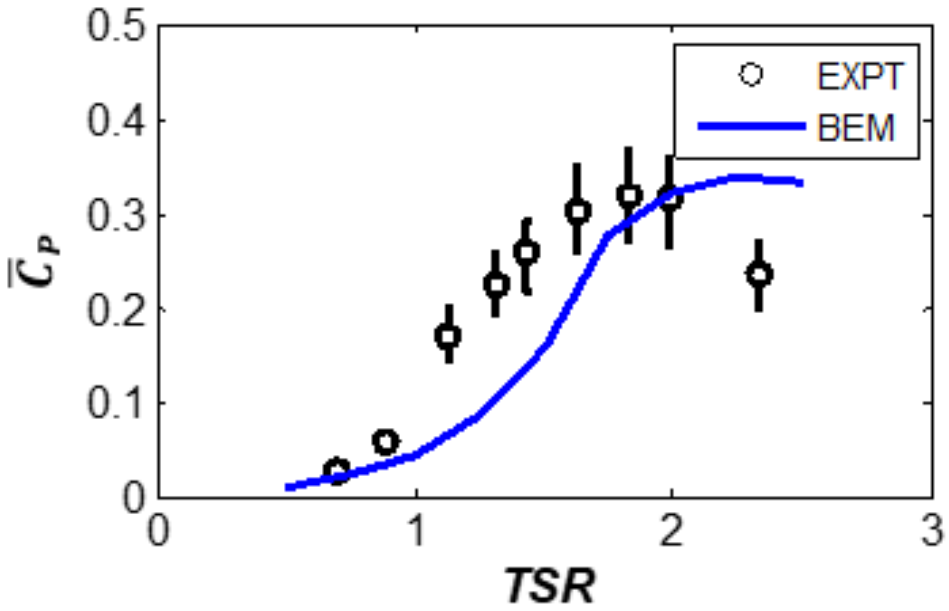

Figure 3-13: Comparison of BEM model predictions against test data of McLaren (2011) for variation of coefficient of power with *TSR* for a three-bladed high solidity straight-bladed vertical-axis turbine.

3.4.2 Design Optimisation

Results from the BEM model design optimisation study of the BTT turbine are now presented. The validated BEM model has been enhanced to incorporate the spiral geometric features of the blade geometry. In identifying the best design of the rotor,

which depends on multiple variables, it is necessary to modify several turbine parameters, including the blade shape, chord length, H/D ratio, number of blades and blade profile, to identify the optimal design. An initial base case design has been identified, and the effects of varying individual parameters relative to this base case are then assessed.

Further investigations consider coupled variations of a discrete number of key parameters, which aims to establish the best possible design and operating conditions based on a specific site flow velocity.

3.4.2.1 Ellipsoidal BTT Geometry

The initial base case design specified for the BTT ellipsoidal blade geometry is defined in terms of the parameters listed in **Table 3-3**. These parameters are assessed individually, one at a time.

Table 3-3: Initial BTT vertical-axis turbine geometrical parameters.

Parameter	**Value**
Height (*H*)	1 m
Diameter (*D*)	1 m
Chord (*c/R*)	0.05 m
Number of blades	3
Blade profile	NACA0015

Figure 3-15 shows the variation of $\bar{C}_P$ with *TSR* for turbines of the three different H/D ratios presented in **Figure 3-14**. The H/D ratio is seen to have a significant effect. A lower H/D ratio leads to a higher peak $\bar{C}_P$ at a higher *TSR*. The most significant difference is between the H/D = 2 design and the other two cases. The two other designs outperform the H/D = 2 case by over 37% at the peak power $\bar{C}_P$. This is due to the greater contribution of torque, and hence power, from the mid-height segment of the turbine, i.e. the largest radius, which is illustrated in **Figure 3-16** for the H/D = 1 case. The most favourable angles of attack ($-12^o < \propto < 12^o$) and Reynolds numbers ($5 \times 10^5 < Re < 7.5 \times 10^5$) are at the mid section of blade. The upper and lower parts of the blades, near the support points, contribute significantly less torque due to the unfavourable values of angle of attack and lower Reynolds number experienced at these sections.

(a) $H/D = 1$ **(b)** $H/D = 2$ **(c)** $H/D = 0.5$

Figure 3-14: Assembled variations the BTT ellipsoidal designs with different *H*/*D* ratios, **(a)** *H*/*D* = 1, **(b)** *H*/*D* = 2 and **(c)** *H*/*D* = 0.5.

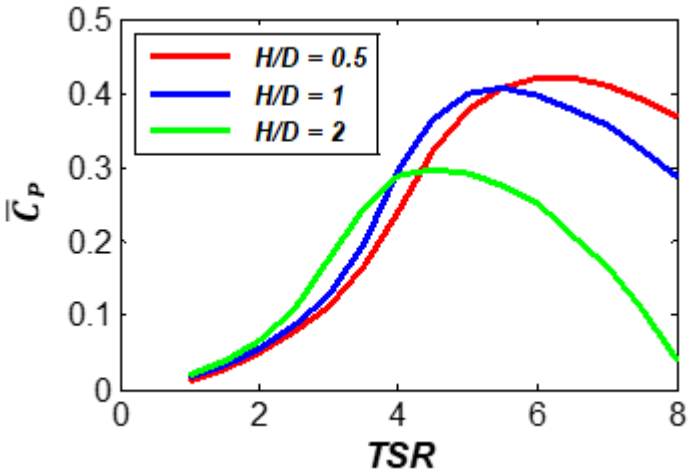

Figure 3-15: Variation of power coefficient with *TSR* for three sample H/D ratio blade designs.

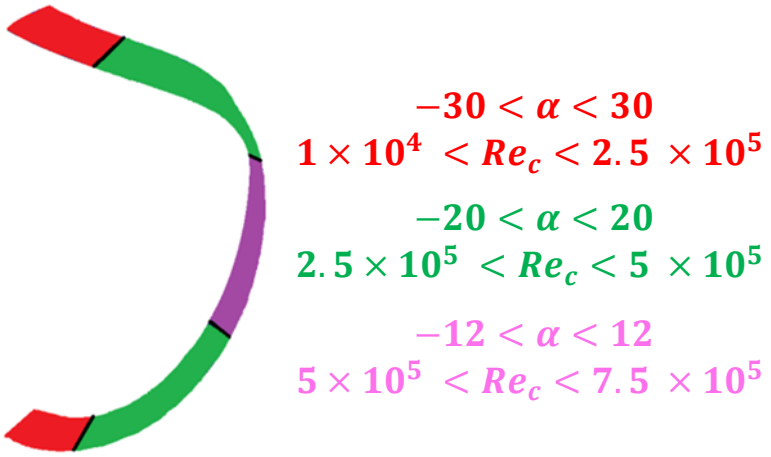

Figure 3-16: Variation of the angle of attack and local Reynolds number for different segments of the sample *H*/*D* = 1 turbine blade. (*TSR* = 4.5)

The effect of the number of blades is shown in **Figure 3-18**. The optimum number of blades is 3, with this configuration giving a slightly higher power performance than the 4-bladed rotor and significantly outperforms the 2-bladed rotor. It should be noted that varying the solidity by increasing the number of blades leads to a lower optimum *TSR*. It should also be noted that the $\bar{C}_P$ distribution is broader with a reduced number of blades, which may be an important design feature for sites with rapidly changing freestream velocities, and hence a continually varying optimal *TSR*.

(a) $N = 2$ **(b)** $N = 3$ **(c)** $N = 4$

Figure 3-17: BTT turbine design concepts with a varying number of blades.

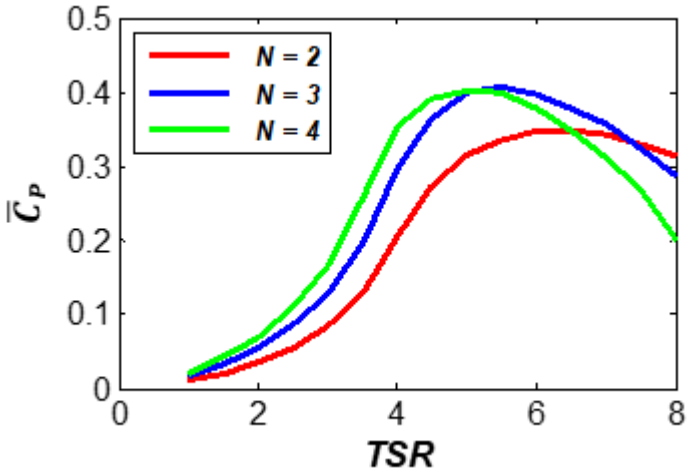

Figure 3-18: Effect of the number of blades on power coefficient variation with *TSR*.

Figure 3-21 shows the variation of $\bar{C}_P$ with *TSR* for three different hydrofoil blade profiles, namely, NACA 0015, NACA 0021 and NACA 0025. A comparison of the lift and drag coefficient variation with angle of attack for these three symmetrical profiles is presented in **Figure 3-20**. Blade profiles with a thinner profile tend to have a higher maximum C_L and lower C_D at the optimal angle of attack. Hence, thinner blade profiles give a higher maximum $\bar{C}_P$, as shown in **Figure 3-19**. One drawback of a thinner blade section is that for angles of attack greater than the optimal, there is a

more dramatic decrease in C_L. It should be noted that the selection of hydrofoil profile should also be influenced by the structural requirements of the turbine.

***(a)** NACA 0015* ***(b)** NACA 0021* ***(c)** NACA 0025*

Figure 3-19: Three blade profiles, namely, (a) NACA 0015, (b) NACA 0021 and (c) NACA 0025.

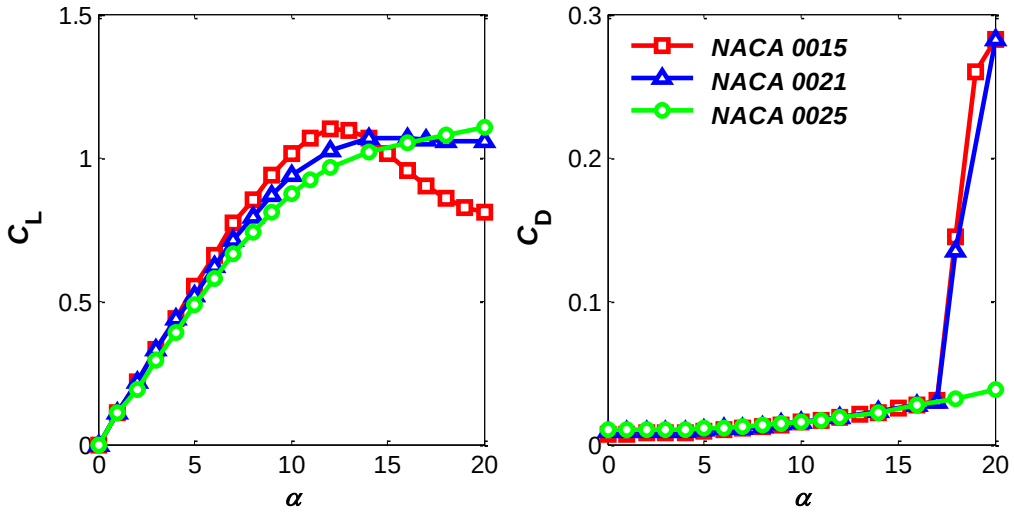

(a) **(b)**

Figure 3-20: (a) Lift coefficient and **(b)** drag coefficient variation as a function of angle of attack for three different NACA profiles for Reynolds number of 1×10^6.

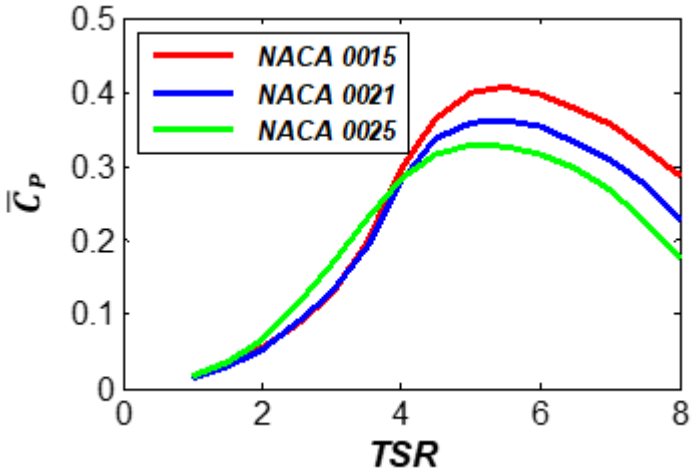

Figure 3-21: Variation of power coefficient with *TSR* for three differing blade profiles, namely NACA 0015, NACA 0021 and NACA 0025.

The rotor solidity can also be varied by changing the chord length.

Figure 3-22 shows the variation of $\bar{C}_P$ with *TSR* for various chord lengths. The peak $\bar{C}_P$ increases with increasing chord length. This peak $\bar{C}_P$ occurs at a lower *TSR* with increasing chord length. On occasion, the maximum chord length investigated by this type of model is limited by convergence issues arising from the iterative approach when solving for the interference factor for highly loaded or high solidity rotors (Klimas and Sheldahl, 1978). No such issues were encountered during this analysis.

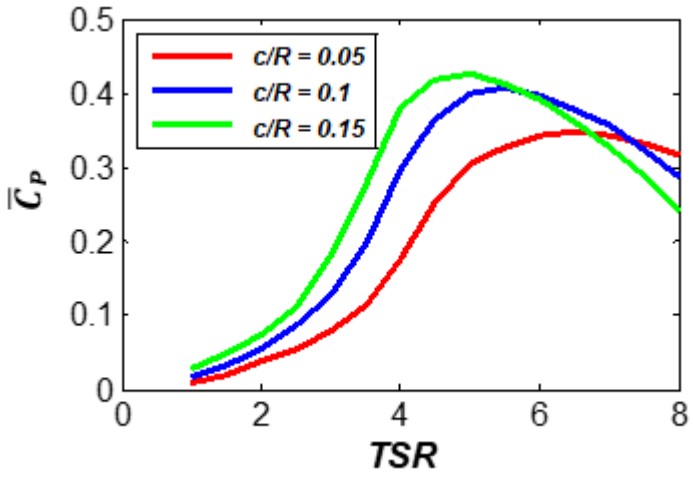

Figure 3-22: Variation of power coefficient with *TSR* for three sample chord lengths.

A fully coupled design optimisation study is performed based on the range of design parameters listed in **Table 3-4**.

Table 3-4. Range of variables investigated in design optimisation for spherical BTT Turbine

Parameter	**Values**
H/D ratio	0.1, 0.2, 0.4, 0.5, 1, 1.5, 2
Chord/Radius	0.05, 0.075, 0.1, 0.125, 0.15
Number of blades	2, 3, 4, 5
Blade profile	NACA 0015, NACA 0021, NACA 0025

The design optimisation is performed subject to the constraint that the frontal area of the turbine is constant. A freestream velocity of 1.5 m s^{-1} is assumed. In **Figure 3-23**, results are presented for a range of H/D ratios. For each value of H/D the maximum power coefficient, $\bar{C}_{P,max}$, is shown. Additionally, the *TSR*, N and c that result in $\bar{C}_{P,max}$ are indicated. The optimum design configuration (yielding the highest value of $\bar{C}_{P,max}$) is a three-bladed turbine, with H/D = 0.5, with NACA 0015 blade profiles of the chord length of $0.15R$, operating at *TSR* = 5. The maximum power coefficient

for this design is 0.447, representing a 5.7% increase relative to the optimal H/D = 0.1 design, and a 20.5% increase relative to the optimal H/D = 2 design.

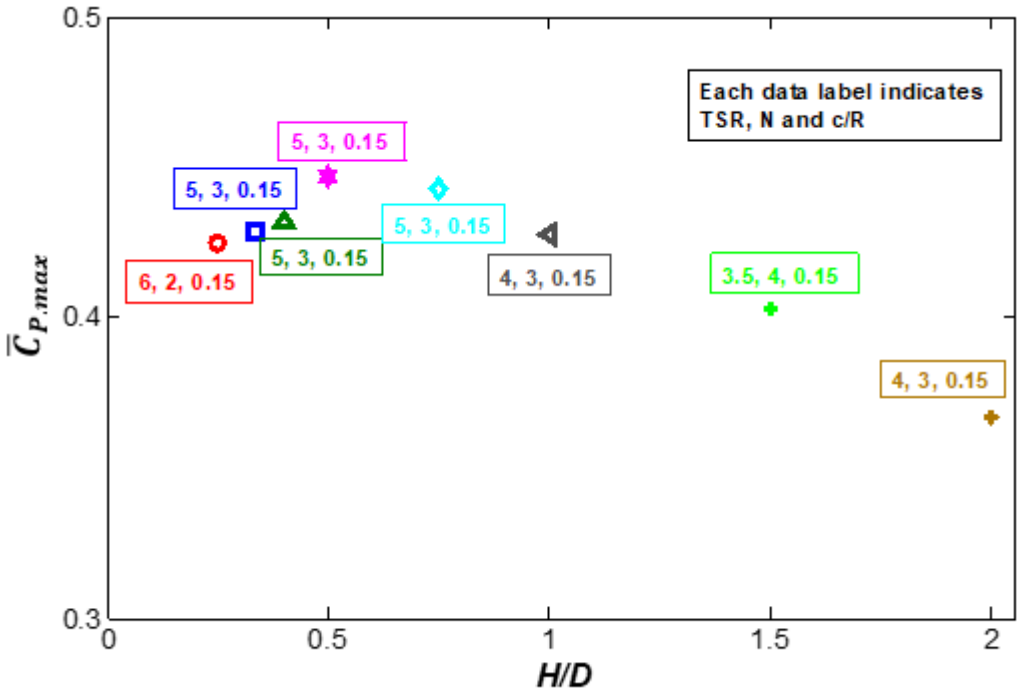

Figure 3-23: Variation of maximum power coefficient with *H*/*D* ratio from coupled design optimisation study. Optimal *TSR* and design parameters (*N*, *c*/*R*) are listed for each *H*/*D* value.

3.4.2.2 Cylindrical BTT Geometry

Following on from the analysis of the initial base case design, a cylindrical variation of the BTT turbine design was conceptualised, as presented in **Figure 3-24**. The motivation behind examining this design over the existing ellipsoidal design was due to the cylindrical blade design's constant blade radius and blade inclination to the incoming flow along the entire length of each blade. Considering again the range of design variables listed in **Table 3-4**, the optimised cylindrical turbine design was determined to be a three-bladed NACAC0015 rotor with a c/R ratio of 0.15. The power curve for this blade configuration is shown in **Figure 3-25**. This blade configuration has a maximum $\bar{C}_P$ of 0.49 at a *TSR* of 3.125. This represents almost a 10% increase in the maximum $\bar{C}_P$ over the optimised ellipsoidal BTT design.

Figure 3-24: Brí Toinne Teoranta (BTT) design concept- cylindrical design.

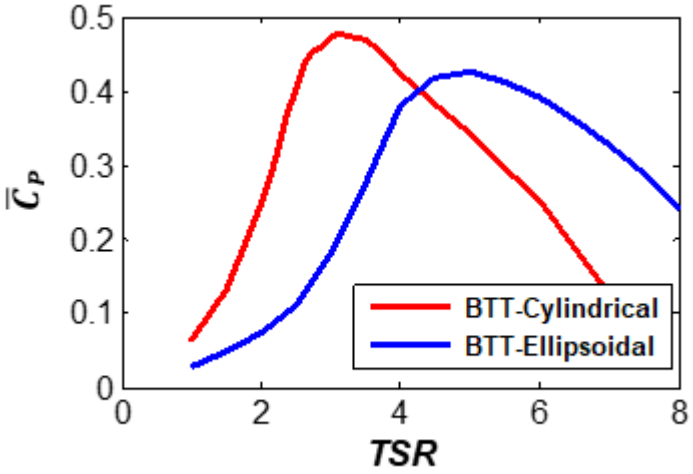

Figure 3-25: Comparison of the power coefficient variation with *TSR* for the optimised BTT cylindrical and ellipsoidal turbine designs.

The optimised turbine design, operating at its optimal *TSR*, is examined in more detail in **Figure 3-26** and **Figure 3-27**. The variation of the angle of attack with the TOCA for several blade heights is shown in **Figure 3-26**. At different heights, the turbine blade experiences different local angles of attack, and therefore each blade section is experiencing a different torque contribution at the same time, resulting in steadier instantaneous torque output, as shown in **Figure 3-27**. This characteristic of the novel turbine design is discussed in further detail in the next section, where the optimised BTT design is compared to an equivalent straight-bladed design.

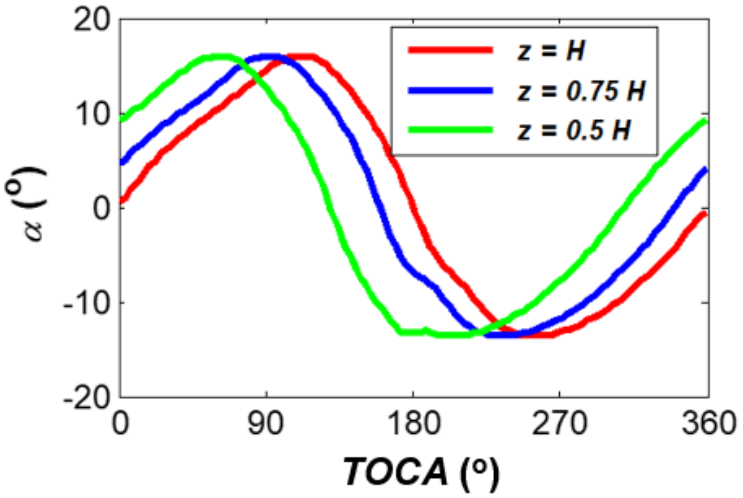

Figure 3-26: Angle of attack variation with TOCA for different blade height sections for *TSR* = 3.125.

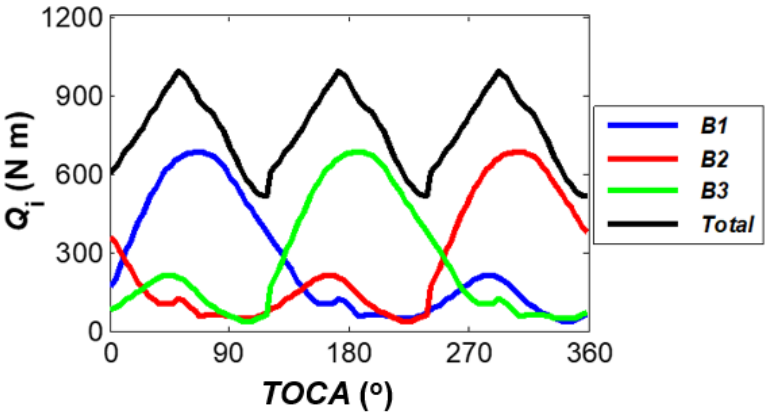

Figure 3-27: Individual and total instantaneous torque contribution variation with TOCA for *TSR* = 3.125.

3.4.3 Turbine Power Predictions Comparison

It is of interest to compare the optimised turbine design to an equivalent straight-bladed design. The turbine has identical design parameters, i.e. overall turbine height, diameter, chord length and blade profile are all the same, and the turbines are examined for the same freestream velocity (U_∞ = 1.5 m s^{-1}). The power curves for the two designs are presented in **Figure 3-28**. The BTT cylindrical turbine design has a maximum $\bar{C}_P$ of 0.49 at a *TSR* of 3.125, while the straight-bladed turbine has a maximum $\bar{C}_P$ of 0.44 at a *TSR* of 3.5. The BTT design outperforms the straight-bladed design in terms of maximum $\bar{C}_P$ by over 10%. The benefits of the BTT design are also evident at lower *TSR*, where the novel turbine design experiences a higher $\bar{C}_P$.

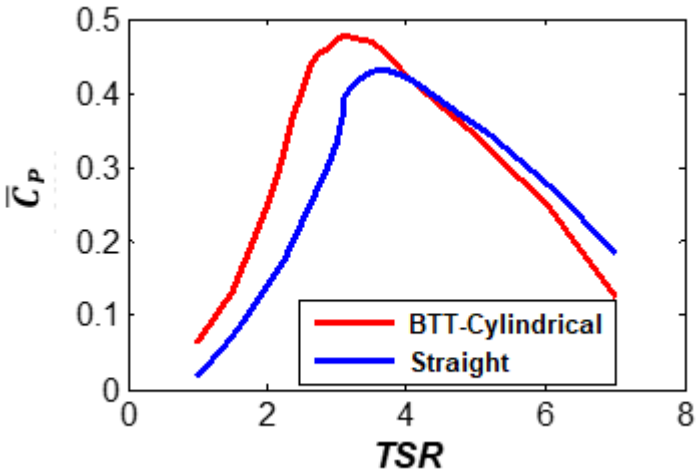

Figure 3-28: Comparison of power coefficient variation with tip-speed ratio between optimised BTT Cylindrical design and an equivalent straight-bladed turbine.

An operational advantage of the BTT design over a straight-bladed design is shown in **Figure 3-29**. In these figures, the instantaneous torque variation with blade position is presented for the two turbine designs. The torque fluctuations shown in **Figure 3-29** will directly affect the fatigue life of various turbine components, e.g. generator, bearings, couplings etc. The fluctuations are also directly related to the fluctuations in electrical power generated by the turbine. Typically torque fluctuations are reduced by increasing the number of blades or installing a pitching mechanism to pitch the turbine blades to achieve their desired angle of attack. Increasing the number of blades leads to an increase in the manufacturing costs of the turbine and has been shown previously to lead to a reduction in the maximum power coefficient (**Figure 3-18**). Installing a pitching mechanism into the turbine will also increase the cost of manufacture while increasing the possibilities of components failing. The novel BTT design achieves a reduction in the torque fluctuations due to the spiral geometry of the turbine blades. The benefits of the spiral design are visible at lower *TSR*. For instance, for *TSR* = 1, the BTT turbine experiences a 57% reduction in the overall torque fluctuation for one rotation when compared to the equivalent straight-bladed turbine, while at *TSR*= 3.125 and *TSR* = 5 reductions of 19% and 3% respectively are observed. The higher torque value at lower *TSR* also indicates the enhanced start-up capabilities of the BTT design.

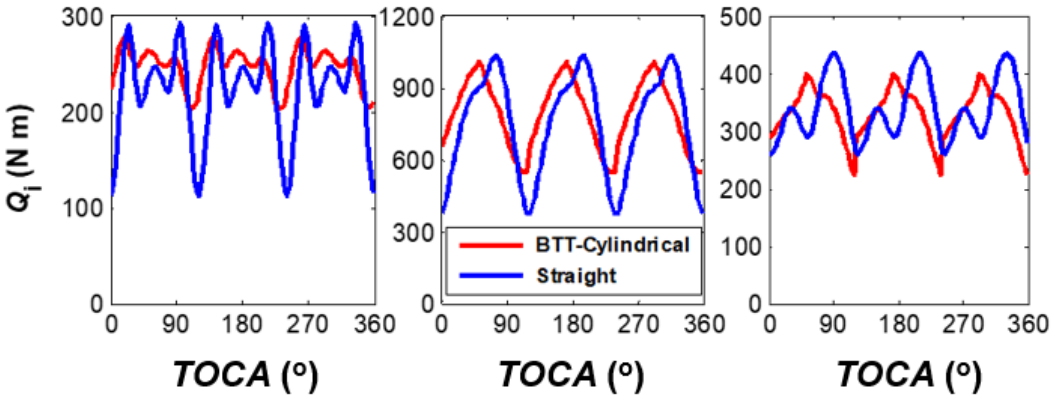

(a) *TSR* = 1 (b) *TSR* = 3.125 (c) *TSR* = 5

Figure 3-29: Comparison of instantaneous torque variation with TOCA between a straight-bladed turbine and equivalent straight-bladed turbine.

3.4.4 Reynolds Scaling Study

The results presented thus far assume a constant freestream velocity of 2 m s^{-1}. An investigation was carried out to determine if the optimised cylindrical design would alter for different freestream velocities, namely 1, 2 and 3 m s^{-1}, for turbines of various sizes. These results are presented in **Figure 3-30**. It was deduced that while the optimised design remained the same for each of the three fluid velocities, the optimal *TSR* differed in each case. It can be noted that the optimal *TSR* decreases with increasing freestream fluid velocity and that with increasing turbine radius, the optimal *TSR* decreases.

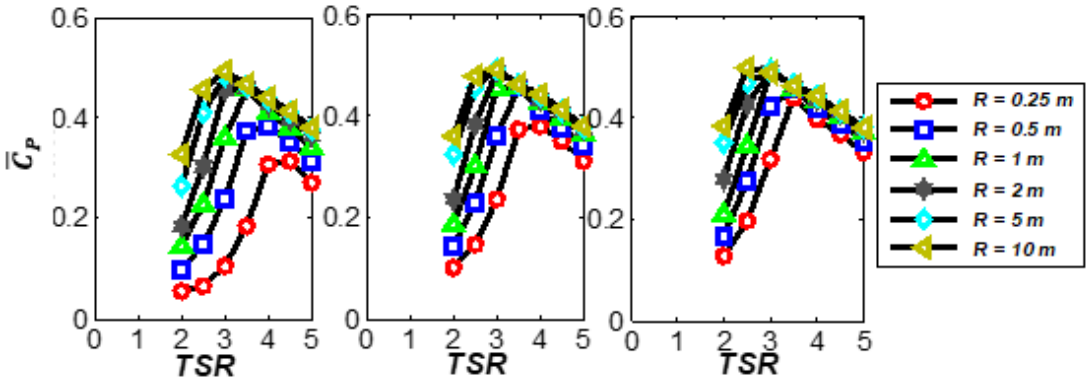

(a) U_∞ = 1 m s^{-1} **(b)** U_∞ = 2 m s^{-1} **(c)** U_∞ = 3 m s^{-1}

Figure 3-30: Variation of power coefficient with tip-speed ratio for a range of turbine sizes for three different freestream velocities.

The effect of rotor radius on $\bar{C}_{P,max}$ can be viewed more distinctly in **Figure 3-31**. The power coefficient is seen to increase asymptotically towards 0.5 with increasing radius, with negligible additional benefits in terms of peak power coefficient above 5 m radius. While $\bar{C}_P$ and TSR are dimensionless parameters; they are dependent on $Re < 5 \times 10^5$, i.e. an higher Re will lead to an increased lift force and a reduced drag force for the same value α for Re. For $Re > 5 \times 10^5$, C_L and C_D become independent of Re. At small radii, for the current tidal velocities, the lower Reynolds numbers lead to lower lift forces, higher drag forces and hence reduced torque. Alternative low Reynolds number hydrofoils, such as the Selig S1223 profile as studied by Selig and Guglielmo (1997), could potentially be implemented to increase power performance at these low Reynolds numbers.

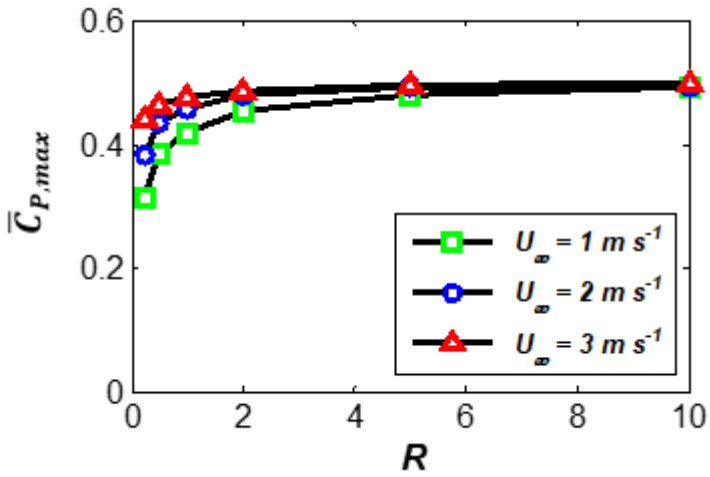

Figure 3-31: Variation of maximum power coefficient with turbine radius for three different freestream velocities.

3.5 Chapter Conclusions

A hydrodynamic analysis methodology is presented for a novel vertical axis turbine concept with a complex spiral blade geometry. The novel design is shown to give significant benefit for hydrodynamic performance, specifically, maximum power coefficient compared to an equivalent straight-bladed vertical-axis design. The methodology adopts a BEM model that incorporates dynamic stall, flow expansion, finite aspect ratio effects and a fluid velocity profile. The model is also capable of predicting the power performance for generic (conventional) vertical axis turbine

designs and is validated against available experimental test data for such designs. A coupled design optimisation study is presented for the identification of peak power performance, with turbine parameters based on specific site flow speed. The optimised design is shown to be a three-bladed cylindrical-shaped turbine with NACA0015 blade profiles with a c/R value of 0.15, operating at a *TSR* of 3.125. The optimised turbine is shown to give a power coefficient benefit of 24% relative to the initial (base case) design; it is also shown to give a benefit of 18% over an equivalent (optimised) straight-blade design with the same swept volume. The increased power, relative to conventional vertical axis designs, is attributed to the greater blade length of the spiral design. The BTT design also experiences fluctuations of significantly lower magnitude to those of an equivalent straight-bladed design. Greater torque is generated at lower *TSR* by the BTT turbine design due to favourable blade positions of certain blade elements. This feature enhances the turbine's start-up ability which reduces the complexity of the overall turbine operation.

Computational fluid dynamics (CFD) modelling offers an alternative to BEM modelling. However, this process is computationally expensive. As an example of the difference in computational cost, analysis of a single straight-bladed (two-dimensional) vertical-axis turbine requires roughly 680 hours run time using 24 processors. In comparison, the full coupled optimisation BEM code developed in this chapter provides results in a matter of minutes on a laptop using four processors. CFD analysis offers the potential to obtain detailed information on a small subset of turbine designs, but our BEM approach provides a highly efficient means of performing design studies for a wide range of turbine parameters. Additional work in **Chapter 6** will aim to develop CFD models of the optimised design, and investigate rotors of higher solidities and provide a more detailed understanding of the flow in the wake of the turbine.

The present methodology uses the blade coefficients (C_L, C_D) published by Shedahl and Klimas (1981). This method is not accurate for flow conditions that result in flow separation, i.e. it should not be used for low Reynolds number values and values of angle of attack within the critical stall region. In **Chapter 4,** an improved BEM model is presented based on hydrodynamic coefficient data derived from CFD methods.

Chapter 4: Two-Dimensional URANS CFD Simulations of a Single Hydrofoil and Full Turbine

4.1 Introduction

Accurate lift and drag coefficient hydrofoil datasets for a wide range of flow conditions are crucial input for a BEM model, as noted in **Chapter 3**. Recent innovations in the tidal energy industry include the development of curved and spiralling blade geometries (Cheng et al., 2017; Talukdar et al., 2017; Walsh et al., 2015), in particular for vertical-axis and cross-flow turbines. The Brí Toinne Teoranta turbine is one such design concept. The complex spiral-type blade geometry encounters an increased range of *Re* and α during operation compared to equivalent straight blade turbine designs.

Existing BEM models implement the panel method (Eppler, 1978) as a means of determining of C_L and C_D for high values of *Re* ($Re > 5 \times 10^5$). Sheldahl and Klimas (1981) presented a panel method (PROFIL) derived C_L and C_D datasets for a range of *Re* values from 10^4 to 10^7 for several standard NACA profiles. This is the dataset which was implemented as input for the BEM model presented in **Chapter 3**. As highlighted in **Figure 2-22**, the panel method is not accurate for conditions that result in flow separation, i.e. it should not be used for high values of α and low values of *Re*.

Due to recent advances in computing power, CFD analysis of hydrofoils under a wide range of test conditions with a sufficiently high spatial and temporal discretisation and an appropriate turbulence model is a viable methodology to characterise the lift and drag data for hydrofoil over a wide range of flow conditions. This analysis could provide more accurate input data for blade element momentum (BEM) analysis of these next-generation VATTs with spiral blade designs.

While 3D CFD studies are required to perform a complete analysis of the Brí Toinne Teoranta design presented in this research, 2D CFD studies provide valuable insight

into turbines' hydrodynamics. 2D CFD studies of turbines is an extensively researched topic (Balduzzi et al., 2016; Lanzafame et al., 2014; Mannion et al., 2018) and, compared to 3D models, have a relatively low computational expense.

The chapter is structured as follows: **Section 4.2 Two-Dimensional CFD Model Methodology** includes details on the hydrofoil and full turbine 2D CFD model development, highlighting turbulence model selection, domain size, meshing techniques, etc. The CFD model results are presented in **Section 4.3 Results.** The results section includes complete discretisation studies, CFD-derived lift and drag coefficients for a specified hydrofoil and power curves for different vertical-axis turbines, including the optimised designs presented in **Chapter 3**. The primary outcomes from this chapter and discussions on future validation of the results are included in **Section 4.4 Conclusions**.

The aims of this chapter are to:

- Establish a CFD methodology that provides accurate and computationally efficient values of C_L and C_D for a hydrofoil geometry under a wide range of flow conditions.
- Demonstrate the improved accuracy of the BEM approach to VATT analysis when CFD derived C_L and C_D datasets are used as model input.
- Compare the computational resource requirement and accuracy of a complete CFD study of a VATT to the CFD-based BEM methodology developed in this chapter.
- Using the newly derived CFD dataset of lift and drag coefficients, investigate the BTT turbine's self-starting capabilities and compare the results with an equivalent straight-bladed turbine.

4.2 Two-Dimensional CFD Model Methodology

4.2.1 Hydrofoil CFD Model Development

4.2.1.1 Scope of the Dataset

Even at the optimal operating conditions, as shown in **Figure 4-1**, the Brí Toinne Teoranta Ellipsoidal design experiences a wide range of α and Re can vary by several orders of magnitude along a blade. To reliably design and optimise next-generation spiral bladed turbines using the BEM approach, C_L and C_D data must be determined

for such an extensive range of operating conditions. A dataset covering α from -30° to 30° and a selection of *Re* from 8×10^4 to 2×10^6 is deemed the focus of this research. While experimentally measured coefficients are available from some sources, this data is typically limited and not extensive enough to cover the wide range of operating conditions experienced by vertical-axis turbines. As noted in **Chapter 2**, for the profile, which is the focus of this study, the NACA 0015, experimental data is confined to a limited range of attack angles (Jacobs and Sherman, 1937) or a small range of Reynolds number (Sheldahl and Klimas, 1981).

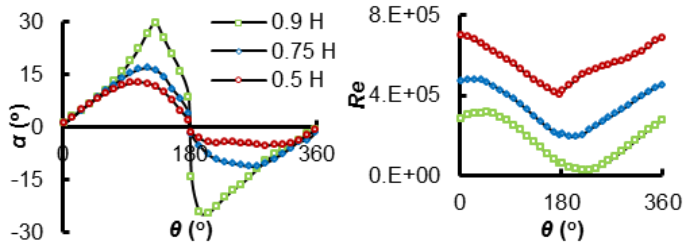

Figure 4-1: Variation of the angle of attack and Reynolds Number with turbine height for Brí Toinne Teoranta Ellipsoidal design for *TSR* = 4. Results are taken from the BEM Model developed in **Chapter 3**.

4.2.1.2 Model Domain & Boundary Conditions

Hydrofoils of varying shapes have different characteristics depending on their operating conditions. When analysing the performance of hydrofoils, it is necessary to compare their non-dimensional C_L and C_D as a function α and *Re*.

The NACA0015 is a commonly studied NACA series profile. The design is frequently used for VATs and is the hydrofoil chosen for the novel turbine design. Its superior power performance is highlighted in **Figure 3-19**. The profile has no camber (as indicated by "00"), and the profile has a maximum thickness of 15% of the overall chord length (as indicated by "15") which occurs at 40% of the distance along the chord line from the leading edge. The equation for 4-digit symmetrical NACA profiles is:

$$y_t = 5t\left[0.2969\sqrt{x} - 0.1260x - 0.3516x^2 + 0.2843x^3 - 0.1015x^4\right] \qquad (4.1)$$

where y_t is the half-thickness at the specified x value, x is the position along the chord (0 - 1.00), and t is the maximum thickness as a fraction of the chord length.

The boundary conditions and domain dimensions are shown in **Figure 4-2**:

1. The inlet velocity applied to the domain varied for each value of *Re*.

2. The hydrofoil surface is defined as a no-slip wall.
3. The outlet is defined as a pressure outlet with 0 Pa gauge pressure.
4. A symmetry boundary condition is applied to the top and bottom surface of the domain.

Parametric studies are performed to determine the necessary domain size as a function of the hydrofoil chord length for a converged solution. This study reveals that to ensure a fully developed wake, the length of the domain is set at 40 m and width at 30 m, both based on a hydrofoil chord length of 1 m.

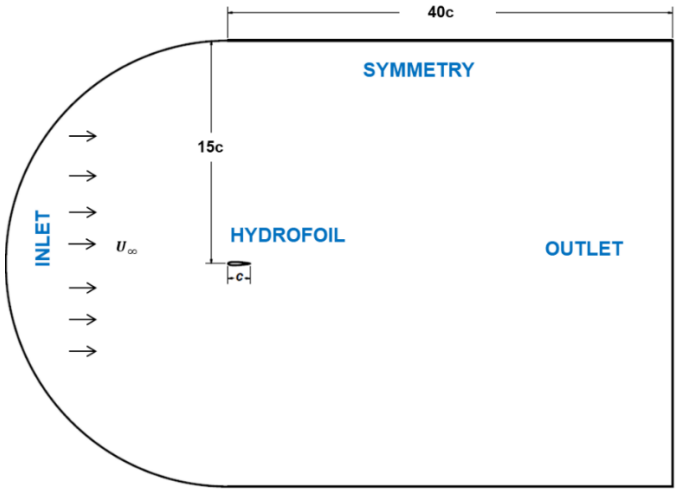

Figure 4-2: Computational domain for 2D simulations of NACA0015 of chord length c with boundary conditions indicated. (Not to scale)

For all simulations, the density of water is set at 998.2 kg m^{-3}, and the viscosity is set at 1.003 × 10^{-3} kg m^{-1} s^{-1}. Re is changed for each case by varying the incoming hydrofoil inlet velocities, $U_{i,H}$. It is calculated as follows:

$$Re = \frac{\rho U_{i,H} c}{\mu} \tag{4.2}$$

where c is the blade chord length.

4.2.1.3 Turbulence Model Selection & Mesh Definition

The SST Transition turbulence model (Menter et al., 2006), detailed in **Appendix A.2**, is selected for the simulations due to its superior capabilities of modelling the transition between laminar and turbulent flow (Langtry et al., 2006). It, therefore, provides an appropriate approach for the analysis of hydrofoils at high angles of attack. This turbulence model has previously been implemented successfully for limited flow conditions for both symmetric and non-symmetric aerofoil analyses (Counsil and Goni Boulama, 2013, 2012; Genç, 2010).

A two-dimensional computational C-grid, shown in **Figure 4-3**, is generated using ICEM within ANSYS Workbench. Mesh definition is of primary importance for this approach when defining a RANS simulation. A blocking framework is implemented to represent the topology of the model. This blocking framework is associated with the model geometry. A structured quadrilateral grid is generated within each block. Three blocks are generated around the hydrofoil wall to ensure adequate refinement close to the hydrofoil wall. Key parameters in determining the mesh refinement include the non-dimensional distance to the first cell from a wall (y^+ value), the growth rate at the walls, the number of elements in the boundary layer, the number of nodes on the surface of the hydrofoil and the overall size of the domain. A key requirement of the SST Transition model is a $y^+ < 1$ (ANSYS, 2013). The initial first layer height, y, is calculated using equation (4.3). Fifty inflation layers are used with a growth rate of 1.15 implemented for all grid generations.

$$y = \frac{y^+ v}{V_*} \tag{4.3}$$

where V_*, the friction velocity is defined as,

$$V_* = \frac{\tau_w}{\rho} \tag{4.4}$$

where τ_w is the fluid wall shear stress. When choosing this turbulence model, additional turbulence boundary conditions are required to be specified. A turbulent intensity of 0.2% and turbulent viscosity ratio of 2 is applied at the inlet and outlet.

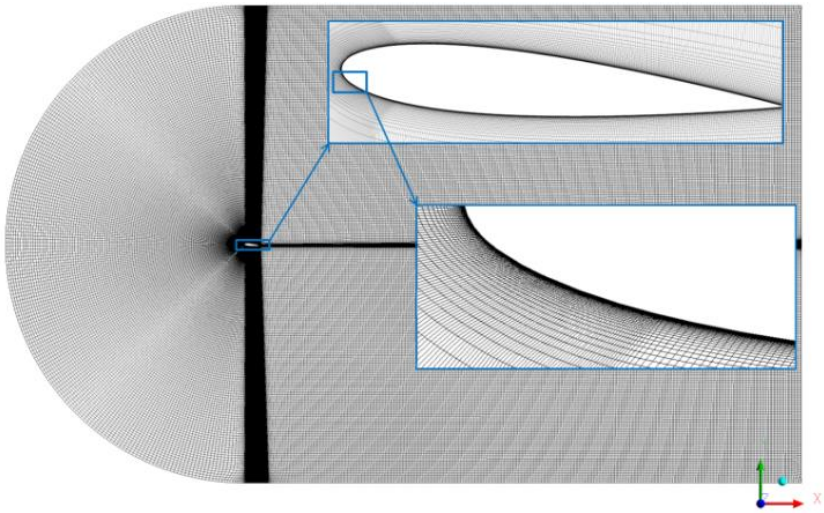

Figure 4-3: Structured mesh around NACA0015 showing detailed inflation around hydrofoil in the critical boundary layer region (α = 10^o).

A systematic approach is adopted to the detailed mesh refinement process to ensure an accurate solution, as detailed below. Five meshes with different numbers of total elements are generated, focusing on refining the critical boundary layer around the hydrofoil surface. Once a suitably refined mesh is identified, a scripting code developed within ICEM is developed to replicate meshing parameters for each α value to ensure the same mesh characteristics are defined in each case.

4.2.1.4 Solution Methods and Convergence Criteria

The models are solved using the finite volume method with the CFD RANS based code within ANSYS FLUENT®. To fully capture the flow effects around the hydrofoil, transient simulations are required. Flow separation and reattachment are time-dependent, so it is necessary to carry out parametric studies to identify the required time step and the required simulation time to achieve a converged solution. As the flow regime in the stall and the post-stall regime is unsteady, a second-order implicit transient simulation formulation is implemented. The Coupled algorithm is used to solve the coupling between the velocity components and pressure in momentum equations. Second-order upwind discretisation methods are applied to the momentum, turbulent kinetic energy, specific dissipating rate, intermittency, and transitional Reynolds number equations. Second-order algorithms result in more accurate predictions as they reduce interpolation errors and false numerical diffusion in comparison to first-order algorithms.

The convergence criterion is set at a target value of 10^{-5} for all residuals to ensure a converged solution is achieved. Lift and drag coefficient outputs from the simulations are also monitored at each time step to ensure a steady-state or quasi-steady-state solution is achieved. Calculations are run using 24 processors, and the total runtime of the simulation was dependant on the values of Re and α. Low values of α require approximately 1-hour run-time to reach a converged solution. Higher α value simulations require between 8 and 24 hours to reach a converged solution, with high values of α at low Re requiring the longest run-times. Further details on the temporal discretisation studies are given below. It should be noted that for angles of attack in the stall and post-stall region, a constant steady-state lift or drag coefficient is not achieved due to the unsteady nature of the flow under these conditions, i.e. vortex shedding.

4.2.2 Full Turbine Model Development

To assess the accuracy of a BEM turbine analysis with CFD based hydrofoil C_L and C_D input, results are compared to a full CFD analysis of a standard straight-bladed vertical axis turbine design. The turbine parameters are listed in Table 4-1.

Table 4-1. Straight-bladed vertical axis turbine geometrical parameters.

Parameter	Value
Length (L)	3 m
Diameter (D)	2.5 m
Chord (c)	0.4 m
Number of blades	3
Blade profile	NACA0015

The full CFD model of the turbine also uses the SST Transition turbulence model. Model boundary conditions and domain dimensions are shown in **Figure 4-4**. The domain dimensions are a function of the turbine diameter and are taken from an extensive study performed by Balduzzi et al. (2016). The boundary conditions simulate free stream conditions ensuring the turbine performance is not affected by blockage effects, and the wake can fully develop. Free-stream conditions were simulated for the CFD calculations to reduce the mesh size requirements. A turbulent intensity of 0.2% and turbulent viscosity ratio of 2 is applied at the inlet and outlet, consistent with the values chosen for the 2D hydrofoil model. The three turbine blade surfaces are set as non-slip walls. Two cell zones are defined to develop a moving reference frame model, also known as 'the frozen rotor approach', to simulate the rotating turbine blades. An interface, highlighted in **Figure 4-4**, is defined between the moving and stationary cell zones. The steady-state flow field solution from the moving reference frame simulation is used as the initial solution for the transient sliding mesh calculation, thus reducing the overall time to achieve a converged solution. A second-order implicit transient simulation formulation is implemented. The Coupled algorithm is used to solve the coupling between the velocity components and pressure in momentum equations. First-order upwind discretisation schemes are applied for the momentum, turbulent kinetic energy, specific dissipating rate, intermittency and the transitional Reynolds number for the first eight turbine rotations before switching to second-order discretisation schemes for the remaining rotations.

The convergence criterion is set at a target value of 10^{-5} for all residuals to ensure a converged solution is achieved. In addition, the average torque coefficient per rotation was also monitored and included in the convergence criterion. Further details are discussed below.

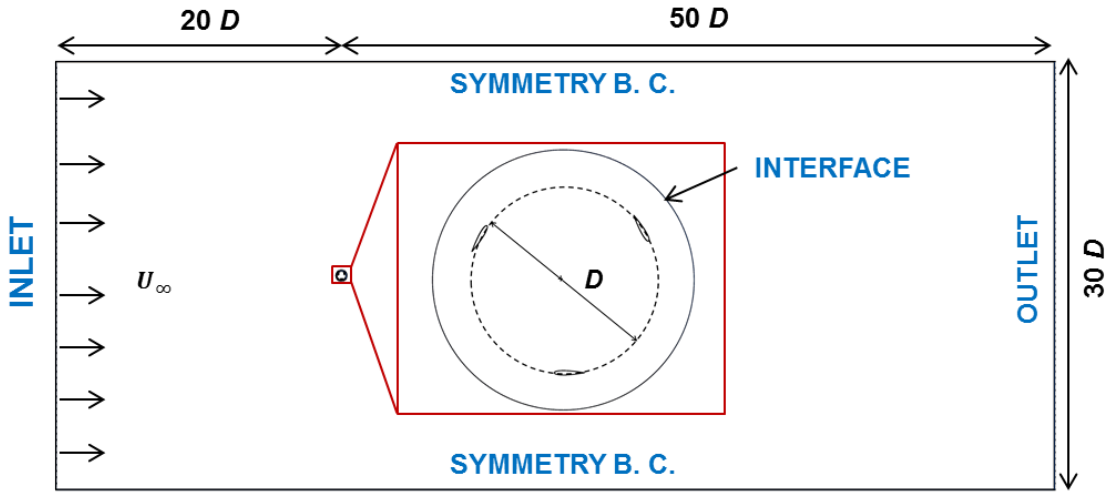

Figure 4-4: Computational domain for 2D simulations of straight-bladed vertical axis turbine of diameter, *D*. Boundary conditions and rotating cell zone indicated. (Not to scale)

The CFD mesh is systematically refined to identify the optimal spatial discretisation, with respect to computational time and accuracy, with the focus placed on the critical region around the blade surfaces. Similar to the hydrofoil study, the initial first layer height, *y*, around the blade surfaces are defined by equation (4.3) to ensure a y^+ value < 1. Similar mesh sizing is applied on either side of the stationary and rotating interface to ensure a uniform mesh size is achieved in this region. Computed results from a spatial discretisation study are presented below. **Figure 4-5** shows a CFD turbine mesh containing 861,660 elements, highlighting mesh refinement at key regions, including inflation layers at hydrofoil walls.

Simulations are carried out for *TSR* varying from 0.5 to 2.5. The rotational velocity, ω_{rot}, is applied to the three blades per equation (4.5), where R is the turbine radius and U_∞ is the fluid freestream velocity.

$$\omega_{\mathrm{rot}} = \frac{U_\infty TSR}{R} \tag{4.5}$$

The instantaneous torque coefficient, C_{Q}, is determined for each time step based on the following equation:

$$C_{\mathrm{Q}} = \frac{Q_{\mathrm{i}}}{0.5\rho A {U_{\infty}}^{2} R} \tag{4.6}$$

where Q_{i} is the instantaneous torque, U_{∞} is the freestream velocity and A is the turbine frontal area. An averaged torque coefficient for each rotation, $\bar{C}_{\mathrm{Q}}$, is calculated by:

$$\bar{C}_{\mathrm{Q}} = \frac{1}{2\pi}\int_{0}^{2\pi} C_{\mathrm{Q}}\, d\theta \tag{4.7}$$

Simulations are run until a converged $\bar{C}_{\mathrm{Q}}$ was achieved. The solution is deemed to have achieved the convergence criterion when the variation of $\bar{C}_{\mathrm{Q}}$ between two subsequent rotations is less than 0.5%. The average power coefficient, $\bar{C}_{\mathrm{P}}$, for the given *TSR*, is calculated as follows:

$$\bar{C}_{\mathrm{P}} = \bar{C}_{\mathrm{Q}} TSR \tag{4.8}$$

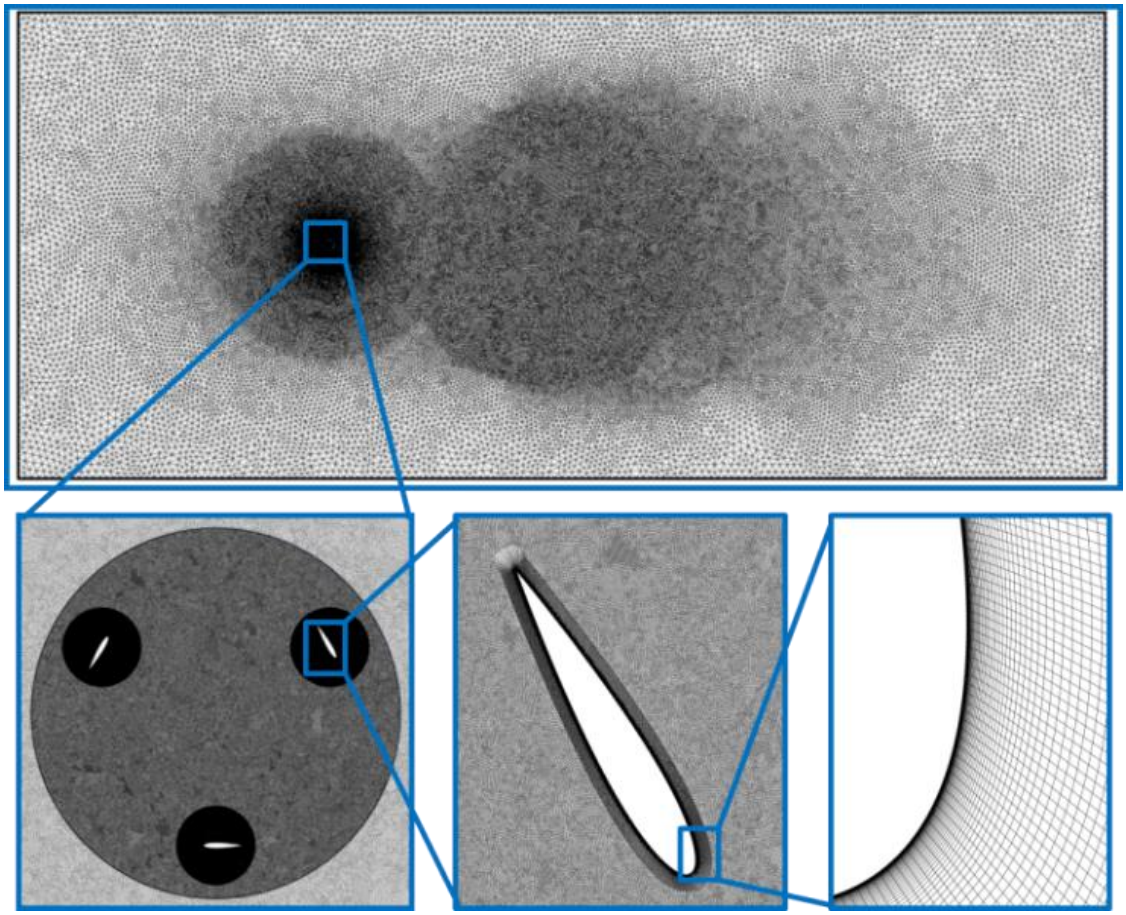

Figure 4-5: Image of Mesh C (see Table 4-6) showing refinement at the near-wall region, including inflation layers at hydrofoil walls.

4.3 Results

4.3.1 Discretisation studies

Fully discretised models in both space and time are developed for both the single hydrofoil and full turbine CFD simulations, ensuring a mesh and time increment independent result is achieved, which provides confidence in the models when validating against physical test data.

4.2.1.1. Hydrofoil model

Various simulations are carried out to determine the required level of mesh refinement to achieve converged solutions for the C_L and C_D. Richardson extrapolation (Roache, 1997), equations (2.46) - (2.49), is used to calculate the exact solution based on the convergence and refinement ratio determined using a series of five increasingly refined meshes. C_L and C_D are determined for each of the five meshes for an α value of 10º and *Re* of 1×10^6. A constant mesh refinement ratio of 1.67 is applied. Equations 2.39 to 2.42 are applied to determine an extrapolated value for C_L and C_D. The results of this study are presented in **Table 4-2**.

Table 4-2. C_L and C_D results for a series of five increasingly refined meshes for α of 10º and *Re* of 1×10^6.

Mesh	Total Elements	C_L	C_D	% C_L	% C_D
M1	9000	0.891	0.0271	10.2	-35.9
M2	25100	0.981	0.0221	1.1	-10.8
M3	70300	0.991	0.0205	0.13	-3.0
M4	195220	0.992	0.0201	0.06	-0.6
M5	544470	0.992	0.0199	0.02	-0.03
Richardson's extrapolation value		**0.992**	**0.02**		

From the spatial discretisation study, it can be concluded that model predictions using M4 and M5 are very similar to each other. **Figure 4-6** shows C_L variation with the normalised mesh size for the five meshes and the final Richardson extrapolation value. M4 results for C_L and C_D are within 1% of the final Richardson's extrapolation value. Spatial discretisation studies were also performed for α = 5º and α = 25º at two Reynolds number Re = 1 x 10^5 and Re = 1 x 10^6. The same mesh, M4, provided the

desired criterion for convergence for each simulation. Based on this analysis, the M4 mesh is used for all subsequent simulations.

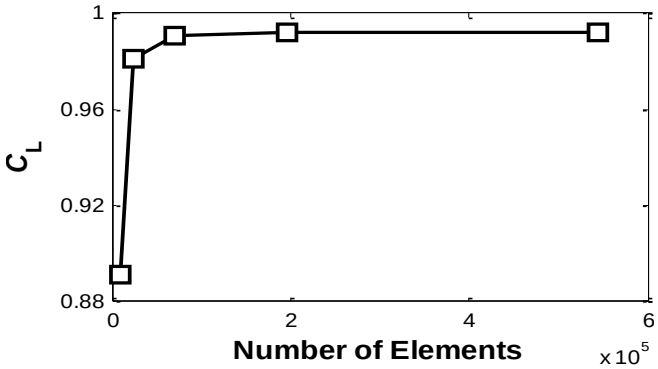

Figure 4-6: Mesh convergence study results for α = 10° and Re = 1×10^6.

Transient simulations are required for all SST Transition turbulence model simulations as this model predicts the transition from laminar to turbulent, which is highly time-dependent. A number of time-steps (Δt) have been investigated (Δt = 0.1 s, Δt = 0.05 s, Δt = 0.01 s, Δt = 0.005 s, Δt = 0.0005 s) to determine the required step size to compute converged solutions for C_L and C_D. This parametric analysis is critical due to the highly transient nature of the flow, particularly at high α. Computed values of C_L and C_D for a range of time steps for three α values, 5°, 15° and 25°, are shown in Table 4-3**,** Table **4-4** and Table 4-5. Different α values require different time steps due to the unsteady nature of the flow under stall conditions. Based on this parametric study the following temporal discretisation is used in subsequent simulations: Δt = 0.05 s for $\alpha \leq 10°$; Δt = 0.01 s for $10° < \alpha \leq 20°$; Δt = 0.005 s for $20° < \alpha \leq 30°$. It should also be noted that for increasing α and decreasing Re the simulations required a longer runtime to reach a converged solution, this is due to the highly unsteady nature of the flow under these circumstances.

Table 4-3. C_L and C_D computed for a range of Δt (α = 5°)

	Re = 1× 10^5		Re = 1× 10^6	
Δt (s)	C_L	C_D	C_L	C_D
0.1	0.611	0.0218	0.561	0.0099
0.05	0.609	0.0217	0.535	0.0092
0.01	0.609	0.0217	0.535	0.0091
0.005	-	-	0.535	0.0091
0.0005	-	-	-	-

Table 4-4. C_L and C_D computed for a range of Δt (α = 15°)

	$Re = 1\times 10^5$		$Re = 1\times 10^6$	
Δt (s)	C_L	C_D	C_L	C_D
0.1	0.669	0.211	1.331	0.0395
0.05	0.675	0.213	1.330	0.0396
0.01	0.677	0.214	1.326	0.0393
0.005	0.677	0.214	1.324	0.0393
0.0005	-	-	1.324	0.0393

Table 4-5. C_L and C_D computed for a range of Δt (α = 25°)

	$Re = 1\times 10^5$		$Re = 1\times 10^6$	
Δt (s)	C_L	C_D	C_L	C_D
0.1	0.994	0.523	1.223	0.652
0.05	0.920	0.495	1.064	0.563
0.01	0.909	0.490	0.930	0.495
0.005	0.905	0.489	0.921	0.490
0.0005	0.905	0.489	0.919	0.489

4.2.1.2. Full turbine model

Four increasingly refined meshes are analysed (details provided in Table 4-6). The number of nodes on blade surfaces and the total number of elements in the inflation layers is consistent with the values used in the hydrofoil spatial discretisation study presented above.

Table 4-6. CFD mesh parameters for spatial discretisation study of vertical-axis turbine.

Mesh	No. Elements Rotating	No. Elements Stationary	Total Elements	No. Nodes on Blade surface	Inflation Layers
A	161065	100317	261382	200	20
B	242916	231660	474576	500	30
C	583015	278645	861660	900	40
D	1169414	415150	1584564	1300	50

Richardson's extrapolation is also applied for the spatial discretisation study of the full turbine. The analysis is performed for *TSR* = 1. Results for the averaged torque coefficient, $\bar{C}_{\mathrm{Q}}$, per cycle for each of the meshes presented in Table 4-7.

Table 4-7. C_Q results for a series of four increasingly refined meshes (*TSR* = 1).

Mesh	$\overline{C_{\mathrm{Q}}}$	$\%\overline{C_{\mathrm{Q}}}$
A	0.007	84.9
B	0.036	23.5
C	0.046	0.05
D	0.047	-0.93
Richardson's extrapolation value		0.046

Figure 4-7 presents the finalised averaged torque coefficient against the normalised mesh size for *TSR* = 1. Mesh C and D are both within 1% of the final extrapolated value. Due to the lower computational resource requirement of running simulations using Mesh C, this is chosen as the mesh for all following simulations.

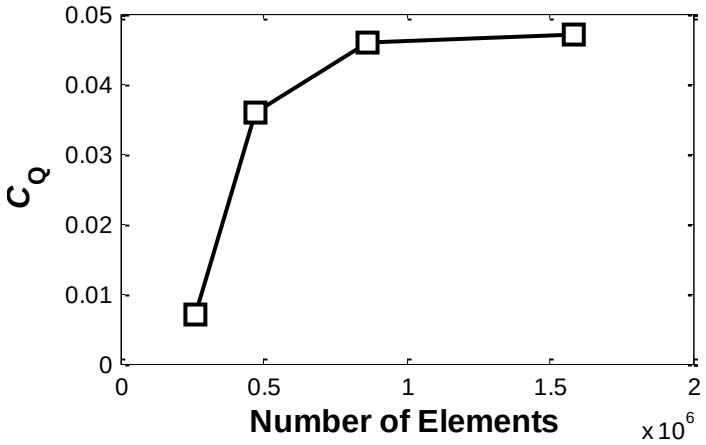

Figure 4-7: Mesh convergence study results for full turbine CFD model (*TSR* = 1).

A temporal discretisation study is carried out for the full turbine CFD model for *TSR* of 1 and 2.5. The study focuses on establishing the most efficient time step size and determining the number of rotations required to achieve the convergence criterion for the average torque coefficient, $\bar{C}_{\mathrm{Q}}$. Table 4-8 and Table 4-9 present results for different time step increments based on the size of each degree increment per time step. To achieve the desired accuracy, a time step increment equivalent to $\Delta\ 0.5^{\mathrm{o}}$ is selected for

TSR $\leq$ 1.5. For *TSR* > 1.5, a time step increment equivalent to Δ 1^o is selected based on the results presented in Table 4-9 for *TSR* = 2.5. A more refined time step is required at lower *TSR* due to complex flow phenomenon that occur at these low speeds relating to the dynamic stall of the turbine.

Table 4-8. C_Q results for a range of Δ^o/step (*TSR* = 1).

Δ^o/step	$\overline{C_Q}$
2^o	0.033
1^o	0.039
0.5^o	0.045
0.25^o	0.046

Table 4-9. C_Q results for a range of Δ^o/step (*TSR* = 2.5).

Δ^o/step	$\overline{C_Q}$
2^o	0.1123
1^o	0.1264
0.5^o	0.1265
0.25^o	-

Figure 4-8 presents the convergence history for a *TSR* = 1. Following 28 rotations, a steady-state solution has been achieved with a convergence factor of 0.05%. The rate of convergence is slower for higher *TSR*; for example, a *TSR* of 2.5 reaches a convergence factor of 0.3% following 28 rotations.

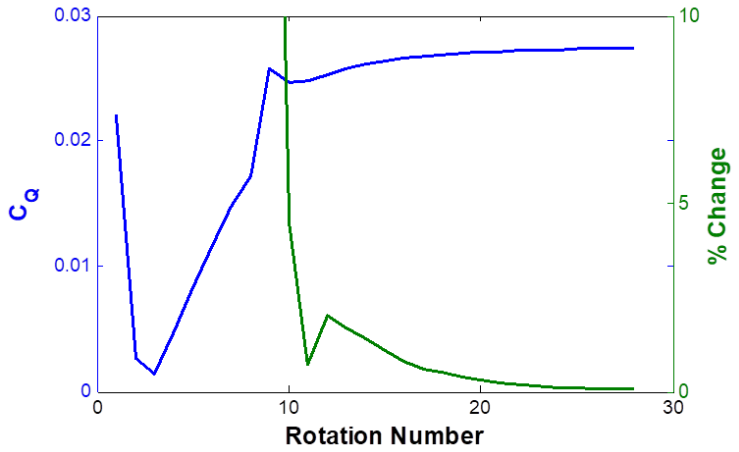

Figure 4-8: Evolution of the average torque coefficient as a function of the number of turbine rotations leading to steady-state solutions (*TSR* = 1). Convergence factor (% change in C_Q from previous rotation) also indicated.

4.3.2 Hydrofoil Lift and Drag Coefficients

Computed values of C_L and C_D from the CFD analyses are compared here to experimental data. The experimental study of Jacobs (1937) reports values of C_L and

C_D for the NACA0015 profile for α between 0° and 24° and a wide range of *Re*. Sheldhal and Klimas (1981) performed experiments for a wide range of α between 0° and 180° over a narrow spread of Re (3.6×10^5, 5×10^5 and 6.7×10^5).

For direct comparison with available experimental data, CFD results are computed for $Re = 8.8 \times 10^4$, 5×10^5 and 1.27×10^6, as shown in **Figure 4-9**. In terms of C_L the CFD model generally achieves close correlation with the experimentally measured maximum value of C_L and the corresponding value of α for all three values of *Re*. The CFD model correctly predicts the onset of stall and is far more accurate than the panel method data. The model also correctly predicts the critical stall region following maximum C_L. The capability of the CFD model to compute the laminar to turbulent transition is critical for such accurate predictions of the complex relationship between C_L, α, and Re. There is a reduced amount of data available for the coefficient of drag, C_D, however, for the data available accurate predictions are achieved by the CFD model. Simulations exhibit a strong dependence of C_L and C_D on *Re* in the stall region. At low α (< 7°) and high α (> 27°) C_L and C_D do not exhibit a significant dependence on Re. This is consistent with experimental measurement; Sheldahl and Klimas (1981) report that C_L and C_D are independent of Re for α > 30°.

Figure 4-10 shows the pressure coefficient, C_p, distribution variation along the chord length of upper and lower surfaces of the hydrofoil profile. The CFD results are validated against published experimental results (Miller, 2008) for a constant *Re* of 2.3×10^5 and α values of 5°, 10° and 15°. The CFD model generally provides an accurate prediction of the experimental data, further validating the modelling approach.

Discrepancies are observed between the CFD model predictions and experimental data for angles of attack in the post-stall region due to the unsteadiness of the flow. The lift and drag coefficients fluctuate, and the CFD results presented in **Figure 4-9** are the mean of these fluctuations. These discrepancies are also evident in the results presented in **Figure 4-10** (c). For a larger angle of attack, α = 15°, there is an increased error in the model predictions, which can be attributed to the unsteadiness of the flow.

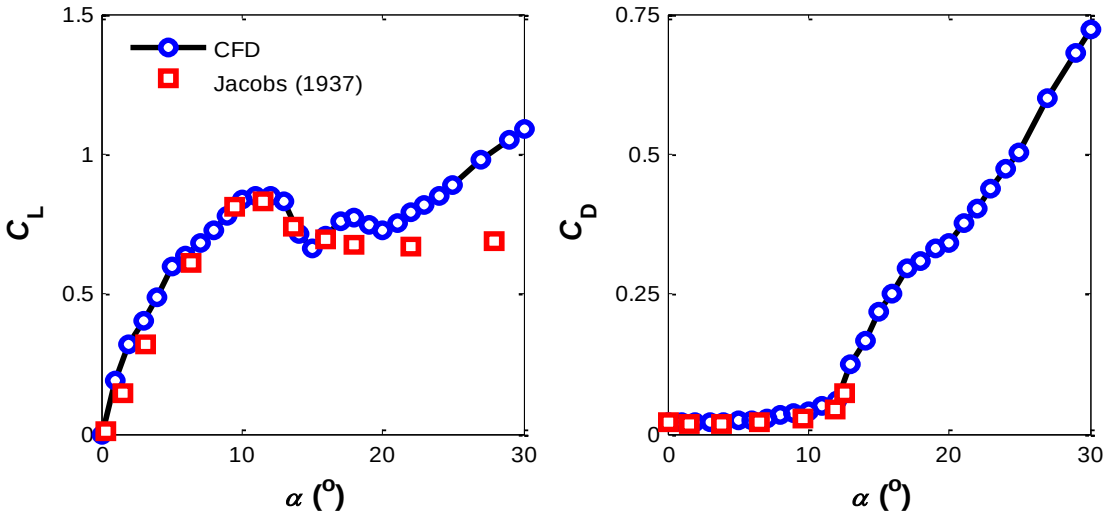

(a) $Re = 8.4 \times 10^4$

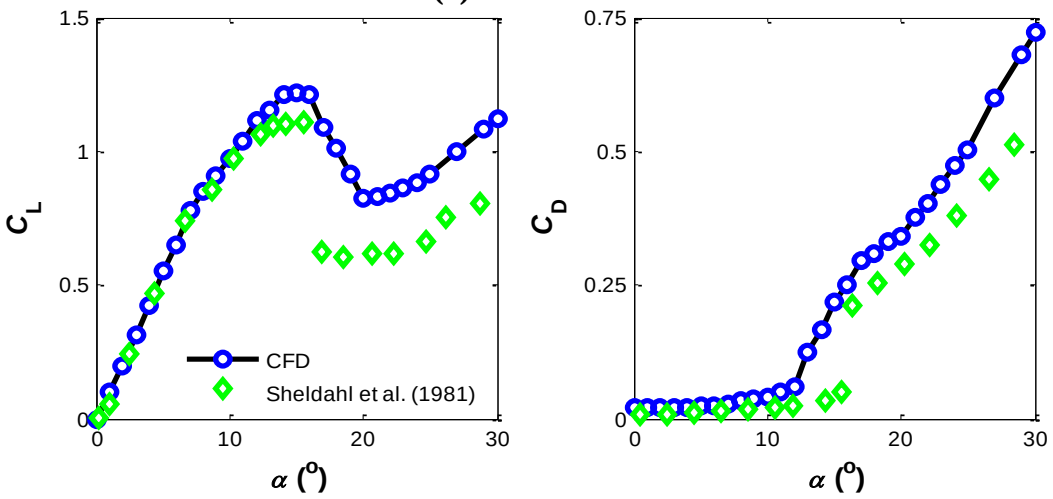

(b) $Re = 5 \times 10^5$

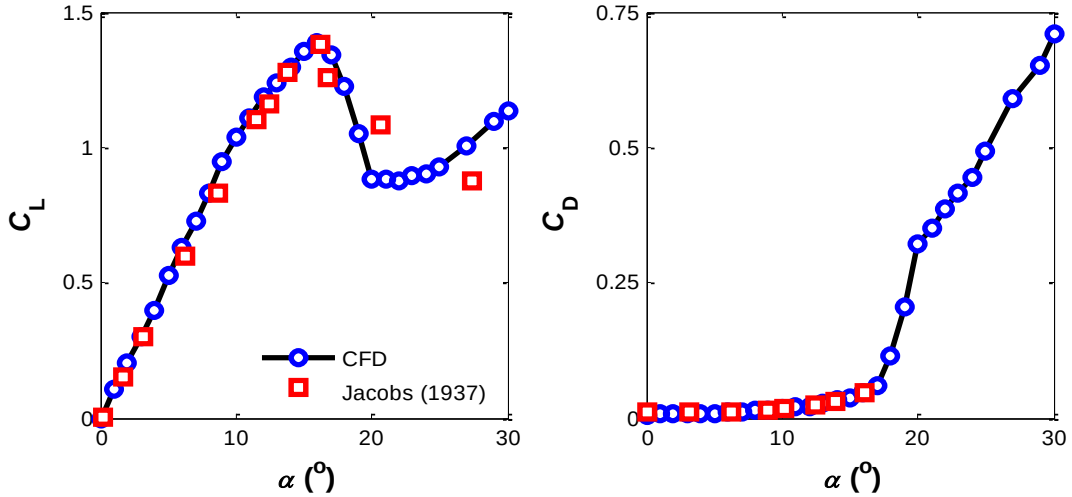

(c) $Re = 1.27 \times 10^6$

Figure 4-9: CFD computed C_L and C_D for NACA0015 hydrofoil for a range of α. Results are compared to available experimental data for three values of Re: **(a)** 8.4×10^4; **(b)** 5×10^5; **(c)** 1.27×10^6.

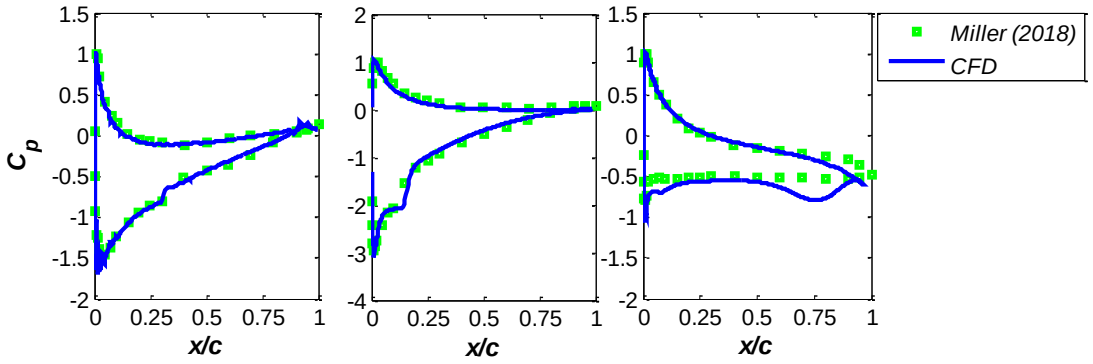

Figure 4-10: Pressure coefficient distributions at hydrofoil surfaces for three values of α: **(a)** 5°; **(b)** 10°; **(c)** 15°. $Re = 2 \times 10^5$ for all cases. Results are compared to published experimental data.

A steady-state C_L or C_D is not achieved for α in the stall and post-stall region due to the unsteady nature of the flow under these conditions, as reflected in the results presented in **Figure 4-11** for $Re = 5 \times 10^5$. For $\alpha = 5^o$ the flow is steady, and this is reflected in the constant values of C_L and C_D achieved. As α increases, the magnitude of the fluctuations of C_L and C_D increases. The period of time for the fluctuations also increases with increasing angle of attack.

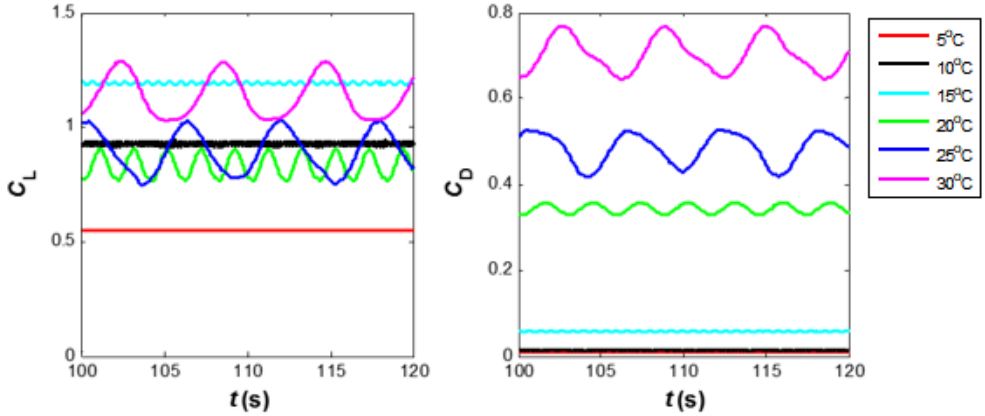

Figure 4-11: Variation of lift and drag coefficients as a function of time for different angles of attack once a periodic nature has been observed (Re = 5×10^5).

The following images detail some of the flow phenomena experienced by the hydrofoil at different angles of attack. **Figure 4-12** is a velocity streamline contour and streamline plot for $\alpha = 2^o$, $Re = 5 \times 10^5$. At this low angle of attack, there is very little to no flow separation. This highlights the rationale behind the high level of accuracy at low angles of attack between the CFD data, panel method data and experimental results comparisons shown in **Figure 4-9**.

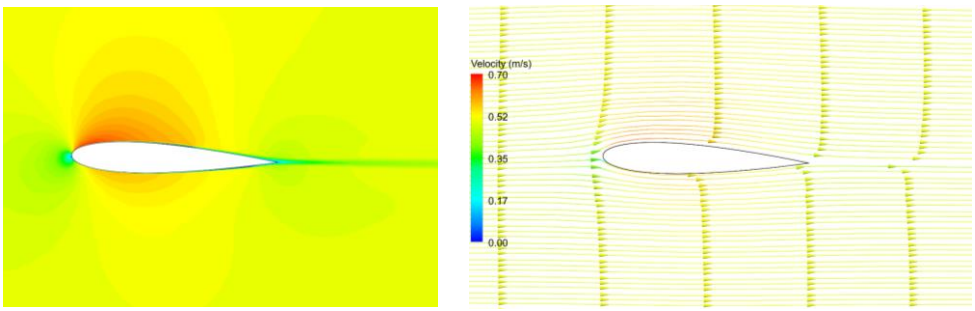

Figure 4-12: A plot of velocity contours and streamlines for $\alpha = 2^o$ ($Re = 5 \times 10^5$).

Figure 4-13 shows a velocity contour and streamline plot for $\alpha = 15^o$, $Re = 5 \times 10^5$. In the velocity contour plot, at the highlighted upper surface of the leading edge, the laminar separation bubble is beginning to form. This demonstrates the beginning of the onset of stall (see also **Figure 4-9 (b)**), where the lift coefficient drops significantly for the angles of attack slightly greater than 15º.

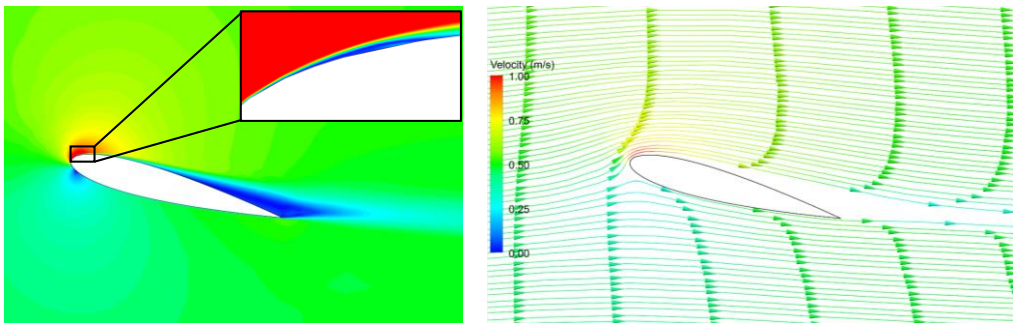

Figure 4-13: A plot of velocity contours and streamlines for $\alpha = 14^o$ ($Re = 5 \times 10^5$) highlighted the beginning of the onset of stall.

Figure 4-14 shows the velocity contours and streamlines for $\alpha = 30^o$, $Re = 5 \times 10^5$. At this angle of attack, the hydrofoil is in deep stall, and the nature of the flow is highly unsteady, as is shown in the lift and drag coefficient predictions in **Figure 4-11**. This unsteadiness in the flow is also reflected in the difference between the two sets of plots presented. In **Figure 4-14 (a)**, at time = 106.5 s, the hydrofoil experiences an instantaneous lift coefficient of 1.03, while in **Figure 4-14 (b)**, at time = 108.5 s, the instantaneous lift coefficient is 1.21. As evident in **Figure 4-14 (a)**, the recirculating flow contributes to reducing the overall lift coefficient on the hydrofoil, while when the flow remains detached, as shown in **Figure 4-14 (b)**, a greater maximum lift coefficient is achieved. These results also demonstrate the capability of the SST Transition model to simulate flow separation and reattachment at high values of α.

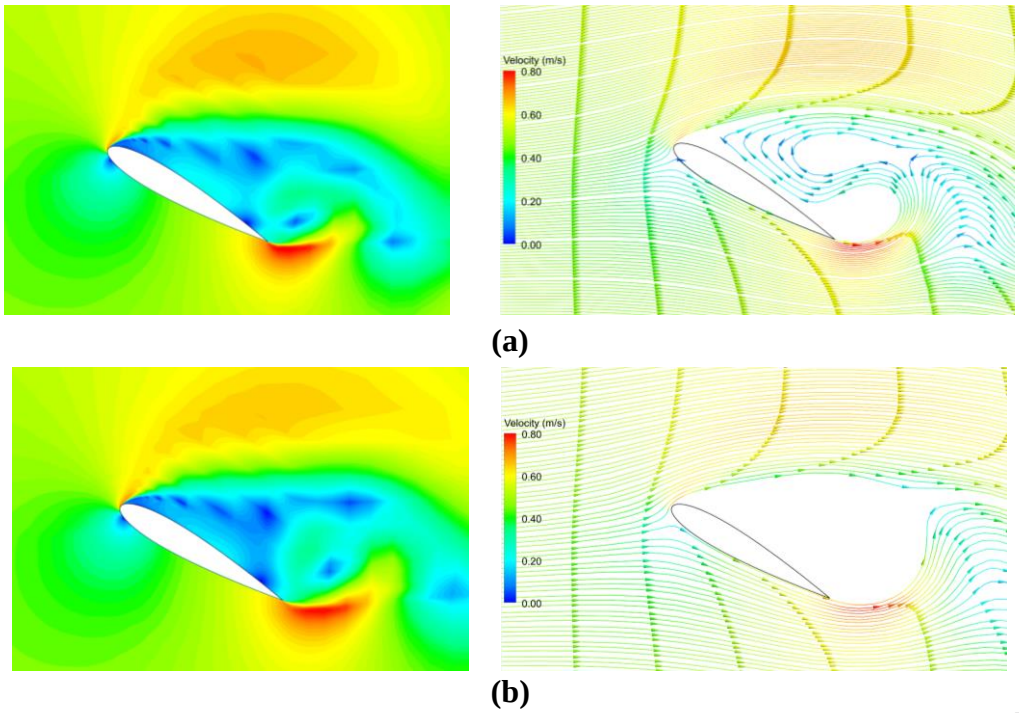

Figure 4-14: Plots of velocity contours and streamlines for α = 30° ($Re = 5 \times 10^5$) **(a)** Minimum lift (time = 106.5 s) and **(b)** Maximum lift (time = 108.5 s).

4.3.3 Turbine Analysis

4.3.3.1 Straight-bladed vertical-axis turbine analysis

A comprehensive dataset for the dependence of C_L and C_D on *Re*, shown in **Figure 4-15**, is generated using the validated SST Transition CFD modelling approach. Simulations were performed for a range of α from 0° to 30° and a range of *Re* from 8.4 × 10^4 to 2 × 10^6, with the critical stall region being identified for each case. The results exhibit the strong dependence of C_L and C_D on Re in this stall region. At low α (< 7°) and high α (> 27°) C_L and C_D do not exhibit a significant dependence on Re. This is consistent with experimental measurement; Sheldahl and Klimas (1981) report that C_L and C_D are independent of *Re* for α > 30°.

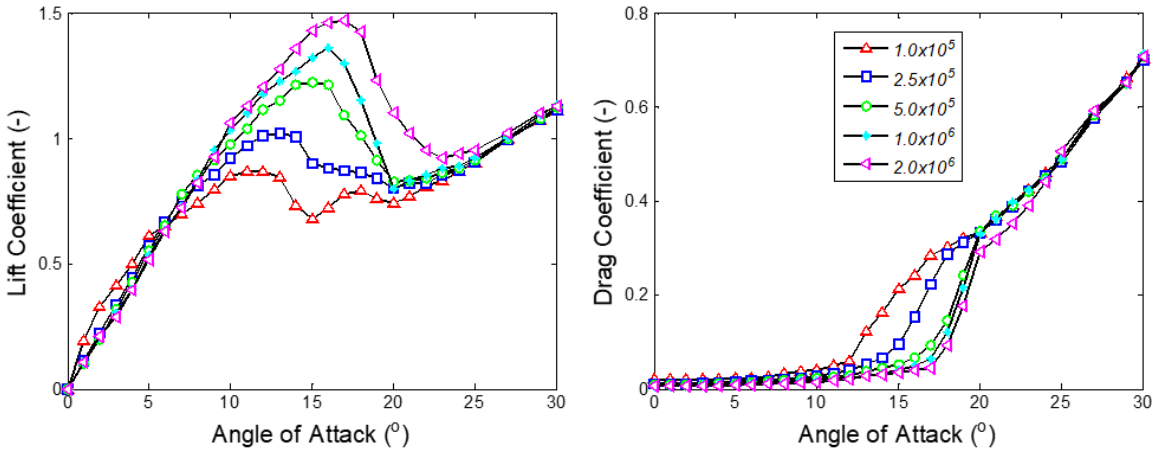

(a) **(b)**

Figure 4-15: CFD dataset showing **(a)** C_L and **(b)** C_D as a function of α for a range of *Re*.

In **Chapter 3**, a blade element momentum code is presented to analyse the power performance of the novel vertical-axis turbine. For the results presented in that Chapter, the panel method dataset (Sheldahl and Klimas, 1981) was used as input into the BEM code. For the results presented in this chapter, this panel method dataset is replaced by the CFD dataset shown in Figure 4-15.

The power performance of the present turbine is assessed by establishing $\bar{C}_P$ over a range of *TSR*. $\bar{C}_P$ and *TSR* (equations 3.1 & 3.2) are dimensionless parameters that readily facilitate comparison of the hydrodynamic performance of different turbine designs under a range of flow conditions. **Figure 4-16** presents a comparison between three sets of model results against experimental data (McLaren, 2011) for a straight-bladed vertical-axis turbine (Table 4-1). While the experimental tests were carried out with a blockage ratio of 3%, testing protocols published by (Bahaj et al., 2008) state that experimental results for tidal current turbines do not require correction when the blockage ratio is below 5%.

Two sets of BEM results are included; one which incorporates the panel method dataset (Sheldahl and Klimas, 1981) and the other, which incorporates the newly developed CFD dataset. A double interpolation, for both α and Re, is carried out within the code. Also included in **Figure 4-16** are results for the full two-dimensional CFD studies of the vertical-axis turbine. Results are compared to wind tunnel experimental data for an identical straight bladed turbine (Table 4-1). Experimental

operational Re values are identical to model values and the low experimental Mach numbers (< 0.3) justify the model assumption of fluid incompressibility.

All the results follow the expected trend of turbine power curves, with poor power performance at low *TSR* followed by a sharp increase to an optimal *TSR* for maximum power performance, before a gradual decrease in power performance at higher *TSR*. Root-mean-squares errors (RMSEs) between experimental data and model predictions shown in Table 4-10 suggest that both the CFD-based BEM model and the full CFD turbine model provide a significantly higher level of accuracy than the PM-based BEM model. The best agreement is obtained between experimental and CFD-based BEM results. For 1.5 >*TSR* > 2.25, the peak power range, the model predictions are within the experimentally observed range.

A very similar level of accuracy to the CFD-based BEM is achieved by the full CFD model, with both models predicting the maximum $\bar{C}_P$ of 0.35 at *TSR* = 2, and both sets of results following similar trends at lower and higher *TSR*. The advantage of the CFD-based BEM model over the full CFD model lies in the dramatically decreased computational cost. The results presented in **Figure 4-16** indicate that the assumptions of blade element momentum theory, coupled with an accurate set of lift and drag coefficients, can provide the same level of accuracy to a full CFD-RANS model. The once-off computational cost of generating a CFD-based hydrofoil data set for the required range of α and Re is 18600 CPU hours. Once generated, a turbine design can be accurately simulated in under 30 seconds on a single CPU. In contrast, an analysis of a single turbine design using the full CFD modelling approach requires 32640 CPU hours. The CFD-based BEM method, therefore, offers a computationally viable approach for the design and optimisation of vertical axis turbines with significant improvements in predictions over the traditional panel method based BEM.

Table 4-10. Goodness of fit of various turbine models with experimental test data (McLaren, 2011).

Comparison	**RMSE**
CFD-based BEM	0.0033
Full 2D CFD	0.0040
PM-based BEM	0.0070

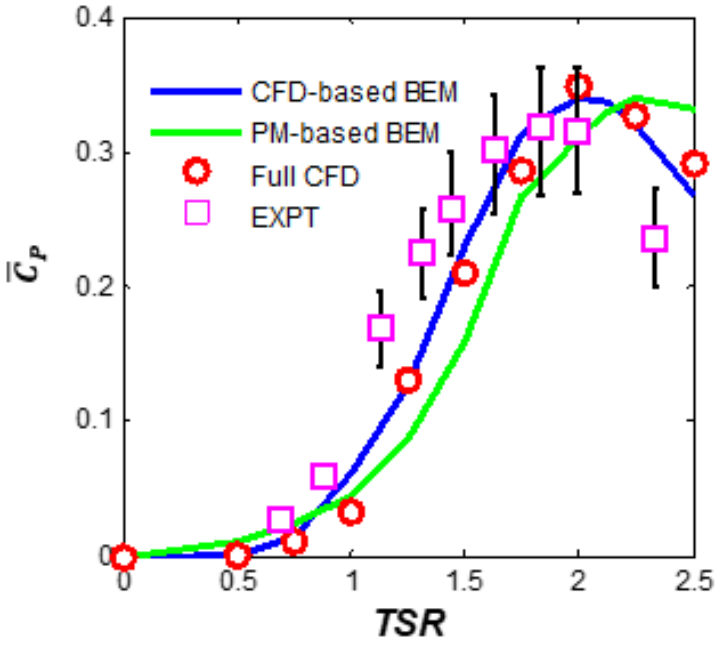

Figure 4-16: Comparison between CFD-based BEM model, Panel Method- (PM-) based BEM model and full CFD model predictions with published experimental results (McLaren, 2011) for a straight-bladed vertical axis turbine (Table 4-1).

Table 4-11. The computational cost of both methodologies

Method	**Time (hrs)**	**No. Processors**	**Total CPU (hrs)**
CFD-generated hydrofoil dataset	775	24	18600
Full 2D CFD model	680	48	32640

One significant benefit that CFD models have over BEM models is the ability to display results visually. These plots allow the reader a clearer insight into the flow through the turbine. **Figure 4-17** shows the variation of vorticity with different blade orientations for a straight-bladed vertical-axis turbine operating at its optimal *TSR* of 2. It can be noted that the magnitude of the flow field vorticity around the hydrofoil is low for azimuthal angles between 0 and 90^o. There is a significant increase in the vorticity as the blade reaches an azimuthal angle of 120^o, followed by the shedding of vortices seen for azimuthal angles between 150 and 210^o.

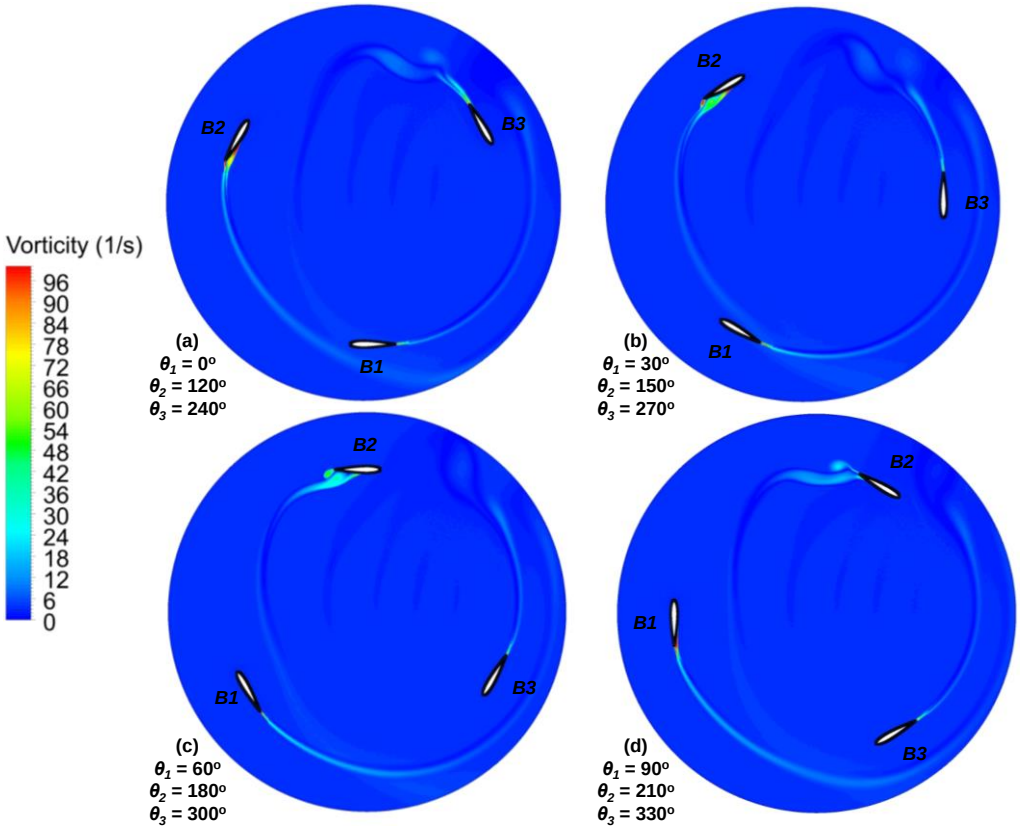

Figure 4-17: The magnitude of the flow vorticity for a straight-bladed vertical-axis turbine (Table 4-1) operating at *TSR* = 2 for four varying blade orientations **(a)** - **(d)** with the freestream flow from left to right in each case.

Another advantage of the full CFD model over the CFD-based BEM approach lies in the ability to visualise and map the flow patterns downstream of the turbine. This information is critical in the context of the design of multi-row array turbines.

4.3.3.2 Novel vertical-axis turbine analysis

Finally, the CFD-based BEM approach is used to analyse the two optimised Brí Toinne Teoranta turbine designs described in Chapter 3. The turbine parameters and fluid conditions are listed in **Table 4-12**. **Figure 4-18** and **Figure 4-19** show the power performance prediction curves of these turbines when implementing the two sets of hydrodynamic coefficients; CFD-based and the traditional panel method dataset. The maximum power coefficient for each result is the same; however, the CFD-based dataset predicts that the maximum power coefficient for the ellipsoidal design will occur at a *TSR* of 4.5 compared to 5.5 for the panel method dataset, while the CFD-based dataset predicts that the maximum power coefficient for the ellipsoidal design

will occur at a *TSR* of 3 compared to 3.5. There are also significant variations in power predictions between the two methods at lower and higher *TSR*.

Table 4-12: Key parameters and turbine features for BEM rotor simulations.

Fluid conditions: Seawater at 5 ºC		
Density	1025 kg m^{-3}	
Viscosity	0.00162 Ns m^{-2}	
Velocity	1.5 m s^{-1}	
Turbine Features	**BTT-Ellipsoidal**	**BTT-Cylindrical**
Chord	0.3 m	0.3 m
Number of blades	3	3
Diameter	2	2
Height	2	2
Blade profile	NACA0015	NACA0015
Blade design	Ellipsoidal	Cylindrical

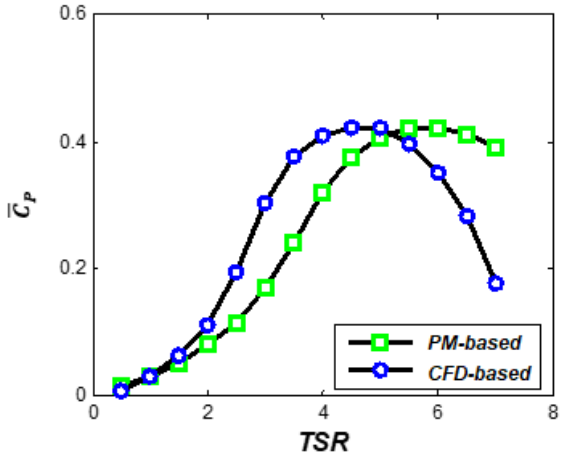

Figure 4-18: Variation of power coefficient with *TSR* for the novel Ellipsoidal Brí Toinne Teoranta vertical-axis turbine design (BTT-Ellipsoidal).

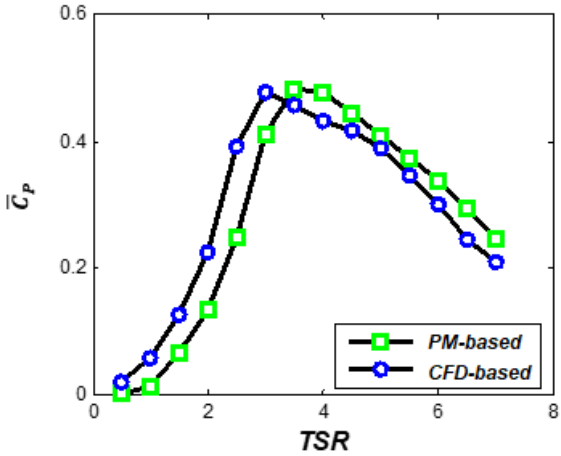

Figure 4-19: Variation of power coefficient with *TSR* for the novel cylindrical Brí Toinne Teoranta vertical-axis turbine design (BTT-Cylindrical).

The variation of the instantaneous torque with azimuthal angle for the novel turbine design is shown in **Figure 4-20**. Three different *TSR* are examined, and results from the BEM code incorporating both the panel method data and the newly developed CFD-based dataset are compared. The CFD-based BEM model has proven to be a more accurate method for analysing alternative turbine designs (**Figure 4-16**). The instantaneous torque loads presented are directly proportional to the structural loads experienced by the turbine, so a failure to accurately predict these loads could have significant effects not only on the power performance but also on the structural integrity and safety of the turbine. We can see that the most significant error occurs in **Figure 4-20 (a)** (*TSR* = 2), which coincides with the operational conditions when the turbine is experiencing its most extensive range of α and Re.

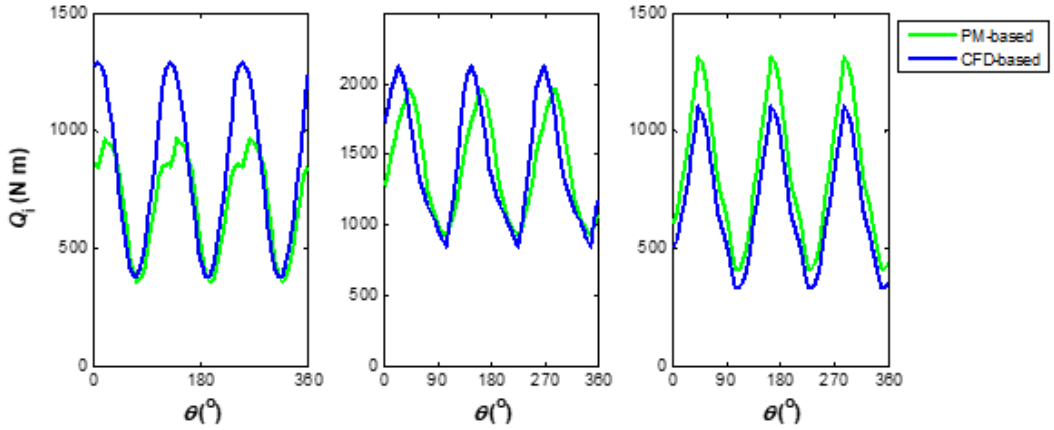

(a) *TSR*= 2 **(b)** *TSR*= 4 **(c)** *TSR*= 6

Figure 4-20: Variation of instantaneous torque with blade position for the spherical novel vertical-axis turbine design (Turbine A). Comparison between CFD-based BEM and PM-based BEM results for (a) *TSR* = 2, (b) *TSR* = 4 and (c) *TSR* = 6.

4.3.4 Turbine Start-up Analysis

The self-start-up capability of vertical-axis turbine is a key design consideration that is influenced by the starting blade position, turbine design, resistive loads and flow conditions. Dominy et al. (2007) noted the significant importance of such capabilities for small to medium-scale low-cost turbines. Turbine designs at this scale with the ability to self-start have reduced operation complexity, with no need for a separate active detection/start-up system. Significant cost and control systems if such turbines require external assistance is required to effect start-up.

Worasinchal et al. (2015) defined a turbine to have the ability to self-start if:

"The turbine can accelerate from rest to the tip speed ratio where thrust is continuously generated over the Darrieus flight path. Its final operating tip speed ratio will be an equilibrium point where aerodynamic and resistive torques match."

Nguyen et al. (2015) assessed the self-starting capabilities of four symmetrical blade profiles on a vertical-axis turbine and concluded that the NACA 0012 had the lowest self-starting capability while the NACA 0021 had the highest likelihood of self-starting. However, as shown in **Figure 3-21**, blade profiles with a greater maximum thickness reduce the power output available from the turbine. Alternative methods to improve self-starting capabilities include the introduction of a blade pitch control system (Chougule et al., 2013; Zhang et al., 2012) or a small drag-based Savonius rotor (Wakui et al., 2005). However, both these options add cost and complexity to the overall turbine design.

In this section, the optimised Brí Toinne Teoranta cylindrical turbine design is compared with an equivalent sized straight-bladed design in terms of start-up capability. Both turbines consist of three blades, have the same dimensions (height, diameter chord length and blade profile), and are analysed when operating in the same freestream conditions. A model of vertical-axis turbine start-up performance is developed within MATLAB®, and the code included in **Appendix C.**

The equation which governs the start-up ability of a turbine is:

$$I\frac{d\omega}{dt} = M \tag{4.9}$$

where I is the moment of inertia, $\frac{d\omega}{dt}$ is the rate of change in the angular velocity (i.e. angular acceleration) of the turbine, and M is the net torque applied to the turbine. A turbine with a smaller moment of inertia will reach its desired operating speed more quickly. The net torque is the difference between the torque acting on the blades from the water and the torque applied by the generator, and other additional losses. When $M = 0$, the hydrodynamic and electric load are balanced, and the turbine will rotate at a constant rotational speed.

Expanding equation (4.9) above:

$$\ddot{\omega} = \frac{d\omega}{dt} = \frac{Q_B - Q_{res}}{I} \tag{4.10}$$

where $\ddot{\omega}$ is the angular acceleration of the turbine blades, Q_B is the torque acting on the blades from the water, and Q_{res} is the resistive torque. Q_B is calculated by blade element theory, with the RANS-derived dataset of lift and drag coefficients, from **Section 4.3.2 Hydrofoil Lift and Drag Coefficients** used as input into these calculations. The model developed incorporates the dynamic stall approach detailed in **Section 3.3.2 Dynamic Stall Model**. Frictional (Q_f), electromagnetic (Q_e), and cogging torque (Q_{cog}) all contribute to the resistive torque of a turbine.

From equation (4.10), and with a defined time interval, Δt, a new rotational velocity and change of angle, $\Delta\theta$, are calculated from:

$$\omega = \omega_0 + \alpha\Delta t \tag{4.11}$$

$$\Delta\theta = \omega_0 t + 0.5\alpha t^2 \tag{4.12}$$

where ω_0 is the rotational velocity from the previous timestep. A small time increment of Δt =0.005 s is implemented. It was determined that reducing this time increment further had no effect on the start-up predictions, so this time increment was chosen to minimise computation time whilst ensuring an accurate result is achieved.

The start-up ability of the two turbine designs is examined for four initial blade orientation, as shown in **Figure 4-21** and **Figure 4-22**, with variations of the rotational velocity as a function of time during turbine start-up presented in **Figure 4-23** and **Figure 4-24** for the straight-bladed and BTT turbines, respectively.

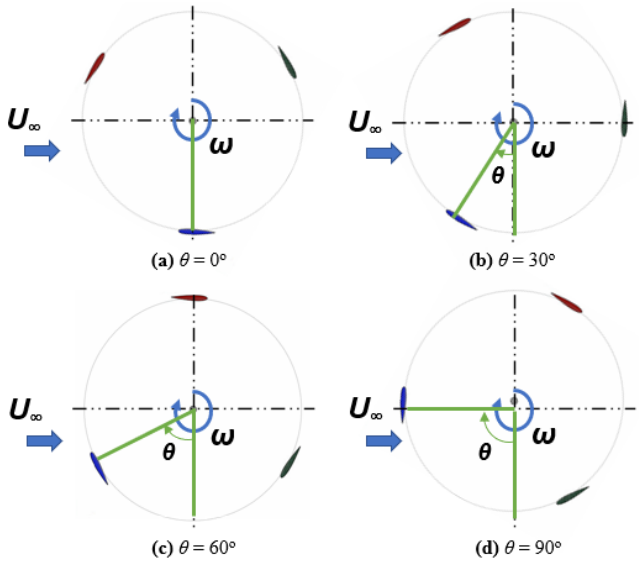

Figure 4-21: Starting blade positions for configuration

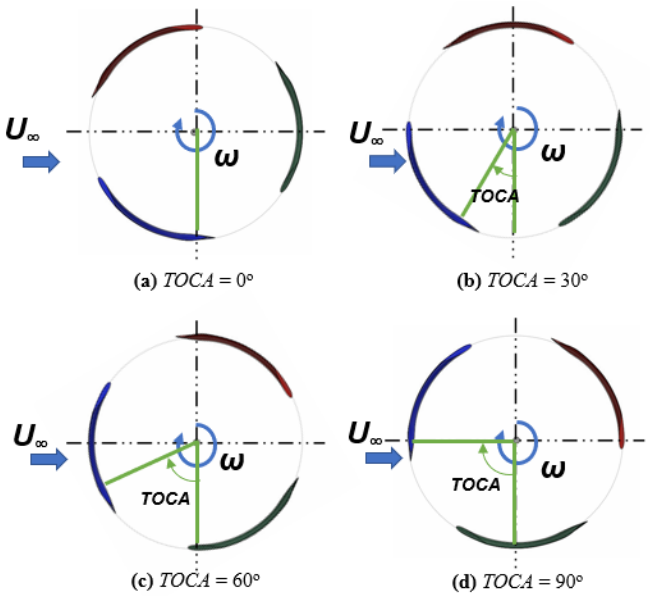

Figure 4-22: Starting blade positions for BTT design.

The analysis is performed initially with no resistive torque applied. As shown in **Figure 4-23**, the straight-bladed design fails to self-start on for three orientation (θ_{B1} = 30º, 60º, 90º). Only for an orientation of θ_{B1} = 0º is the straight-bladed turbine computed to self-start. In contrast, the BTT cylindrical design successfully starts at all four simulated orientations, highlighted in **Figure 4-24**.

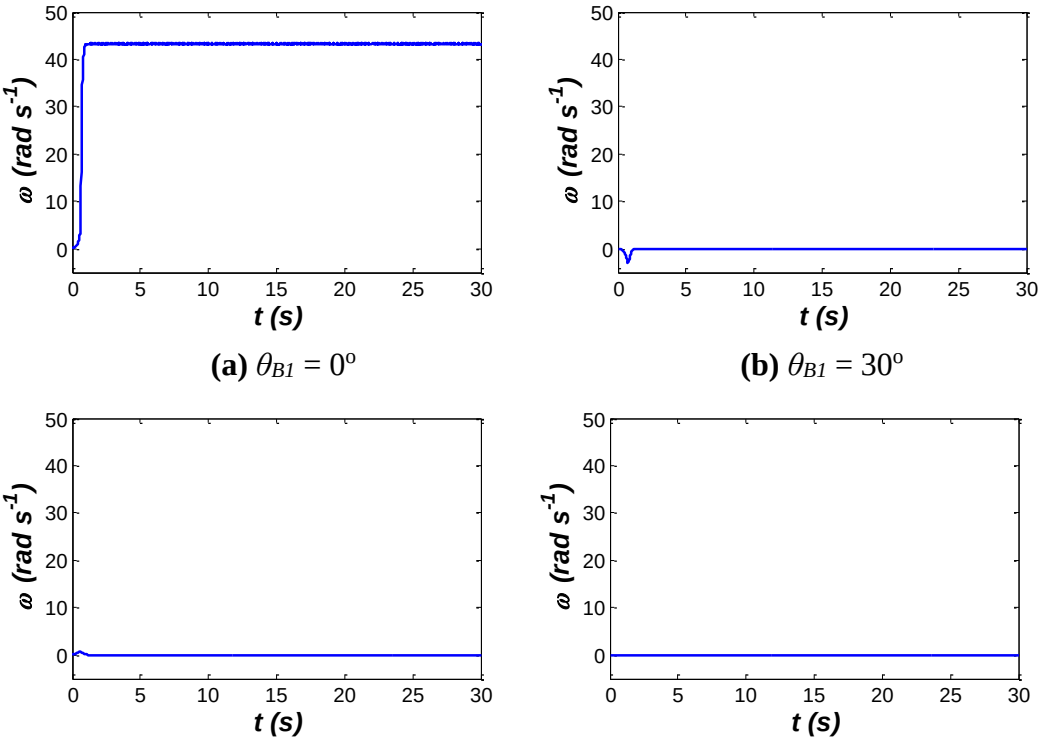

(a) θ_{B1} = 0º **(b)** θ_{B1} = 30º

(c) θ_{B1} = 60º **(d)** θ_{B1} = 90º

Figure 4-23: Rotational velocity variation with time at start-up for a straight-bladed vertical-axis turbine at four different initial turbine orientations (U_∞ = 1 m s^{-1}).

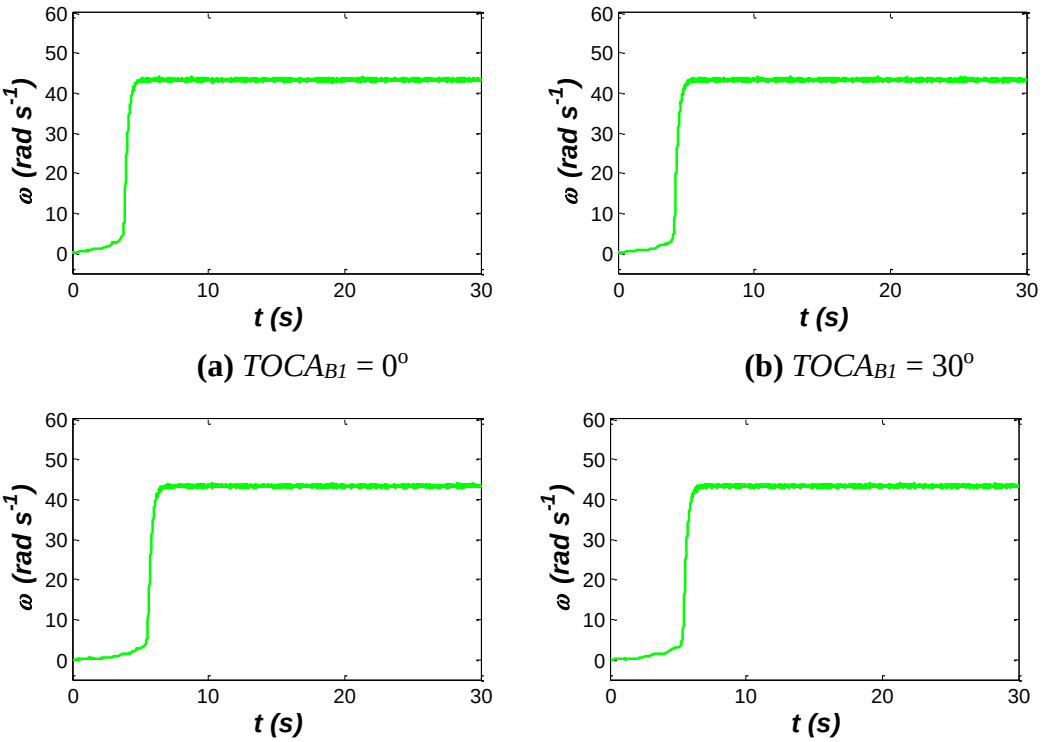

Figure 4-24: Rotational velocity variation with time at start-up for the BTT cylindrical vertical-axis turbine design at four different initial turbine orientations (U_∞ = 2 m s^{-1}).

A more comprehensive range of blade starting positions for both turbines is examined in **Figure 4-25**. The results presented demonstrate that the straight blade turbine self-starts only if one of the blades are initially in the position $0^o \leq \theta < 20^o$ or $105^o \leq \theta < 115^o$. In contrast, the BTT is computed to self-start for all starting blade orientations.

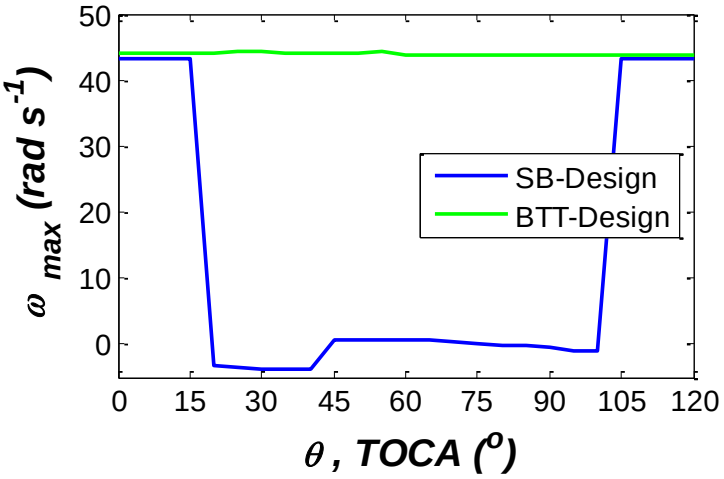

Figure 4-25: Comparison of the maximum angular velocity achieved by both turbine designs based on initial blade 1 starting position (θ, TOCA).

From the BEM analysis performed on the BTT design, the optimal *TSR* for peak power coefficient was determined as 3 (**Figure 4-19**). **Figure 4-26** presents a simulation of the self-starting performance of the BTT turbine when a variable resistance generator including a control system that ensures constant *TSR* operation, with the resistive torque equal to the total blade torque, i.e. $Q_f+Q_e+Q_{cog}= Q_B$. Permanent magnet synchronous generators are often selected for turbine application due to their low-speed operation and low maintenance cost, as a gearbox is not typically required (Chung and You, 2015). This type of generators do experience issues with cogging torque, which caused by the interaction between the rotor's permanent magnets and stator slots. Cogging torque is present under no-load conditions and must be overcome for the turbine to self-start. A value of 0.6 N m is assumed for the maximum cogging torque in these calculations, based on other analysis of a similar-sized generator (Berges, 2007). **Figure 4-26 (a)** and **(b)** shows the computed evolution of angular velocity and *TSR* during the self-starting stage of turbine operation. The optimal TSR is achieved in under four seconds. The computed instantaneous power output at this *TSR* is shown in **Figure 4-26 (c).** As expected, optimal power output is achieved when the optimal TSR is reached. **Figure 4-26 (d)** shows that although the angle of attack of the mid-plane of Blade 1 exhibits large fluctuations during start-up, a steady-state range is quickly achieved such that power output is optimised. Similar variations in the angle of attack are computed for all sections of the three blades during start-up and steady-state conditions.

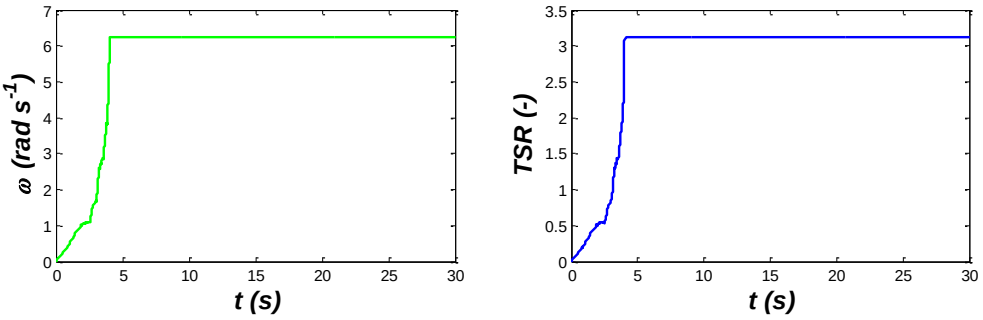

(a) **(b)**

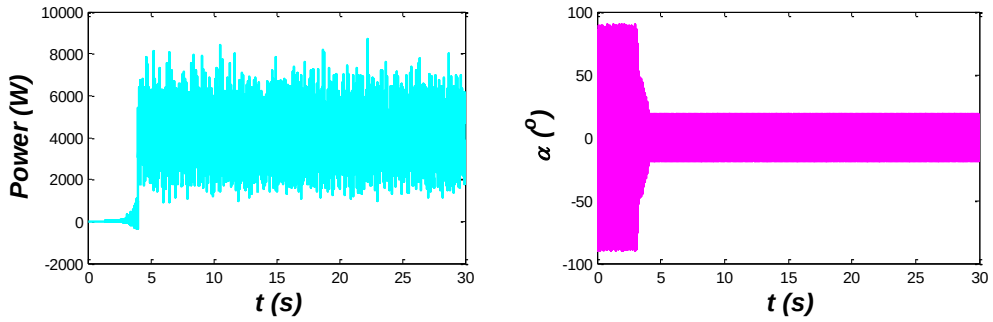

(c) **(d)**

Figure 4-26: Simulated start-up of the BTT with resistive loads included. **(a)** Variation of angular velocity with time; **(b)** Variation of TSR with time; **(c)** Variation of instantaneous power with time; **(d)** Variation of the angle of attack with time for Blade 1 at the blade mid-height section.

The spiralling geometrical features of the BTT design ensure that sufficient portions of the turbine blade will be favourably positioned such that the required torque is generated to effect self-starting of the turbine. The reliable and robust start-up capability computed for the BTT turbine presents a significant advantage over traditional straight bladed turbines. A complex start-up system will not be required for the BTT turbine, thereby reducing the cost of manufacture, operation and maintenance.

4.4 Conclusions

The development of a new BEM-CFD method is presented for hydrodynamic assessment and preliminary design investigation of the Brí Toinne Teoranta tidal turbine. The method uses a database of CFD lift and drag coefficient data for a range of angles of attack and Reynolds numbers to replace experimental or panel method data as input to the BEM code, which to the author's knowledge has never been done before. Accurate lift and drag coefficient data are critical for BEM modelling of vertical axis turbines, particularly for spiral geometrical turbines, which is the focus of this research. Such intricate turbine designs experience significant variations of angles of attack and Reynolds numbers under standard operational conditions.

Using the example of a NACA0015 hydrofoil, this study demonstrates that an SST Transitional turbulence URANS modelling approach can accurately determine the lift and drag coefficients across a wide range of Reynolds numbers and angles of attack required for vertical axis turbine analysis. Previous SST Transition analyses of aerofoils have considered only a limited range of Reynolds number and angle of

attack. The ability of the modelling approach to capture flow transition from laminar to turbulent is essential in generating accurate data, particularly in the stall region. In contrast, the widely used panel method data (Sheldahl and Klimas, 1981) does not accurately represent the relationship between the coefficient of lift and angle of attack for low Reynolds numbers.

It is demonstrated that the BEM model developed in **Chapter 3** provides improved predictions of vertical axis turbine performance when RANS generated lift and drag coefficients are used as input, rather than coefficients generated by the widely used panel-method. It has been shown that a BEM model which implements a RANS generated hydrofoil dataset achieves a similar level of accuracy to a full CFD turbine model but at a significantly lower computational cost. The computational efficiency of RANS CFD analysis of hydrofoils combined with the BEM modelling of turbine performance provides an efficient design platform for the development of the Brí Toinne Teoranta design.

The results presented in this chapter highlight that RANS modelling offers a computationally viable means of determining lift and drag coefficients for a range of angles of attack and Reynolds numbers. At angles of attack in the deep stall region ($\alpha > 20^o$), the accuracy of the model is reduced due to the highly unsteady behaviour of the flow. Turbulence in its nature is three-dimensional so that future studies will examine three-dimensional RANS modelling of the Brí Toinne Teoranta design. By investigating these three-dimensional flow fields, possible reasons for discrepancies between the two-dimensional numerical results and experimental data may be identified. 3D CFD investigations will be presented in **Chapter 5** and **6**.

A series of analysis was performed to assess two optimised vertical-axis turbines' self-starting ability with the newly derived CFD dataset. Start-up predictions for the optimised straight-bladed design and the cylindrical BTT design from **Chapter 3** were compared at different starting blade positions under the same operating conditions. The results presented demonstrate that the straight blade turbine self-starts only if one of the blades are initially in the position $0^o \leq \theta < 20^o$ or $105^o \leq \theta < 115^o$. In contrast, the BTT is computed to self-start for all starting blade orientations. This robust capability of the BTT to self-start presents a significant advantage over traditional turbine designs.

Chapter 5: Development and Validation of a Low-Cost Test Platform for Small-Scale Prototypes

5.1 Introduction

Proof-of-concept is the first step in the development of any tidal turbine design (McCombes et al., 2012). Fundamental mathematical models, coupled with small-scale physical testing, can be used to assess whether a novel design has the potential to be successful. Once proof-of-concept is established, one can advance the technology and quantify performance metrics through testing a medium-scaled prototype in a controlled lab environment.

The availability of suitable laboratories for controlled testing of medium-scaled tidal turbines is limited owing to the high cost associated with supporting infrastructure. Therefore, it is critical to establish proof of concept before securing funding for access to these expensive test laboratories. In this chapter, a low-cost experimental platform is explored for the initial evaluation of the Brí Toinne Teoranta (BTT) prototype design. The primary purpose of the test platform developed is to provide preliminary experimental data for model validation. A key technical challenge entails the development of a robust, low-cost methodology for measuring torque generated by the turbine.

This chapter is structured as follows: In **Section 5.2 Experimental Setup**, the development of the internal small-scale test facility and low-cost torque measurement methodology is presented. In **Section 5.3 Model Development**, the two modelling approaches for the simulation of experimental tests are introduced, based on blade element (BE) theory and computational fluid dynamics (CFD). **Section 5.4 Results and Discussion** includes a comparison of experimental test results and model predictions. To conclude, a synopsis of the learnings and outcomes from the experimental tests are summarised in **Section 5.5 Conclusions**. The limitations of the small-scale, low-cost test approach and suggestions for the future developments of the methodology are discussed in this section.

The specific aims of this chapter are as follows:

- Develop a low-cost test platform for small-scale devices, including the implementation of a robust technique for torque measurement. Perform preliminary tests on the BTT spherical rotor.
- Validate three-dimensional CFD and blade element (BE) theory modelling approaches with small-scale experimental test data.

5.2 Experimental Setup

5.2.1 Flow Visualisation Tank Tests

Due to the limited project budget, modification of existing non-customised test facilities at NUI Galway was deemed to be the only viable approach for the development of in-house turbine testing capability. Initially, a small-scale flow visualisation tank (250 × 100 × 600 mm) was used to assess exceptionally small-scale (< 80 mm in height) design concepts. Three scaled BTT concepts, shown in **Figure 5-1**, with varying turbine height: diameter ratios were manufactured and tested in the flow visualisation tank shown in **Figure 5-2**. These tests were performed at the very early stage of the PhD to attain preliminary visual qualitative tests, without quantitative measurement of torque. Unfortunately, due to several problems during testing, the results were inconclusive. Issues arose with difficulty in manufacturing such small turbine blades and the inability to achieve the required flow velocities in the flow visualisation tank.

(a) **(b)** **(c)**

Figure 5-1: Scaled prototypes of the BTT turbine concept **(a)** H/D = 0.5, **(b)** H/D = 1 and **(c)** H/D = 2.

Each of the turbines was 80 mm in height, with a corresponding maximum blade thickness of 0.9 mm. Such small scales proved beyond the capabilities of the rapid

prototyping machine to maintain a consistent blade profile (NACA 0015). Attempts were made to increase the velocity in the tank by narrowing the flow path, and tilted the test setup; however, the maximum blade Reynolds number achieved for these tests was < 2,000. As noted in **Chapter 2 (Figure 2-17)** and also observed in the test results presented in **Chapter 3 (Figure 3-31)**, at low Reynolds numbers with such high viscous forces within the fluid relative to inertial forces, the drag on the turbine blades far outweighs the lift.

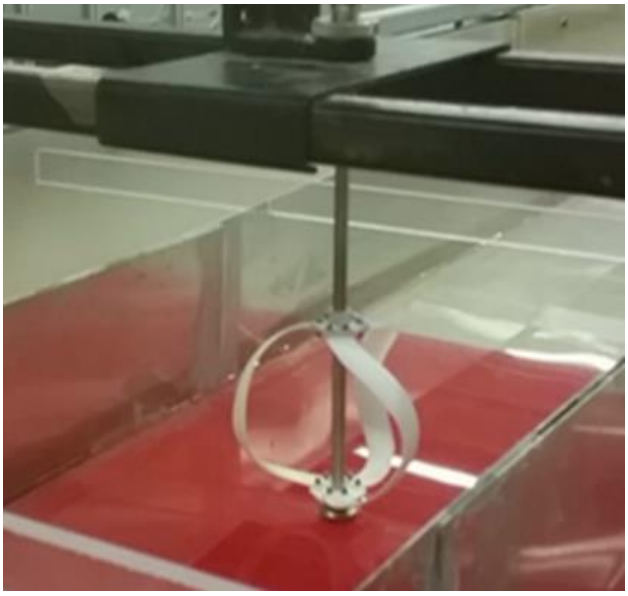

Figure 5-2: Initial tests in the flow visualisation tank on a scaled prototype (turbine height- 80 mm)

5.2.2 Towing Tank Setup and Operation

The next option considered was redesigning an existing wave tank in the hydraulics lab at NUI Galway to incorporate a form of towing carriage that would facilitate testing of a previously manufactured small-scale prototype. The tank had previously operated solely as a wave tank for testing scaled wave energy converters, such as the oscillating water column design shown in **Figure 5-3**. The tank dimensions are 1 m × 1 m × 10 m (width × depth × length).

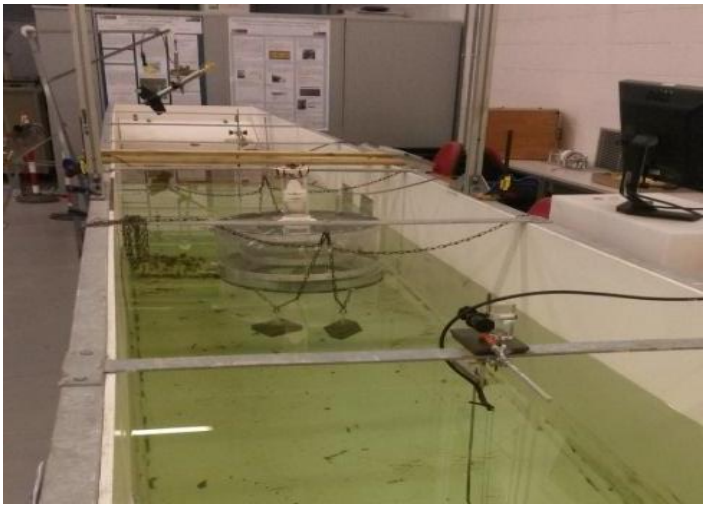

Figure 5-3: Image of the wave tank at NUI Galway with a small-scale wave energy converter.

Considerations for designs on how to drive the towing carriage were given to two concepts:

- **Concept 1:** Mount the motor onto the carriage and use this motor to drive wheels along the track.
- **Concept 2:** Mount the motor at the end of the tank, attach a rope to the carriage and use a rail and slider system.

An advantage of Concept 1 was the ability to precisely control and measure the speed of the carriage at different stages of the tow sequence. The disadvantages of concept one were that the carriage would be very heavy, and therefore a larger motor would be required to move the carriage, increasing the cost. Having an electrical cable supplying power to the motor while the carriage travelled through the water was also deemed a high-risk safety issue. Due to these safety concerns, Concept 2 was selected and implemented, as shown in **Figure 5-4.** The ability to test the turbine at varying tow speeds was a vital requirement of the towing tank facility. A variable speed drive had been considered for this task; however, with limited resources available, a cost-effective sprocket and chain design, shown in **Figure 5-5,** was installed- facilitating testing at three towing velocities. Several safety features were included in the design, such as a dead man switch, shown in **Figure 5-6 (a),** to switch off the motor once the carriage reached a specified point along the tow track. Also, to ensure no risk of injury, a safety casing was built and installed covering the motor and drive train during operation (**Figure 5-6 (b)**).

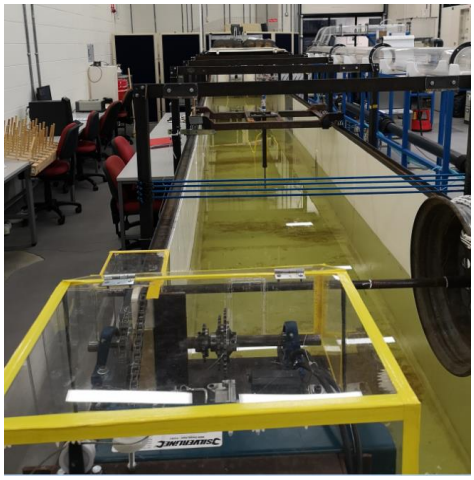

Figure 5-4: Image of the redesigned wave and tow tank at NUI Galway with the completion of the installation of the towing rig.

Figure 5-5: Towing tank motor showing the different gearing ratios for various tow speeds.

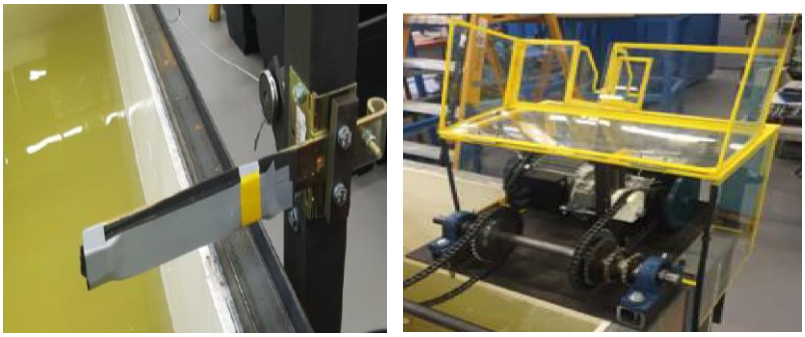

(a) **(b)**

Figure 5-6: Safety features of the towing tank. **(a)** Deadman switch and **(b)** Safety casing around the motor and drivetrain.

5.2.3 Turbine Design

The primary design investigated during this series of tests was a spherical shaped 3-bladed turbine with the design parameters listed in **Table 5-1**. This turbine design, shown in **Figure 5-7**, was fabricated by the industry partner, Brí Toinne Teoranta, before this research started. The design optimisation study presented in **Chapter 3** did not contribute to this turbine design.

Figure 5-7: BTT scaled prototype tested in the tow tank

Twelve M6 bolts were used to secure the blades to the top and bottom supports. These supports were connected to the 12mm stainless steel shaft turbine using two grub screws. Grub screws were deemed sufficient to fix the turbine to the shaft as the torque experienced by this small-scale turbine would not be significant.

Table 5-1. List of design parameters for the BTT turbine (**Figure 5-7**).

Parameter	Value
Radius [m]	0.15
Height [m]	0.3
Chord length [m]	0.025
Blade profile	NACA 0015
Number of Blades	3
Blade Shape	Spherical

5.2.4 Strain Measurement and Calibration Test

Strain gauges are used to measure the strain on the shaft. The steps required to convert recorded strain values to torque values are described in the following. When using strain gauges, the strain, ε, is calculated as follows:

$$\varepsilon = \frac{\Delta R/R_G}{GF} \tag{5.1}$$

where ΔR is the change in resistance (Ω) in the gauge, R_G is the rated resistance of the gauge (Ω), and GF is the gauge factor of the gauge. The GF is information provided by the strain gauge supplier for a specified gauge. It is defined as the ratio of change in electrical resistance to the change in length. The strain gauges used are TechniMeasure FRA-6-11 rosettes. The specifications of the strain gauges are listed in **Table 5-2**. These strain gauge rosettes consist of two strain gauges at 45^o and -45^o. The two strain gauge rosettes, wired in a full Wheatstone bridge, as shown in **Figure 5-8 (a)**, are placed on the turbine shaft directly opposite each other to negate any bending forces which may occur during turbine operation.

An Accsense VersaLogger BR data logger is used to collect the strain values. The logger contained internal storage and had a sampling interval of 30 ms when an independent power supply was used. Siteview software, provided by Accsense, was available to set up the logger and also to analyse the test results. The strain gauges were wired and connected to an Accsense VersaLog data logger, as shown in **Figure 5-8 (b)**.

Table 5-2. TechniMeasure FRA-6-11 strain gauge specifications.

Parameter	Value
Resistance (R_G)	120Ω
Applicable specimen	Metal, Glass, Ceramics
Backing	Epoxy
Operational temperature (°C)	-20~+80°C
Element	Cu-Ni
Strain Limit	5% (50000×10^{-6} strain)
Bonding adhesive	CN, P-2, EB-2
Gauge Factor (GF)	2.1

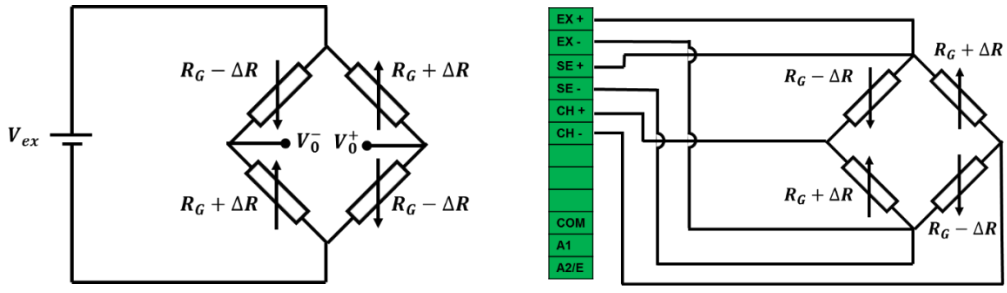

(a) **(b)**

Figure 5-8: **(a)** Full Wheatstone bridge configuration. **(b)** Wiring diagram for full Wheatstone bridge using VersaLog Data Logger

The calibration of the strain gauges was done both analytically and experimentally. For the experimental calibration, the shaft was fixed on one end and simply supported at the other. Known torques are applied using a lever arm and weights between the strain gauges and the simply supported end.

Strain gauges were placed between the turbine and the brake disc. Initially, the terminals to connect the strain gauges into a full Wheatstone bridge were located directly onto the shaft. Due to the relatively small diameter on the shaft, this proved challenging to solder and led to shorting of the wiring and inaccurate results. A nylon piece was fixed to the shaft, and the terminal connections were made on this insulated surface to overcome this issue. The linear relationship determined between the applied torque and measured strain for the 12mm stainless steel shaft is presented in **Figure 5-9**. Also included in this plot is the calculated theoretical relationship between torque and strain.

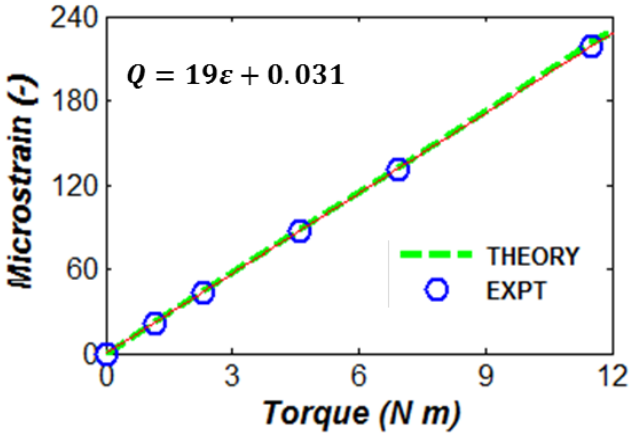

Figure 5-9: Plot depicting the linear relationship between the measured microstrain values and applied torque, including both measured and theoretical relationships.

5.2.5 Test Procedure

A total of 12 test runs were carried out; at three tow speeds, 1.2, 1.5 and 1.8 m s^{-1}, with the blades in four different fixed orientations, depicted in **Figure 5-10**. The turbine blades were rotated 30^{o} for each different orientation. Further details on the blade orientations are discussed later in the modelling section. The freestream velocity of the fluid relative to the turbine is U_{∞}. A mechanical brake disc was positioned above the strain gauges, as shown in **Figure 5-11**. This brake disc was installed to provide a load to oppose the rotation of the turbine as it was towed through the water, i.e. the

mechanical brake disc was acting as a generator would and created a load on the turbine.

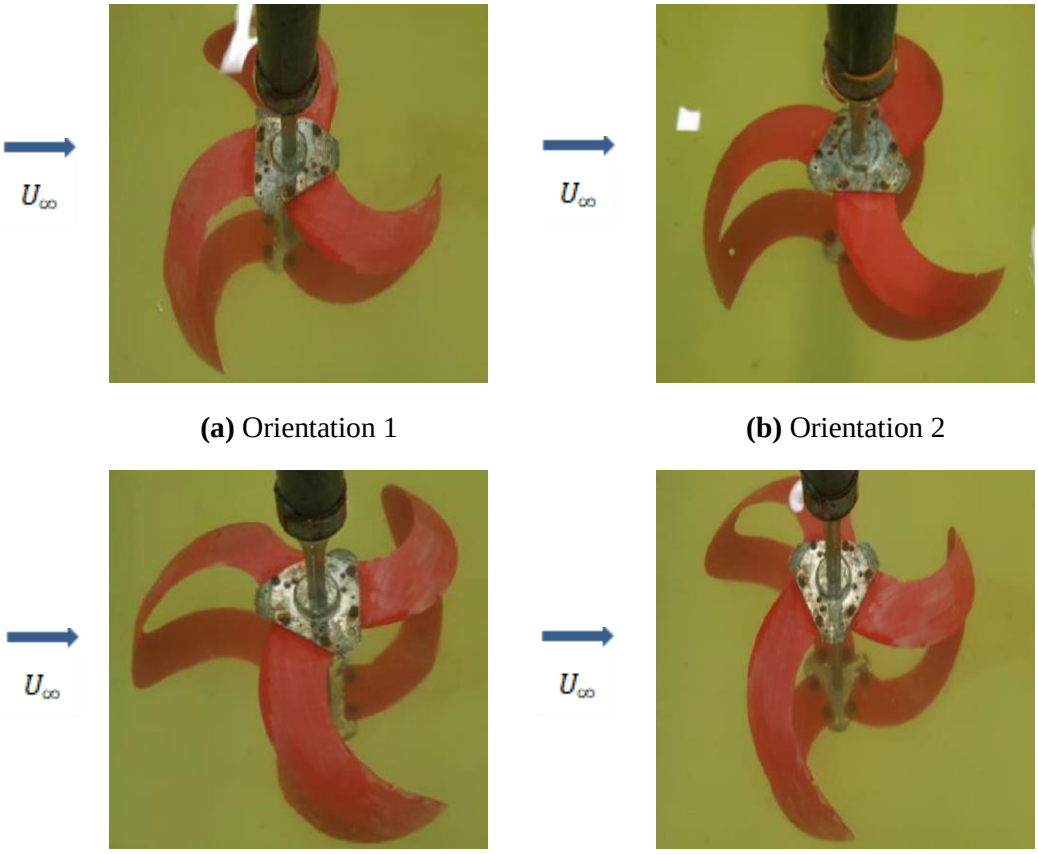

(a) Orientation 1 **(b)** Orientation 2

(c) Orientation 3 **(d)** Orientation 4

Figure 5-10: Setup for the physical testing of various turbine orientations in the towing with the freestream velocity of the fluid relative to the turbine (U_∞), i.e. opposite to the towing direction.

The original test plan was to use the brake disc to generate torque and measure the strain and rotational velocity of the turbine, which would facilitate the hydrodynamic power calculation of the prototype design. However, issues with the sensitivity of the mechanical brake disc meant that when even a minimum braking load was placed upon the disc, the turbine blades would not rotate freely at a consistent speed. In contrast, removing the brake disc load facilitated the free rotation of the turbine at all tow velocities. Due to these test constraints, physical testing focused on attaining the variation in torque on the turbine blades at different fixed orientations for the three unique tow speeds.

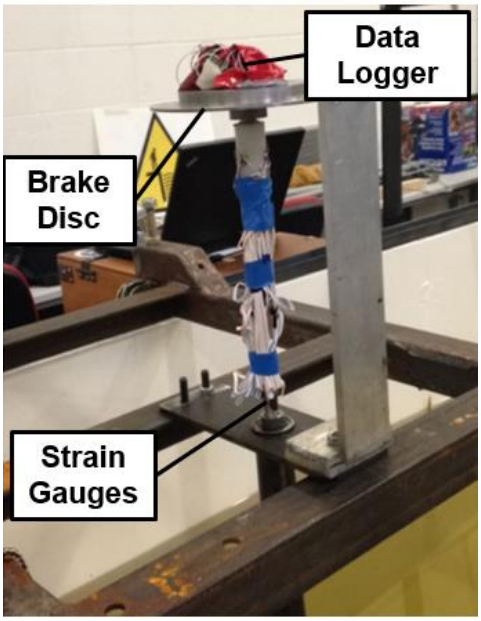

Figure 5-11: Brake disc installation with associated strain gauge wiring. The strain gauge datalogger is fixed on top of the brake disc.

5.3 Model Development

Two modelling techniques, blade element (BE) theory and computational fluid dynamics (CFD), are utilised to provide results for comparison against the experimental data. In contrast to experimental testing where the fluid is fixed, for both models developed, the fluid passes through the turbine, and the turbine remains in a fixed position. As outlined in **Chapter 2**, tow tank tests results are generally acceptable for model validation provided specific considerations are taken into account. The same blade orientations examined in the experimental study (**Figure 5-10**) are reviewed using the models presented.

The Turbine Orientation Configuration Angle (TOCA), outlined in **Chapter 3**, is used in this chapter to describe the overall blade's angular position. The four fixed blade positions are shown in **Figure 5-12**. For each orientation, the turbine blades are rotated 30^{o} clockwise.

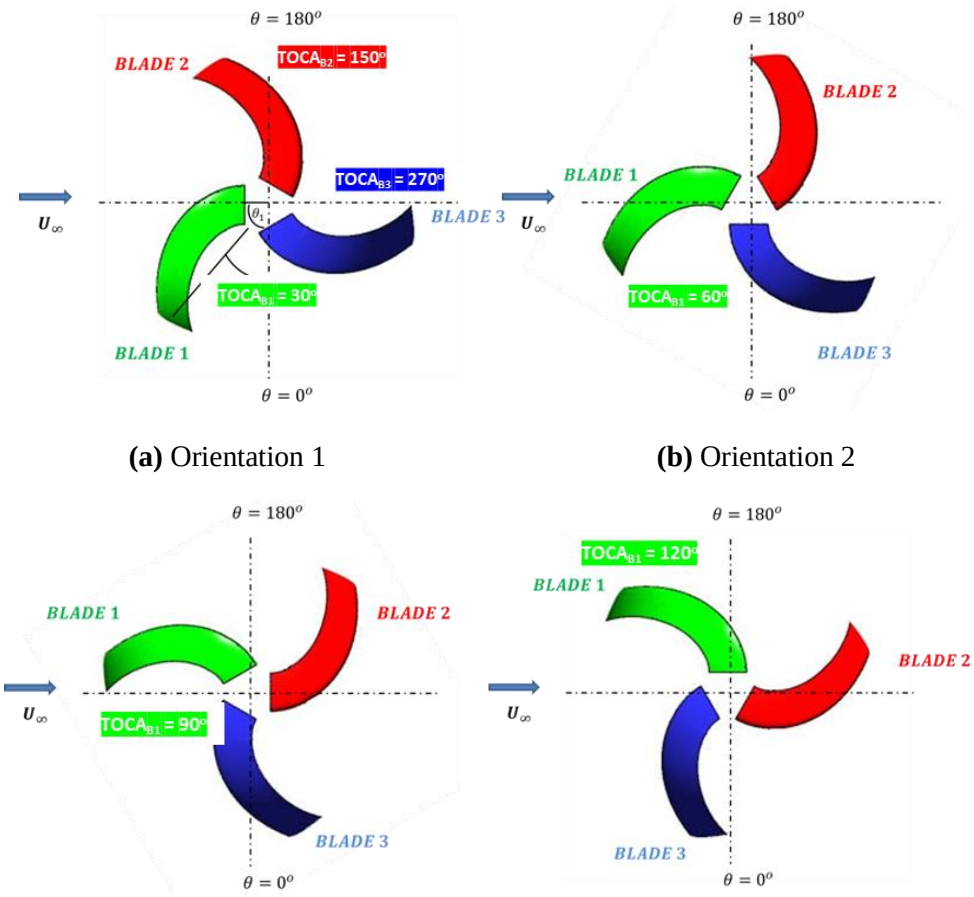

(a) Orientation 1 **(b)** Orientation 2

(c) Orientation 3 **(d)** Orientation 4

Figure 5-12: Various turbine orientations for towing tank tests with the freestream velocity of the fluid relative to the turbine (U_∞), i.e. opposite to the towing direction.

5.3.1 Blade Element Theory Model

Blade element (BE) theory forms the basis of the numerical model applied to analyse the turbine design described in **Table 5-1**. It is one aspect of the blade element-momentum (BEM) model presented in **Chapter 2**. For this model, each turbine blade is discretised into many blade elements/heights. One such blade element is shown in **Figure 5-13**. The torque is calculated for each element and summed over the length of the blade for the three blades. It is assumed that there was no interaction between each blade element. The angle of attack for each blade element is calculated and this value, combined with the local Reynolds number (Re_c), facilitates the calculation of the lift and drag coefficients from the CFD-based dataset of coefficients presented in **Chapter 4**. The following equation is used to determine the torque on each blade element:

$$Q_{i,el} = F_T r \tag{5.1}$$

where r is the radius for that turbine element height, and F_T the tangential force is defined as:

$$F_T = \frac{1}{2} C_T \rho \frac{\Delta h c}{sin\,\gamma} {U_\infty}^2 \tag{5.2}$$

where Δh is the turbine blade element height, c is the chord length, ρ is the density of the fluid, angle, γ is local blade inclination angle, U_∞ is the freestream velocity of the fluid and C_T is the tangential force coefficients defined as:

$$C_T = C_L sin\,\alpha\ - C_D cos\,\alpha \tag{5.3}$$

The total turbine torque is calculated by summing the elemental torque over the entirety of the length of each blade.

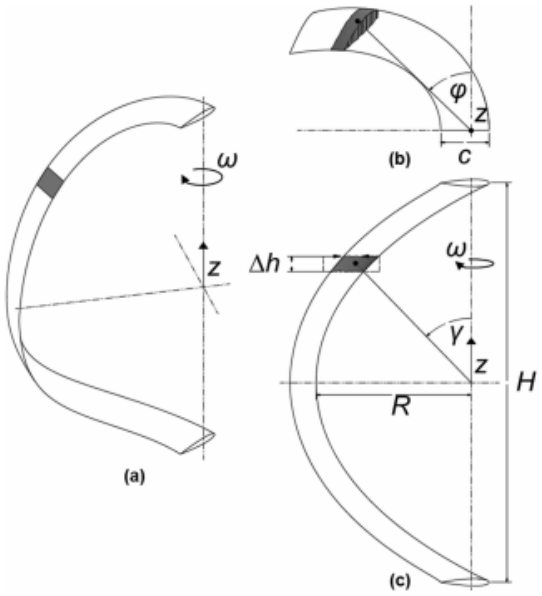

Figure 5-13: Definition of BTT blade geometry: **(a)** isometric view of single blade showing the axis of rotation, *z*, and rotational velocity and direction, *ω*; **(b)** plan view showing chord length, *c*, and local azimuthal angle, *θ*, for a specific blade section; and **(c)** elevation view detailing the local blade inclination angle, *γ*, for a specified blade section of height of Δ*h*, total turbine height, *H*, and maximum blade radius, *R*.

5.3.2 Computational Fluid Dynamics Model

A three-dimensional CFD model of the BTT spherical turbine described in **Table 6-1** is presented. Similar to the BE theory model, the fluid flow velocity is set at a fixed non-zero value. As with the BE theory model and the experimental tests, the rotational velocity of the turbine blades is fixed at 0 rad s^{-1}. The validated two-dimensional CFD methodologies in **Chapter 4** were considered and adapted for the three-dimensional model in this Chapter.

Model boundary conditions implemented are shown in **Figure 5-14**. The inlet velocity is varied for each simulation to match three applied tow speeds. Following on from the recommendations listed by Gaurier et al. (2015), as the results are to be compared to tow tank results, a low turbulent intensity value of 0.005% was selected as an inlet boundary condition. A turbulent viscosity ratio of 2 and an intermittency inlet value of 0 was also applied. The three turbine blade surfaces were set as non-slip walls. A non-slip wall was also defined for three exterior surfaces, i.e. the tank walls. As surface dynamics were not of interest in these simulations, a zero-shear surface was assumed for the free surface of the water. This assumption allowed for a symmetry boundary condition to be applied here. It was assumed that the flow had fully recovered at the outlet, so a 0 Pa gauge pressure condition was applied along with matching turbulent boundary conditions to those of the inlet.

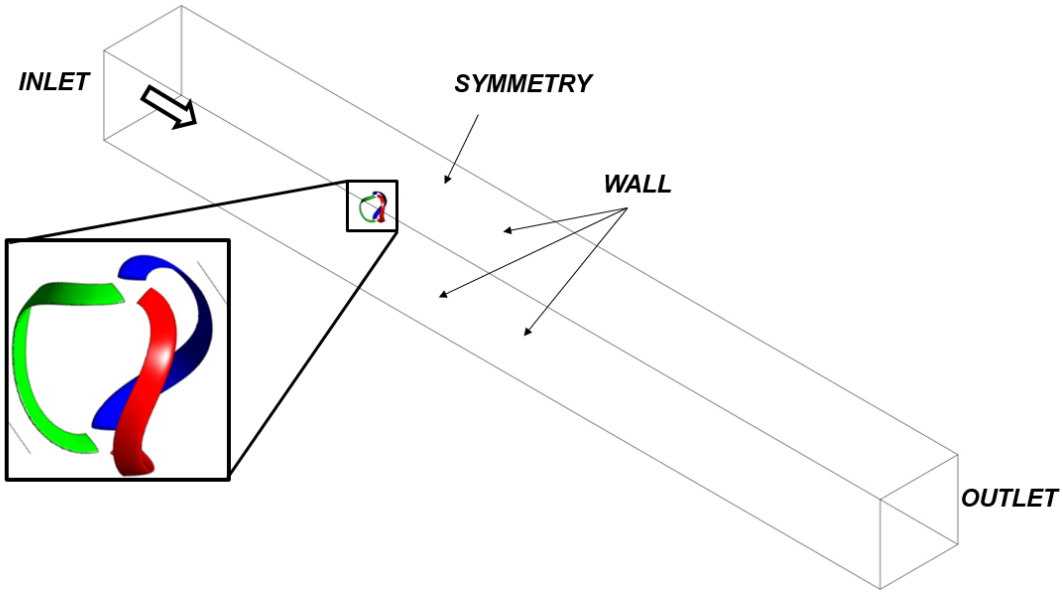

Figure 5-14: CFD model domain and boundary conditions

Meshes are generated using the ANSYS Meshing Tool, with emphasis placed on refining the critical region around the blade surfaces. The SST Transition turbulence model (Menter et al., 2006) is selected for the simulations due to its superior capabilities of modelling the transition between laminar and turbulent flow. The robust capabilities of this turbulence model to predict the onset of stall for hydrofoils were highlighted in **Chapter 4**. A vital requirement of the SST Transition model is a $y^+ < 1$. The initial first layer height, y, is calculated using equations (4.3) and (4.4). Fifty inflation layers are defined with a growth rate of 1.15 implemented for all grid generations. An example mesh highlighting these inflation layers is shown in **Figure 5-15** and **Figure 5-16**.

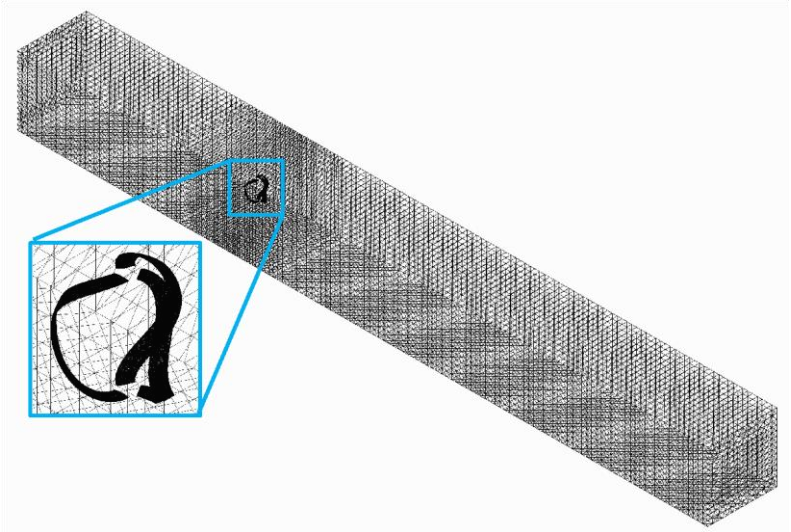

Figure 5-15: Isometric view of the full three-dimensional CFD mesh.

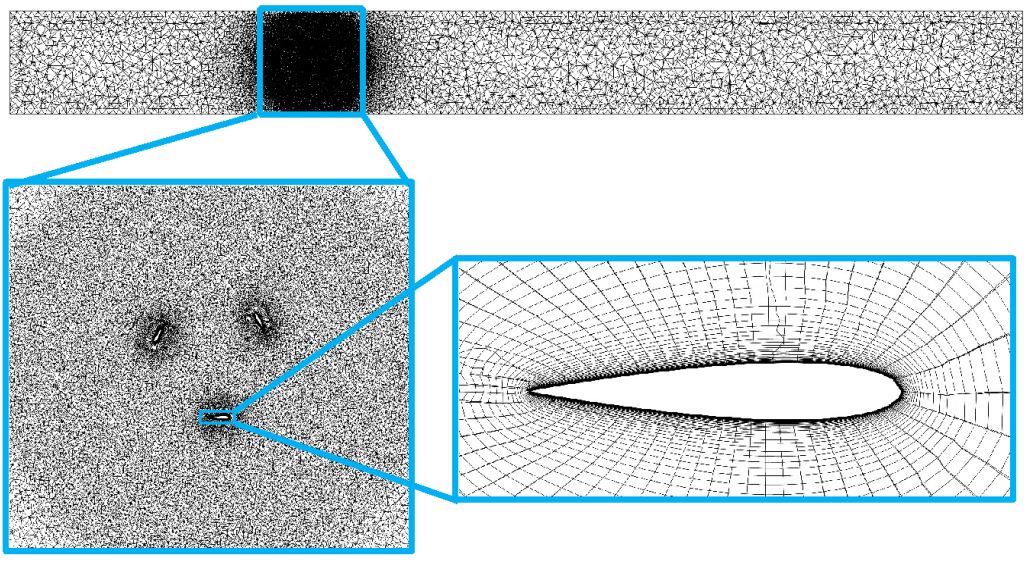

Figure 5-16: CFD mesh showing a section along the midline of the turbine showing the critical boundary layer inflation layers.

The steady-state flow field solution is provided as the initialisation of the transient calculation, thus reducing the overall time to achieve a converged solution and achieving a more accurate solution. The pressure and velocity are coupled using the COUPLED algorithm. First-order upwind discretisation schemes are applied for the momentum, turbulent kinetic energy, specific dissipation rate, intermittency and the transitional Reynolds number for the first 2 seconds of the transient simulations. For the remaining simulation time, second-order discretisation schemes are implemented to increase the solution accuracy. A second-order temporal discretisation scheme is applied to the simulations.

A global convergence criterion of 10^{-5} is set for the residuals, and the turbine torque output is monitored per time interval until a steady-state or quasi-steady-state solution is achieved ($\Delta\bar{Q} < 1\%$). A systematic approach is adopted to carry out a detailed mesh refinement study to ensure an accurate solution is achieved. Five meshes with different numbers of elements are generated, with the focus being placed on refining the critical boundary layer around the turbine blade surface. An investigation into the temporal discretisation is also carried out. Results from these investigations are presented below. The same mesh parameters and boundary conditions are applied for each of the four blade orientations.

5.4 Results and Discussion

5.4.1 CFD Discretisation Studies

As in **Chapter 4**, spatial and temporal discretisation studies are performed for the CFD simulations to ensure an adequately refined mesh and an appropriate time step were selected. The analysis is performed for Orientation 3 (**Figure 5-12 (c)**) at two freestream velocities, namely 1.2 m s^{-1} and 1.8 m s^{-1}. A series of five meshes of increasing density are analysed. Richardson's extrapolation, described in detail in **Chapter 4**, is implemented to determine the accuracy of each mesh relative to a final mesh independent extrapolated value. The results of the mesh refinement are presented in **Table 5-3**, with the torque variation per total number of mesh elements illustrated in **Figure 5-17**.

Table 5-3. Calculated total torque values for a series of five increasingly refined meshes for U_∞ = 1.2 m s^{-1} and U_∞ = 1.8 m s^{-1} (Orientation 3)

Mesh	Number of Elements	Q (N m) $U_\infty = 1.2\ m\ s^{-1}$	Q (N m) $U_\infty = 1.8\ m\ s^{-1}$
M1	1.8 × 10^6	0.364	0.573
M2	6.1 × 10^6	0.294	0.512
M3	8.0 × 10^6	0.255	0.472
M4	11.9 × 10^6	0.252	0.446
M5	16.2 × 10^6	0.251	0.440
Richardson's extrapolation value		**0.25**	**0.44**

From the spatial discretisation study, it is concluded that model predictions using M4 and M5 are very similar to each other. For both freestream velocities, M4 results for the total torque are within 0.5% of the final Richardson's extrapolation value. The same mesh, M4, provides the desired criterion for convergence for both simulations and hence is used for all subsequent simulations.

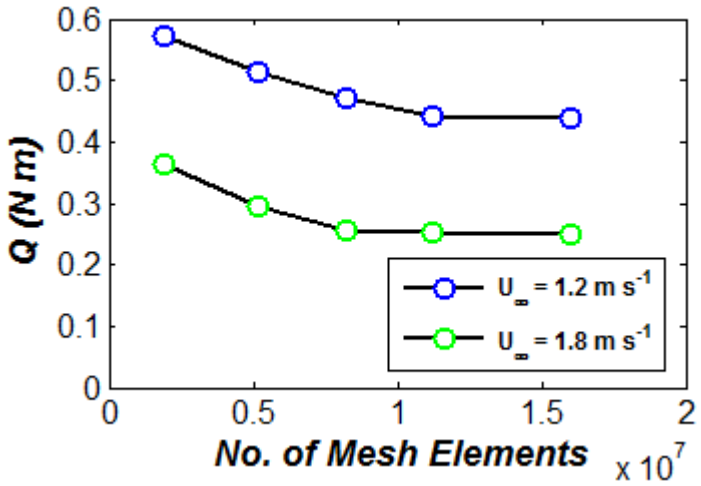

Figure 5-17: Spatial discretisation study for Orientation 3 (U_∞ = 1.2 m s^{-1} and U_∞ = 1.8 m s^{-1}).

M4 also satisfied the mesh refinement requirement for the SST Transition turbulence model. **Figure 5-18** shows a Y+ value < 1 is achieved for all blade surfaces, which satisfies the condition of the turbulence model for an adequately refined mesh.

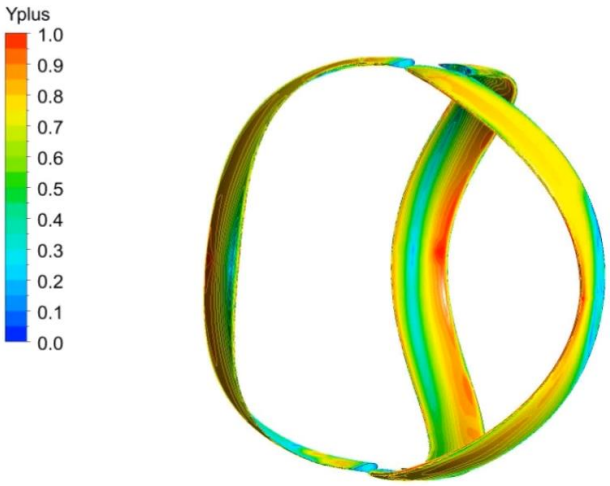

Figure 5-18: Y^+ value for M4 mesh (Orientation 3, U_∞ = 1.8 m s^{-1})

To ensure an adequate time step is chosen, four different time step sizes are investigated. From the results presented in **Chapter 4** (**Table 4-3 - Table 4-5**), the optimum CFD simulation time step is influenced by the local Reynolds number. The lower the Reynolds number, the small time-step required to achieve a converged solution. For this reason, the temporal discretisation study is performed at the lowest freestream velocity, U_∞ = 1.2 m s^{-1}. Each test time simulated is ten seconds. Based on this study, a time step of 0.01 seconds is used for all remaining simulations.

Table 5-4. Computed average torque values (U_∞ = 1.2 m s^{-1})

Δt (s)	$\bar{Q}$ $U_\infty = 1.2\ m\ s^{-1}$
0.1	0.280
0.05	0.257
0.01	.252
0.005	.25

5.4.2 Comparison of Model Predictions with Experimental Data

One example of the experimental instantaneous torque values determined from the tow tank tests is shown in **Figure 5-19**. In this Figure, the instantaneous torque is plotted against test time. The measured torque oscillates around 0 N m for the initial 5 seconds before the towing motor is activated. For each run, a zero strain value was established based on the recorded strain values time-averaged over 30 seconds before activation of the towing motor. Activation of the motor (time = 820 s; **Figure 5-19**) results in turbine movement through the water and a corresponding increase in the

measured torque. This period of accelerating turbine movement and increasing torque is referred to as the start-up phase. The start-up phase is followed by the test-phase of duration ~ 3-4.5 seconds (depending on the applied maximum turbine velocity) of approximately constant turbine velocity and approximately steady-state torque. During the test phase, the torque fluctuates about a steady-state mean value. The mean (time-averaged), minimum and maximum torque values are noted for this period. While torque fluctuations during the test phase are of the same order as the torque fluctuations under static (zero velocity) conditions, suggesting that measured fluctuations are primarily due to baseline noise in the strain-gauge measurement system. However, during the test phase, fluctuations in the torque measured may be increased due to:

- turbulence and flow interference as a result of fluid flow around the blades and through the turbine;
- dynamic friction and vibration of the towing carriage during travel along the track.

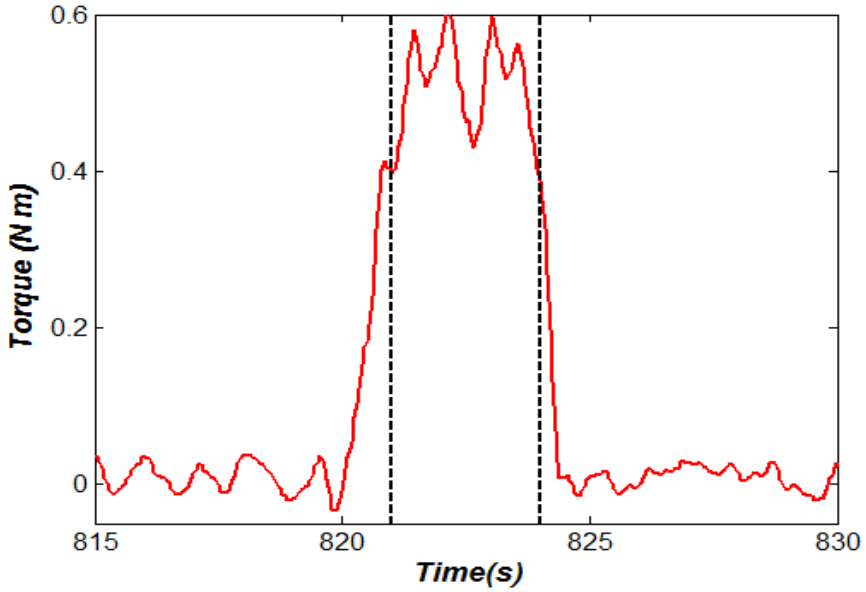

Figure 5-19: Calculated experimental torque variation for one test run (Orientation 3, $U_\infty = 1.2$ m s^{-1}).

Comparisons between the experimental results and numerical results are presented in **Figure 5-20**. The average torque variation with freestream velocity is given for the four different blade configurations (previously outlined in **Figure 5-12**). Errors bars associated with the experimental data indicate the maximum and minimum torque value recorded from each test run, as highlighted in **Figure 5-20**.

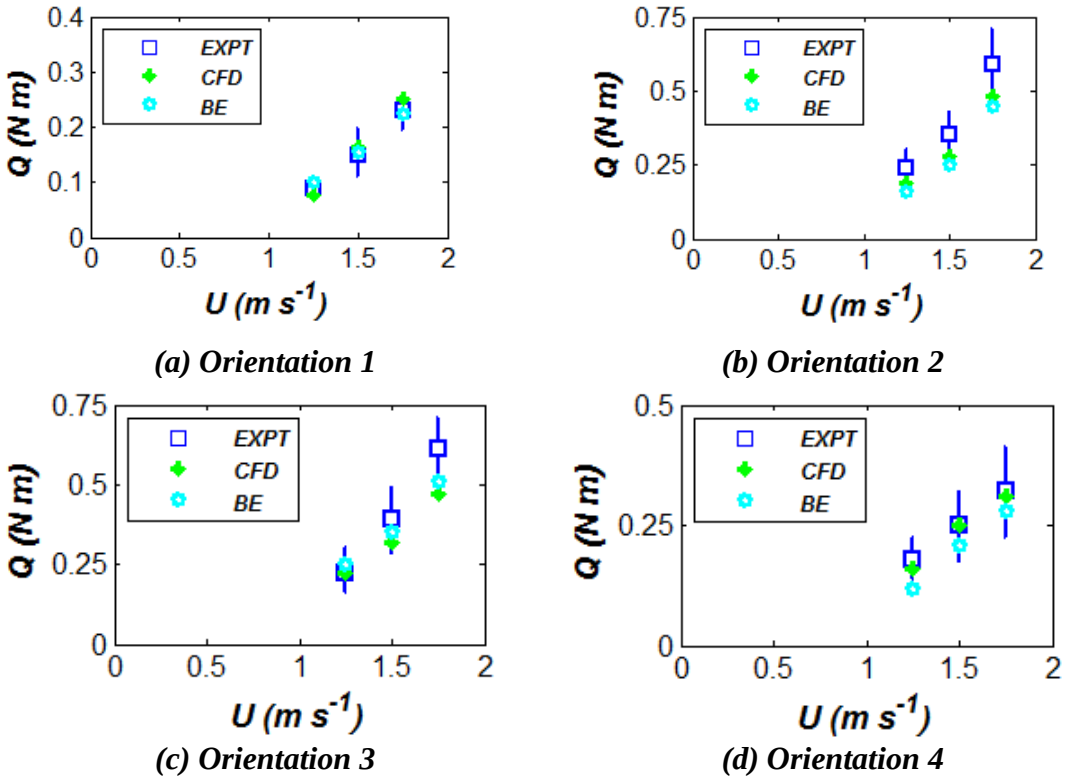

(a) Orientation 1 *(b) Orientation 2*

(c) Orientation 3 *(d) Orientation 4*

Figure 5-20: Comparison between experimental and numerical results for overall torque

As expected, an increase in applied velocity results in an increase in torque. This trend is observed experimentally and accurately predicted, both by the BE theory and CFD models. The observed experimental variance in torque measurement increases with increasing velocity, which may be attributed to the increased turbulence levels and increased vibrations in the towing carriage at higher tow velocities. The turbine orientation significantly influences the measured torque. This variation in torque is investigated in more detail in the following section, where model predictions for the individual blade contributions to the overall blade torque are investigated.

5.4.3 Individual Blade Contributions to Overall Torque

The individual torque contribution of each of the three turbine blades is determined for the BE and CFD models. Results are presented in **Figure 5-21** for Orientation 1 (**Figure 5-10 (a)**) for a freestream velocity of 1.5 m s^{-1}.

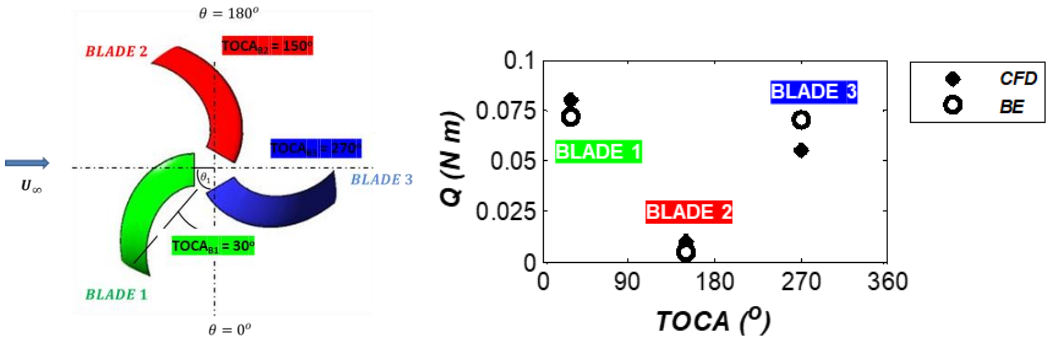

Figure 5-21: Comparison between two sets of numerical results for overall torque measurement

Approximately equal torque is generated by Blade 1 and Blade 3. Blade 2 is at a sub-optimal TOCA, and it is predicted to generate only ~13% as much torque as the other two blades. The ranges of angles of attack experienced by each blade are presented in **Figure 5-22**, noting that the angle of attack each blade element experiences changes along the length of the blade. The lift and drag coefficient dataset used in these calculations is a combination of the CFD derived values presented in **Chapter 4** and experimental data presented by Sheldahl and Klimas (1981). The data for angles of attack between -30° and +30° are CFD derived values, while the data outside of this range is experimental data. Due to the constraint on turbine rotation, wide-ranging angles of attack are computed along the length of each blade turbine. Favourable angles of attacks that result in maximising lift and minimising drag coefficients can be seen for Blade 1 and Blade 3. In contrast, the range of angles of attack Blade 2 experiences result in higher drag forces, which in turn results in reduced torque. The overall torque results presented in **Figure 5-21** reflect the low torque contribution for Blade 2 from both the CFD and BE theory model.

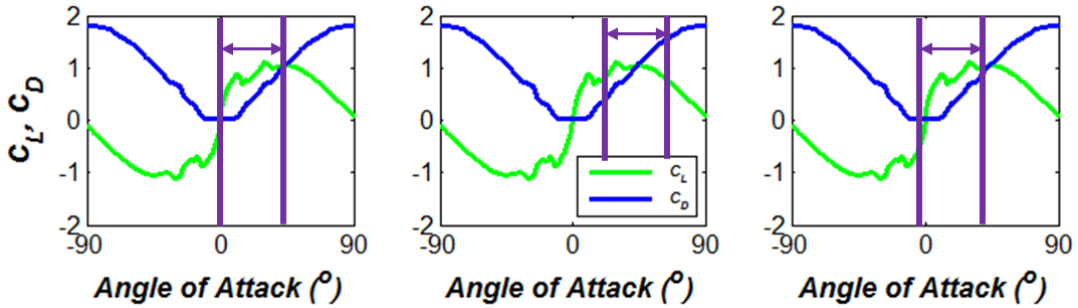

(a) Blade 1 **(b)** Blade 2 **(c)** Blade 3

Figure 5-22: Lift and drag coefficients as a function of angle of attack (Re = 1×10^5). Range of angles of attack experienced by each blade indicated in purple.

Figure 5-23 presents the pressure coefficient distribution at the mid-section of the turbine height for the CFD simulation of Orientation 1 at U_∞ = 1.5 m s^{-1}. The spherical-designed turbine has its largest radius at its mid-section, and therefore this is often where the largest contribution to the overall torque is produced. The distribution of pressure shown for Blade 1 indicates favourable lift conditions with high pressure on the upper blade surface near the blade leading edge and low pressure on the lower blade surface. These visual results are reflected in the higher calculated torque value from the CFD simulations for Blade 1 presented in **Figure 5-21**. In contrast Blade 2, is not at a favourable position for maximising lift, and this is reflected in the considerably lower torque contribution from this blade.

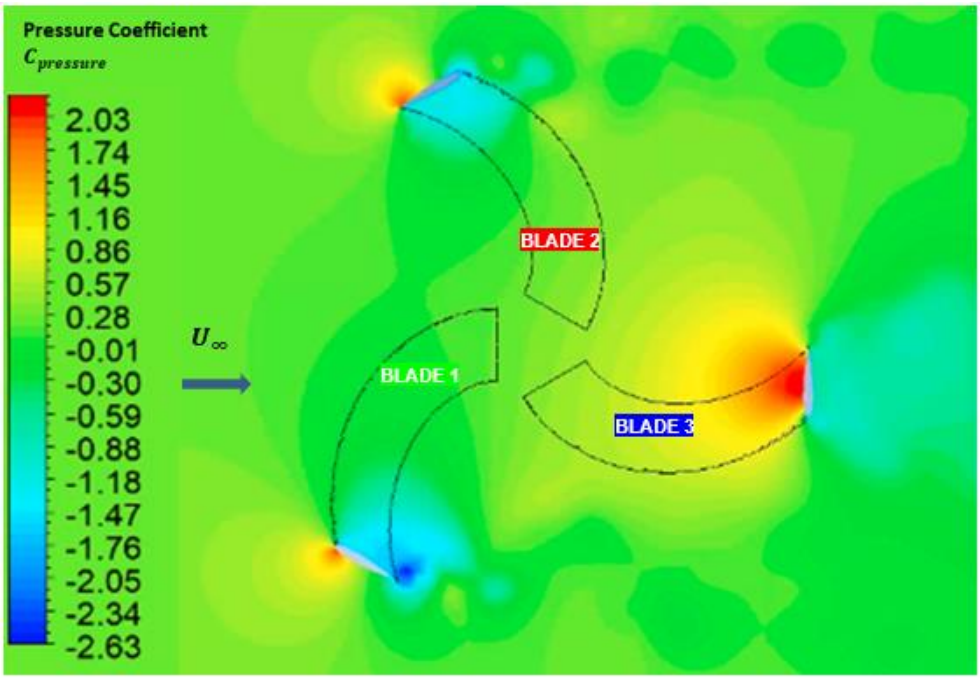

Figure 5-23: Pressure coefficient distribution at the midplane of the turbine (Orientation 1, U_∞ = 1.5 m s^{-1})

5.4.4 Proof-of-Concept and Initial Design Observations

Proof-of-concept for the Brí Toinne Teoranta concept design was established through the test results and model predictions demonstrated in this Chapter. An insensitive braking system combined with low Reynolds numbers and a short tank length meant that overall power predictions of the prototype design were not achieved. However, test results demonstrated show that the novel turbine blades designs have the potential to generate torque. The test results, coupled with the general agreement with two

model predictions, provided confidence to advance the technology to the next TRL and lead to the testing presented in **Chapter 6**.

CFD predictions of out-of-plane flows are presented in **Figure 5-24**. Out-of-plane flows reduce the fluid velocity imparted on the downstream turbine blades. The magnitude of the out-of-plane flow at the mid-height of the turbine (0.5 H) is relatively small, while significant out-of-plain flows are observed at other sections along the blade (e.g. 0.05 H and 0.75 H). These flows are observed both within the turbine and are also evident in the wake of the turbine. Further testing and simulations would be required to confirm these observations, but the initial results would indicate that an alternative, possibly cylindrical-shaped design, would provide a marked power performance over the spherical turbine. The turbulent kinetic energy at two section heights. 0.05 *H* and 0.75 *H*, are presented in **Figure 5-25**.

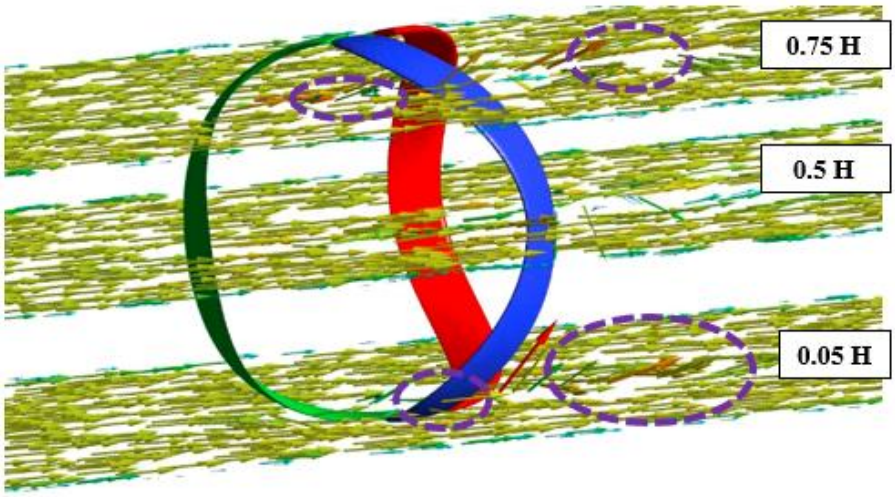

Figure 5-24: Velocity vector profile at various section heights, 0.05 *H*, 0.5 *H* and 0.75 *H*. The out-of-plane fluid velocity observed are marked in purple (Orientation 1, U_∞ = 1.5 m s^{-1}).

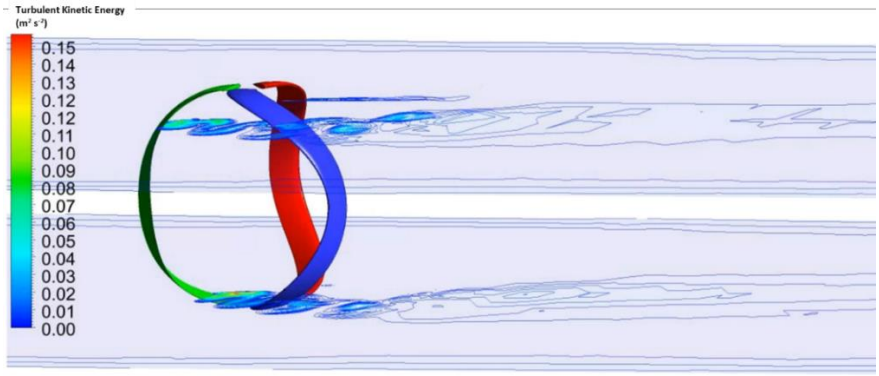

Figure 5-25: Two-dimensional turbulent kinetic energy profile at two section heights, 0.05 *H* and 0.75 *H* (Orientation 1, U_∞ = 1.5 m s^{-1}).

5.5 Conclusions

In this chapter, the development of a small-scale, low-cost turbine test facility was explored. A towing tank concept was designed, developed and fabricated. A mechanical braking system was developed to enforce a controlled and quantifiable resistance to turbine rotation. Preliminary testing of the mechanical braking system revealed that such an approach was not sufficiently sensitive to enforce a prescribed turbine angular velocity. Project budget constraints prevented the acquisition of an electromagnetic braking system. Based on this limitation, a series of tests were performed in which the small-scale turbine design was subjected to towing at a constant velocity (freestream velocity) with turbine rotation fully constrained. Four fixed turbine orientations were tested, and resultant steady-state torque during the constant velocity test phase was measured. BE theory and CFD models of the rotationally constrained turbines were developed. General agreement was achieved between experimental measurements and BE and CFD model predictions in terms of the relationship between towing velocity and resultant torque in terms of the influence of fixed turbine orientation and resultant torque.

The study presented in this chapter provides a partial validation of the developed low-cost, small-scale test facility for preliminary design concept assessment. Future work should include the installation of an electromagnetic brake in place of the mechanical braking system. This updated system would allow for more sensitive control and measurement of the load applied to the turbine. Ideally, no load/resistance should be applied to the turbine on start-up. Once the turbine has reached a desired rotational speed, the load/resistance should then be applied. The ability to vary the load/resistance would facilitate the optimisation of the operating tip-speed ratio (*TSR*) and power generation. The length of the tow tank proved adequate for the rotationally constrained turbine tests presented in this chapter. However, an extended towing tank would be required to provide a longer duration of constant tow velocity (i.e. a longer test phase) and would allow for the application of higher towing velocities. Application of higher tow velocities/Reynolds number is critical for testing of up-scaled turbines, as presented in **Chapter 6** of this thesis.

Chapter 6: Controlled Experimental Testing and 3D CFD Model Validation for a Scaled Prototype in a state-of-the-art Facility

6.1 Introduction

Precise, accurate and repeatable testing of a medium scale (< 1:50) tidal turbine device in a controlled environment is a crucial stepping stone in the progression of a device's technology readiness level (TRL) (McCombes et al., 2012). This series of tests also offer an indication of the potential power performance of a full-scale device and help to secure funding for development, further advancing the TRL of the device.

Through a successful Horizon 2020 funding application to the MaRINET 2 project, access was granted to test two novel tidal turbine prototypes in the recirculating flume at the IFREMER facility at Boulogne-Sur-Mer. This state-of-the-art testing facility has been utilised to investigate a wide range of applications over its 30 years in operation, including mooring systems, fishnets characteristics, and a range of prototype turbine designs (IFREMER, 2020).

Experimental test results are a vital validation tool for numerical methods, such as computational fluid dynamics (CFD) models and blade element momentum (BEM) models. As discussed in previous Chapters, both BEM (**Chapter 3**) and CFD (**Chapter 4**) models offer attractive options to evaluate different turbines designs. Due to the three-dimensionality of the Brí Toinne Teoranta turbine blade geometry, full 3D CFD models are required to analyse this type of next-generation turbine design. With recent advancements in computational power resources availability, 3D CFD simulations are now a viable option to assess the three-dimensionality of the flow around, through and past the turbine (Mannion et al., 2018; Marsh et al., 2015). Experimental results can also be used to validate and compare the accuracy and computational resources required for different modelling approaches.

This Chapter is divided into four sections; **Section 6.2 Experimental Methodology** provides information on the test facility and details on the design of the turbines and test setup, including installation, instrumentation and procedures implemented. **Section 6.3 Three-Dimensional CFD Methodology** details the CFD modelling approach implemented, including domain setup, meshing techniques and validation, solution methods and post-processing of results. In **Section 6.4 Results and Discussion,** the experimentally measured power coefficient variation with tip-speed ratio and wake flow measurements are presented. 3D CFD predictions and the BEM model predictions from work in previous chapters are compared and validated with the experimental results. The Chapter concludes with a discussion on the experiences and lessons learned from different aspects of the experimental tests in **Section 6.5 Conclusions**.

The specific aims of this Chapter are to:

- Characterise the power performance of the scaled prototypes by determining the variation of power coefficient with tip-speed-ratio (*TSR*) for several freestream velocities
- Develop a three-dimensional CFD model
- Validate the blade element momentum approach detailed in **Chapter 3**. This BEM model uses the CFD-based hydrofoil coefficient dataset from **Chapter 4**.
- Determine the flow field around and in the wake of the turbine using the laser Doppler velocimeter (LDV) available at the IFREMER facility. These results will be used as further validation of the three-dimensional CFD model presented.

6.2 Experimental Methodology

This section provides details of the experimental methodology adopted in the testing of the two prototype turbine designs.

6.2.1 Test Facility

The IFREMER recirculating flume is a world-leading centre for testing small to medium scale tidal turbines is a central partner in the MaRINET 1 and MaRINET 2

projects. The research team at this facility are crucial contributors to the establishment of testing standards best practice techniques, in addition to contributing several scientific advances in leading journals in the field of turbine testing (Elsaesser et al., 2013; Gaurier et al., 2015; McCombes et al., 2012; Mycek et al., 2014).

Details of the recirculation flume at IFREMER are shown in **Figure 6-1** (Gaurier et al., 2015). The flume has a working section of 18 m × 4 m × 2 m (length × width × depth), and the total water capacity of the tank is 700 m^3. Flow is driven by two 250 kW pumps operating on variable speed drives. The tank has a freestream velocity range of 0.1 to 2.2 m s^{-1}, and the turbulence intensity can be varied from 1.5 to 15%. The variation in turbulence intensity in the flow is achieved by installing different grids and honeycombs, which act to disrupt the flow. In the current study, to ensure consistency when comparing each turbine design, the turbulence intensity was fixed at 1.5% for all tests. 1.5% is the default level of turbulence intensity in the flow at this facility and did not require the addition of any extra equipment, e.g. flow grids. As noted by Mycek et al. (2014), a variation in turbulence intensity has proven to have little effect on the average power coefficient, which is of primary concern for this research.

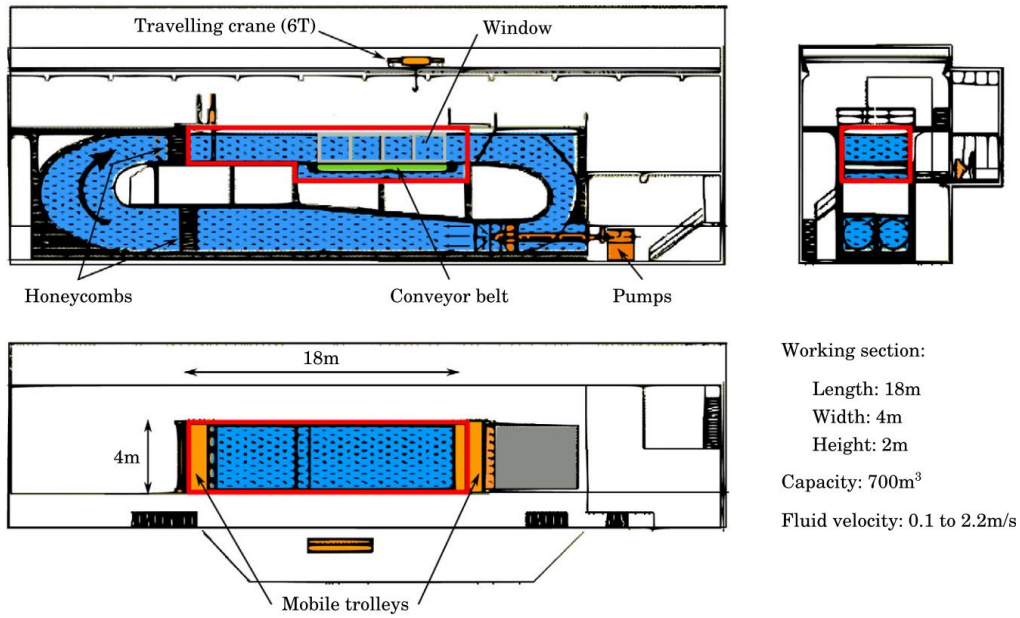

Figure 6-1: Recirculating tank layout and information at the IFREMER facility at Boulogne-sur-Mer (Gaurier et al., 2015).

A 2-component laser doppler velocimeter (LDV) system to characterise the flow in the tank is also available at this facility. This system uses lasers to track the movement of micro-particles mixed in the water (50 μm glass balls coated in silver) and allows the velocity to be measured in two dimensions at specified points in the flow.

6.2.2 Turbine Prototypes

Experimental tests are performed on two medium-scale (~1:50) novel tidal turbine prototype designs. The first turbine tested, hereafter referred to as Turbine A, is shown in **Figure 6-2 (a)**. Three spiralling blades are arranged in a spherical configuration. This turbine prototype design was devised and manufactured by the project industry partner, Brí Toinne Teoranta, before the commencement of this PhD. The BEM design optimisation study presented in **Chapter 3** did not contribute to this turbine design. Geometric parameters for Turbine A, listed in **Table 6-1**.

The second prototype design is based on BEM parametric optimisation analysis presented in **Chapter 3**. Spiralling blades are arranged in a cylindrical configuration, as shown in **Figure 6-2 (b)**. Geometric parameters for Turbine B are based on the design optimisation study presented in **Chapter 3** and are listed in **Table 6-1.** The prototype for Turbine B was manufactured by the wind turbine blade manufacturing company, Heverin Energies. Images depicting the various stages of manufacturing are shown in **Figure 6-3**.

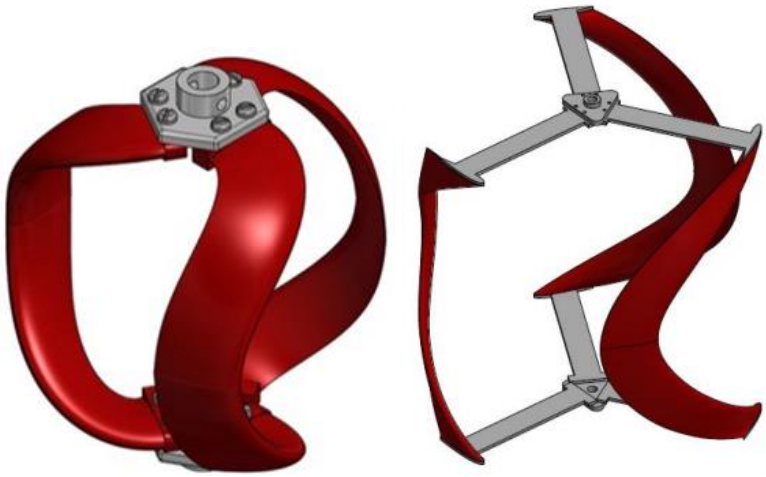

(a) **(b)**

Figure 6-2: Images of the two design concepts tested (a) Turbine A and (b) Turbine B. (Not to scale)

A form was built primarily from the plaster in the shape of one half the blade profile (NACA 0015). This form was used to create a fibreglass reinforced polyester resin mould in the desired shape of the blade profile. On completion of one half of the mould, a plater blade was constructed within this mould. A second mould was mould on top of this and allowed to harden. The plaster blade was removed from the mould leaving two halves that were joined together to establish the correct profile along the entire length of the blades. The two halves of the blade mould were laid up with fibreglass reinforced polyester resin and a gel coat exterior. The two halves were held together, resulting in contact between the two fibreless layups. The remaining surface defects were filed and sanded down using coarse (80 grit) and fine (400 grit) sandpaper. Expanding foam was inserted into the blade to fill the interior, and stainless steel inserts were placed and secured at the top and bottom of each blade to attach the support arms.

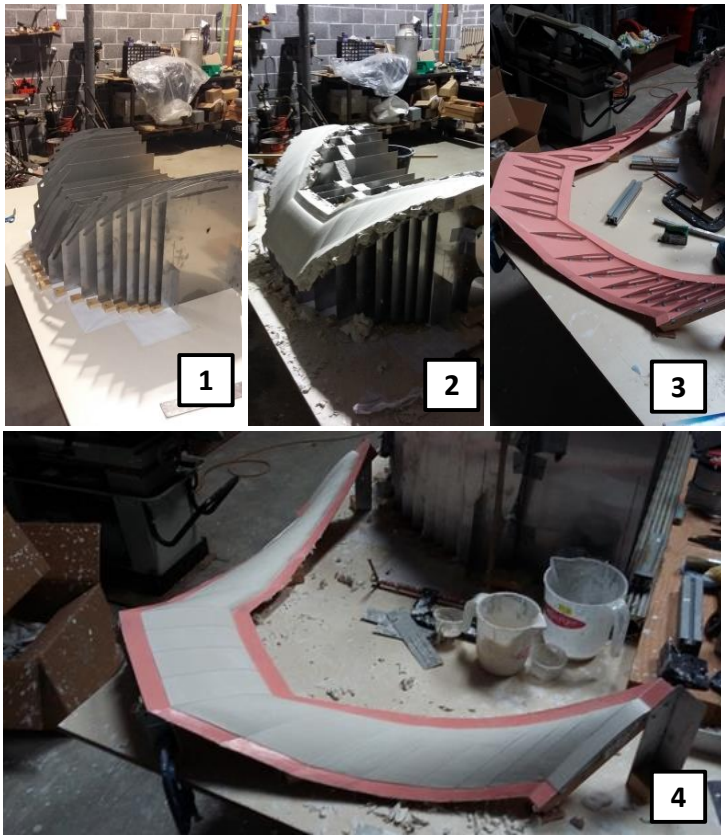

Figure 6-3: Various stages of the design and manufacture of the turbine blade. Pictures provided by Heverin Renewables.

Each turbine blade is supported by two stainless steel support arms, as shown in **Figure 6-4**. The thickness of each supports is 3 mm, and the edges of each edge were

rounded to reduce drag effects. The 0.4 m long supports are bolted to a stainless steel mount which in turn is connected to the stainless steel shaft via grub screws. The same top and bottom mounts are used for both turbine designs.

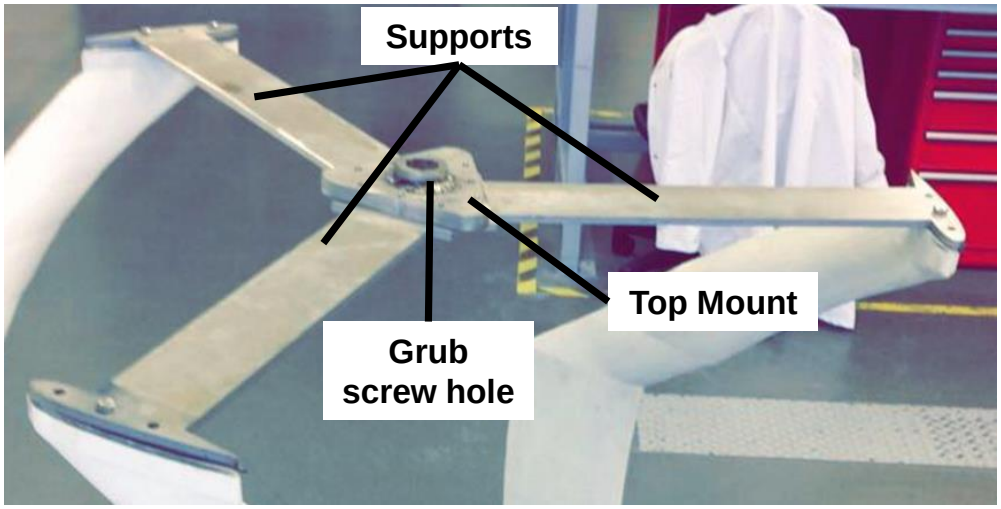

Figure 6-4: Image of stainless steel supports used to mount the turbine on to the rotor shaft.

Table 6-1. List of Turbine A and B design parameters.

Parameter	Turbine A	Turbine B
Radius [m]	0.25	0.5
Height [m]	0.5	1
Chord length [m]	0.04	0.085
Blade profile	NACA 0015	NACA 0015
Number of Blades	3	3
Blade Shape	Spherical	Cylindrical

Stainless steel (316L) is chosen as the shaft material due to its resistance to corrosion and its high strength-to-weight ratio. The shaft diameter is calculated based on the maximum design loads for Turbine B. Under-sizing the shaft could cause it to shear or suffer severe bending depending on the hydrodynamic loading, whereas oversizing the shaft could adversely affect power performance.

Static analysis is carried out for this chosen material to determine the minimum shaft diameter. As this shaft is only to being used in testing for a short period of time, fatigue is not considered in these calculations. Including fatigue effects would lead to an increased minimum shaft diameter. A maximum bending moment and maximum instantaneous torque of 310 N m and 675 N m, respectively, are the operational limits

set, calculated from the BEM model (**Chapter 3**). Mohr's circle, **Figure 6-5**, is applied to determine the maximum in-plane shear stress (τ_{max}) and the maximum and minimum principal stress (σ_1, σ_2).

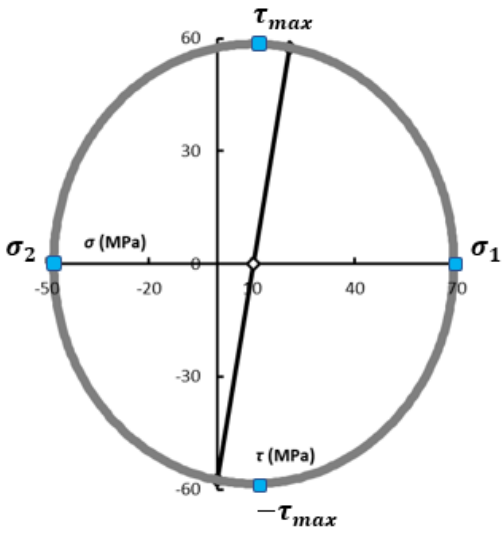

Figure 6-5: Mohr's circle showing maximum in-plane shear stress (τ_{max}) and the maximum and minimum principal stress (σ_1, σ_2).

Von Mises stress (σ_v) is calculated by as:

$$\sigma_v = \sqrt{\sigma_1^2 - \sigma_1\sigma_2 + \sigma_2^2} \tag{6.1}$$

Table 6-2 details the values of the computed stress for this analysis. A shaft diameter of 0.03 m is determined to be a suitable dimension for these tests. The yield strength of stainless steel 316L is 205 MPa, resulting in a factor of safety of 2 for a shaft of 0.03 m diameter.

Table 6-2. Computed stresses for stainless steel (316L) 0.03 m diameter shaft.

Parameter	Value
Bending stress	21.18 MPa
Shear stress	57.53 MPa
Maximum principal stress (σ_1)	69.08 MPa
Minimum principal stress (σ_2)	-47.91 MPa
Maximum shear stress (τ_{max})	58.49 MPa
Von-Mises stress (σ_v)	101.87 MPa
Factor of safety	2.0

6.2.3 Test Setup

The overall test layout and all the associated instrumentation is shown in **Figure 6-6**. The shaft of the turbine is supported by two bearings above and below the turbine. A bottom support housing is mounted onto a U-beam on the floor of the recirculating flume. A thrust bearing, with a corresponding shaft seal, is placed in this housing to support both the radial and axial load experienced. The turbine is also supported at the top by a bearing that is secured into a flat plate. The flat plate is secured to two I-beams that run across the top of the tank using G-clamps.

Scaled turbine experimental tests are generally based on a flow-driven or motor-driven basis Araya and Dabiri (2015). For the flow-driven case, the turbine rotational speed is controlled by balancing the hydrodynamic load against the electrical load or any bearing friction. A generator is required to generate an electrical load, and this increases the costs associated with this method. For flow-driven cases, issues may arise when scaled turbines are unable to produce sufficient torque at start-up to reach a desired rotational velocity. To avoid this issue, a motor can be used to drive the turbine blades actively. This technique is known as motor-driven testing and is the technique applied to these experimental tests. Araya and Dabiri (2015) report no significant difference between the two testing techniques when measuring the power coefficient variation with *TSR*.

The rotational velocity of the turbine is controlled using an Invertek Variable Speed Drive. The rotational velocity of the turbine, along with other critical aspects of the motor performance, are controlled, monitored, and recorded using the software OptiTools studio, Invertek. A range of turbine rotational velocities was applied in a series of tests to identify the precise *TSR* at which peak power performance occurs.

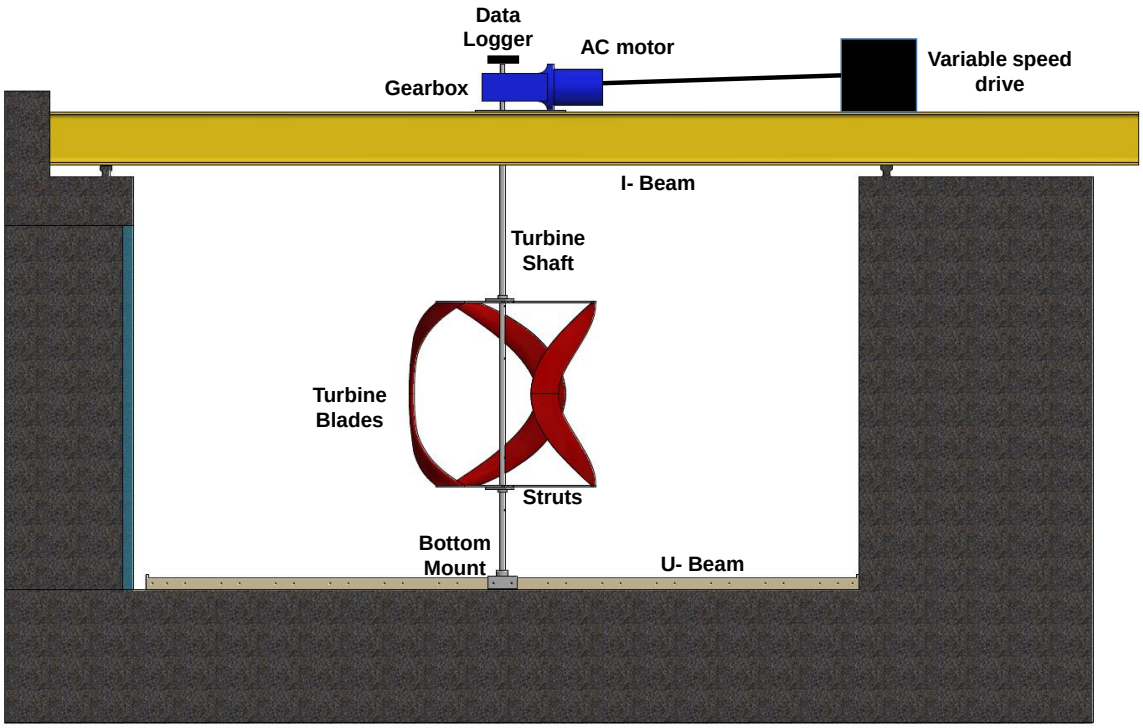

Figure 6-6: The layout of the test setup showing various test components.

A 1.5 kW 3-phase AC TEC motor is used with a 7.5:1 hollow output bore gearbox to drive the turbine. A 1.5 kW braking resistor is installed as a safety feature in the instance of the turbine overpowering the motor. The data logger is mounted on the top of the shaft and rotated with the shaft to ensure the wires from the strain gauges did not become entangled. The motor and gearbox were secured onto the flat plate, as shown in **Figure 6-7.**

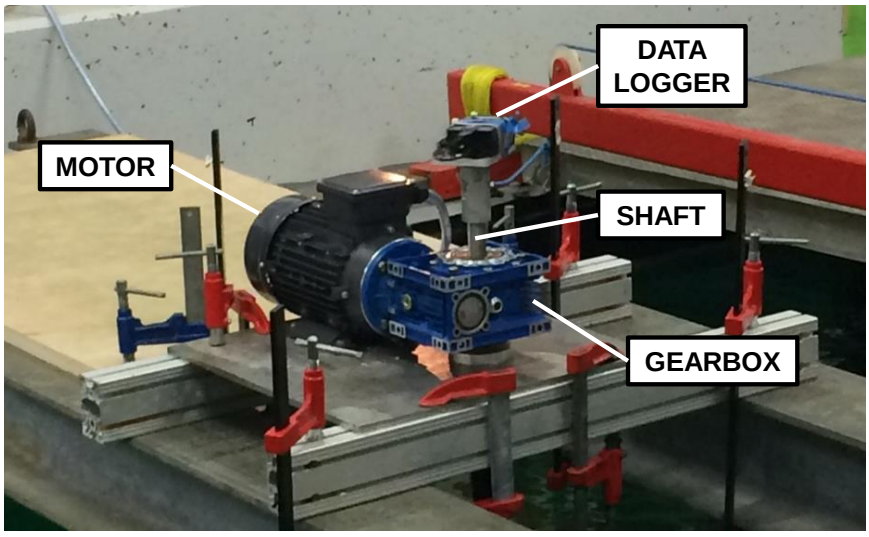

Figure 6-7: Test setup installed at the IFREMER facility showing AC motor, right-angle hollow bore gearbox and VersaLog data logger for recording the strain values.

In determining the turbine power output, the torque is measured under imposed conditions of constant rotational velocity, and the power coefficient ($\bar{C}_P$) is determined for a range of *TSR*. $\bar{C}_P$ and *TSR* are vital indicators of the power performance of the turbine and facilitate the comparison of similar scaled turbine designs. The *TSR* is defined as:

$$TSR = \frac{\omega R}{U_\infty} \tag{6.2}$$

where ω is the turbine rotational velocity, R is the turbine radius (m) and U_∞ is the freestream velocity of the fluid.

The power coefficient, defined as the total power output from the turbine divided by the total power of the fluid passing through the turbine area, is given as:

$$\bar{C}_P = \frac{P}{P_\infty} = \frac{\bar{Q}\omega}{0.5\rho A U_\infty^3} \tag{6.3}$$

where P is the power from the turbine, P_∞ is the total power available from the fluid, $\bar{Q}$ is the average torque per rotation, ρ is the fluid density, and A is the total turbine frontal area. The average torque per rotation, Q_{avg}, is determined by:

$$Q_{avg} = \frac{1}{n}\sum_{i}^{n} Q_i \tag{6.4}$$

where Q_i is the instantaneous torque on the turbine shaft, and n is the number of measurements per rotation. In this experimental study, a fixed turbine rotational velocity was imposed, and the resultant torque is measured. Tests are performed for a range of imposed turbine rotational velocities.

The applied torque to measured strain calibration methodology is the same as described in **Chapter 5**. The applied torques placed on the shaft and corresponding strain measurements are listed in **Table 6-3**. Each torque is applied to the shaft for 60-seconds, each with a 30-second changeover period between each applied torque. The strain value variations with time for the entire calibration tests and the measured values of strain against the corresponding values of applied torque are shown in **Figure 6-8 (a)** and **(b),** respectively. As expected, a linear relationship is obtained, and the equation to convert measured strain to torque is readily established. The calibration

was repeated after the series of testing at IFREMER to ensure consistent strain gauge measurements.

Table 6-3. List of applied torque values (N m) with corresponding measured change in microstrain (-) value.

Applied torque (N m)	Change in measured microstrain (-)
0	0
12.2625	26.41
24.525	50.23
36.7875	76.01

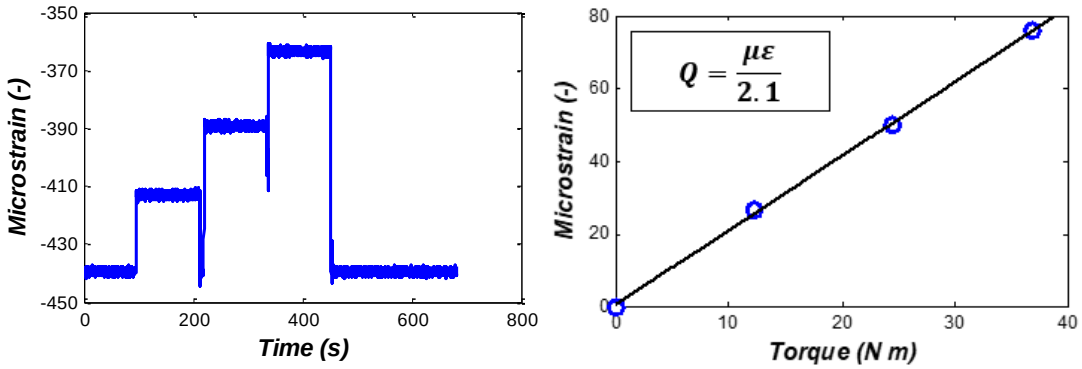

(a) **(b)**

Figure 6-8: (a) Results from the calibration test showing the variation of microstrain measurements with time for applied torques, **(b)** Plot depicting the linear relationship between the measured microstrain ($\mu\varepsilon$) and applied torque (Q). The linear equation relating strain to torque is also included.

6.2.4 Test Procedure

The testing procedure to analyse the performance of each turbine is described in the following. For each experimental test run carried out, the depth of the mid-height of the turbine was fixed at 1 m below the water's free surface. The turbine was positioned equidistant at 2 m from either side wall of the tank.

Table 6-4 and **Table 6-5** present a summary of the test parameters, namely: the freestream velocity (U_∞), rotational velocity (ω), *TSR* and turbine Reynolds Number (Re_D) for each series of tests. As outlined in Bachant et al. (2016), Reynolds number scaling factors which vary by orders of magnitude, may contribute significantly to final test results from full-scale tidal turbines prototypes. BEM results presented in **Chapter 3** (**Figure 3-31**) show that scaling effects contribute significantly to the maximum predicted power coefficient for turbine operation at $Re_D < 2 \times 10^5$. Due to

a mismatch in Reynolds number and other scaling issues, scale models may not perform as well in tank tests as full-scale turbines would during regular operation (Stringer et al., 2016). The turbine prototypes are relevantly scaled based on the Reynolds number (Re_D), so that $Re_D > 10^5$, whereby:

$$Re_D = \frac{\rho D U_\infty}{\mu}. \tag{6.5}$$

where D is the turbine diameter, ρ is the fluid density, U_∞ is the freestream velocity and μ is the fluid viscosity. When comparing the two turbine designs for peak power performance, it is best practice to compare both designs at the same operational Reynolds Number. Reynolds number scaling effects should also be considered when comparing experimental results to model predictions. Each test condition is ran and logged for 1 minute with a changeover of 30 seconds between each condition to ensure steady-state operation.

Table 6-4. List of experimental tests carried out for Turbine A.

U_∞ (m s^{-1})	ω (rad s^{-1})	TSR (-)	Re_D
0.5	0-11	0 – 5.5	2.5×10^5
0.75	0-15	0 – 5	3.75×10^5
1	0-18	0 – 4.5	5.0×10^5
1.25	0-22.5	0 – 4.5	6.25×10^5
1.5	0-24	0 - 4	7.5×10^5

Table 6-5. List of experimental tests carried out for Turbine B.

U_∞ (m s^{-1})	ω (rad s^{-1})	TSR	Re_D
0.5	0-5	0-5	5.0×10^5
0.75	0-7.5	0-5	7.5×10^5
1	0-8.5	0-4.25	1.0×10^6

A flow characterisation study is carried out for Turbine B operating at its optimal *TSR* for a freestream velocity U_∞= 1 m s^{-1} using a laser Doppler velocimeter (LDV) system, as shown in **Figure 6-9 (a)**. The measurement system provides the flow velocity components in the x-direction (parallel to the freestream velocity) and y-direction (perpendicular to the freestream flow and parallel to the free surface of the water). Due to the orientation of the laser, it was not possible to measure the flow in the z-direction. The flow measurements are taken at the mid-height of the turbine at the locations shown in **Figure 6-9 (b)**. Recordings are taken over 4 minutes at each location at a sampling rate of 100 Hz.

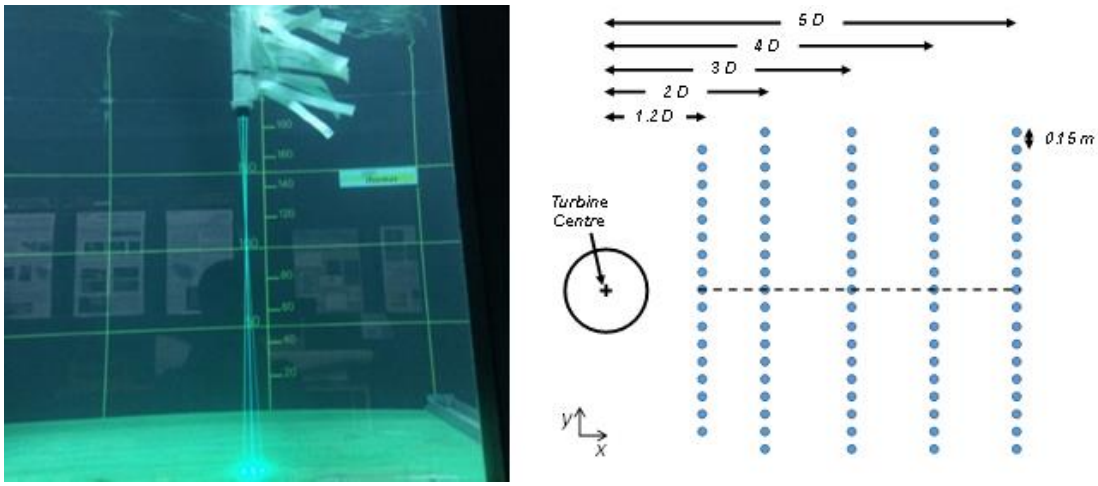

(a) **(b)**

Figure 6-9: (a) Laser Doppler velocimeter (LDV) system operating in the recirculation flume and **(b)** LDV measurement locations downstream of the turbine. All measurements were taken at the mid-height of the turbine.

6.2.5 Blockage Correction

The blockage percentage is the ratio of the frontal area of the turbine to the cross-sectional area of the tank and is a crucial parameter when testing a scaled tidal turbine in a restricted area. Elevated blockage levels can lead to substantial variations in power performance, optimal tip-speed ratio and also wake effects (McCombes et al., 2010). Testing protocols, published by Bahaj et al. (2008), state that experimental power curves for tidal current turbines require a correction coefficient only for blockage ratios greater than 5%. For blockage ratios between 5% and 20%, the results are considered acceptable, provided that an appropriate blockage correction model is implemented. Experimental results achieved for tests with a blockage ratio over 20% are deemed to be inaccurate and thereby unsuitable for model validation. In this series of tests, Turbine A's blockage ratio is 3.5%, so no blockage correction model is required, and measured results are used without adjustment. For Turbine B, the blockage ratio is 13%, so a blockage correction model is implemented before the comparison of results with computational predictions where appropriate.

Ross and Polagye (2020) recommended the implementation of methods developed by Barnsley and Wellicome (1990) or Houlsby et al. (2008); however, both methods require thrust measurements which are not recorded from this series of tests. In the absence of this measurement, a method developed by Werle (2010) is applied to the

data when comparing tests results to model predictions. Werle (2010) gives the following approximations for this model:

$$\frac{\bar{C}_{P,\infty}}{\bar{C}_{P,\infty,max}} \approx \frac{\bar{C}_{P,B}}{\bar{C}_{P,B,max}} \tag{6.6}$$

$$\frac{u_{R,\infty}}{u_{R,\infty,max}} \approx \frac{u_{R,B}}{u_{R,B}} \tag{6.7}$$

where the subscripts ∞ and B indicate the freestream and blocked values and u_R is the radial velocity. From the Betz limit (1920):

$$\bar{C}_{P,\infty,max} = \frac{16}{27} \tag{6.8}$$

$$u_{R,\infty,max} = \frac{2}{3} U_\infty \tag{6.9}$$

and $\bar{C}_{P,B,max}$ and $u_{R,B}$ are taken from Garrett and Cummins (2007) as:

$$\bar{C}_{P,B,max} = \frac{16}{27} \frac{1}{1-\beta} \tag{6.10}$$

$$u_{R,\infty,max} = \frac{2}{3} \frac{U_B}{(1+\beta)} \tag{6.11}$$

where β is the blockage ratio:

$$\beta = \frac{A_D}{A_C} \tag{6.12}$$

A_D is the frontal area of the device, including the turbine, supports and shaft and A_C is the channel area. Combining equations (6.7) - (6.12), the following corrections are derived by Werle (2010):

$$\bar{C}_{P,\infty} \approx \bar{C}_{P,B}(1-\beta)^2 \tag{6.13}$$

$$\frac{u_{R,\infty}}{U_\infty} \approx \frac{u_{R,\infty}}{U_\infty}(1-\beta) \tag{6.14}$$

or in other terms of tip-speed ratio:

$$TSR_\infty \approx TSR_B(1-\beta) \tag{6.15}$$

6.3 Three-Dimensional CFD Methodology

CFD models are developed to assess the capability of RANS modelling techniques in predicting the experimentally measured turbine performance accurately. Learnings and model development procedures presented in this Chapter are taken from the 2D models presented in **Chapter 4** and adapted for the three-dimensionality of the turbine design. Due to the significant computational resources required for full 3D CFD turbine analysis, analyses are limited to Turbine B only. Numerical comparisons between Turbine A and Turbine B are instead performed using BEM-CFD analysis developed in **Chapters 3** and **4**.

6.3.1 Model Development, Boundary Conditions and Grid Generation

The CFD domain dimensions and locations of the turbine are based on the physical tank tests (dimensions listed in **Figure 6-1)**. Model boundary conditions are implemented, as shown in **Figure 6-10**. The boundary conditions simulate as close to the conditions of the experimental tests as computationally realistic. Two cell zones are defined to develop a moving reference frame model to simulate the rotating turbine blades and shaft. The rotating domain extended the full height of the domain and had a diameter of 1.5 D. The domain is assumed symmetrical, so only the bottom half of the turbine is included in the simulation, and a symmetry boundary condition is applied along the plane that passes through the turbine mid-plane. Marsh et al. (2015) adopted this approach to minimise the grid size and recorded minimal differences to results from full-domain simulations. An interface boundary condition is defined between the moving and stationary cell zones. The inlet velocity applied to the domain is set at 1 m $s^{-1,}$ and the turbulent intensity value was set at 1.5% to match the turbulent intensity levels for experimental tests: the turbine blades and shaft surfaces defined as a no-slip wall. Simulations are performed at limited conditions without the inclusion of the rotating shaft for comparison. The supporting struts that connect the blades to the shaft are not included. It was assumed that the flow had fully recovered at the outlet, so a 0 Pa gauge pressure condition was applied there along with matching turbulent boundary conditions to those of the inlet. The turbulence model selected is the SST Transition turbulence. This turbulence model is detailed in **Chapter 2** and **Appendix**

A.2. The strengths of this turbulence model have been identified in **Chapter 4**. Specific meshing requirements for this turbulence model are presented below.

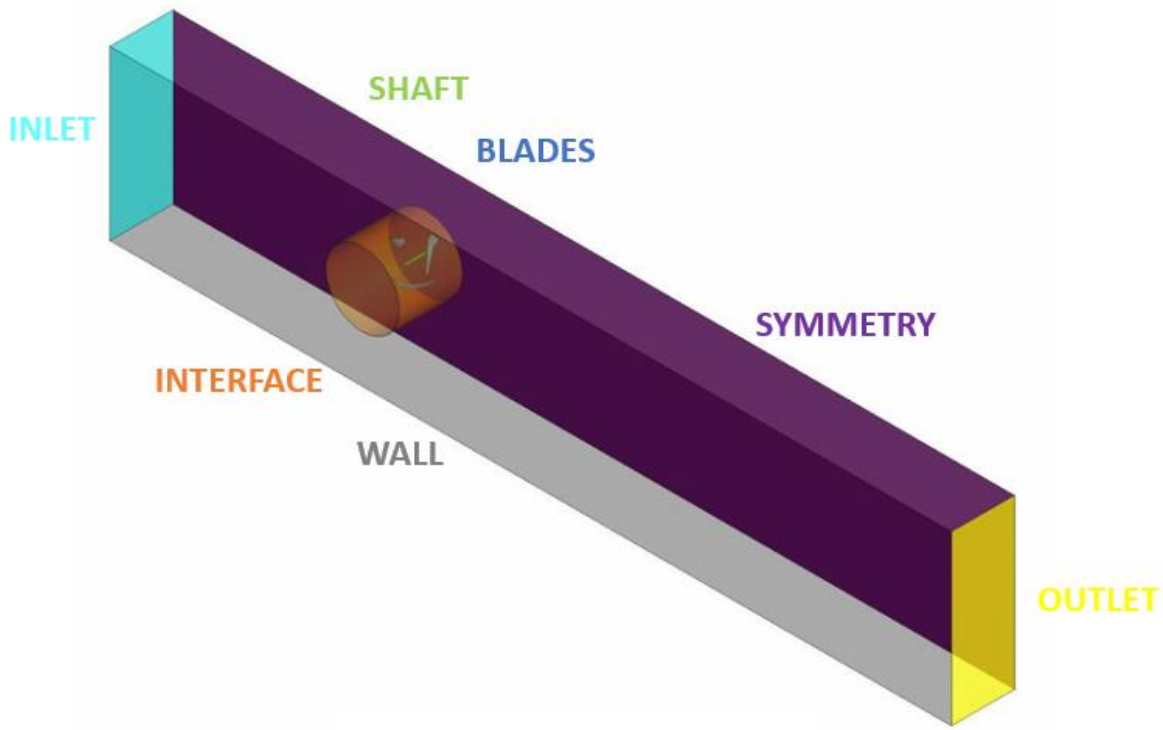

Figure 6-10: Computational domain for 3D CFD simulations of Turbine B. Boundary conditions and rotating cell zone highlighted.

The rotational velocity, ω_{rot}, applied to the three blades is given as:

$$\omega_{\mathrm{rot}} = \frac{U_{\infty} TSR}{R} \tag{6.16}$$

where R is the turbine radius and U_{∞} is the fluid freestream velocity. The instantaneous torque coefficient, $C_{\mathrm{Q,i}}$, is given as:

$$C_{\mathrm{Q,i}} = \frac{Q_{\mathrm{i}}}{0.5\rho A {U_{\infty}}^{2} R} \tag{6.17}$$

where Q_{i} is the instantaneous torque, U_{∞} is the freestream velocity and A is the turbine frontal area. An averaged torque coefficient for each rotation, $\bar{C}_{\mathrm{Q}}$, is computed as:

$$\bar{C}_{\mathrm{Q}} = \frac{1}{2\pi} \int_{0}^{2\pi} C_{\mathrm{Q,i}} \, d\theta \tag{6.18}$$

Finally, the average power coefficient is computed by:

$$\bar{C}_P = \bar{C}_{\mathrm{Q}}\, TSR \tag{6.19}$$

6.3.2 3D CFD Discretisation and Validation

The steady-state flow field solution from the moving reference frame simulation is used as the initial solution for the transient sliding mesh calculation, thus reducing the overall time to achieve a converged solution. The pressure and velocity are coupled using the COUPLED algorithm. The Green-Gauss node-based method is used for the evaluation of gradients. First-order upwind discretisation schemes are applied for the momentum, turbulent kinetic energy, specific dissipating rate, intermittency and the transitional Reynolds number for the first two turbine rotations before switching to second-order discretisation schemes for the remaining rotations to increase the solution accuracy. A second-order temporal discretisation scheme is applied to the simulations. The convergence criterion for the residuals is set to 10^{-5} per time step, and the convergence of the average torque coefficient per rotation (equation 5.12) is also monitored. A convergence criterion of 1% is set for the variation of the average torque coefficient from one rotation to the next.

As shown in **Table 6-6**, the mesh is systematically refined to identify the optimal spatial discretisation with focus placed on the critical region around the blade surfaces. Similar mesh sizing is applied on either side of the stationary and rotating interface to ensure a uniform mesh size is achieved in this region. A mesh containing 13.1×10^6 elements is used for all subsequent simulations. This discretised model is shown in **Figure 6-11**, highlighting mesh refinement at critical regions, including inflation layers at hydrofoil walls. An initial first layer height, *y*, is specified around the blade surfaces and shaft (equation 4.3) to ensure a y^+ value < 1, as shown in **Figure 6-12**.

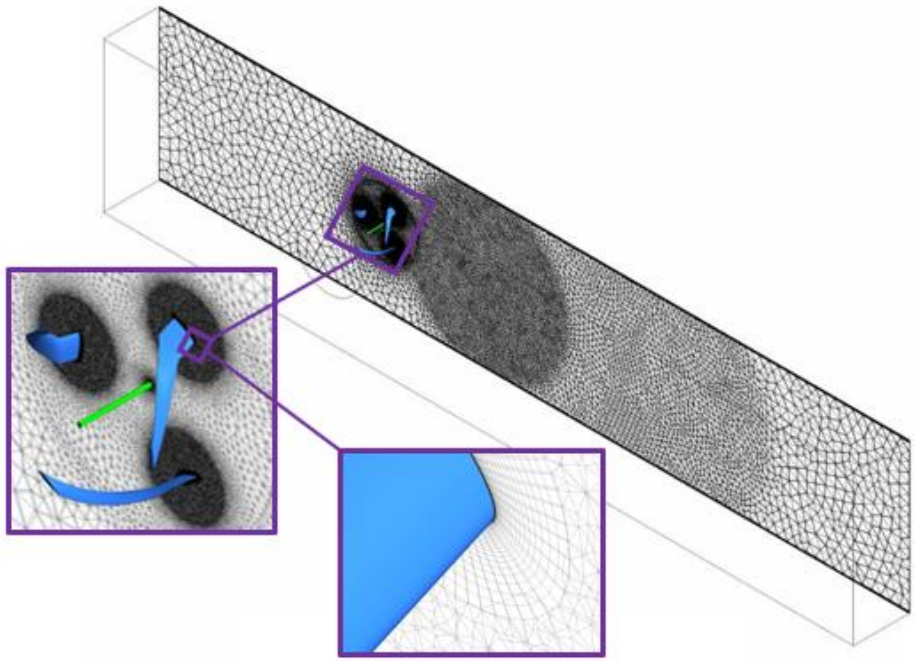

Figure 6-11: Two-dimensional section of the mesh showing refinement at the wall regions, including inflation layers at the blade and shaft surfaces. Inflation layers are also applied to the bottom and side walls of the domain.

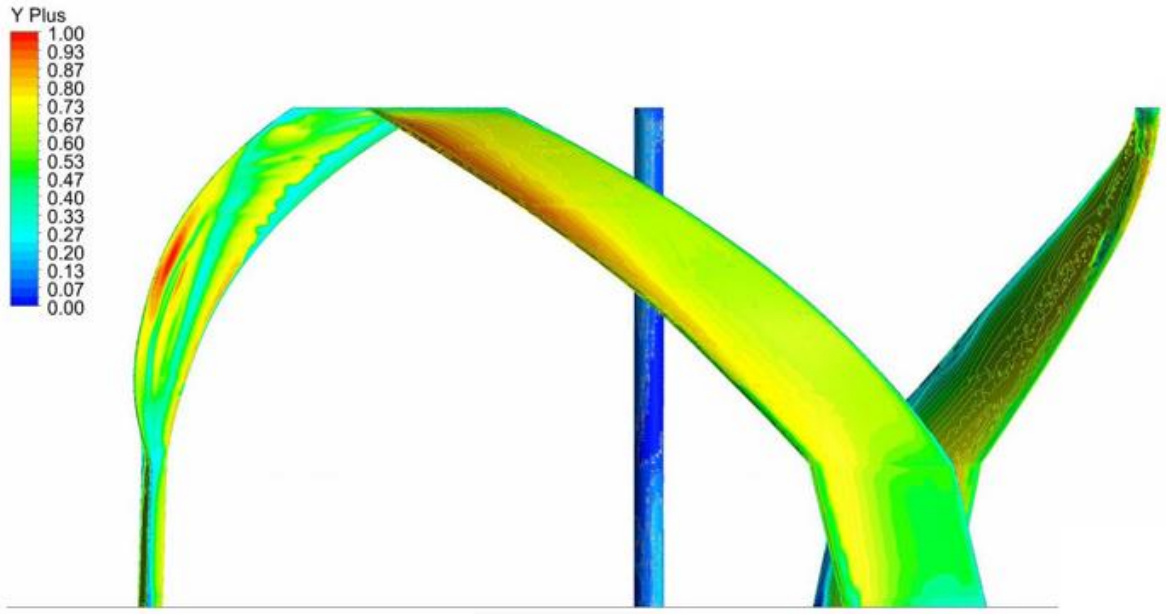

Figure 6-12: Average y+ value along the blade surfaces and turbine shaft, evaluated over a full rotation (*TSR* = 3).

Richardson's Extrapolation (equations. (4.13) - (4.15)) is applied to assess the spatial discretisation of the full turbine 3D CFD model for *TSR* = 3. Results for the converged averaged power coefficient, $\bar{C}_P$ for each of the four meshes is presented in **Table 6-6**.

Table 6-6. Mean power coefficient C_P, results for a series of four increasingly refined meshes for *TSR* = 3.

Mesh	Total Elements	$\overline{C}_P$	% $\overline{C}_P$
A	5.2×10^6	0.265	-28.9
B	8.7×10^6	0.293	-11.1
C	13.1×10^6	0.320	-2.9
D	19.4×10^6	0.324	0.7
Richardson's extrapolation value		0.327	

A temporal discretisation study is carried out for the full turbine CFD model for a *TSR* = 3. The study focuses on establishing the optimal time step size and determining the number of rotations required to achieve the convergence criterion for the average torque coefficient.

Table 6-7 present results for different time step increments based on the size of each degree increment per time step. To achieve the desired accuracy, a time step increment equivalent to $\Delta\ 1^o$ is selected for all simulations.

Table 6-7. C_P results for a range of Δ^o/step for *TSR* = 3.

Δ^o/step	$\overline{C}_P$
4^o	0.290
2^o	0.311
1^o	0.320
0.5^o	0.322

The average time for a single simulation of steady-state turbine performance using a mesh containing 13.1×10^6 elements and a time-step equating to 1^o of rotations took 168 hours on 72 processers using the Irish Centre for High-End Computing (ICHEC) multi-core machine. There are limited previous 3D CFD studies of vertical-axis turbines simulations that implement a comparably high number of elements that the author is aware of (Mannion et al., 2018; Marsh et al., 2015).

6.4 Results and Discussion

In this section, experimental test data characterising the performance of Turbine A and Turbine B are presented. Comparisons of test results with model predictions are also

included. Images of the two scaled prototype designed mounted in the recirculating flume at IFREMER are shown in **Figure 6-13**.

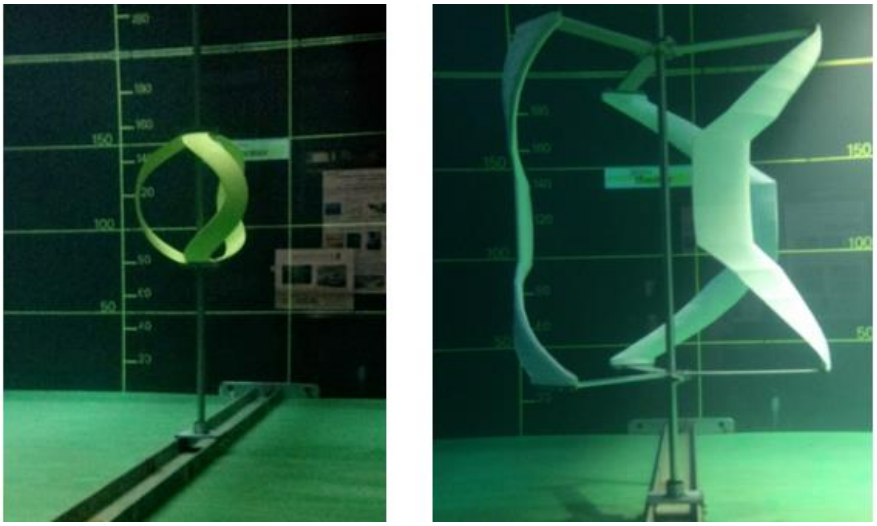

(a) **(b)**

Figure 6-13: Image of scaled prototypes tested at the IFREMER facility, Boulogne sur-Mer. **(a)** Turbine A and **(b)** Turbine B.

6.4.1 Experimental Test Results

Figure 6-14 and **Figure 6-15** show plots of the variation of $\bar{C}_P$ with *TSR* for five different freestream velocities ranging from 0.5 to 1.5 m s^{-1} for Turbine A and Turbine B, respectively. For the experimental results presented in this section, blockage ratio corrections detailed in **Section 6.2.6** are applied to Turbine B, which has a blockage ratio of 13.5%. These corrections are not required for Turbine A, which has a blockage ratio of 3.5%. Mean power coefficients are presented, while error bars indicate maximum and minimum mean power coefficient value per rotation. Each plot follows a typical power curve; an increase in *TSR* leads to an increase in $\bar{C}_P$ until a peak $\bar{C}_P$ is achieved. Further increases in *TSR* beyond the optimal *TSR* result in a reduction in $\bar{C}_P$. The increase observed in the fluctuations between the minimum and maximum $\bar{C}_P$ as the *TSR* increases is likely attributable to secondary flow effects from the rotating shaft and struts, which has a more pronounced impact on the flow at higher rotational velocities. The peak power coefficient observed for Turbine A ranges from 0.22 to 0.27 at *TSR* between 2.5 and 3 for the tested freestream velocities. For Turbine B, the peak power coefficients ranged from 0.3 to 0.33 at optimal *TSR* between 3.25 and 3.5.

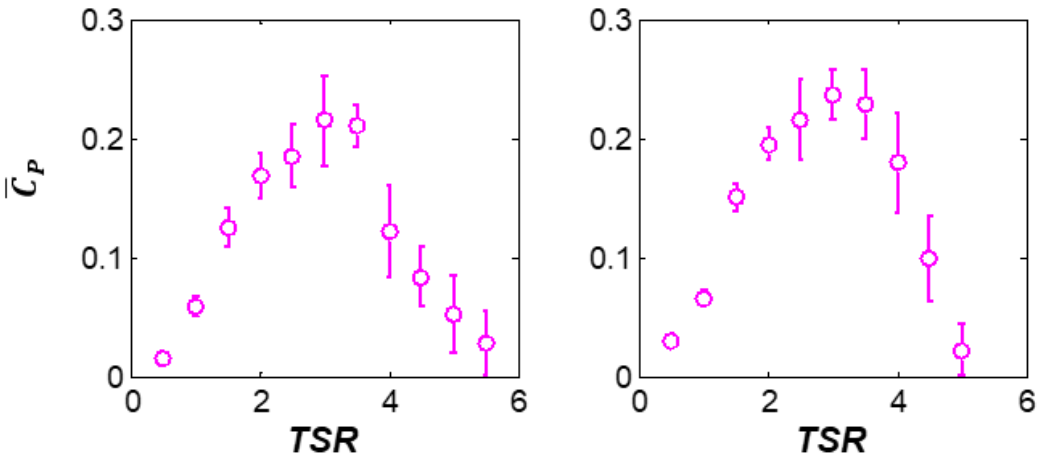

(a) *U_∞ = 0.5 m s^{-1}* ***(b)*** *U_∞ = 0.75 m s^{-1}*

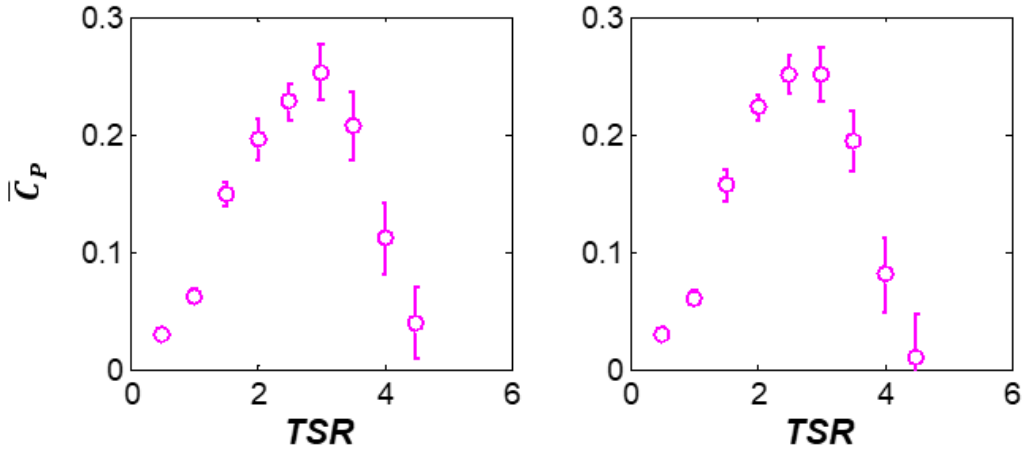

(c) *U_∞ = 1 m s^{-1}* ***(d)*** *U_∞ = 1.25 m s^{-1}*

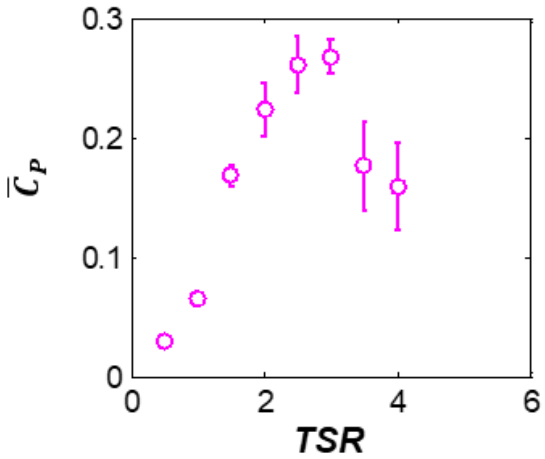

(e) *U_∞ = 1.5 m s^{-1}*

Figure 6-14: Variation of power coefficient with tip-speed ratio for Turbine A for: **(a)** U_∞ = 0.5 m s^{-1}; **(b)** U_∞ = 0.75 m s^{-1}; **(c)** U_∞ = 1 m s^{-1}; **(d)** U_∞ = 1.25 m s^{-1} and **(e)** U_∞ = 1.5 m s^{-1}. The error bars shown reflect the minimum and maximum average power coefficient values recorded per rotation at each *TSR*.

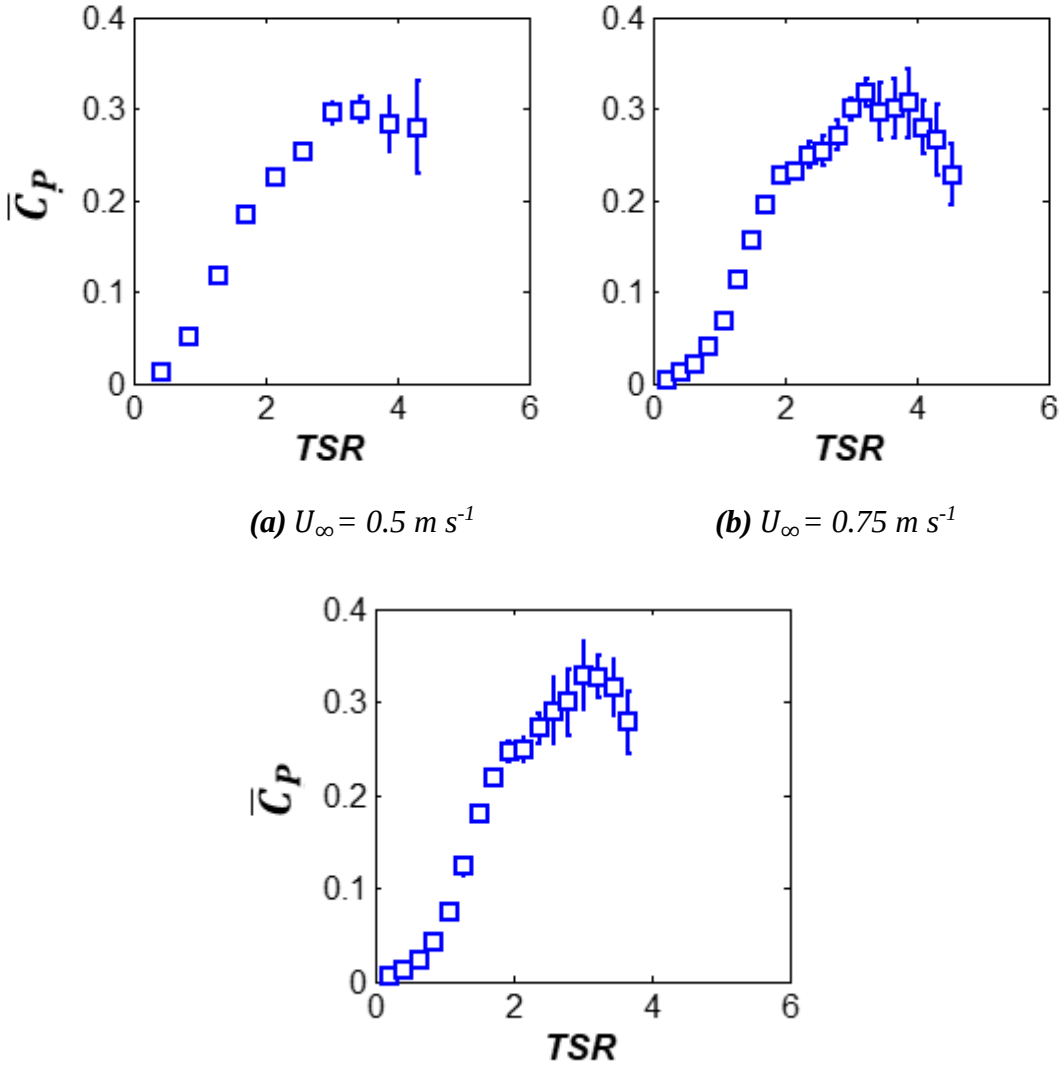

(a) *U_∞ = 0.5 m s^{-1}* ***(b)*** *U_∞ = 0.75 m s^{-1}*

(c) *U_∞ = 1 m s^{-1}*

Figure 6-15: Variation of power coefficient with tip-speed ratio for Turbine B. **(a)** U_∞ = 0.5 m s^{-1} **(b)** U_∞ = 0.75 m s^{-1} ; and **(c)** U_∞ = 1 m s^{-1} .

Reynolds number scaling results are presented in Figure 6-16 **(a)**. Hydrodynamic forces, i.e. lift and drag, are heavily influenced by Reynolds numbers < 10^6. As presented in **Chapter 4**, at lower Reynolds numbers, for the same angles of attack, lift forces decrease while drag forces increase. It can be noted from the results presented in this Chapter that with increasing Reynolds number, i.e. increasing freestream velocity, the maximum power coefficient increases. As the Reynolds number increases, the hydrodynamic forces become independent of the Reynolds number, and the maximum power coefficient is trending towards a Reynolds number independent results.

The variation of maximum power coefficient with freestream velocity for Turbine A is presented in **Figure 6-16**. Freestream velocities from 0.5 m s^{-1} to 1.5 $m\ s^{-1}$ corresponds to a range of Reynolds number, Re_D, from 2.5×10^5 to 7.5×10^5. The optimal *TSR* for peak power performance is between 2.75 and 3.25 for the freestream velocities investigated. As observed in the results, as the free-stream velocity is increased, the maximum power coefficient is also increasing, indicating that a Reynolds number independent solution has not been achieved for this prototype under the applied test conditions.

Similar results are presented for Turbine B in Figure 6-16. For these tests, Re_D varied from 0.5×10^6 to 1×10^6, and the optimal *TSR* for peak power performance is between 3.25 and 4. Again from these results, it is noted that the experimentally applied freestream velocities are not in the regime of Reynolds number independence for Turbine B, suggesting that an up-scaling of the turbine prototype size would lead to an increased maximum power coefficient. Comparing both sets of results, it is clear that Turbine B is closer to achieving a Reynolds Number independent solution, as expected due to the higher Reynolds number associated with that series of tests.

While experimental results for Turbine A and Turbine B have not achieved Reynolds number independence, they can still be used effectively to validate CFD and BEM models, provided that prototype dimensions and test flow conditions, e.g. Reynolds numbers, are accurately matched.

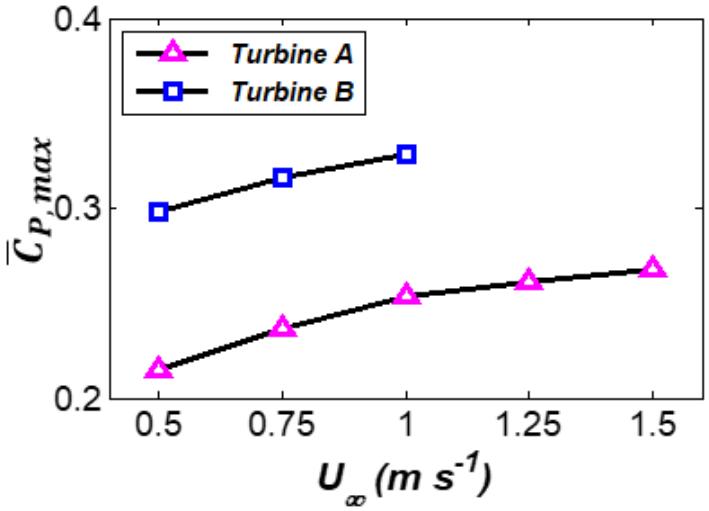

Figure 6-16: Variation of maximum power coefficient with Reynolds number/freestream velocity for Turbine A and Turbine B.

The power performance curves for Turbine A and Turbine B for the same Reynolds number ($Re_D = 7.5 \times 10^5$) are presented for comparison in **Figure 6-17**. The maximum power coefficient for Turbine B is 25% higher than that of Turbine A. Turbine B's optimal *TSR* (at maximum power coefficient) is ~3.3, while Turbine A's optimal *TSR* is 3. The torque generated by a turbine blade is directly proportional to the turbine radius. Turbine B's blades design spiral around a spherical surface, and therefore the radius from the shaft to a blade section is uniform throughout the height of the turbine. In contrast, Turbine A is designed so that the blades spiral around the surface of a sphere. Therefore, the radius from the shaft to a section of the blade depends on the coordinate along the turbine height. The maximum radius is at the mid-height plane, with the minimum/zero radius at the top and bottom of the turbine. As highlighted in **Figure 3-25**, this significantly contributes to the decreased power in turbine designs that are based on mapping of blade geometries onto cylindrical surfaces.

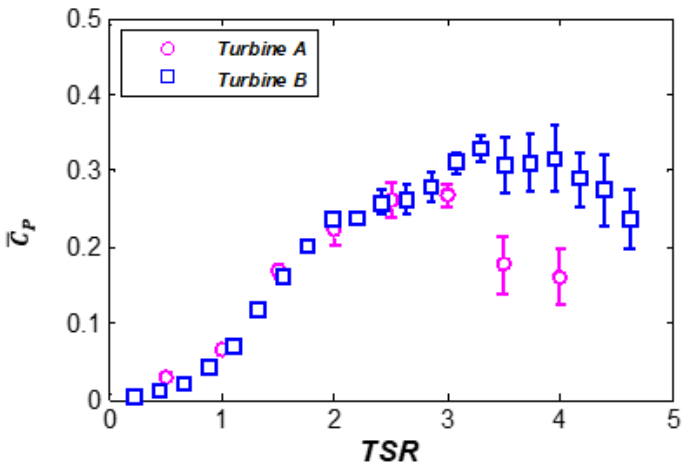

Figure 6-17: Variation of power coefficient with *TSR* for Turbine A (U_∞= 1.5 m s^{-1}) and Turbine B (U_∞= 0.75 m s^{-1}), both turbine Reynolds numbers is Re_D = 7.5 x 10^5. Turbine B results have been corrected to account for blockage effects.

6.4.2 CFD Model Visualisations

In this section, preliminary observations from CFD model visualisation plots are presented for Turbine B operating at its optimal *TSR* in a freestream velocity of 1 m s^{-1}. **Figure 6-18** shows the computed flow velocity magnitude distributions and pressure distributions at three plane sections for a free-stream velocity of 1 m s^{-1}. The three planes, P1, P2 and P3, are three horizontal sections at 5%, 25% and 45% of the total turbine height. Results are shown for steady-state operation with the instantaneous

blade position corresponding to high instantaneous power output. The turbine orientational configuration angle (TOCA), defined in **Chapter 3**, for Blade 1 is 90º. For this TOCA, a favourable pressure distribution is observed at the blade surface at section P2 and P3, as shown in **Figure 6-18 (b)** and **(c)**. These favourable pressure distributions contribute to larger lift forces while minimising drag, maximising the torque contribution from that blade. However, for the same blade, at the same TOCA, at section P1 (**Figure 6-18 (a)**), Blade 1 is not favourably oriented, with a corresponding reduction in pressure and lift force. This again illustrates the key design benefit of the turbine design (as demonstrated in the BEM analysis in Chapters 3 and 4); at any given position, a partial section of one of the turbine blades will be optimally positioned so that torque and power fluctuations during a rotation are lower than an equivalent straight bladed turbine design. Simulations also predict that the flow reduction (i.e. the velocity applied to downstream blades) is ~$0.2U_\infty$ at sections P2 and P3, and ~$0.3U_\infty$ at section P1.

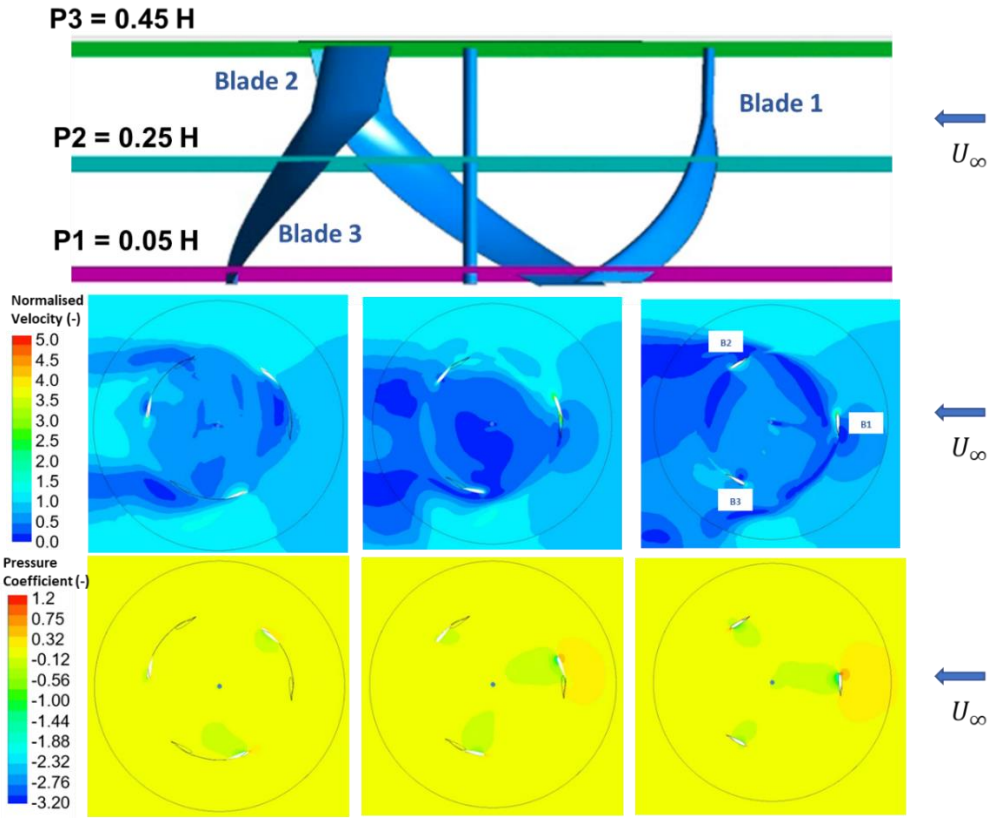

(a) P1 **(b)** P2 **(c)** P3

Figure 6-18: Pressure coefficient and normalised velocity distribution at three horizontal sections through the turbine. Blade numbers and freestream velocity direction indicated (TSR = 3.25, U_∞ = 1 m s^{-1}).

Figure 6-19 (a) shows the computed velocity vectors through the turbine at select elements on planes P1, P2 and P3, revealing highly complex 3D flow patterns. Complex flow patterns are computed near to the turbine, particularly at the transition from straight to curved sections of each blade. Significant out-of-plane flow is computed in such regions on planes P1 and P2, but not plane P3 due to the symmetrical turbine design. To highlight this observation, the out-of-plane flow velocity components in the z-direction are plotted directly in **Figure 6-19 (b**). The largest out of plane flows are observed for Blade 1 (TOCA = 90º) in the upstream half of the turbine at P2.

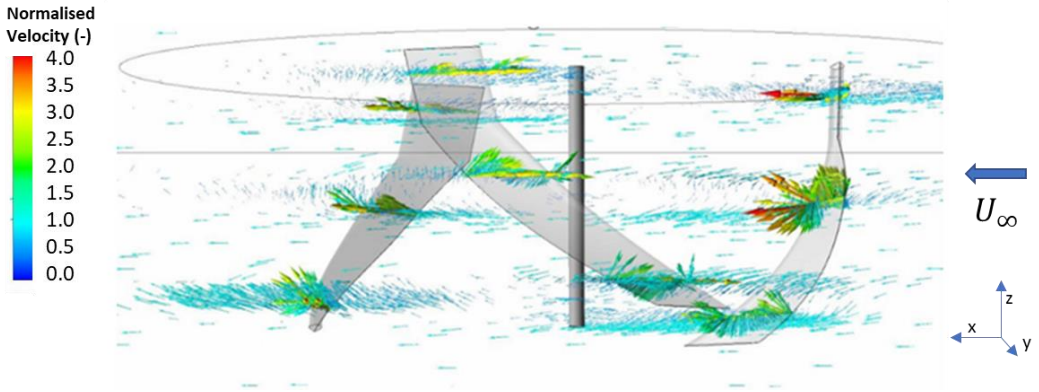

(a)

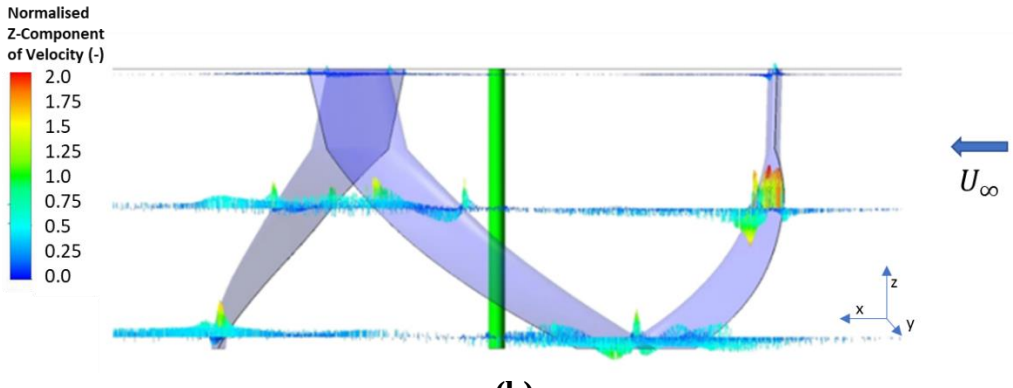

(b)

Figure 6-19: Velocity vector plots for Turbine B at three section heights (U_∞ = 1 m s^{-1}, *TSR* =3.25), **(a)** Normalised three-dimensional velocity vector plots and **(b)** Normalised out of plane flow.

6.4.3 Comparison of Model Predictions and Test Results

In this section, experimental results are compared to available model predictions for both turbine designs. The BEM results presented are generated using the model described in **Chapter 3** utilising the CFD-based hydrofoil dataset presented in **Chapter 4** as model input for the NACA 0015 profile. The experimental results for

Turbine A can be directly compared to BEM model predictions due to a blockage ratio of less than 5%. The experimental results for Turbine B are adjusted using the blockage ratio model described above.

Figure 6-20 presents a comparison between the experimental results and the BEM model predictions for Turbine A for freestream velocities of 0.5, 1 and 1.5 m s^{-1}, respectively. The root-mean-squares errors (RMSE) for all applied freestream velocities are presented in **Table 6-8**. The model accurately predicts the optimal *TSR*. The model over-predicts the maximum coefficient by between 5 and 18% across the range of tests. In all cases, the BEM model predicts within the error bars of the experimental results at peak performance.

BEM model predictions in all cases are most accurate at lower and optimal *TSR*. Dynamic stall effects heavily influence the turbine performance in this regime and the strengths of the dynamic stall model, implemented in the BEM code in **Chapter 3**, are evident. The CFD-based lift and drag coefficients presented in **Chapter 4** also proved to increase the accuracy of predictions in the critical stall region, linked to turbine operating at low *TSR*.

Beyond the optimal *TSR*, the BEM predictions are less accurate. However, such excessively high *TSR* (and corresponding low power coefficients) are suboptimal and are avoided in standard operation. The discrepancies may be attributed to the BEM model's inability to account for the effects of the turbine shaft and supports on the flow downstream. The influence of these flow effects, often referred to as secondary effects, are more predominately noticed at higher *TSR*, as noted by Parschivoiu (2002).

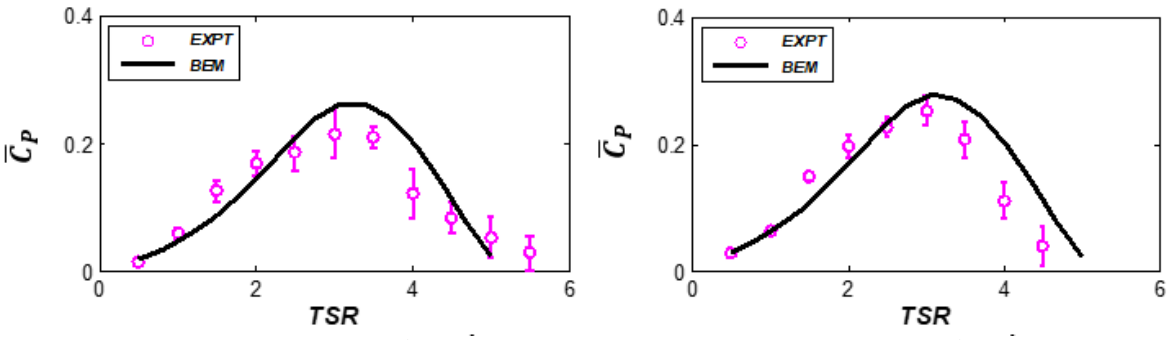

(a) U_∞ *= 0.5 m* s^{-1} ***(b)*** U_∞ *= 1 m* s^{-1}

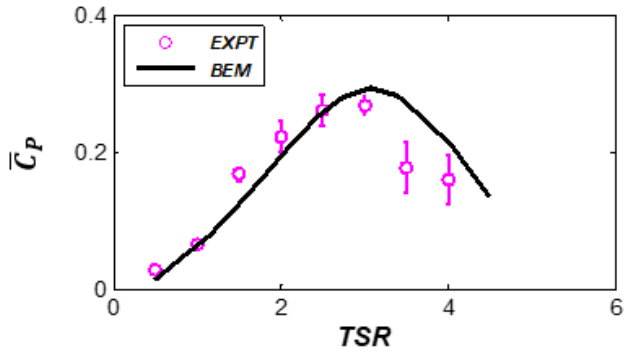

(c) U_∞ *= 1.5 m s*$^{-1}$

Figure 6-20: Comparison between experimental data and model predictions of the variation of power coefficient with tip-speed ratio for Turbine A. **(a)** U_∞ = 1.5 m s^{-1}, **(b)** U_∞ = 1.0 m s^{-1} and **(c)** U_∞ = 1.5 m s^{-1}.

Table 6-8. RMSE between model predictions and experimental test data for Turbine A.

U_∞ (m s^{-1})	RMSE
0.5	0.049
1	0.055
1.5	0.057

In **Chapter 4,** a direct comparison between experimental data and BEM model predictions for a straight-bladed vertical-axis turbine was presented. The advantages of the newly developed CFD-based dataset of lift and drag coefficients over the traditional panel-method (PM) based dataset (Sheldahl and Klimas, 1981) were highlighted. Similarly, in this Chapter, this comparison is carried out for Turbine B with the results presented in **Figure 6-21**. The results presented in this figure are corrected to account for blockage correction as appropriate to facilitate direct comparison with the freestream conditions implemented in the BEM models. The BEM model incorporating a CFD-based lift and drag dataset (BEM-CFD model) is found to be more accurate than a standard panel method BEM approach (BEM-PM model) in terms of the RMSE across a wide range of *TSR* (0< *TSR* < 3.5), as presented in **Table 6-10**. While the BEM-PM model provides accurate predictions of the peak power coefficient, it overpredicts the *TSR* at which peak power output occurs.

The BEM-CFD approach accurately predicts the optimal *TSR* compared to the experimentally measured value. This approach also provides accurate results at lower *TSR* and a computed peak power coefficient of 0.38, compared to the experimentally observed, blockage corrected, value of 0.33 ± 0.025. This overprediction may be

attributable to the BEM assumption that there is no hydrodynamic interaction between different blade elements. This assumption is likely not entirely agreeable for this design case due to the BTT blades' spiral geometry. This is investigated further below using CFD flow visualisation techniques. The BEM model's inability to account for shaft flow effects downstream may also contribute to this over prediction.

Also included in **Figure 6-21** are the predictions from the full 3D CFD simulations. Due to limited computational resources, CFD simulations focused on the peak power range, $2.5 < TSR < 4$. The 3D CFD model accurately predicts the optimal *TSR*, ~3.2, and slightly under predicts the peak power coefficient. This predicted power coefficient, 0.30, is at the lower limit of the error recorded in the experimental data at peak power, 0.33 ± 0.025.

The computational cost and RMSE when comparing model predictions to test data are presented in **Table 6-9**. It is worth noting that BEM calculations, covering the range of appropriate TSR, take 30 seconds on a single processor, compared to 7 days on 72 processors for a single TSR 3D simulation. The only significant computational cost associated with the BEM-CFD method lies in generating the CFD-based dataset of lift and drag coefficients. However, once generated for a specific hydrofoil design, these data can readily be input to a BEM calculation with negligible additional computational cost, resulting in improved accuracy compared to the BEM-PM method. Therefore, the BEM-CFD methodology provides a computationally efficient and accurate design and analysis tool that can be used to optimise turbine design parameters (e.g. chord length, turbine radius, blade curvature).

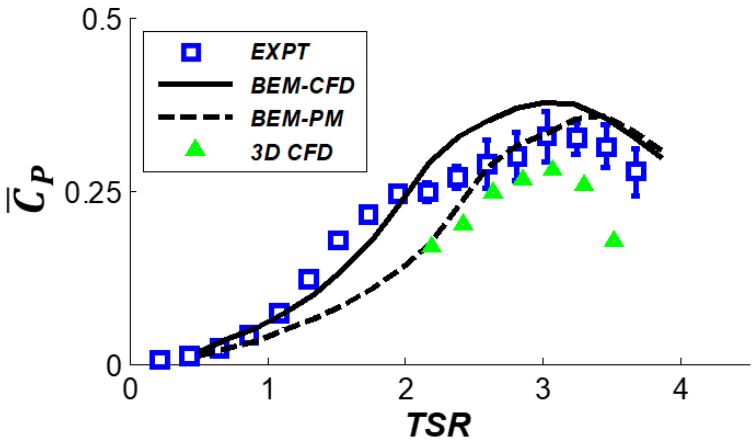

Figure 6-21: Comparison of results for power coefficient variation with *TSR* from experimental tests, 3D CFD simulation and BEM model predictions which

implement CFD-based dataset and the panel-method based dataset for Turbine B (U_∞ = 1 m s^{-1}).

Table 6-9. RMSE between experimental test data and model predictions for Turbine B. The computational expense of each model is also listed.

	RMSE-BEM-CFD	**RMSE-BEM-PM**	**RMSE-3D CFD***
RMSE	0.045	0.062	0.036
CPU Hours	18,600	N/A	72,500

*Only 6 points included for 3D CFD simulations

It should be noted at this point that the blockage correction model (Werle, 2010), applied to the experimental data in the results presented in **Figure 6-17** and **Figure 6-21**, is disputed. Ross and Polagye (2020) implemented several blockage corrections methods for high blockage (β = 36%) test data for a vertical-axis turbine and compared results to low blockage (β = 3%) test data. They noted that although the method presented by Werle (2010) accurately corrected the maximum power coefficient, it predicted this maximum power coefficient at a lower optimal *TSR* than what was recorded in the low blockage tests. Methods developed by Barnsley and Wellicome (1990) or Houlsby et al. (2008) are recommended instead. However, these correction models require measured thrust measurements, which were not recorded as part of the tests at IFREMER. Future developments should consider the addition of a load-cell to the test-set up to measure this force. Ross and Polagye (2020) suggest that these correction factors may not be sufficiently accurate for all test cases, and further investigation in the area is required to establish customised test specific blockage factors.

Vertical-axis turbines hold a distinct advantage over their horizontal-axis counterparts in the context of large-scale multi-row array layouts, as such designs can be placed in closer proximity (Bachant and Wosnik, 2015). Accurate model predictions of the bypass and wake flow can facilitate the optimal placement of turbines to maximise power output. One strength of CFD models over BEM is the ability to predict flow velocities and visualise flow patterns through and downstream of the turbine. **Figure 6-22** shows the CFD predicted flow velocity distributions at five equidistant sections, 1 m apart, downstream of the turbine. Significant non-uniform disruption of the free

stream velocity is computed downstream of the turbine. Close to the turbine, significant reductions (~80%) in the flow velocity are computed in a 2 m width region. With increasing distance from the turbine, the zone of disrupted flow becomes wider. At the final section, 5 m from the turbine, the wake zone extends almost the full width of the flume (~4 m); however, the reduction in velocity is not as pronounced and is only a maximum of ~25% lower than the freestream velocity. The computed velocities downstream of the turbine indicate a significant power reduction in an aligned array. Even at a distance of five diameters downstream of the turbine, the velocity is reduced by up to 15%, resulting in a ~40% reduction in total power output at a typical tidal stream site with a freestream velocity of 2 m s^{-1}. This highlights the importance of optimising the positioning of turbines in the context of a multi-row array layout.

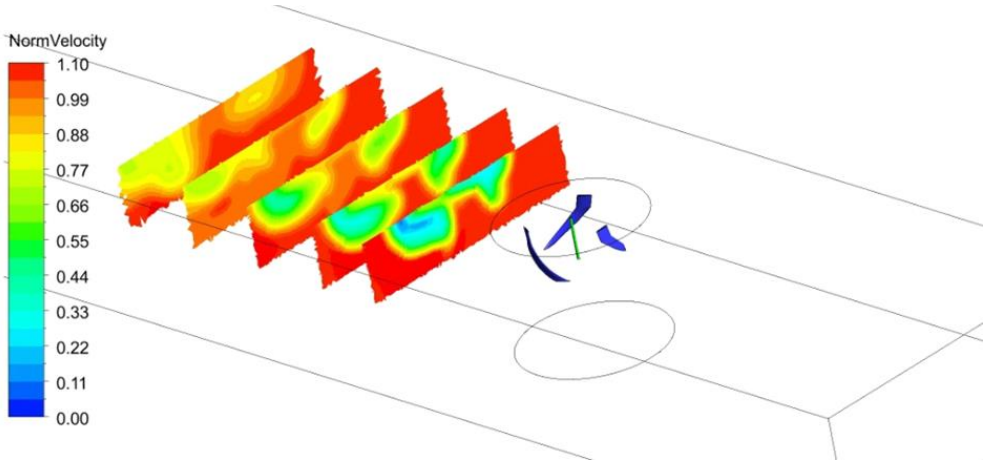

Figure 6-22: Normalised wake velocity profile downstream of Turbine B at five equidistant sections (U_∞ = 1 m s^{-1}, *TSR* = 3.5).

CFD simulations were also carried out without the inclusion of the turbine shaft for this test condition *(U_∞* = 1 m s^{-1}, *TSR* = 3.5*)*. Excluding the shaft had negligible effects on power performance prediction; however, effects were noted in downstream flow patterns. In **Figure 6-23**, model predictions with and without the shaft are compared to experimentally measured data for the first section downstream. Model predictions with the shaft included provide better accuracy when compared to measured test values, with an r^2 value of 0.79 achieved. An r^2 value of 0.53 is determined between the test data and model predictions, with the shaft excluded. There are negligible impacts computationally when including the shaft in the CFD simulations.

A comparison between the CFD model predictions and LDV experimentally measured velocity values for five vertical sections downstream of the turbine are presented in

Figure 6-24. Values are compared at the mid-height of the turbine. The model predictions are averaged over one steady-state rotation, while the experimental measurements are taken over four minutes for each of the points indicated in **Figure 6-9**. A slight increase in velocity is observed close to the wall at the initial downstream sections, **Figure 6-24 (a)** and **(b)**. This behaviour is expected due to the relatively high blockage percentage for these experimental tests. Larger discrepancies between the model and measured velocities are observed further downstream of the turbine, as shown in **Figure 6-24 (d)** and **(e)**. Reduced mesh density and the selection of CFD modelling approach are likely two contributing factors to these discrepancies. The RANS modelling approach involves averaging the flow and may lead to inaccuracies in dissipating the flow downstream of the turbine. The implementation of large-eddy simulations (LES) methods would increase the accuracy. However, such simulations require a much more refined mesh to solve the flow field accurately, which would require additional computational resources beyond the scope of this research. It is an area of possible future research as the ability to predict the flow field downstream of the turbine accurately would facilitate the optimal positions of additional turbines for maximum power output in the case of a multi-row array layout.

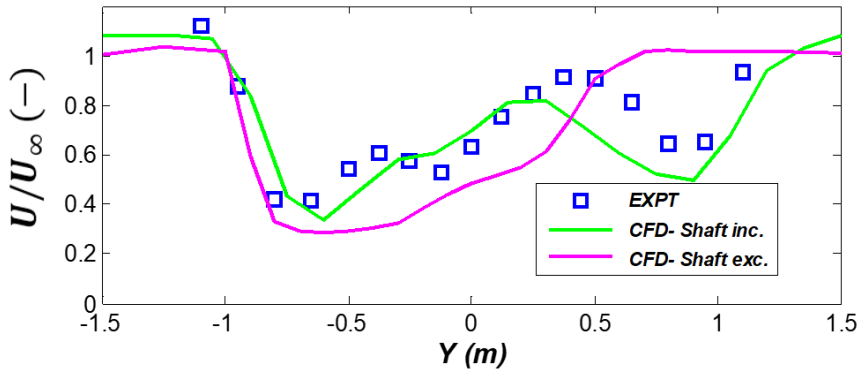

Figure 6-23: Flow velocity measurements variation with distance downstream of Turbine B at the mid-plane of the turbine. (U_∞ = 1 m s^{-1}, *TSR* = 3.5).

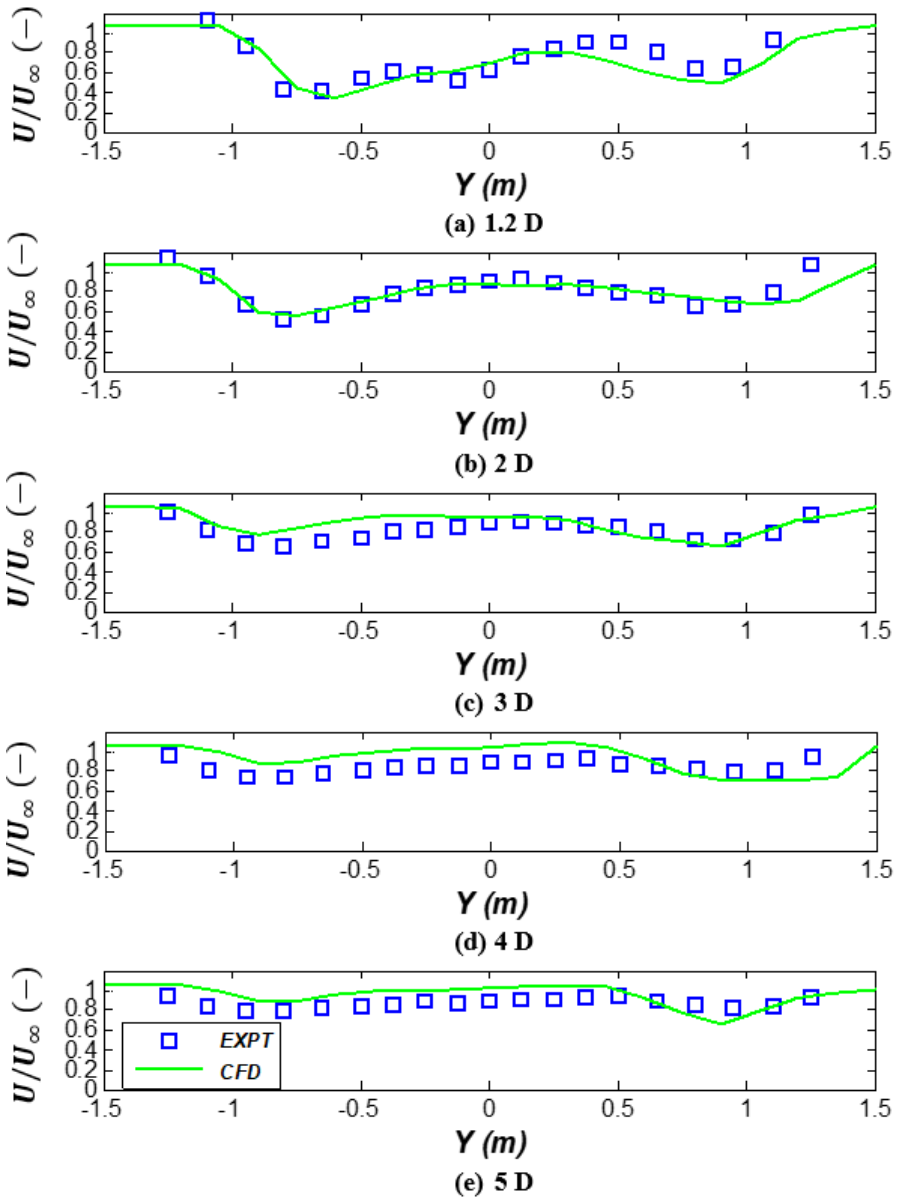

Figure 6-24: Flow velocity measurements variation with distance downstream of Turbine B at the mid-plane of the turbine. (U_∞ = 1 m s^{-1}, *TSR* = 3.5).

6.5 Conclusions

To conclude, two novel turbines designs, which have never been previously investigated, have been successfully tested with the results applied as a validation tool to developed numerical models, allowing advantages, shortcomings and possible improvements of each modelling technique to be analysed and discussed in detail.

A systematic test procedure for the assessment of the mechanical power performance of scaled vertical-axis turbines is presented in this Chapter. The instrumentation and

methodologies presented are directly applicable to the testing of any tidal turbine device. The power curves for two novel turbine designs are presented using the dimensionless parameters, mean power coefficient and tip-speed ratio. For scaled tests with the same operational Reynolds numbers, these dimensionless parameters facilitate direct comparison between the two novel turbine design concepts presented in this Chapter. From this comparison, it is noted that Turbine B (spiral blades on a cylindrical profile) has a significantly increased maximum power coefficient over Turbine A (spiral blades on a spherical profile). Taking blockage effects into account and assuming the same operational Reynolds number to account for scaling effects, Turbine B has a maximum power coefficient of 0.32 at a *TSR* of 3.3, while Turbine A has a maximum power coefficient of 0.27 at a *TSR* of 3.5. An investigation into the Reynolds scaling effects is performed; it was concluded that a Reynolds number independent solution had not been achieved for either turbine.

A rigorous model development approach, adopted from lessons in previous Chapters, resulted in an accurate 3D CFD model of Turbine B. While alternative, more computationally demanding CFD methods, DES and LES, may become viable options in the future, the results presented in this Chapter prove that the RANS CFD modelling technique with the adoption of the SST Transition turbulence model provides acceptable levels of accuracy in predicting turbine performance. The CFD model accurately predicts the peak power coefficient within 6%. The CFD model produced excellent predictions of wake downstream compared to detailed experimental measurements. These predictions can be used to optimise turbine position in the context of multi-turbine arrays.

The strength of the BEM model, **Chapter 3**, coupled with the CFD dataset generated for the NACA 0015 profile, **Chapter 4**, is highlighted again in this chapter. The implementation of the CFD-based dataset improved the accuracy of the predictions over the traditional panel method dataset (Sheldahl and Klimas, 1981) by 30% for the novel turbine design. The BEM-CFD method shows comparable accuracy to the full 3D CFD simulations in terms of peak power coefficient and identification of optimal *TSR* at a considerably reduced computational cost.

The 3D CFD methods presented in this chapter offer potential for improving BEM methods. The iterative approach for solving for the interference factor, presented in

Chapter 3, struggles when solving for high solidity rotors, i.e. high number of blades and, or high chord length to front area ratio. Also, the flow expansion model implemented in **Chapter 3** only accounts for the expansion of flow in one direction out of the flow direction. As seen with the intricate novel design studied in this Chapter, significant out of plane flows are experienced in all directions. Both shortcomings of the BEM approach could be tackled with CFD methods and investigations into the flow pattern through the turbine. The BEM method has proven to be a powerful design tool to quickly and accurately perform design optimisation studies. 3D CFD models do not offer the same opportunities for quick design optimisation studies, so any approached to improve the BEM methods further would be very beneficial.

Time and financial constraints limited the experimental tests carried out. Ideally, different configurations of turbines would have been tested, which would include varying parameters such as the number of blades, blade profile and chord length. Also, large vibrations were experienced in the shaft at moderate to high *TSR* at higher flow velocities, in particular for the larger turbine, Turbine B. This issue limited the range of available freestream velocities due to safety concerns. A more adequately supported turbine would have allowed for greater velocities to be achieved, and the Reynolds number scaling effects could be further analysed. The use of a load cell would have allowed the overall drag of the turbine device to be calculated and provide useful information for the shaft and bearing designs for up-scaled turbines.

Due to the limited computational power and resources available, the CFD simulations focused on the peak power range of *TSR*. As seen with the 2D turbine models presented in **Chapter 4**, a smaller time-step (~0.5^{o} per time-step) is required to solve lower *TSR* simulations accurately. Ideally, the performance at these lower *TSR* would be included in this analysis, but this would have lead to a doubling of CPU time per simulation at these lower *TSR*. The performance of the turbine at lower *TSR* would provide valuable information for the development of an appropriate power take-off system.

From a commercial view, the test results and associated design optimisation with model validation facilitate TRL 5. The next steps in the development would be extended tests of a medium to large-scale prototype in a real-life test environment. The

focus of these tests would be on investigating power take-off systems, durability and reliability testing, and further turbine characterisation (McCombes et al., 2012).

Chapter 7: Conclusions

7.1 Introduction

This thesis focuses on the hydrodynamic performance of vertical axis tidal turbines, with a specific focus on the novel patented Brí Toinne Teoranta (BTT) design. The novelty of the turbine relates primarily to the spiral geometry of the blades. The design aims to circumvent the disadvantages of existing vertical-axis turbines, specifically reduced power coefficient, inconsistent self-start capabilities and larger torque fluctuations when compared to horizontal-axis designs. The overall aim of this research was to develop a combined analytical, computational, and experimental methodology for characterisation of the hydrodynamic performance of the novel BTT vertical-axis tidal turbine concept and also to optimise the turbine design for peak power performance.

7.2 Summary of Conclusions

The following are the key conclusions from the research conducted:

- An initial base case design of the BTT turbine with spherical blades was investigated through experimentally validated computational methods. A design optimisation study followed, focusing on identifying peak power performance through varying turbine parameters, including height: diameter ratio, blade design (cylindrical/ ellipsoidal), chord length, number of blades and blade profile. A 24% improvement in maximum power coefficient was established with a cylindrical blade design. This optimised design provided an 18% improvement over an equivalent, optimised straight-blade design of an equal frontal area.
- At the optimal *TSR* for peak power performance, reduced fluctuations in torque with the variation of azimuthal angle were observed with the optimised BTT design compared to an equivalent straight-bladed design. These reduced load fluctuations are a significant design benefit for the optimised BBT turbine in

terms of the fatigue life of mechanical components over current straight-bladed vertical-axis turbines.

- Greater torque is observed at lower speeds for the BTT turbine design due to the more efficient blade geometry. This feature enhances the self-starting ability of the turbine, thus reducing the complexity of the overall turbine operation. A series of analysis was performed to assess two optimised vertical-axis turbines' self-starting ability. A straight-bladed design and the cylindrical BTT design were investigated. The straight-bladed design failed to rotate successfully when the initial blade position was between 20^{o} and 100^{o}, indicating that this design would require external power to begin operation. The BTT started successfully for all orientations, highlighting another one of the BTT design's benefits over conventional straight-bladed turbines, especially at small- and medium-scale designs.
- A new model based on blade element momentum theory was developed for the analysis of next-generation spiral blade turbines. The new aspect of this model involved stepping through both the blade height and blade position when solving the blade element momentum equations, which facilitated the analysis of complex blade geometries. The experimentally validated model was developed in MATLAB® and was shown to be highly efficient in analysing different types of vertical-axis turbines, including straight-bladed, Darrieus and the new spiral blade designs.
- The SST Transition URANS turbulence model was implemented to establish a dataset of lift and drag coefficients, as a function of angle of attack and Reynolds number, to replace the existing panel method data (Shedahl and Klimas, 1981), which is currently used in the literature as input into BEM models. BEM predictions implementing (1) the existing panel method dataset and (2) the novel CFD-based dataset were compared against experimental data for a straight-bladed turbine. The latter reduced the RMSE by 50% relative to the panel method dataset compared to experimental results.
- The computational time and accuracy of full turbine CFD URANS models and the blade element momentum approach were validated and compared with experimental data. In the case of a straight-blade vertical-axis turbine, the computational efficiency of URANS CFD analysis of hydrofoils combined

with the BEM modelling of turbine performance was highlighted, with these predictions achieving a similar accuracy level to the full 2D CFD turbine model but at a significantly lower computational cost.

- For the analysis of the optimised BTT turbine design, experimental results were recorded from a series of testing at the state-of-the-art tidal turbine test laboratory at IFERMER, Boulogne Sur Mer. A full 3D URANS CFD model was also developed for the optimised BTT turbine design. The CFD model predicted the measured peak power coefficient to within 6% accuracy. The new BEM-CFD model (i.e. BEM model with 2D CFD-generated dataset) was shown to have comparable accuracy to the full 3D CFD at the maximum power coefficient but at a fraction of the computational cost. The strength of the CFD model is predicting in visualising the flow through, and downstream of the turbine was presented with CFD predictions showing general correlation with experimental measurements in the immediate wake of the turbine.

7.3 Recommendations for Future Work

During this thesis, opportunities for further research have been identified. This section details several prospective fields for further research and discusses potential next steps towards the commercialisation of the BTT turbine.

As part of this thesis, improvements were made to the well-established BEM methodology by adapting the model to predict the power performance of intricate turbine blade designs and also establishing an improved hydrodynamic coefficient dataset using RANS modelling. 3D CFD methods offer other opportunities for improving aspects of the BEM methodology. The iterative approach for solving the interference factor has difficulty at high solidity. Also, the flow expansion model only accounts for the expansion of flow in one direction out of the streamwise flow. As seen with the intricate novel design studied here, significant out of plane flow are experienced in all directions. While current computational resources may deem this analysis prohibitive, looking to the future, opportunities may arise in the application of direct numerical simulation (DNS), large eddy simulation (LES) and detached-Eddy simulations (DES) modelling techniques to tackle these challenges. Both methods offer improvements in accuracy over the URANS approach when delving into the intricate flow patterns associated with next-generation turbine designs. The

strength of the BEM model compared to 3D CFD models lies in its suitability for efficient design optimisation studies. Any approaches to further improve BEM methods would significantly benefit the improved design of turbines and devices.

Although the URANS predictions were in agreement with the measured flow downstream of the turbine, it is known that, in general, due to their averaging calculations, URANS leads to the underestimation of turbine wake lengths. More computationally intensive methods, LES and DES, could provide more accurate predictions for improved insight into the effects of multi-row array layouts of turbines.

Future work could focus on further development and application of the small-scale, in-house test facility developed in NUI Galway during this research to measure the power performance of a scaled turbine prototype. With some adjustments to this facility and the test setup, a state-of-the-art test laboratory for small-scale (1:100 – 1:50) prototypes could be established. An extended-length towing tank (~30 m) would provide a longer duration of constant tow velocity (i.e. longer test-phase) and higher towing velocities. Higher towing velocities are critical at smaller scales to increase the turbine Reynolds number more consistent with comparable larger scale designs. The installation of an electromagnetic brake in place of the mechanical braking system would allow for more sensitive control and measurement of the load applied to the turbine to facilitate the optimal *TSR* identification.

Looking at the commercial future development of the BTT turbine, the successful round of testing in the controlled test laboratory at IFEREMER Boulogne sur Mer, with accompanying model validation, presents opportunities to advance the technology readiness level (TRL). With TRL 5 achieved from this round of testing, future testing of a larger scale model (1:10 – 1:4) would be the next target. At this scale, the development would focus on optimising the power take-off system, further design validation and preparation for real-world sea conditions. Testing would be required over an extended period to investigate the durability and reliability of the overall turbine design. A possible site, previously used for similar size turbines, is the European Marine Energy Centre (EMEC) Shapinsay Sound tidal test site. This site acts as a progressive step from tank tests towards real sea conditions, offering water depths of between 21 m and 25m and peak tidal current velocities of 1.5m s^{-1}.

Although the BTT turbine can be deployed on small-scale, off-grid locations, e.g. in rivers, this design could contribute towards Ireland's transition away from fossil fuels to a greener renewable energy-based future through a successful up-scaling of the technology. Two key challenges to be addressed to facilitate this include manufacturability and structural integrity. Fibre-reinforced polymer composites are typically used for large scale turbine blades. To successfully implement up-scaling of the spiral blade design, analysis and assessment of the stiffness and dynamic performance of up-scaled spiral geometries are required. A first step here is to use numerical methods for the assessment of the likely dynamic behaviour of the relatively flexible blade design. Finite element analysis (FEA) provides a suitable methodology to facilitate such assessment, at least for preliminary assessment of expected behaviour and for structural and materials design of larger scale devices. Ultimately, following an appropriate design and manufacturing process, experimental test validation for structural integrity and stability would be required. BEM predictions from the validated model in this thesis could provide essential input into FEA structural design studies. Other options would include coupling the 3D CFD model with a solid mechanics model to develop a fluid-structure interaction (FSI) model (Arnold et al., 2016). The large structure test cell at NUI Galway offers both static and fatigue testing facilities for large-scale blades and support structures (de la Torre et al., 2018). Cavitation is a potential issue for all marine products, which occurs when the pressure on the surface of the object drops below the water vapour pressure, resulting in the quick formation and collapse of separation bubbles. Cavitation can accelerate fatigue and cause unsteady performance(Barber and Motley, 2016). Alternative blade profiles or blade pitching mechanisms to avoid operation leading to cavitation can be applied to avoid these undesirable effects. Specific test facilities are available for testing cavitation effects on scaled prototypes (MARIN, 2020).

References

Abbott, I.H., Von Doenhoff, A.E., 1959. Theory of wing sections: including a summary of airfoil data. Dover Publications Inc., New York.

Alaimo, A., Esposito, A., Messineo, A., Orlando, C., Tumino, D., 2015. 3D CFD analysis of a vertical axis wind turbine. Energies 8, 3013–3033.

Almohammadi, K.M., Ingham, D.B., Ma, L., Pourkashan, M., 2013. Computational fluid dynamics (CFD) mesh independency techniques for a straight blade vertical axis wind turbine. Energy 58, 483–493.

Almohammadi, K.M., Ingham, D.B., Ma, L., Pourkashanian, M., 2012. CFD Sensitivity Analysis of a Straight-Blade Vertical Axis Wind Turbine. Wind Eng. 36, 571–588.

American Institute of Aeronautics and Astronautics, 1998. AIAA Guide for the Verification and Validation of Computational Fluid Dynamics Simulations.

ANSYS, 2013. ANSYS Fluent Theory Guide, 15.0.

ANSYS, 2009. ANSYS Fluent User Guide, 12.0.

Araya, D.B., Dabiri, J.O., 2015. A comparison of wake measurements in motor-driven and flow-driven turbine experiments. Exp. Fluids 56, 1–15.

Arnold, M., Biskup, F., Cheng, P.W., 2016. Impact of structural flexibility on loads on tidal current turbines. Int. J. Mar. Energy 15, 100–111.

Azeez, A., Paul, J., 2014. CFD Analysis of NACA 63-018 Airfoil at Different Reynolds Number. Int. J. Eng. Trends Technol. 12, 258–264.

Bachant, P., Wosnik, M., 2016. Modeling the near-wake of a vertical-axis cross-flow turbine with 2-D and 3-D RANS. J. Renew. Sustain. Energy 8.

Bachant, P., Wosnik, M., 2015. Performance measurements of cylindrical- and spherical-helical cross-flow marine hydrokinetic turbines, with estimates of exergy efficiency. Renew. Energy 74, 318–325.

Bachant, P., Wosnik, M., Gunawan, B., Neary, V.S., 2016. Experimental Study of a Reference Model Vertical-Axis Cross-Flow Turbine. PLoS One 11, 1–20.

Bahaj, A.S., Blunden, L.S., Anwar, A., 2008. Tidal-current Energy Device Development and Evaluation Protocol. Universirty of Southampton, UK.

Balduzzi, F., Bianchini, A., Maleci, R., Ferrara, G., Ferrari, L., 2016. Critical issues in the CFD simulation of Darrieus wind turbines. Renew. Energy 85, 419–435.

Baldwin, B., Lomax, H., 1978. Thin-layer approximation and algebraic model for separated turbulentflows, in: 16th Aerospace Sciences Meeting, Aerospace Sciences Meetings. American Institute of Aeronautics and Astronautics, Huntsville, Alabama.

Barber, R.B., Motley, M.R., 2016. Cavitating response of passively controlled tidal turbines. J. Fluids Struct. 66, 462–475.

Barnsley, M.J., Wellicome, J.F., 1990. Final report on the 2nd phase of development

and testing of a horizontal axis wind turbine test rig for the investigation of stall regulation aerodynamics. Carried Out Under ETSU Agreem. No. E. A 5.

Batten, W.M.J., Bahaj, a. S., Molland, a. F., Chaplin, J.R., 2008. The prediction of the hydrodynamic performance of marine current turbines. Renew. Energy 33, 1085–1096.

Battisti, L., Brighenti, A., Benini, E., Castelli, M.R., 2016. Analysis of Different Blade Architectures on small VAWT Performance. J. Phys. Conf. Ser. 753, 062009.

Berg, D.E., 1983. An improved double-multiple streamtube model for the darrieus-type vertical axis wind turbine, in: Sixth Biannual Wind Energy Conference and Workshop. Minneapolis.

Berges, B., 2007. Development of Small Wind Turbines Development of Small Wind Turbines, Thesis.

Beri, H., 2011. Double Multiple Streamtube Model and Numerical Analysis of Vertical Axis Wind Turbine. Energy Power Eng. 03, 262–270.

Betz, A., 1920. Das Maximum der theoretisch möglichen Ausnutzung des Windes durch Windmotoren. Zeitschrift für das gesamte Turbinenwes. 26, 307–309.

Bhargav, M.M.S.R.S., Ratna Kishore, V., Laxman, V., 2016. Influence of fluctuating wind conditions on vertical axis wind turbine using a three dimensional CFD model. J. Wind Eng. Ind. Aerodyn. 158, 98–108.

Blazek, J., 2001. Computational Fluid Dynamics: Principles and Applications, First Edit. ed. Elsevier, Oxford.

Boussinesq, J., 1897. Théorie de l'écoulement tourbillonnant et tumultueux des liquides dans les lits rectilignes a grande section, Théorie de l'écoulement tourbillonnant et tumultueux des liquides dans les lits rectilignes a grande section. Gauthier-Villars et fils.

British Petroleum, 2017. BP Statistical Review of World Energy 2017, British Petroleum.

Castelli, M.R., Fedrigo, A., Benini, E., 2012. Effect of Dynamic Stall , Finite Aspect Ratio and Streamtube Expansion on VAWT Performance Prediction using the BE-M Model. World Acad. Sci. Eng. Technol. 6, 426–438.

Chen, J., Chen, L., Xu, H., Yang, H., Ye, C., Liu, D., 2016. Performance improvement of a vertical axis wind turbine by comprehensive assessment of an airfoil family. Energy 114, 318–331.

Cheng, Q., Liu, X., Ji, H.S., Kim, K.C., Yang, B., 2017. Aerodynamic Analysis of a Helical Vertical Axis Wind Turbine. Energies 10, 575.

Chougule, P.D., Nielsen, S.R.K., Basu, B., 2013. Active blade pitch control for straight bladed darrieus vertical axis wind turbine of new design. Key Eng. Mater. 569–570, 668–675.

Chowdhury, A.M., Akimoto, H., Hara, Y., 2016. Comparative CFD analysis of Vertical Axis Wind Turbine in upright and tilted configuration. Renew. Energy 85, 327–337.

Chung, D.W., You, Y.M., 2015. Cogging torque reduction in permanent-magnet brushless generators for small wind turbines. J. Magn. 20, 176–185.

Counsil, J.N.N., Goni Boulama, K., 2013. Low-Reynolds-Number Aerodynamic Performances of the NACA 0012 and Selig–Donovan 7003 Airfoils. J. Aircr. 50,

204–216.

Counsil, J.N.N., Goni Boulama, K., 2012. Validating the URANS shear stress transport γ −Reθ model for low-Reynolds-number external aerodynamics. Int. J. Numer. Methods Fluids 69, 1411–1432.

Dabiri, J.O., 2011. Potential order-of-magnitude enhancement of wind farm power density via counter-rotating vertical-axis wind turbine arrays. J. Renew. Sustain. Energy 3.

Daroczy, L., Janiga, G., Petrasch, K., Webner, M., Thevenin, D., 2015. Comparative analysis of turbulence models for the aerodynamic simulation of H-Darrieus rotors. Energy 90, 680–690.

Dash, A., 2016. CFD Analysis ofWind Turbine Airfoil at Various Angles of Attack. IOSR J. Mech. Civ. Eng. 13, 18–24.

de la Torre, O., Moore, D., Gavigan, D., Goggins, J., 2018. Accelerated life testing study of a novel tidal turbine blade attachment. Int. J. Fatigue 114, 226–237.

Dominy, R., Lunt, P., Bickerdyke, A., Dominy, J., 2007. Self-starting capability of a Darrieus turbine. Proc. Inst. Mech. Eng. Part A J. Power Energy 221, 111–120.

Douvi, E., Tsavalos, A., Margaris, D., 2012. Evaluation of the turbulence models for the simulation of the flow over a National Advisory Committee for Aeronautics (NACA) 0012 airfoil. J. Mech. Eng. Res. 4, 100–111.

Drela, M., Youngren, H., 2013. XFOIL- Subsonic Airfoil Development System [WWW Document].

Drzewiecki, S., 1892. Méthode Pour la Détermination des Eléments Mécaniques des Propulseurs Hélicoidaux. Bull. l'Association Tech. Marit.

Elsaesser, B., Schmitt, P., Boake, C., Lidderdale, A., Lawrence, J., Salvatore, F., Germain, G., Colicchio, G., Jacob, B., 2013. Tidal Measurement Best Practice Manual.

Eppler, R., 1978. Turbulent airfoils for general aviation. J. Aircr. 15, 93–99.

Eppler, R., Somers, D., 1980. A computer program for the design and analysis of low-speed airfoils. Hampton, VA.

Erickson, L., 1990. Panel Methods- An Introduction. Moffiett Field, California.

European Marine Energy Centre, 2020. Tidal Devices [WWW Document].

Ferziger, J.H., Peric, M., 2002. Computational Methods For Fluid Dynamics, 3rd Editio. ed. Springer-Verlag, New York.

Froude, R.E., 1889. On the Part Played in Propulsion by Difference in Pressure. Trans. Inst. Nav. Archit. 390–423.

Garrett, C., Cummins, P., 2007. The efficiency of a turbine in a tidal channel. J. Fluid Mech. 588, 243–251.

Gaurier, B., Germain, G., Facq, J. V., Johnstone, C.M., Grant, A.D., Day, A.H., Nixon, E., Di Felice, F., Costanzo, M., 2015. Tidal energy "Round Robin" tests comparisons between towing tank and circulating tank results. Int. J. Mar. Energy 12, 87–109.

Genç, M.S., 2010. Numerical simulation of flow over a thin aerofoil at a high Reynolds number using a transition model. Proc. Inst. Mech. Eng. Part C J. Mech. Eng. Sci. 224, 2155–2164.

Glauert, H., 1926. A General Theory of the Autogyro. Sci. Res. Air Minist. - Reports Memo. No. 1111.

Gormont, R.E., 1973. A mathematical model of unsteady aerodynamics and radial flow for application to helicopter rotors. Fort Eustis, Virginia.

Goundar, J.N., Ahmed, M.R., 2013. Design of a horizontal axis tidal current turbine. Appl. Energy 111, 161–174.

Gupta, S., Leishman, J., 2005. Comparison Of Momentum And Vortex Methods For The Aerodynamic Analysis Of Wind Turbines. 43rd AIAA Aerosp. Sci. Meet. Exhib. 1–24.

Heavey, S., Leen, S., McGarry, P., 2018a. Hydrodynamic design and analysis of a novel vertical axis turbine. Int. J. Offshore Polar Eng.

Heavey, S., Leen, S., McGarry, P., 2018b. An efficient computational framework for hydrofoil characterisation and tidal turbine design. Ocean Eng.

Heavey, S., Leen, S., McGarry, P., 2017. An efficient and accurate methodology for hydrofoil characterisation and tidal turbine design, in: Proceedings of the 12th European Wave and Tidal Energy Conference. Cork, Ireland, pp. 1–10.

Heavey, S.C., McGarry, P.J., Leen, S.B., 2016. Analytical Modelling of a Novel Tidal Turbine, in: Proceedings of the Twenty-Sixth (2016) International Ocean and Polar Engineering Conference. International Society of Offshore and Polar Engineers, Rhodes, Greece, pp. 717–724.

Hepperle, M., 2018. JavaFoil- Analysis of Airfoils [WWW Document].

Hill, N., Dominy, R., Ingram, G., Dominy, J., 2009. Darrieus turbines: the physics of self-starting. Proc. Inst. Mech. Eng. Part A J. Power Energy 223, 21–29.

Houlsby, G.T., Draper, S., Oldfield, M.L.., 2008. Application of Linear Momentum Actuator Disc Theory to Open Channel Flow, Technical Report OUEL 2296/08.

HydroQuest, 2020. HydroQuest- OceanQuest [WWW Document].

IFREMER, 2020. IFREMER- Testing Infrastructure, Testing Facililities [WWW Document].

International Renewable Energy Agency, 2020. Renewable Power Generation Costs in 2019, International Renewable Energy Agency.

Jacobs, E.N., Sherman, A., 1937. Airfoil section characteristics as affected by variations of the Reynolds number. NACA Rep. 586.

James, G., 1996. Modern Engineering Mathematics, 2nd Editio. ed. Pearson Education, Harlow.

Klimas, P.C., Sheldahl, R.E., 1978. Four Aerodynamic Prediction Schemes for Vertical-Axis: A Compendium. Albuquerque.

Langtry, R.B., Menter, F.R., Likki, S.R., Suzen, Y.B., Huang, P.G., Völker, S., 2006. A Correlation-Based Transition Model Using Local Variables—Part II: Test Cases and Industrial Applications. J. Turbomach. 128, 423–434.

Lanzafame, R., Mauro, S., Messina, M., 2014. 2D CFD Modeling of H-Darrieus Wind Turbines Using a Transition Turbulence Model. Energy Procedia 45, 131–140.

Launder, B.E., Spalding, D.B., 1972. Lectures in mathematical models of turbulence, 3rd ed. Academic Press, London, England.

Leishman, J.G., 2002. Challenges in modeling the unsteady aerodynamics of wind

turbines. ASME 2002 Wind Energy Symp. Wind. 132, 141–167.

Li, C., Zhu, S., Xu, Y., Xiao, Y., 2013. 2.5D large eddy simulation of vertical axis wind turbine in consideration of high angle of attack flow. Renew. Energy (UK) 51, 1–27.

LucidEnergy, 2020. Spinning Gravity Into Renewable Energy [WWW Document].

Maître, T., Amet, E., Pellone, C., 2013. Modeling of the flow in a Darrieus water turbine: Wall grid refinement analysis and comparison with experiments. Renew. Energy 51, 497–512.

Mannion, B., Leen, S.B., Nash, S., 2020. Development and assessment of a blade element momentum theory model for high solidity vertical axis tidal turbines. Ocean Eng. 197.

Mannion, B., Leen, S.B., Nash, S., 2018. A two and three-dimensional CFD investigation into performance prediction and wake characterisation of a vertical axis turbine. J. Renew. Sustain. Energy 10, 1–20.

Mannion, B., McCormack, V., Kennedy, C., Leen, S.B., Nash, S., 2019. An experimental study of a flow-accelerating hydrokinetic device. Proc. Inst. Mech. Eng. Part A J. Power Energy 233, 148–162.

MARIN, 2020. MARIN- Caviataion Tunnel [WWW Document].

Marsh, P., Ranmuthugala, D., Penesis, I., Thomas, G., 2015. Three-dimensional numerical simulations of straight-bladed vertical axis tidal turbines investigating power output, torque ripple and mounting forces. Renew. Energy 83, 67–77.

Massé, B., 1981. Description de deux programmes d'ordinateur pour le calcul des performance et des charges aérodynamiques pour les éoliennes à axe vertical. Inst. Rech. l'Hydro IREQ-2379.

Masters, I., Chapman, J.C., Willis, M.R., Orme, J.A.C., 2011. A robust blade element momentum theory model for tidal stream turbines including tip and hub loss corrections. J. Mar. Eng. Technol. 10, 25–35.

Mcadam, R.A., Houlsby, G.T., Oldfield, M.L.G., 2013. Experimental measurements of the hydrodynamic performance and structural loading of the Transverse Horizontal Axis Water Turbine : Part 3. Renew. Energy 59, 82–91.

McCombes, T., Iyer, A.S., Falchi, M., Elsäßer, B., Scheijgrond, P., Lawrence, J., 2012. WP2: Marine Energy System Testing - Standardisation and Best Practice, D2.2: Collation of Tidal Test Options, WP2: Marine Energy System Testing-Standardisation and Best Practice.

McCombes, T., Johnstone, C., Holmes, B., Myers, L.E., Bahaj, A.., Heller, V., Kofoed, J.., Flinn, J., Bittencourt, C., 2010. Assessment of current practice for tank testing of small marine energy devices.

McGuire, B., 2014. Turbine and a rotor for a turbine. US 8690541 B2.

McIntosh, S.C., Babinsky, H., Bertenyi, T., 2009. Convergence Failure and Stall Hysteresis in Actuator-Disk Momentum Models Applied to Vertical Axis Wind Turbines. J. Sol. Energy Eng. 131, 034502.

McLaren, K., 2011. A numerical and experimental study of unsteady loading of high solidity vertical axis wind turbines. McMaster University.

Mellen, C.P., Frohlich, J., Rodi, W., 2003. Lessons from LESFOIL Project on Large-Eddy Simulation of Flow Around an Airfoil. AIAA J. 41, 573–581.

Menter, F.R., 1994. Two-equation eddy-viscosity turbulence models for engineering applications. AIAA J. 32, 1598–1605.

Menter, F.R., Langtry, R.B., Likki, S.R., Suzen, Y.B., Huang, P.G., Völker, S., 2006. A Correlation-Based Transition Model Using Local Variables—Part I: Model Formulation. J. Turbomach. 128, 413.

Miller, S.D., 2008. Lift, drag and moment of a NACA 0015 airfoil. Ohio State University.

Minesto, 2020. Minesto- The future of renewable energy [WWW Document].

Mycek, P., Gaurier, B., Germain, G., Pinon, G., Rivoalen, E., 2014. Experimental study of the turbulence intensity effects on marine current turbines behaviour. Part I: One single turbine. Renew. Energy 66, 729–746.

Myers, L., Bahaj, A.S., 2006. Power output performance characteristics of a horizontal axis marine current turbine. Renew. Energy 31, 197–208.

Nguyen, C., Le, T., Tran, P., 2015. A numerical study of thickness effect of the symmetric NACA 4-digit airfoils on self starting capability of a 1kW H-type vertical axis wind turbine. Int. J. Mech. Eng. Appl. 3, 7–16.

O'Rourke, F., Boyle, F., Reynolds, A., 2010. Tidal current energy resource assessment in Ireland: Current status and future update. Renew. Sustain. Energy Rev. 14, 3206–3212.

O 'Doherty, T., Mason-Jones, A., O 'Doherty, D.M., Byrne, C.B., Owen, I., Wang, Y.X., 2009. Experimental and Computational Analysis of a Model Horizontal Axis Tidal Turbine. 8th Eur. wave tidal energy Conf. 833–841.

Orbital Marine Energy, 2020a. SR 2000- The Industry Breakthrough [WWW Document].

Orbital Marine Energy, 2020b. O2- Project Site [WWW Document].

Orlandi, A., Collu, M., Zanforlin, S., Shires, A., 2015. 3D URANS analysis of a vertical axis wind turbine in skewed flows. J. Wind Eng. Ind. Aerodyn. 147, 77–84.

Paraschivoiu, I., 2002. Wind Turbine Design with Emphasis on Darrieus Concept. Polytechnique Presses Internationales, Québec.

Paraschivoiu, I., 1982. Aerodynamic Loads and Performance of the Darrieus Rotor. J. Energy 6, 406–412.

Preen, R.J., Bull, L., 2015. Toward the Coevolution of Novel Vertical-Axis Wind Turbines. IEEE Trans. Evol. Comput. 19, 284–294.

Reed, S., Sharpe, D., 1980. An Extended Multiple Streamtube Theory for Vertical Axis Wind Turbines, in: Proceedings of the Second BWEA Wind Energy Workshop. Cranfield.

Reynolds, O., 1895. On the dynamical theory of incompressible viscous fluids and the determination of the criterion. Philos. Trans. R. Soc. London A Math. Phys. Eng. Sci. 186, 123–164.

Roache, P.J., 1997. Quantification of uncertainty in computational fluid dynamics. Annu. Rev. Fluid Mech. 19, 123–160.

Roberts, A., Thomas, B., Sewell, P., Khan, Z., Balmain, S., Gillman, J., 2016. Current tidal power technologies and their suitability for applications in coastal and

marine areas. J. Ocean Eng. Mar. Energy 2, 227–245.

Ross, H., Polagye, B., 2020. An experimental assessment of analytical blockage corrections for turbines. Renew. Energy 152, 1328–1341.

Sabella, 2020. Sabella Tidal Turbines [WWW Document].

Sagmo, K., Bartl, J., Saetran, L., 2016. Numerical simulations of the NREL S826 airfoil. J. Phys. Conf. Ser. 753, 1–9.

Şahin, İ., Acir, A., 2015. Numerical and Experimental Investigations of Lift and Drag Performances of NACA 0015 Wind Turbine Airfoil. Int. J. Mater. Mech. Manuf. 3, 22–25.

Selig, M.S., Guglielmo, J.J., 1997. High-Lift Low Reynolds Number Airfoil Design. J. Aircr. 34, 72–79.

Seo, J., Lee, S.-J., Choi, W.-S., Park, S.T., Rhee, S.H., 2016. Experimental study on kinetic energy conversion of horizontal axis tidal stream turbine. Renew. Energy 97, 784–797.

Shan, H., Jiang, L., Liu, C., 2005. Direct numerical simulation of flow separation around a NACA 0012 airfoil. Comput. Fluids 34, 1096–1114.

Sheldahl, R.E., Klimas, P., Feltz, L., 1980. Aerodynamic Performance of a 5-Metre-Diameter Darrieus Turbine With Extruded Aluminum NACA-0015 Blades. Sandia Lab.

Sheldahl, R.E., Klimas, P.C., 1981. Aerodynamic characteristics of seven symmetrical airfoil sections through 180-degree angle of attack for use in aerodynamic analysis of vertical axis wind turbines.

Shiono, M., Suzuki, K., Kiho, S., 2000. An experimental study of the characteristics of a Darrieus turbine for tidal power generation. Electr. Eng. Japan 132, 38–47.

SIMEC Atlantic Energy, 2020a. Turbines [WWW Document].

SIMEC Atlantic Energy, 2020b. Tidal Stream Projects- MeyGen [WWW Document].

Smith, A., Cebeci, T., 1967. Numerical solution of the turbulent-boundary-layer equations. Defense Technical Information Center, Ft. Belvoir.

Spalart, P., Allmaras, S., 1992. A One-Equation Turbulence Model for Aerodynamic Flows, AIAA.

Stergiannis, N., Lacor, C., Beeck, J. V, Donnelly, R., 2016. CFD modelling approaches against single wind turbine wake measurements using RANS. J. Phys. Conf. Ser. 753, 032062.

Stivers, L.S., Abbott, I.H., Doenhoff, V., Albert, E., n.d. Summary of Airfoil Data.

Strickland, J.H., 1975. The Darrieus Turbine: A performance prediction model using multiple streamtubes. Albuquerque.

Stringer, R.M., Hillis, A.J., Zang, J., 2016. Numerical investigation of laboratory tested cross-flow tidal turbines and Reynolds number scaling. Renew. Energy 85, 1316–1327.

Talukdar, P.K., Kumar, S., Kulkarni, V., Das, A.K., Saha, U.K., 2017. On site testing of a zero head vertical axis helical turbine, in: Proceedings of the ASME 2015 Gas Turbine India Conference. pp. 1–6.

Templin, R., 1974. Aerodynamic performance theory for the NRC vertical-axis wind turbine. National Research Council Canada, National Aeronautical

Establishment, Ottawa, Canada.

Tidal Energy Pty Ltd, 2013. Davidson-Hill Venturi Turbine [WWW Document].

University of Strathclyde, 2020. Stingray- Oscillating Hydrofoil [WWW Document].

Versteeg, H.K., Malalasekera, W., 1995. An Introduction to Computational Fluid Dynamics - The Finite Volume Method, McGraw-Hill. Pearson Prentice Hall.

Viterna, L., Corrigan, R.D., 1982. Fixed pitch rotor performance of large horizontal axis wind turbines. Annu. Rev. Fluid Mech. 15, 69–85.

Wakui, T., Tanzawa, Y., Hashizume, T., Nagao, T., 2005. Hybrid configuration of darrieus and savonius rotors for stand-alone wind turbine-generator systems. Electr. Eng. Japan (English Transl. Denki Gakkai Ronbunshi) 150, 13–22.

Walsh, G.P., Keough, R., Mullaley, V., Sinclair, H., Hinchey, M.J., 2015. Cross-flow helical turbine for energy production in reversing tidal and ocean currents. 2014 Ocean. - St. John's, Ocean. 2014 2–7.

Werle, M.J., 2010. Wind turbine wall-blockage performance corrections. J. Propuls. Power 26, 1317–1321.

White, F.M., 2009. Fluid Mechanics, 7th Editio. ed. McGraw-Hill, New York.

Wilcox, D.C., 1998. Turbulence Modeling for CFD. DCW Industries, La Canada, California.

Wilcox, D.C., 1988. Reassessment of the scale-determining equation for advanced turbulence models. AIAA J. 26, 1299–1310.

Worasinchal, S., Ingram, G.L., Dominy, R.G., 2015. The Physics of H-Darrieus Turbine Starting Behaviour 138.

World Energy Council, 2016. World Energy Resources: Marine Energy.

Worstell, M.H., 1978. Aerodynamic Performance of the 17 Meter Diameter Darrieus Wind Turbine. Albuquerque.

Zhang, X., Wang, S., Wang, F., Zhang, L., Sheng, Q., 2012. The hydrodynamic characteristics of free variable-pitch vertical axis tidal turbine. J. Hydrodyn. Ser. B 24, 834–839.

Appendix A Turbulence Models Formulation

A.1. k-ω SST Turbulence Model

The k-ω Shear-Stress Transport (SST) turbulence model was developed by Menter (1994) and is based on the original k-ω turbulence model (Wilcox, 1988) and modified k-ε turbulence model. The following details the formulation of this turbulence model within ANSYS Fluent®.

The transport equations for the turbulent kinetic energy (k) and specific dissipation rate (ω) are defined as follows:

$$\frac{\partial(\rho k)}{\partial t} + \frac{\partial\left(\rho u_j k\right)}{\partial x_j} = G_k - Y_k + \frac{\partial}{\partial x_j}\left[\Gamma_k \frac{\partial k}{\partial x_j}\right] \tag{A.1}$$

and

$$\frac{\partial(\rho \omega)}{\partial t} + \frac{\partial\left(\rho u_j \omega\right)}{\partial x_j} = G_\omega - Y_\omega + D_\omega + \frac{\partial}{\partial x_j}\left[\Gamma_\omega \frac{\partial \omega}{\partial x_j}\right] \tag{A.2}$$

where G_k and G_ω represent the production of k and ω, Y_k and Y_ω are the dissipation of k and ω, Γ_k and Γ_ω are the effective diffusivities of k and ω, and D_ω represents the cross-diffusion term.

The effective diffusivity of k and ω is given by:

$$\Gamma_k = \mu + \frac{\mu_t}{\sigma_k} \tag{A.3}$$

and,

$$\Gamma_\omega = \mu + \frac{\mu_t}{\sigma_\omega} \tag{A.4}$$

where σ_k and σ_ω are the turbulent Prandtl numbers for k and ω, and μ_t is the turbulent viscosity defined as:

σ_k and σ_ω are defined as:

$$\sigma_k = \frac{1}{F_1/\sigma_{k,1} + (1 - F_1)/\sigma_{k,2}} \tag{A.5}$$

$$\sigma_\omega = \frac{1}{F_1/\sigma_{\omega,1} + (1 - F_1)/\sigma_{\omega,2}} \tag{A.6}$$

where F_1 and F_2 are the blending functions, with the following definitions:

$$F_1 = \tanh(\Phi_1^4) \tag{A.7}$$

$$\Phi_1 = min\left[max\left(\frac{\sqrt{k}}{0.09\omega y}, \frac{500\mu}{\rho y^2 \omega}\right), \frac{4\rho k}{\sigma_{\omega,2} D_\omega^+ y^2}\right] \tag{A.8}$$

$$D_\omega^+ = max\left[2\rho \frac{1}{\sigma_{\omega,2}} \frac{1}{\omega} \frac{\partial k}{\partial x_j}, 10^{-10}\right] \tag{A.9}$$

$$F_2 = \tanh(\Phi_2^2) \tag{A.10}$$

$$\Phi_2 = max\left[2\frac{\sqrt{k}}{0.09\omega y}, \frac{500\mu}{\rho y^2 \omega}\right] \tag{A.11}$$

where y is the distance to the next wall surface and D_ω^+ is the positive part of the cross-diffusion term.

The turbulent viscosity, μ_t, is calculated as follows:

$$\mu_t = \frac{\rho k}{\omega} = \frac{1}{max\left[\frac{1}{\alpha^*}, \frac{SF_2}{\alpha_1 \omega}\right]} \tag{A.12}$$

where S is the modulus of the mean rate-of-strain tensor, defined as:

$$S = \sqrt{2S_{ij}S_{ij}} \tag{A.13}$$

where the mean strain rate, S_{ij} is:

$$S_{ij} = \frac{1}{2}\left(\frac{\partial u_j}{\partial x_i} - \frac{\partial u_i}{\partial x_j}\right) \tag{A.14}$$

The damping coefficient, α^*, is defined as:

$$\alpha^* = \alpha_\infty^* \left(\frac{\alpha_0^* + Re_t/R_k}{1 + Re_t/R_k}\right) \tag{A.15}$$

where:

$$Re_t = \frac{\rho k}{\mu \omega} \tag{A.16}$$

G_k represents the production of k and is defined as follows:

$$G_k = \mu_t S^2 \tag{A.17}$$

where μ_t and S are defined as above.

The production of ω is defined as:

$$G_\omega = \frac{\alpha}{v_t} \check{G}_k \tag{A.18}$$

where the coefficient α is given by:

$$\alpha = \frac{\alpha_\infty}{\alpha^*}\left(\frac{\alpha_0^* + Re_t/R_\omega}{1 + Re_t/R_\omega}\right) \tag{A.19}$$

α_∞ is defined as:

$$\alpha_\infty = F_1\alpha_{\infty,1} + (1 - F_1)\alpha_{\infty,2} \tag{A.20}$$

where

$$\alpha_{\infty,1} = \frac{\beta_{i,1}}{\beta_\infty^*} - \frac{\kappa^2}{\sigma_{\omega,1}\sqrt{\beta_\infty^*}} \tag{A.21}$$

$$\alpha_{\infty,2} = \frac{\beta_{i,2}}{\beta_\infty^*} - \frac{\kappa^2}{\sigma_{\omega,2}\sqrt{\beta_\infty^*}} \tag{A.22}$$

The dissipation of k, Y_k, is defined as:

$$Y_k = \rho\beta^* k\omega \tag{A.23}$$

where:

$$\beta^* = \beta_i^*[1 + \zeta^* F(M_t)] \tag{A.24}$$

$$\beta_i^* = \beta_\infty^*\left(\frac{4/15 + (Re_t/R_\beta)^4}{1 + (Re_t/R_\beta)^4}\right) \tag{A.25}$$

$F(M_t)$ is the compressibility function and is defined as:

$$F(M_t) = \begin{cases} 0 & M_t \le M_{t0} \\ M_t^2 - M_{t0}^2 & M_t > M_{t0} \end{cases} \tag{A.26}$$

where

$$M_t^2 = \frac{2k}{a^2} \tag{A.27}$$

$$a = \sqrt{\gamma RT} \tag{A.28}$$

For incompressible simulations, $\beta^* = \beta_\infty^*$.

Y_ω, the dissipation of ω, is defined as:

$$Y_\omega = \rho\beta\omega^2 \tag{A.29}$$

where

$$\beta = \beta_i\left[1 - \frac{\beta_i^*}{\beta_i}\zeta^* F(M_t)\right] \tag{A.30}$$

where

$$\beta_i = F_1\beta_{i,1} + (1 - F_1)\beta_{i,2} \tag{A.31}$$

As the k-ω SST model is based on both the k-ε and the standard k-ω model, a cross-diffusion term (D_ω) is introduced, defined as:

$$D_\omega = 2(1 - F_1)\rho \frac{1}{\omega \sigma_{\omega.2}} \frac{\partial k}{\partial x_j} \frac{\partial \omega}{\partial x_j} \tag{A.32}$$

The following are the model constants implemented for this turbulence model approach:

$\sigma_{k;1} = 1.176;\ \sigma_{k;2} = 1.0;\ \sigma_{\omega;1} = 2.0;\ \sigma_{\omega;2} = 1.168;\ \alpha_1 = 0.31;\ \alpha_\infty^* = 1.0;\ \alpha_\infty = 0.52;\ \alpha_0 = \frac{1}{9};\ \alpha_0^* = 0.024;\ \beta_i = 0.072;\ \beta_{i;1} = 0.075;\ \beta_{i;2} = 0.0828;\ \beta_\infty^* = 0.09;\ \kappa = 0.41;\ R_\beta = 8;\ R_k = 6;\ R_\omega = 2.95;\ \zeta^* = 1.5;\ M_{t0} = 0.25.$

A.2. SST Transition Turbulence Model

The SST Transition turbulence model (Langtry et al., 2006; Menter et al., 2006), also referred to as the γ-$\widetilde{Re}_{\theta t}$ turbulence model, is a four-equation model built on the k-ω SST turbulence model. The following details the formulation of this turbulence model within ANSYS Fluent®.

The transport equations for the intermittency (γ) and transition momentum thickness Reynolds number ($\widetilde{Re}_{\theta t}$) are given as:

$$\frac{\partial(\rho\gamma)}{\partial t} + \frac{\partial(\rho u_j \gamma)}{\partial x_j} = P_{\gamma 1} - E_{\gamma 1} + P_{\gamma 2} - E_{\gamma 2} + \frac{\partial}{\partial x_j}\left[\left(\mu + \frac{\mu_t}{\sigma_\gamma}\right)\frac{\partial \gamma}{\partial x_j}\right] \tag{A.33}$$

and

$$\frac{\partial(\rho\widetilde{Re}_{\theta t})}{\partial t} + \frac{\partial(\rho u_j \widetilde{Re}_{\theta t})}{\partial x_j} = P_{\theta t} + \frac{\partial}{\partial x_j}\left[\sigma_{\theta t}(\mu + \mu_t)\frac{\partial \widetilde{Re}_{\theta t}}{\partial x_j}\right] \tag{A.34}$$

where $P_{\gamma 1}$ and $E_{\gamma 1}$ are the transition terms for γ and $P_{\gamma 2}$ and $E_{\gamma 2}$ are the destruction/ relaminarisation terms for γ. $P_{\theta t}$ is the source term for $\widetilde{Re}_{\theta t}$.

The transition sources terms, $P_{\gamma 1}$ and $E_{\gamma 1}$, for γ are defined as:

$$P_{\gamma 1} = c_{a1} F_{length} \rho S [\gamma F_{onset}]^{C_{\gamma 3}} \tag{A.35}$$

$$E_{\gamma 1} = c_{e1} \rho P_{\gamma 1} \gamma \tag{A.36}$$

where F_{length} is an empirical correlation that controls the length of the transition region and S is the strain rate magnitude defined in equation (A.13). F_{onset} is defined as:

$$F_{onset} = \max(F_{onset2} - F_{onset3}, 0) \tag{A.37}$$

where

$$F_{onset1} = \frac{Re_v}{2.193\ Re_{\theta c}} \tag{A.38}$$

$$Re_v = \frac{\rho y^2 S}{\mu} \tag{A.39}$$

$$F_{onset2} = \min\left(\max(F_{onset1}, F_{onset1}^4), 2.0\right) \tag{A.40}$$

$$R_T = \frac{\rho k}{\mu \omega} \tag{A.41}$$

$$F_{onset3} = \max\left(1 - \left(\frac{R_T}{2.5}\right)^3, 0\right) \tag{A.42}$$

where y is the wall distance and $Re_{\theta c}$ is the critical Reynolds number defined as the Reynolds number where the intermittency starts to increase in the boundary layer. $Re_{\theta c}$ is an empirical correlation that is a strong function of F_{length}.

The destruction and relaminarisation terms, $P_{\gamma 2}$ and $E_{\gamma 2}$, are defined as:

$$P_{\gamma 2} = C_{a2} \rho \Omega \gamma F_{turb} \tag{A.43}$$

$$E_{\gamma 2} = c_{e2} P_{\gamma 2} \gamma \tag{A.44}$$

where Ω is the voracity magnitude and F_{turb} is defined as:

$$F_{turb} = e^{-\left(\frac{R_T}{4}\right)^4} \tag{A.45}$$

The source term for the transition momentum thickness Reynolds number is defined as:

$$P_{\theta t} = c_{\theta t} \frac{\rho}{t}\left(Re_{\theta t} - \widetilde{Re}_{\theta t}\right)(1.0 - F_{\theta t}) \tag{A.46}$$

where,

$$t = \frac{500\mu}{\rho U^2} \tag{A.47}$$

$$U = \sqrt{u_k u_k} \tag{A.48}$$

$$F_{\theta t} = min\left[\max\left(F_{wake}\, e^{\left(-\frac{y}{\delta}\right)^4}, 1.0 - \left(\frac{\gamma - 1/50}{1.0 - 1/50}\right)^2\right), 1.0\right] \tag{A.49}$$

$$\delta = \frac{50 \Omega y}{U} \delta_{BL} \tag{A.50}$$

$$\delta_{BL} = \frac{15}{2}\theta_{BL} \tag{A.51}$$

$$\theta_{BL} = \frac{\widetilde{Re}_{\theta t}\mu}{\rho U} \tag{A.52}$$

$$F_{wake} = e^{-\left(\frac{Re_\omega}{1\times10^5}\right)^2} \tag{A.53}$$

$$Re_\omega = \frac{\rho\omega y^2}{\mu} \tag{A.54}$$

The model constants for the additional transport equations are:

$c_{a1} = 2.0,\ \ c_{e1} = 1.0,\ \ c_{a2} = 0.06,\ \ c_{e2} = 50,\ \ c_{\gamma 3} = 0.5,\ \ \sigma_\gamma = 1.0,\ \ c_{\theta t} = 0.03,$ $\sigma_{\theta t} = 2.0.$

The modification for separation-induced transition is:

$$\gamma_{sep} = min\left(C_{s1}max\left[\left(\frac{Re_v}{3.235Re_{\theta c}}\right) - 1{,}0\right]F_{reattch}, 2\right)F_{\theta t} \tag{A.55}$$

where,

$$F_{reattch} = e^{-\left(\frac{R_T}{20}\right)^4} \tag{A.56}$$

$$\gamma_{eff} = max\left(\gamma, \gamma_{sep}\right) \tag{A.57}$$

C_{s1} is a constant with a value of 2.0.

To couple the transition model to the SST turbulence model, the k- transport equation (A.1) needs to be modified as follows:

$$\frac{\partial(\rho k)}{\partial t} + \frac{\partial\left(\rho u_j k\right)}{\partial x_j} = G_k^* - Y_k^* + \frac{\partial}{\partial x_j}\left[\Gamma_k \frac{\partial k}{\partial x_j}\right] \tag{A.58}$$

where,

$$G_k^* = \gamma_{eff} G_k \tag{A.59}$$

$$Y_k^* = min\left(max\left(\gamma_{eff}, 0.1\right). 1.0\right)Y_k \tag{A.60}$$

where G_k and Y_k are the original production and destruction terms for the SST k-ω model.

Appendix B BEM Code

```
clear all
close all
data=xlsread('NACA_0015_CFD_FINAL.xlsx');tt=117;
ang=data(1:tt,1);C_l1=data(1:tt,2);C_d1=data(1:tt,3);C_l2=data(1:tt,
4);C_d2=data(1:tt,5);C_l3=data(1:tt,6);C_d3=data(1:tt,7);C_l4=data(1
:tt,8);C_d4=data(1:tt,9);C_l5=data(1:tt,10);C_d5=data(1:tt,11);
rho=1000; mu=1.62e-3; cwater=1482; uinf=0.75;
R=0.5; no=41; H=2*R; H0=1; N=3; dh=(H)/no; c=0.135*R; xc=0; yc=0;
zc=0; xr=R; yr=R; zr=H/2;
t1=linspace(0,1,(no/2)+1); diff=t1(2)-t1(1); t2=linspace(1-
diff,0,no/2); t=[t1 t2];
TSREQ=3;omega=TSREQ*uinf/R;
for i=1:no
    x(i)=R*t(i)*cos(t(i));y(i)=R*t(i)*sin(t(i)); x2(i)=sqrt((R^2)-
(y(i)^2));
    if i <= no/2
        z(i)=zr*abs(sqrt(1-((x(i)^2)/(xr^2))-((y(i)^2)/(yr^2))));
    else
        z(i)=-zr*abs(sqrt(1-((x(i)^2)/(xr^2))-((y(i)^2)/(yr^2))));
    end
    r(i)=R; angle2(i)=abs(atand(y(i)/x2(i)));
angle(i)=90;%angle(i)=abs(atand(z(i)/r(i)))%
end
for bb=2:no
    d(bb)=sqrt(((x(bb)-x(bb-1))^2)+((y(bb)-y(bb-1))^2)+((z(bb)-z(bb-
1))^2));
end
Le=sum(d(:));
amax=max(angle2);angle3=angle2-amax;w=0.1;
HEQ=H0+(H/2);
n=72;convv=0.000001;
theta=linspace(0,360,n);
for ii=2:n
    dtheta(ii)=theta(ii)-theta(ii-1);
end
dtheta(1)=dtheta(2);
t_c=.15; AM=6; SC=0.06+(1.5*(0.06-t_c)); C_L0=0; alpha0=0;
M1L=0.4+(5*(0.06-t_c));M2L=0.9+(2.5*(0.06-t_c));ymaxL=1.4-(6*(0.06-
(t_c)));M1D=0.2;M2D=0.7+(2.5*(0.06-(t_c)));ymaxD=1.0-(2.5*(0.06-
(t_c)));AR=Le/c;
if AR > 50
    CDMAX=1.11+(0.018*AR);
else
    CDMAX= 2.01;
end

for u=1:no
    %y1(u)=H0+R+z(u);
    %h(u)=y1(u)+2;
    %Vinf(u)=uinf*((h(u)/HEQ)^(1/7));
    Vinf(u)=uinf;
end
```

```
for m=1:n/2
    for k=1:no
        an=0.1;
        conv=1000;
        icount(k,m)=0;
        while conv > convv
            icount(k,m)=icount(k,m)+1;
            if icount(k,m)>=100
                break
            end
            a=an;
            newangle(k,m)=theta(m)+angle2(k);
            if newangle(k,m)>-2 & newangle(k,m)<0
                newangle(k,m)=-2;
            else if newangle(k,m)>=0 & newangle(k,m)<2
                    newangle(k,m)=2;
                else if newangle(k,m)>177 & newangle(k,m)<180
                        newangle(k,m)=177;
                    else if newangle(k,m)>=180 & newangle(k,m)<182
                            newangle(k,m)=182;
                        else if newangle(k,m)>358 &
newangle(k,m)<360
                                newangle(k,m)=358;
                            else if newangle(k,m)>=360 &
newangle(k,m)<362
                                    newangle(k,m)=362;
                                end
                            end
                        end
                    end
                end
            end
            L(k,m)=R*sind(newangle(k,m))*(dtheta(m)*pi/180);
            V(k,m)=(1-a)*Vinf(k);
            V_t(k,m)=omega*r(k); %

alpha(k,m)=atand((V(k,m)*sind(newangle(k,m))*sind(angle(k)))/((V(k,m
)*cosd(newangle(k,m)))+V_t(k,m)));

W(k,m)=V(k,m)*(sind(newangle(k,m))*sind(angle(k)))/sind(alpha(k,m));
            Re(k,m)=abs((W(k,m)*c*rho)/mu);
            Ma(k,m)=abs(W(k,m)/cwater);
            time(k,m)=(dtheta(m)*(pi/180))/omega;
            if m==1
                alphadot(k,m)=(((alpha(k,m)-0))*pi/180)/time(k,m);
            else
                alphadot(k,m)=(((alpha(k,m)-alpha(k,m-
1)))*pi/180)/time(k,m);
            end
            if alphadot(k,m)>=0
                K1= 1.0;
            else
                K1= -0.5;
            end
            S=sqrt(abs((c*alphadot(k,m))/(2*W(k,m))));
            y2L=ymaxL*max(0,(min(1,((Ma(k,m)-M2L)/(M1L-M2L)))));
            y2D=ymaxD*max(0,(min(1,((Ma(k,m)-M2D)/(M1D-M2D)))));
            y1L=y2L/2;
            y1D=0;
```

```
            if S<=SC
                dalphaL=y1L*S;
                dalphaD(k,m)=y1D*S;
                pp(k,m)=1;
            else
                dalphaL=(y1L*SC)+(y2L*(S-SC));
                dalphaD(k,m)=(y1D*SC)+(y2D*(S-SC));
                pp(k,m)=2;
            end
            alpharL(k,m)=alpha(k,m)-(K1*dalphaL);
            alpharD(k,m)=alpha(k,m)-(K1*dalphaD(k,m));
            if Re(k,m) <= 100000
                C_LS(k,m)=interp1(ang,C_l1,alpha(k,m));
C_DS(k,m)=interp1(ang,C_d1,alpha(k,m));
                C_LG(k,m)=interp1(ang,C_l1,alpharL(k,m));
C_DG(k,m)=interp1(ang,C_d1,alpharD(k,m));
                mm(k,m)=1; alphass(k,m)=5; alphas(k,m)=12;

C_LSS(k,m)=interp1(ang,C_l1,alphass(k,m));C_DSS(k,m)=interp1(ang,C_d
1,alphass(k,m));
            else if Re(k,m) > 100000 && Re(k,m) <= 250000
                    C_LS_low=interp1(ang,C_l1,alpha(k,m));
C_DS_low=interp1(ang,C_d1,alpha(k,m));
                    C_LS_high=interp1(ang,C_l2,alpha(k,m));
C_DS_high=interp1(ang,C_d2,alpha(k,m));
                    C_LS(k,m)=C_LS_low+(((Re(k,m)-100000)/(250000-
100000))*(C_LS_high-C_LS_low));
                    C_DS(k,m)=C_DS_low+(((Re(k,m)-100000)/(250000-
100000))*(C_DS_high-C_DS_low));
                    C_LG_low=interp1(ang,C_l1,alpharL(k,m));
C_DG_low=interp1(ang,C_d1,alpharL(k,m));
                    C_LG_high=interp1(ang,C_l2,alpharD(k,m));
C_DG_high=interp1(ang,C_d2,alpharD(k,m));
                    C_LG(k,m)=C_LG_low+(((Re(k,m)-100000)/(250000-
100000))*(C_LG_high-C_LG_low));
                    C_DG(k,m)=C_DG_low+(((Re(k,m)-100000)/(250000-
100000))*(C_DG_high-C_DG_low));
                    mm(k,m)=2; alphass(k,m)=8; alphas(k,m)=13;

C_LSS(k,m)=interp1(ang,C_l2,alphass(k,m));C_DSS(k,m)=interp1(ang,C_d
2,alphass(k,m));
                else if Re(k,m)>250000 && Re(k,m)<=500000
                        C_LS_low=interp1(ang,C_l2,alpha(k,m));
C_DS_low=interp1(ang,C_d2,alpha(k,m));
                        C_LS_high=interp1(ang,C_l3,alpha(k,m));
C_DS_high=interp1(ang,C_d3,alpha(k,m));
                        C_LS(k,m)=C_LS_low+(((Re(k,m)-
250000)/(500000-250000))*(C_LS_high-C_LS_low));
                        C_DS(k,m)=C_DS_low+(((Re(k,m)-
250000)/(500000-250000))*(C_DS_high-C_DS_low));
                        C_LG_low=interp1(ang,C_l2,alpharL(k,m));
C_DG_low=interp1(ang,C_d2,alpharL(k,m));
                        C_LG_high=interp1(ang,C_l3,alpharD(k,m));
C_DG_high=interp1(ang,C_d3,alpharD(k,m));
                        C_LG(k,m)=C_LG_low+(((Re(k,m)-
250000)/(500000-250000))*(C_LG_high-C_LG_low));
                        C_DG(k,m)=C_DG_low+(((Re(k,m)-
250000)/(500000-250000))*(C_DG_high-C_DG_low));
                        mm(k,m)=3; alphass(k,m)=11; alphas(k,m)=15;
```

```
C_LSS(k,m)=interp1(ang,C_l3,alphass(k,m));C_DSS(k,m)=interp1(ang,C_d
3,alphass(k,m));
                    else if Re(k,m)>500000 && Re(k,m)<=1000000
                            C_LS_low=interp1(ang,C_l3,alpha(k,m));
C_DS_low=interp1(ang,C_d3,alpha(k,m));
                            C_LS_high=interp1(ang,C_l4,alpha(k,m));
C_DS_high=interp1(ang,C_d4,alpha(k,m));
                            C_LS(k,m)=C_LS_low+(((Re(k,m)-
500000)/(1000000-500000))*(C_LS_high-C_LS_low));
                            C_DS(k,m)=C_DS_low+(((Re(k,m)-
500000)/(1000000-500000))*(C_DS_high-C_DS_low));
                            C_LG_low=interp1(ang,C_l3,alpharL(k,m));
C_DG_low=interp1(ang,C_d3,alpharL(k,m));

C_LG_high=interp1(ang,C_l4,alpharD(k,m));
C_DG_high=interp1(ang,C_d4,alpharD(k,m));
                            C_LG(k,m)=C_LG_low+(((Re(k,m)-
500000)/(1000000-500000))*(C_LG_high-C_LG_low));
                            C_DG(k,m)=C_DG_low+(((Re(k,m)-
500000)/(1000000-500000))*(C_DG_high-C_DG_low));
                            mm(k,m)=4; alphass(k,m)=12;
alphas(k,m)=16;

C_LSS(k,m)=interp1(ang,C_l4,alphass(k,m));C_DSS(k,m)=interp1(ang,C_d
4,alphass(k,m));
                        else if Re(k,m)>1000000 && Re(k,m)<=2000000

C_LS_low=interp1(ang,C_l4,alpha(k,m));
C_DS_low=interp1(ang,C_d4,alpha(k,m));

C_LS_high=interp1(ang,C_l5,alpha(k,m));
C_DS_high=interp1(ang,C_d5,alpha(k,m));
                                C_LS(k,m)=C_LS_low+(((Re(k,m)-
1000000)/(2000000-1000000))*(C_LS_high-C_LS_low));
                                C_DS(k,m)=C_DS_low+(((Re(k,m)-
1000000)/(2000000-1000000))*(C_DS_high-C_DS_low));

C_LG_low=interp1(ang,C_l4,alpharL(k,m));
C_DG_low=interp1(ang,C_d4,alpharD(k,m));

C_LG_high=interp1(ang,C_l5,alpharL(k,m));
C_DG_high=interp1(ang,C_d5,alpharD(k,m));
                                C_LG(k,m)=C_LG_low+(((Re(k,m)-
1000000)/(2000000-1000000))*(C_LG_high-C_LG_low));
                                C_DG(k,m)=C_DG_low+(((Re(k,m)-
1000000)/(2000000-1000000))*(C_DG_high-C_DG_low));
                                mm(k,m)=5; alphass(k,m)=13;
alphas(k,m)=16;

C_LSS(k,m)=interp1(ang,C_l5,alphass(k,m));C_DSS(k,m)=interp1(ang,C_d
5,alphass(k,m));
                            else

C_LS(k,m)=interp1(ang,C_l5,alpha(k,m));
C_DS(k,m)=interp1(ang,C_d5,alpha(k,m));

C_LG(k,m)=interp1(ang,C_l5,alpharL(k,m));
C_DG(k,m)=interp1(ang,C_d5,alpharD(k,m));
```

```
                                    mm(k,m)=6; alphass(k,m)=13;
alphas(k,m)=16;

C_LSS(k,m)=interp1(ang,C_l5,alphass(k,m));C_DSS(k,m)=interp1(ang,C_d
5,alphass(k,m));
                                end
                            end
                        end
                    end
                end
                mmm(k,m)=min(((C_LG(k,m)-0)/(alpharL(k,m)-
alpha0)),((C_LSS(k,m)-0)/(alphass(k,m)-alpha0)));
                C_LD(k,m)=C_L0+(mmm(k,m)*(alpha(k,m)-alpha0));
C_DD(k,m)=C_DG(k,m);
                check(k,m)=AM*alphass(k,m);
                if alpha(k,m)>check(k,m)
                    C_L(k,m)=C_LS(k,m); C_D(k,m)=C_DS(k,m);
                    bb(k,m)=1;
                else
                    C_L(k,m)=C_LS(k,m)+((check(k,m)-
alpha(k,m))/(check(k,m)-alphass(k,m)))*(C_LD(k,m)-C_LS(k,m));
                    C_D(k,m)=C_DS(k,m)+((check(k,m)-
alpha(k,m))/(check(k,m)-alphass(k,m)))*(C_DD(k,m)-C_DS(k,m));
                    bb(k,m)=2;
                end
                if alpha(k,m)<alphass(k,m) && alpha(k,m)>-alphass(k,m)
                    C_L_AR(k,m)= C_L(k,m);
                    C_D_AR(k,m)=C_D(k,m);
                    rrr(k,m)=1;
                else
                    A1(k,m)=CDMAX/2;
                    A2(k,m)=(C_LSS(k,m)-
(CDMAX*sind(alphas(k,m))*cosd(alphas(k,m))))*(sind(alphas(k,m))/(cos
d(alphas(k,m))^2));
                    B1(k,m)=CDMAX/2;
                    B2(k,m)=C_DSS(k,m)-
((CDMAX*(sind(alphas(k,m))^2))/cosd(alphas(k,m)));

C_L_A(k,m)=(A1(k,m)*sind(2*alpha(k,m)))+(A2(k,m)*((cosd(alpha(k,m))^
2)/(sind(alpha(k,m)))));

C_D_A(k,m)=(B1(k,m)*(sind(alpha(k,m))^2))+(B2(k,m)*cosd(alpha(k,m)))
;
                    C_L_AR(k,m)=(C_L_A(k,m)+C_L(k,m))/2;
                    C_D_AR(k,m)=(C_D_A(k,m)+C_D(k,m))/2;
                end
                C_T(k,m)=(C_L_AR(k,m)*sind(alpha(k,m)))-
(C_D_AR(k,m)*cosd(alpha(k,m)));

C_N(k,m)=(C_L_AR(k,m)*cosd(alpha(k,m)))+(C_D_AR(k,m)*sind(alpha(k,m)
));
                F_N(k,m)=-
0.5*C_N(k,m)*rho*(dh*c/(sind(angle(k))))*(W(k,m)^2);

F_T(k,m)=0.5*C_T(k,m)*rho*(dh*c/(sind(angle(k))))*(W(k,m)^2);
                Fx(k,m)=-
((F_N(k,m)*sind(angle(k))*sind(newangle(k,m)))+(F_T(k,m)*cosd(newang
le(k,m))));
```

```
F_x(k,m)=(N*Fx(k,m))/(4*pi*r(k)*rho*dh*abs(sind(newangle(k,m)))*(Vin
f(k)^2));
            if a<=0.4
                an=F_x(k,m)+(a^2);
            else
                an=F_x(k,m)+(a^2)*((5-(3*a))/4);
            end
            an=(w*an)+((1-w)*a);
            conv=abs((an-a)/an);
        end
        Save_conv(k,m)=conv;
        Save_a(k,m)=a;
        V_e(k,m)=Vinf(k)*(1-(2*Save_a(k,m)));

Q_i(k,m)=0.5*rho*r(k)*C_T(k,m)*(c*dh/sind(angle(k)))*(W(k,m)^2);
        Leq(k,m)=Vinf(k)*L(k,m)/V_e(k,m);
    end
end
for rr=1:no
    for pp=1:n/4
        if pp==n/4
            Vee(rr,pp)=V_e(rr,pp);
            mo(rr,pp)=3;
        else
            if L(rr,pp+1)+L(rr,pp)-Leq(rr,pp+1)>=0
                Vee(rr,pp)=((V_e(rr,pp+1)*((Leq(rr,pp+1)-
L(rr,pp+1))))+(V_e(rr,pp)*(L(rr,pp+1)+L(rr,pp)-
Leq(rr,pp+1))))/L(rr,pp);
                mo(rr,pp)=1;
            else
                Vee(rr,pp)=V_e(rr,pp+1);
                mo(rr,pp)=2;
            end
        end
    end
    for pp=(n/4)+1:n/2
        if pp==(n/4)+1;
            Vee(rr,pp)=V_e(rr,pp);
            mo(rr,pp)=3;
        else
            if L(rr,pp-1)+L(rr,pp)-Leq(rr,pp-1)>=0
                Vee(rr,pp-1)=V_e(rr,pp-1);
                Vee(rr,pp)=((V_e(rr,pp-1)*((Leq(rr,pp-1)-L(rr,pp-
1))))+(V_e(rr,pp)*(L(rr,pp-1)+L(rr,pp)-Leq(rr,pp-1))))/L(rr,pp);
                mo(rr,pp)=1;
            else
                Vee(rr,pp)=V_e(rr,pp-1);
                mo(rr,pp)=2;
            end
        end
    end
    for qqq=1:n/2
        V_E(rr,qqq+n/2)=Vee(rr,qqq);
    end
end
for m=(n/2)+1:n
    for k=1:no
        an=0;
        conv=1000;
```

```
        icount(k,m)=0;
        while conv > convv
            icount(k,m)=icount(k,m)+1;
            if icount(k,m)>=100
                break
            end
            a=an;
            newangle(k,m)=theta(m)+angle2(k);
            if newangle(k,m)>-2 & newangle(k,m)<0
                newangle(k,m)=-2;
            else if newangle(k,m)>=0 & newangle(k,m)<2
                    newangle(k,m)=2;
                else if newangle(k,m)>177 & newangle(k,m)<180
                        newangle(k,m)=177;
                    else if newangle(k,m)>=180 & newangle(k,m)<182
                            newangle(k,m)=182;
                        else if newangle(k,m)>358 &
newangle(k,m)<360
                                newangle(k,m)=358;
                            else if newangle(k,m)>=360 &
newangle(k,m)<362
                                    newangle(k,m)=362;
                                end
                            end
                        end
                    end
                end
            end
            L(k,m)=R*sind(newangle(k,m))*(dtheta(m)*pi/180);
            V(k,m)=(1-a)*V_E(k,m);
            V_t(k,m)=omega*r(k); %

alpha(k,m)=atand((V(k,m)*sind(newangle(k,m))*sind(angle(k)))/((V(k,m
)*cosd(newangle(k,m)))+V_t(k,m)));

W(k,m)=V(k,m)*(sind(newangle(k,m))*sind(angle(k)))/sind(alpha(k,m));
            Re(k,m)=abs((W(k,m)*c*rho)/mu);
            Ma(k,m)=abs(W(k,m)/cwater);
            time(k,m)=(dtheta(m)*(pi/180))/omega;
            if m==1
                alphadot(k,m)=(((alpha(k,m)-0))*pi/180)/time(k,m);
            else
                alphadot(k,m)=(((alpha(k,m)-alpha(k,m-
1)))*pi/180)/time(k,m);
            end
            if alphadot(k,m)>=0
                K1= 1.0;
            else
                K1= -0.5;
            end
            S=sqrt(abs((c*alphadot(k,m))/(2*W(k,m))));
            y2L=ymaxL*max(0,(min(1,((Ma(k,m)-M2L)/(M1L-M2L)))));
            y2D=ymaxD*max(0,(min(1,((Ma(k,m)-M2D)/(M1D-M2D)))));
            y1L=y2L/2;
            y1D=0;
            if S<=SC
                dalphaL=y1L*S;
                dalphaD(k,m)=y1D*S;
                pp(k,m)=1;
            else
```

```
                dalphaL=(y1L*SC)+(y2L*(S-SC));
                dalphaD(k,m)=(y1D*SC)+(y2D*(S-SC));
                pp(k,m)=2;
            end
            alpharL(k,m)=alpha(k,m)-(K1*dalphaL);
            alpharD(k,m)=alpha(k,m)-(K1*dalphaD(k,m));
            if Re(k,m) <= 100000
                C_LS(k,m)=interp1(ang,C_l1,alpha(k,m));
C_DS(k,m)=interp1(ang,C_d1,alpha(k,m));
                C_LG(k,m)=interp1(ang,C_l1,alpharL(k,m));
C_DG(k,m)=interp1(ang,C_d1,alpharD(k,m));
                mm(k,m)=1; alphass(k,m)=5; alphas(k,m)=12;

C_LSS(k,m)=interp1(ang,C_l1,alphass(k,m));C_DSS(k,m)=interp1(ang,C_d
1,alphass(k,m));
            else if Re(k,m) > 100000 && Re(k,m) <= 250000
                    C_LS_low=interp1(ang,C_l1,alpha(k,m));
C_DS_low=interp1(ang,C_d1,alpha(k,m));
                    C_LS_high=interp1(ang,C_l2,alpha(k,m));
C_DS_high=interp1(ang,C_d2,alpha(k,m));
                    C_LS(k,m)=C_LS_low+(((Re(k,m)-100000)/(250000-
100000))*(C_LS_high-C_LS_low));
                    C_DS(k,m)=C_DS_low+(((Re(k,m)-100000)/(250000-
100000))*(C_DS_high-C_DS_low));
                    C_LG_low=interp1(ang,C_l1,alpharL(k,m));
C_DG_low=interp1(ang,C_d1,alpharL(k,m));
                    C_LG_high=interp1(ang,C_l2,alpharD(k,m));
C_DG_high=interp1(ang,C_d2,alpharD(k,m));
                    C_LG(k,m)=C_LG_low+(((Re(k,m)-100000)/(250000-
100000))*(C_LG_high-C_LG_low));
                    C_DG(k,m)=C_DG_low+(((Re(k,m)-100000)/(250000-
100000))*(C_DG_high-C_DG_low));
                    mm(k,m)=2; alphass(k,m)=8; alphas(k,m)=13;

C_LSS(k,m)=interp1(ang,C_l2,alphass(k,m));C_DSS(k,m)=interp1(ang,C_d
2,alphass(k,m));
                else if Re(k,m)>250000 && Re(k,m)<=500000
                        C_LS_low=interp1(ang,C_l2,alpha(k,m));
C_DS_low=interp1(ang,C_d2,alpha(k,m));
                        C_LS_high=interp1(ang,C_l3,alpha(k,m));
C_DS_high=interp1(ang,C_d3,alpha(k,m));
                        C_LS(k,m)=C_LS_low+(((Re(k,m)-
250000)/(500000-250000))*(C_LS_high-C_LS_low));
                        C_DS(k,m)=C_DS_low+(((Re(k,m)-
250000)/(500000-250000))*(C_DS_high-C_DS_low));
                        C_LG_low=interp1(ang,C_l2,alpharL(k,m));
C_DG_low=interp1(ang,C_d2,alpharL(k,m));
                        C_LG_high=interp1(ang,C_l3,alpharD(k,m));
C_DG_high=interp1(ang,C_d3,alpharD(k,m));
                        C_LG(k,m)=C_LG_low+(((Re(k,m)-
250000)/(500000-250000))*(C_LG_high-C_LG_low));
                        C_DG(k,m)=C_DG_low+(((Re(k,m)-
250000)/(500000-250000))*(C_DG_high-C_DG_low));
                        mm(k,m)=3; alphass(k,m)=11; alphas(k,m)=15;

C_LSS(k,m)=interp1(ang,C_l3,alphass(k,m));C_DSS(k,m)=interp1(ang,C_d
3,alphass(k,m));
                    else if Re(k,m)>500000 && Re(k,m)<=1000000
                            C_LS_low=interp1(ang,C_l3,alpha(k,m));
C_DS_low=interp1(ang,C_d3,alpha(k,m));
```

```
                                C_LS_high=interp1(ang,C_l4,alpha(k,m));
C_DS_high=interp1(ang,C_d4,alpha(k,m));
                                C_LS(k,m)=C_LS_low+(((Re(k,m)-
500000)/(1000000-500000))*(C_LS_high-C_LS_low));
                                C_DS(k,m)=C_DS_low+(((Re(k,m)-
500000)/(1000000-500000))*(C_DS_high-C_DS_low));
                                C_LG_low=interp1(ang,C_l3,alpharL(k,m));
C_DG_low=interp1(ang,C_d3,alpharL(k,m));

C_LG_high=interp1(ang,C_l4,alpharD(k,m));
C_DG_high=interp1(ang,C_d4,alpharD(k,m));
                                C_LG(k,m)=C_LG_low+(((Re(k,m)-
500000)/(1000000-500000))*(C_LG_high-C_LG_low));
                                C_DG(k,m)=C_DG_low+(((Re(k,m)-
500000)/(1000000-500000))*(C_DG_high-C_DG_low));
                                mm(k,m)=4; alphass(k,m)=12;
alphas(k,m)=16;

C_LSS(k,m)=interp1(ang,C_l4,alphass(k,m));C_DSS(k,m)=interp1(ang,C_d
4,alphass(k,m));
                            else if Re(k,m)>1000000 && Re(k,m)<=2000000

C_LS_low=interp1(ang,C_l4,alpha(k,m));
C_DS_low=interp1(ang,C_d4,alpha(k,m));

C_LS_high=interp1(ang,C_l5,alpha(k,m));
C_DS_high=interp1(ang,C_d5,alpha(k,m));
                                    C_LS(k,m)=C_LS_low+(((Re(k,m)-
1000000)/(2000000-1000000))*(C_LS_high-C_LS_low));
                                    C_DS(k,m)=C_DS_low+(((Re(k,m)-
1000000)/(2000000-1000000))*(C_DS_high-C_DS_low));

C_LG_low=interp1(ang,C_l4,alpharL(k,m));
C_DG_low=interp1(ang,C_d4,alpharD(k,m));

C_LG_high=interp1(ang,C_l5,alpharL(k,m));
C_DG_high=interp1(ang,C_d5,alpharD(k,m));
                                    C_LG(k,m)=C_LG_low+(((Re(k,m)-
1000000)/(2000000-1000000))*(C_LG_high-C_LG_low));
                                    C_DG(k,m)=C_DG_low+(((Re(k,m)-
1000000)/(2000000-1000000))*(C_DG_high-C_DG_low));
                                    mm(k,m)=5; alphass(k,m)=13;
alphas(k,m)=16;

C_LSS(k,m)=interp1(ang,C_l5,alphass(k,m));C_DSS(k,m)=interp1(ang,C_d
5,alphass(k,m));
                                else
C_LS(k,m)=interp1(ang,C_l5,alpha(k,m));
C_DS(k,m)=interp1(ang,C_d5,alpha(k,m));

C_LG(k,m)=interp1(ang,C_l5,alpharL(k,m));
C_DG(k,m)=interp1(ang,C_d5,alpharD(k,m));
                                    mm(k,m)=6; alphass(k,m)=13;
alphas(k,m)=16;

C_LSS(k,m)=interp1(ang,C_l5,alphass(k,m));C_DSS(k,m)=interp1(ang,C_d
5,alphass(k,m));
                                end
                            end
                        end
```

```
                end
            end
            mmm(k,m)=min(((C_LG(k,m)-0)/(alpharL(k,m)-
alpha0)),((C_LSS(k,m)-0)/(alphass(k,m)-alpha0)));
            C_LD(k,m)=C_L0+(mmm(k,m)*(alpha(k,m)-alpha0));
C_DD(k,m)=C_DG(k,m);
            check(k,m)=AM*alphass(k,m);
            if alpha(k,m)>check(k,m)
                C_L(k,m)=C_LS(k,m); C_D(k,m)=C_DS(k,m);
                bb(k,m)=1;
            else
                C_L(k,m)=C_LS(k,m)+((check(k,m)-
alpha(k,m))/(check(k,m)-alphass(k,m)))*(C_LD(k,m)-C_LS(k,m));
                C_D(k,m)=C_DS(k,m)+((check(k,m)-
alpha(k,m))/(check(k,m)-alphass(k,m)))*(C_DD(k,m)-C_DS(k,m));
                bb(k,m)=2;
            end
            if alpha(k,m)<alphass(k,m) && alpha(k,m)>-alphass(k,m)
                    C_L_AR(i,j,k)=C_LS(k,m);
                    C_D_AR(i,j,k)=C_DS(k,m);
            else
                A1(k,m)=CDMAX/2;
                A2(k,m)=(C_LSS(k,m)-
(CDMAX*sind(alphas(k,m))*cosd(alphas(k,m))))*(sind(alphas(k,m))/(cos
d(alphas(k,m))^2));
                B1(k,m)=CDMAX/2;
                B2(k,m)=C_DSS(k,m)-
((CDMAX*(sind(alphas(k,m))^2))/cosd(alphas(k,m)));

C_L_A(k,m)=(A1(k,m)*sind(2*alpha(k,m)))+(A2(k,m)*((cosd(alpha(k,m))^
2)/(sind(alpha(k,m)))));

C_D_A(k,m)=(B1(k,m)*(sind(alpha(k,m))^2))+(B2(k,m)*cosd(alpha(k,m)))
;
                C_L_AR(k,m)=(C_L_A(k,m)+C_L(k,m))/2;
                C_D_AR(k,m)=(C_D_A(k,m)+C_D(k,m))/2;
            end
            C_T(k,m)=(C_L_AR(k,m)*sind(alpha(k,m)))-
(C_D_AR(k,m)*cosd(alpha(k,m)));

C_N(k,m)=(C_L_AR(k,m)*cosd(alpha(k,m)))+(C_D_AR(k,m)*sind(alpha(k,m)
));
            F_N(k,m)=-
0.5*C_N(k,m)*rho*(dh*c/(sind(angle(k))))*(W(k,m)^2);

F_T(k,m)=0.5*C_T(k,m)*rho*(dh*c/(sind(angle(k))))*(W(k,m)^2);
            Fx(k,m)=-
((F_N(k,m)*sind(angle(k))*sind(newangle(k,m)))+(F_T(k,m)*cosd(newang
le(k,m))));
F_x(k,m)=(N*Fx(k,m))/(4*pi*r(k)*rho*dh*abs(sind(newangle(k,m)))*(V_E
(k,m)^2));
            if a<=0.4
                an=F_x(k,m)+(a^2);
            else
                an=F_x(k,m)+(a^2)*((5-(3*a))/4);
            end
            an=(w*an)+((1-w)*a);
            conv=abs((an-a)/an);
        end
        Save_conv(k,m)=conv;
```

```
        Save_a(k,m)=a;
Q_i(k,m)=0.5*rho*r(k)*C_T(k,m)*(c*dh/sind(angle(k)))*(W(k,m)^2);
    end
end
for zz=1:n
    Q1(zz)=sum(Q_i(:,zz));
    CQ(zz)=Q1(zz)/(0.5*rho*R*c*H*(uinf^2));
end
for jj=1:no
    x(jj)=2*r(jj)*dh*(Vinf(jj)^3);
end
Qavg=(N/n)*sum(Q1);
CP=(Qavg*omega)/(0.5*rho*sum(x));
SAVE_CP=CP
```

Appendix C Start-up Model

```
clear all
close all
R=1; no=41; H=2; N=3; dh=(H)/no; c=0.12*R; xc=0; yc=0; zc=0; xr=R;
yr=R; zr=H/2; J=12;
t1=linspace(0,1,(no/2)+1); diff=t1(2)-t1(1); t2=linspace(1-
diff,0,no/2); t=[t1 t2]; H0=0;
for l=1:no
    x(l)=R*t(l)*cos(t(l)); y(l)=R*t(l)*sin(t(l)); x2(l)=sqrt((R^2)-
(y(l)^2));
    if l <= no/2
        z(l)=zr*abs(sqrt(1-((x(l)^2)/(xr^2))-((y(l)^2)/(yr^2))));
    else
        z(l)=-zr*abs(sqrt(1-((x(l)^2)/(xr^2))-((y(l)^2)/(yr^2))));
    end
    angle2(l)=abs(atand(y(l)/x2(l)));dH(l)=H/no;
end
for bb=2:no
    d(bb)=sqrt(((x(bb)-x(bb-1))^2)+((y(bb)-y(bb-1))^2)+((z(bb)-z(bb-
1))^2));
end
Le=sum(d(:));
data=xlsread('NACA_0015_CFD_FINAL.xlsx');tt=117;
ang=data(1:tt,1);C_l1=data(1:tt,2);C_d1=data(1:tt,3);C_l2=data(1:tt,
4);C_d2=data(1:tt,5);C_l3=data(1:tt,6);C_d3=data(1:tt,7);C_l4=data(1
:tt,8);C_d4=data(1:tt,9);C_l5=data(1:tt,10);C_d5=data(1:tt,11);
rho=997; mu=1.62e-3; cwater=1482; u_inf=2;
n=30000;deltat=0.001;tmax=n*deltat;t=linspace(0,tmax,n);
theta1=30; thetai=[theta1 theta1+120 theta1+240];
Qi=0;
kQL=0;
TSR_d=3.125;
omega_d=(u_inf*TSR_d)/R;
ang_vel(1)=0;ang_dis(1)=0;TSR(1)=0;v(1)=0;
cf=0.002;dshaft=0.03;Q_cog=0.6;
t_c=.15; AM=6; SC=0.06+(1.5*(0.06-t_c)); C_L0=0; alpha0=0;
```

```
M1L=0.4+(5*(0.06-t_c));M2L=0.9+(2.5*(0.06-t_c));ymaxL=1.4-(6*(0.06-
(t_c)));M1D=0.2;M2D=0.7+(2.5*(0.06-(t_c)));ymaxD=1.0-(2.5*(0.06-
(t_c)));AR=Le/c;
if AR > 50
    CDMAX=1.11+(0.018*AR);
else
    CDMAX= 2.01;
end
for i = 1:n
    if i == 1
        TSR(i)=(ang_vel(i)*R)/u_inf;
        for j = 1:N
            for k = 1:no
            theta(i,j,k)=thetai(j)+angle2(k);

alpha(i,j,k)=atand(sind(theta(i,j,k))/(cosd(theta(i,j,k))+TSR(i)));

W(i,j,k)=u_inf*(sqrt((sind(theta(i,j,k))^2)+((cosd(theta(i,j,k))+TSR
(i))^2)));
            Re(i,j,k)=(rho*W(i,j,k)*c/mu);
            Ma(i,j,k)=abs(W(i,j,k)/cwater);
            if i==1
                    alphadot(i,j,k)=(((alpha(i,j,k)-
0))*pi/180)/deltat;
            else
                    alphadot(i,j,k)=(((alpha(i,j,k)-alpha(i-
1,j,k)))*pi/180)/deltat;
            end
                if alphadot(i,j,k)>=0
                    K1= 1.0;
                else
                    K1= -0.5;
                end
                S=sqrt(abs((c*alphadot(i,j,k))/(2*W(i,j,k))));
                y2L=ymaxL*max(0,(min(1,((Ma(i,j,k)-M2L)/(M1L-
M2L)))));
                y2D=ymaxD*max(0,(min(1,((Ma(i,j,k)-M2D)/(M1D-
M2D)))));
                y1L=y2L/2;
                y1D=0;
                if S<=SC
                    dalphaL=y1L*S;
                    dalphaD(i,j,k)=y1D*S;
                else
                    dalphaL=(y1L*SC)+(y2L*(S-SC));
                    dalphaD(i,j,k)=(y1D*SC)+(y2D*(S-SC));
                end
                alpharL(i,j,k)=alpha(i,j,k)-(K1*dalphaL);
                alpharD(i,j,k)=alpha(i,j,k)-(K1*dalphaD(i,j,k));
                if Re(i,j,k) <= 100000
                    C_LS(i,j,k)=interp1(ang,C_l1,alpha(i,j,k));
C_DS(i,j,k)=interp1(ang,C_d1,alpha(i,j,k));
                    C_LG(i,j,k)=interp1(ang,C_l1,alpharL(i,j,k));
C_DG(i,j,k)=interp1(ang,C_d1,alpharD(i,j,k));
                    mm(i,j,k)=1; alphass(i,j,k)=5; alphas(i,j,k)=12;

C_LSS(i,j,k)=interp1(ang,C_l1,alphass(i,j,k));C_DSS(i,j,k)=interp1(a
ng,C_d1,alphass(i,j,k));
                else if Re(i,j,k) > 100000 && Re(i,j,k) <= 250000
```

```
                        C_LS_low=interp1(ang,C_l1,alpha(i,j,k));
C_DS_low=interp1(ang,C_d1,alpha(i,j,k));
                        C_LS_high=interp1(ang,C_l2,alpha(i,j,k));
C_DS_high=interp1(ang,C_d2,alpha(i,j,k));
                        C_LS(i,j,k)=C_LS_low+(((Re(i,j,k)-
100000)/(250000-100000))*(C_LS_high-C_LS_low));
                        C_DS(i,j,k)=C_DS_low+(((Re(i,j,k)-
100000)/(250000-100000))*(C_DS_high-C_DS_low));
                        C_LG_low=interp1(ang,C_l1,alpharL(i,j,k));
C_DG_low=interp1(ang,C_d1,alpharL(i,j,k));
                        C_LG_high=interp1(ang,C_l2,alpharD(i,j,k));
C_DG_high=interp1(ang,C_d2,alpharD(i,j,k));
                        C_LG(i,j,k)=C_LG_low+(((Re(i,j,k)-
100000)/(250000-100000))*(C_LG_high-C_LG_low));
                        C_DG(i,j,k)=C_DG_low+(((Re(i,j,k)-
100000)/(250000-100000))*(C_DG_high-C_DG_low));
                        mm(i,j,k)=2; alphass(i,j,k)=8;
alphas(i,j,k)=13;

C_LSS(i,j,k)=interp1(ang,C_l2,alphass(i,j,k));C_DSS(i,j,k)=interp1(a
ng,C_d2,alphass(i,j,k));
                    else if Re(i,j,k)>250000 && Re(i,j,k)<=500000
                            C_LS_low=interp1(ang,C_l2,alpha(i,j,k));
C_DS_low=interp1(ang,C_d2,alpha(i,j,k));

C_LS_high=interp1(ang,C_l3,alpha(i,j,k));
C_DS_high=interp1(ang,C_d3,alpha(i,j,k));
                            C_LS(i,j,k)=C_LS_low+(((Re(i,j,k)-
250000)/(500000-250000))*(C_LS_high-C_LS_low));
                            C_DS(i,j,k)=C_DS_low+(((Re(i,j,k)-
250000)/(500000-250000))*(C_DS_high-C_DS_low));

C_LG_low=interp1(ang,C_l2,alpharL(i,j,k));
C_DG_low=interp1(ang,C_d2,alpharL(i,j,k));

C_LG_high=interp1(ang,C_l3,alpharD(i,j,k));
C_DG_high=interp1(ang,C_d3,alpharD(i,j,k));
                            C_LG(i,j,k)=C_LG_low+(((Re(i,j,k)-
250000)/(500000-250000))*(C_LG_high-C_LG_low));
                            C_DG(i,j,k)=C_DG_low+(((Re(i,j,k)-
250000)/(500000-250000))*(C_DG_high-C_DG_low));
                            mm(i,j,k)=3; alphass(i,j,k)=11;
alphas(i,j,k)=15;

C_LSS(i,j,k)=interp1(ang,C_l3,alphass(i,j,k));C_DSS(i,j,k)=interp1(a
ng,C_d3,alphass(i,j,k));
                        else if Re(i,j,k)>500000 &&
Re(i,j,k)<=1000000

C_LS_low=interp1(ang,C_l3,alpha(i,j,k));
C_DS_low=interp1(ang,C_d3,alpha(i,j,k));

C_LS_high=interp1(ang,C_l4,alpha(i,j,k));
C_DS_high=interp1(ang,C_d4,alpha(i,j,k));
                                C_LS(i,j,k)=C_LS_low+(((Re(i,j,k)-
500000)/(1000000-500000))*(C_LS_high-C_LS_low));
                                C_DS(i,j,k)=C_DS_low+(((Re(i,j,k)-
500000)/(1000000-500000))*(C_DS_high-C_DS_low));
```

```
C_LG_low=interp1(ang,C_l3,alpharL(i,j,k));
C_DG_low=interp1(ang,C_d3,alpharL(i,j,k));

C_LG_high=interp1(ang,C_l4,alpharD(i,j,k));
C_DG_high=interp1(ang,C_d4,alpharD(i,j,k));
                                C_LG(i,j,k)=C_LG_low+(((Re(i,j,k)-
500000)/(1000000-500000))*(C_LG_high-C_LG_low));
                                C_DG(i,j,k)=C_DG_low+(((Re(i,j,k)-
500000)/(1000000-500000))*(C_DG_high-C_DG_low));
                                mm(i,j,k)=4; alphass(i,j,k)=12;
alphas(i,j,k)=16;

C_LSS(i,j,k)=interp1(ang,C_l4,alphass(i,j,k));C_DSS(i,j,k)=interp1(a
ng,C_d4,alphass(i,j,k));
                            else if Re(i,j,k)>1000000 &&
Re(i,j,k)<=2000000

C_LS_low=interp1(ang,C_l4,alpha(i,j,k));
C_DS_low=interp1(ang,C_d4,alpha(i,j,k));

C_LS_high=interp1(ang,C_l5,alpha(i,j,k));
C_DS_high=interp1(ang,C_d5,alpha(i,j,k));

C_LS(i,j,k)=C_LS_low+(((Re(i,j,k)-1000000)/(2000000-
1000000))*(C_LS_high-C_LS_low));

C_DS(i,j,k)=C_DS_low+(((Re(i,j,k)-1000000)/(2000000-
1000000))*(C_DS_high-C_DS_low));

C_LG_low=interp1(ang,C_l4,alpharL(i,j,k));
C_DG_low=interp1(ang,C_d4,alpharD(i,j,k));

C_LG_high=interp1(ang,C_l5,alpharL(i,j,k));
C_DG_high=interp1(ang,C_d5,alpharD(i,j,k));

C_LG(i,j,k)=C_LG_low+(((Re(i,j,k)-1000000)/(2000000-
1000000))*(C_LG_high-C_LG_low));

C_DG(i,j,k)=C_DG_low+(((Re(i,j,k)-1000000)/(2000000-
1000000))*(C_DG_high-C_DG_low));
                                mm(i,j,k)=5; alphass(i,j,k)=13;
alphas(i,j,k)=16;

C_LSS(i,j,k)=interp1(ang,C_l5,alphass(i,j,k));C_DSS(i,j,k)=interp1(a
ng,C_d5,alphass(i,j,k));
                                else

C_LS(i,j,k)=interp1(ang,C_l5,alpha(i,j,k));
C_DS(i,j,k)=interp1(ang,C_d5,alpha(i,j,k));

C_LG(i,j,k)=interp1(ang,C_l5,alpharL(i,j,k));
C_DG(i,j,k)=interp1(ang,C_d5,alpharD(i,j,k));
                                mm(i,j,k)=6; alphass(i,j,k)=13;
alphas(i,j,k)=16;

C_LSS(i,j,k)=interp1(ang,C_l5,alphass(i,j,k));C_DSS(i,j,k)=interp1(a
ng,C_d5,alphass(i,j,k));
                                end
                            end
```

```
                        end
                    end
                end
                mmm(i,j,k)=min(((C_LG(i,j,k)-0)/(alpharL(i,j,k)-
alpha0)),((C_LSS(i,j,k)-0)/(alphass(i,j,k)-alpha0)));
                C_LD(i,j,k)=C_L0+(mmm(i,j,k)*(alpha(i,j,k)-alpha0));
C_DD(i,j,k)=C_DG(i,j,k);
                check(i,j,k)=AM*alphass(i,j,k);
                if alpha(i,j,k)>check(i,j,k)
                    C_L(i,j,k)=C_LS(i,j,k); C_D(i,j,k)=C_DS(i,j,k);
                else
                    C_L(i,j,k)=C_LS(i,j,k)+((check(i,j,k)-
alpha(i,j,k))/(check(i,j,k)-alphass(i,j,k)))*(C_LD(i,j,k)-
C_LS(i,j,k));
                    C_D(i,j,k)=C_DS(i,j,k)+((check(i,j,k)-
alpha(i,j,k))/(check(i,j,k)-alphass(i,j,k)))*(C_DD(i,j,k)-
C_DS(i,j,k));
                end
                if alpha(i,j,k)<alphass(i,j,k) && alpha(i,j,k)>-
alphass(i,j,k)

C_L_AR(i,j,k)=(2*3.14*sind(alpha(i,j,k)))/(1+(2*AR));

C_D_AR(i,j,k)=C_D(i,j,k)+((C_L_AR(i,j,k)^2)/(3.14*AR));
                else
                    A1(i,j,k)=CDMAX/2;
                    A2(i,j,k)=(C_LSS(i,j,k)-
(CDMAX*sind(alphas(i,j,k))*cosd(alphas(i,j,k))))*(sind(alphas(i,j,k)
))/(cosd(alphas(i,j,k))^2));
                    B1(i,j,k)=CDMAX/2;
                    B2(i,j,k)=C_DSS(i,j,k)-
((CDMAX*(sind(alphas(i,j,k))^2))/cosd(alphas(i,j,k)));

C_L_A(i,j,k)=(A1(i,j,k)*sind(2*alpha(i,j,k)))+(A2(i,j,k)*((cosd(alph
a(i,j,k))^2)/(sind(alpha(i,j,k)))));

C_D_A(i,j,k)=(B1(i,j,k)*(sind(alpha(i,j,k))^2))+(B2(i,j,k)*cosd(alph
a(i,j,k)));
                    C_L_AR(i,j,k)=(C_L_A(i,j,k)+C_L(i,j,k))/2;
                    C_D_AR(i,j,k)=(C_D_A(i,j,k)+C_D(i,j,k))/2;
                end
            C_T(i,j,k)=(C_L(i,j,k)*sind(alpha(i,j,k)))-
(C_D(i,j,k)*cosd(alpha(i,j,k)));
            F_T(i,j,k)=0.5*C_T(i,j,k)*rho*dH(k)*c*(W(i,j,k)^2);
            Q_i(i,j,k)=F_T(i,j,k)*R;
            end
        end
        Q_iT(i,j)=sum(Q_i(i,j,:));
        Q_iTT(i)=sum(Q_iT(i,:));
        P(i)=Q_iTT(i)*ang_vel(i);
        Q_res(i)=(0.5*cf*P(i)*dshaft)+Q_cog;
        ang_acc(i)=(Q_iTT(i)-Q_res(i))/J;
    else
        ang_vel(i)=ang_vel(i-1)+(ang_acc(i-1)*deltat);
        if ang_vel(i) >= omega_d
            ang_vel(i)= omega_d;
        else
            ang_vel(i)=ang_vel(i);
        end
```

```
        ang_dis(i)=(ang_vel(i-1)*deltat+(0.5*ang_acc(i-
1)*(deltat^2)))*(180/pi);
        TSR(i)=(ang_vel(i)*R)/u_inf;
        for j=1:3
            for k = 1:no
            theta(i,j,k)=wrapTo360(theta(i-
1,j,k)+angle2(k)+ang_dis(i));

alpha(i,j,k)=atand(sind(theta(i,j,k))/(cosd(theta(i,j,k))+TSR(i)));

W(i,j,k)=u_inf*(sqrt((sind(theta(i,j,k))^2)+((cosd(theta(i,j,k))+TSR
(i))^2)));
            Re(i,j,k)=(rho*W(i,j,k)*c/mu);
            Ma(i,j,k)=abs(W(i,j,k)/cwater);
            if i==1;
                    alphadot(i,j,k)=(((alpha(i,j,k)-
0))*pi/180)/deltat;
            else
                    alphadot(i,j,k)=(((alpha(i,j,k)-alpha(i-
1,j,k)))*pi/180)/deltat;
            end
                if alphadot(i,j,k)>=0
                    K1= 1.0;
                else
                    K1= -0.5;
                end
                S=sqrt(abs((c*alphadot(i,j,k))/(2*W(i,j,k))));
                y2L=ymaxL*max(0,(min(1,((Ma(i,j,k)-M2L)/(M1L-
M2L)))));
                y2D=ymaxD*max(0,(min(1,((Ma(i,j,k)-M2D)/(M1D-
M2D)))));
                y1L=y2L/2;
                y1D=0;
                if S<=SC
                    dalphaL=y1L*S;
                    dalphaD(i,j,k)=y1D*S;
                else
                    dalphaL=(y1L*SC)+(y2L*(S-SC));
                    dalphaD(i,j,k)=(y1D*SC)+(y2D*(S-SC));
                end
                alpharL(i,j,k)=alpha(i,j,k)-(K1*dalphaL);
                alpharD(i,j,k)=alpha(i,j,k)-(K1*dalphaD(i,j,k));
                if Re(i,j,k) <= 100000
                    C_LS(i,j,k)=interp1(ang,C_l1,alpha(i,j,k));
C_DS(i,j,k)=interp1(ang,C_d1,alpha(i,j,k));
                    C_LG(i,j,k)=interp1(ang,C_l1,alpharL(i,j,k));
C_DG(i,j,k)=interp1(ang,C_d1,alpharD(i,j,k));
                    mm(i,j,k)=1; alphass(i,j,k)=5; alphas(i,j,k)=12;

C_LSS(i,j,k)=interp1(ang,C_l1,alphass(i,j,k));C_DSS(i,j,k)=interp1(a
ng,C_d1,alphass(i,j,k));
                else if Re(i,j,k) > 100000 && Re(i,j,k) <= 250000
                            C_LS_low=interp1(ang,C_l1,alpha(i,j,k));
C_DS_low=interp1(ang,C_d1,alpha(i,j,k));
                            C_LS_high=interp1(ang,C_l2,alpha(i,j,k));
C_DS_high=interp1(ang,C_d2,alpha(i,j,k));
                            C_LS(i,j,k)=C_LS_low+(((Re(i,j,k)-
100000)/(250000-100000))*(C_LS_high-C_LS_low));
                            C_DS(i,j,k)=C_DS_low+(((Re(i,j,k)-
100000)/(250000-100000))*(C_DS_high-C_DS_low));
```

```
                        C_LG_low=interp1(ang,C_l1,alpharL(i,j,k));
C_DG_low=interp1(ang,C_d1,alpharL(i,j,k));
                        C_LG_high=interp1(ang,C_l2,alpharD(i,j,k));
C_DG_high=interp1(ang,C_d2,alpharD(i,j,k));
                        C_LG(i,j,k)=C_LG_low+(((Re(i,j,k)-
100000)/(250000-100000))*(C_LG_high-C_LG_low));
                        C_DG(i,j,k)=C_DG_low+(((Re(i,j,k)-
100000)/(250000-100000))*(C_DG_high-C_DG_low));
                        mm(i,j,k)=2; alphass(i,j,k)=8;
alphas(i,j,k)=13;

C_LSS(i,j,k)=interp1(ang,C_l2,alphass(i,j,k));C_DSS(i,j,k)=interp1(a
ng,C_d2,alphass(i,j,k));
                    else if Re(i,j,k)>250000 && Re(i,j,k)<=500000
                            C_LS_low=interp1(ang,C_l2,alpha(i,j,k));
C_DS_low=interp1(ang,C_d2,alpha(i,j,k));

C_LS_high=interp1(ang,C_l3,alpha(i,j,k));
C_DS_high=interp1(ang,C_d3,alpha(i,j,k));
                            C_LS(i,j,k)=C_LS_low+(((Re(i,j,k)-
250000)/(500000-250000))*(C_LS_high-C_LS_low));
                            C_DS(i,j,k)=C_DS_low+(((Re(i,j,k)-
250000)/(500000-250000))*(C_DS_high-C_DS_low));

C_LG_low=interp1(ang,C_l2,alpharL(i,j,k));
C_DG_low=interp1(ang,C_d2,alpharL(i,j,k));

C_LG_high=interp1(ang,C_l3,alpharD(i,j,k));
C_DG_high=interp1(ang,C_d3,alpharD(i,j,k));
                            C_LG(i,j,k)=C_LG_low+(((Re(i,j,k)-
250000)/(500000-250000))*(C_LG_high-C_LG_low));
                            C_DG(i,j,k)=C_DG_low+(((Re(i,j,k)-
250000)/(500000-250000))*(C_DG_high-C_DG_low));
                            mm(i,j,k)=3; alphass(i,j,k)=11;
alphas(i,j,k)=15;

C_LSS(i,j,k)=interp1(ang,C_l3,alphass(i,j,k));C_DSS(i,j,k)=interp1(a
ng,C_d3,alphass(i,j,k));
                        else if Re(i,j,k)>500000 &&
Re(i,j,k)<=1000000

C_LS_low=interp1(ang,C_l3,alpha(i,j,k));
C_DS_low=interp1(ang,C_d3,alpha(i,j,k));

C_LS_high=interp1(ang,C_l4,alpha(i,j,k));
C_DS_high=interp1(ang,C_d4,alpha(i,j,k));
                                C_LS(i,j,k)=C_LS_low+(((Re(i,j,k)-
500000)/(1000000-500000))*(C_LS_high-C_LS_low));
                                C_DS(i,j,k)=C_DS_low+(((Re(i,j,k)-
500000)/(1000000-500000))*(C_DS_high-C_DS_low));

C_LG_low=interp1(ang,C_l3,alpharL(i,j,k));
C_DG_low=interp1(ang,C_d3,alpharL(i,j,k));

C_LG_high=interp1(ang,C_l4,alpharD(i,j,k));
C_DG_high=interp1(ang,C_d4,alpharD(i,j,k));
                                C_LG(i,j,k)=C_LG_low+(((Re(i,j,k)-
500000)/(1000000-500000))*(C_LG_high-C_LG_low));
                                C_DG(i,j,k)=C_DG_low+(((Re(i,j,k)-
500000)/(1000000-500000))*(C_DG_high-C_DG_low));
```

```
                                    mm(i,j,k)=4; alphass(i,j,k)=12;
alphas(i,j,k)=16;

C_LSS(i,j,k)=interp1(ang,C_l4,alphass(i,j,k));C_DSS(i,j,k)=interp1(a
ng,C_d4,alphass(i,j,k));
                                else if Re(i,j,k)>1000000 &&
Re(i,j,k)<=2000000

C_LS_low=interp1(ang,C_l4,alpha(i,j,k));
C_DS_low=interp1(ang,C_d4,alpha(i,j,k));

C_LS_high=interp1(ang,C_l5,alpha(i,j,k));
C_DS_high=interp1(ang,C_d5,alpha(i,j,k));

C_LS(i,j,k)=C_LS_low+(((Re(i,j,k)-1000000)/(2000000-
1000000))*(C_LS_high-C_LS_low));

C_DS(i,j,k)=C_DS_low+(((Re(i,j,k)-1000000)/(2000000-
1000000))*(C_DS_high-C_DS_low));

C_LG_low=interp1(ang,C_l4,alpharL(i,j,k));
C_DG_low=interp1(ang,C_d4,alpharD(i,j,k));

C_LG_high=interp1(ang,C_l5,alpharL(i,j,k));
C_DG_high=interp1(ang,C_d5,alpharD(i,j,k));

C_LG(i,j,k)=C_LG_low+(((Re(i,j,k)-1000000)/(2000000-
1000000))*(C_LG_high-C_LG_low));

C_DG(i,j,k)=C_DG_low+(((Re(i,j,k)-1000000)/(2000000-
1000000))*(C_DG_high-C_DG_low));
                                        mm(i,j,k)=5; alphass(i,j,k)=13;
alphas(i,j,k)=16;

C_LSS(i,j,k)=interp1(ang,C_l5,alphass(i,j,k));C_DSS(i,j,k)=interp1(a
ng,C_d5,alphass(i,j,k));
                                    else

C_LS(i,j,k)=interp1(ang,C_l5,alpha(i,j,k));
C_DS(i,j,k)=interp1(ang,C_d5,alpha(i,j,k));

C_LG(i,j,k)=interp1(ang,C_l5,alpharL(i,j,k));
C_DG(i,j,k)=interp1(ang,C_d5,alpharD(i,j,k));
                                        mm(i,j,k)=6; alphass(i,j,k)=13;
alphas(i,j,k)=16;

C_LSS(i,j,k)=interp1(ang,C_l5,alphass(i,j,k));C_DSS(i,j,k)=interp1(a
ng,C_d5,alphass(i,j,k));
                                    end
                                end
                            end
                        end
                    end
                    mmm(i,j,k)=min(((C_LG(i,j,k)-0)/(alpharL(i,j,k)-
alpha0)),((C_LSS(i,j,k)-0)/(alphass(i,j,k)-alpha0)));
                    C_LD(i,j,k)=C_L0+(mmm(i,j,k)*(alpha(i,j,k)-alpha0));
C_DD(i,j,k)=C_DG(i,j,k);
                    check(i,j,k)=AM*alphass(i,j,k);
                    if alpha(i,j,k)>check(i,j,k)
                        C_L(i,j,k)=C_LS(i,j,k); C_D(i,j,k)=C_DS(i,j,k);
```

```
                else
                    C_L(i,j,k)=C_LS(i,j,k)+((check(i,j,k)-
alpha(i,j,k))/(check(i,j,k)-alphass(i,j,k)))*(C_LD(i,j,k)-
C_LS(i,j,k));
                    C_D(i,j,k)=C_DS(i,j,k)+((check(i,j,k)-
alpha(i,j,k))/(check(i,j,k)-alphass(i,j,k)))*(C_DD(i,j,k)-
C_DS(i,j,k));
                end
                if alpha(i,j,k)<alphass(i,j,k) && alpha(i,j,k)>-
alphass(i,j,k)
                    C_L_AR(i,j,k)=C_LS(i,j,k);
                    C_D_AR(i,j,k)=C_DS(i,j,k);
                else
                    A1(i,j,k)=CDMAX/2;
                    A2(i,j,k)=(C_LSS(i,j,k)-
(CDMAX*sind(alphas(i,j,k))*cosd(alphas(i,j,k))))*(sind(alphas(i,j,k)
))/(cosd(alphas(i,j,k))^2));
                    B1(i,j,k)=CDMAX/2;
                    B2(i,j,k)=C_DSS(i,j,k)-
((CDMAX*(sind(alphas(i,j,k))^2))/cosd(alphas(i,j,k)));

C_L_A(i,j,k)=(A1(i,j,k)*sind(2*alpha(i,j,k)))+(A2(i,j,k)*((cosd(alph
a(i,j,k))^2)/(sind(alpha(i,j,k)))));

C_D_A(i,j,k)=(B1(i,j,k)*(sind(alpha(i,j,k))^2))+(B2(i,j,k)*cosd(alph
a(i,j,k)));
                    C_L_AR(i,j,k)=(C_L_A(i,j,k)+C_L(i,j,k))/2;
                    C_D_AR(i,j,k)=(C_D_A(i,j,k)+C_D(i,j,k))/2;
                end
            C_T(i,j,k)=(C_L(i,j,k)*sind(alpha(i,j,k)))-
(C_D(i,j,k)*cosd(alpha(i,j,k)));
            C_T(i,j,k)=(C_LS(i,j,k)*sind(alpha(i,j,k)))-
(C_DS(i,j,k)*cosd(alpha(i,j,k)));
            F_T(i,j,k)=0.5*C_T(i,j,k)*rho*dH(k)*c*(W(i,j,k)^2);
            Q_i(i,j,k)=F_T(i,j,k)*R;
            end
        end
        Q_iT(i,j)=sum(Q_i(i,j,:));
        Q_iTT(i)=sum(Q_iT(i,:));
        P(i)=Q_iTT(i)*ang_vel(i);
        Q_res(i)=(0.5*cf*P(i)*dshaft)+Q_cog;
        ang_acc(i)=(Q_iTT(i)-QL(i)-Q_res(i))/J;
    end
end
w_max=max(abs(ang_vel))
```